DYNAMICAL CHARACTERISTICS OF REACTING BLUFF BODY WAKES

A Dissertation
Presented to
The Academic Faculty

By

Benjamin Emerson

In Partial Fulfillment
Of the Requirements for the Degree
Doctor of Philosophy in Aerospace Engineering

Georgia Institute of Technology

August, 2013

Copyright © Benjamin Emerson 2013

DYNAMICAL CHARACTERISTICS OF REACTING BLUFF BODY WAKES

Approved by:

Dr. Tim Lieuwen, Advisor
School of Aerospace Engineering
Georgia Institute of Technology

Dr. Jechiel Jagoda
School of Aerospace Engineering
Georgia Institute of Technology

Dr. Jerry Seitzman
School of Aerospace Engineering
Georgia Institute of Technology

Dr. Ari Glezer
School of Mechanical Engineering
Georgia Institute of Technology

Dr. Suresh Menon
School of Aerospace Engineering
Georgia Institute of Technology

Date Approved: June 13, 2013

ACKNOWLEDGEMENTS

I would like to sincerely thank and acknowledge a number of people for helping me with my graduate studies, the writing of this PhD thesis, and my personal development. First, I would like to thank my advisor, Professor Tim Lieuwen, for his guidance and instruction. Tim has committed a significant amount of his own time to guiding this project, and has led me to a valuable analytical mindset that I could not have developed without him, and which has been critical to my success. Also, I would like to acknowledge Tim's leadership. I have met no other person who can lead such a strong-spirited, happy group of hard working, high achievers. It has been a pleasure working with him, and I am very thankful for the experience.

Next, I would like to thank the Aerospace Engineering faculty at Georgia Tech for their guidance, advice, and many hours dedicated to teaching me. In particular, I would like to thank Professors Jerry Seitzman, Ben Zinn, Jechiel Jagoda, Suresh Menon, P. K. Yeung, Krishan Ahuja, and Tim Lieuwen. In addition, I would like to explicitly thank my committee members, Professors Lieuwen, Seitzman, Menon, Jagoda, and Glezer, for taking the time to help polish my work.

I cannot close this chapter of my life without acknowledging my wife, Kelsey. Her encouragement has led me into graduate school as well as the PhD program. Kelsey has been extremely supportive, and always knows what to say to keep my confidence high. I can never thank her enough for supporting me during the late nights, the qualifying exams, and my annoying tendency to point out exciting fluid dynamic phenomena in every day situations.

I would also like to acknowledge my parents, Nancy and Ben Emerson. They have both served as role models for my personal development, behavior, and general attitude towards life. The wide range of activities and experiences that they have handed to me from my first day through today have helped me discover who I am, what I am good at, and what I enjoy. They have been extremely supportive of all of my major life decisions. In addition, I should also acknowledge my brother, Taylor. Whenever I had a wild idea, from turbocharging one of the family cars to building rockets, he was the first to hear about it and he never doubted the eventual success of the endeavor. I was truly blessed to grow up with such a good best friend. It is much easier to flourish when you have strong roots.

Finally, I must acknowledge my fellow grad students and research engineers at the combustion lab. Special thanks first to Bobby Noble, who took notice of me when I was an undergraduate researcher and made sure that I had a shot at grad school. Thank you to Karthik Periagaram, Caleb Cross, Jacqueline O'Connor, Jack Crawford, Dong-Hyuk Shin, Prabhakar Venkateswaran, David Scarborough, Brad Ochs, and Oleksandr Bibik for teaching me so much. Thank you to the members of the coffee room: Andrew M, Matt, Chris, and Ben, for all of the long, intellectual conversations (and coffee!) Thank you to Aimee and Alex for making the ITAR office feel like home. Thank you to Ryan, Julia, Andrew I, Mike M, Mike A, Brandon, Ianko, Travis, Nick, Vishal, Alberto, and Luke- you are fantastic colleagues. Ianko, thank you for the friendship and for making me a better athlete. Thank you Shane for pushing me to begin every day with an early start, good exercise, and great conversation, and for all of your help in the lab. Finally,

thank you to the general combustion community members at Georgia Tech- you have been great friends and colleagues.

TABLE OF CONTENTS

LIST OF TABLES

LIST OF FIGURES

NOMENCLATURE

A_f	Forcing amplitude
A_{lip}	Cross sectional flow area at bluff body lip
$\hat{B}$	Bispectrum of discrete signal
C_3	Third order cumulant spectrum (bispectrum)
D	Bluff body diameter (transverse span)
F	Fraction of time that $r_f > r_t$
H	Cross-stream channel width
I_{turb}	Turbulence intensity
$L_{\max}$	Axial position of maximum reverse flow
L_r	Recirculation zone length
$L_{Stagger}$	Distance required for vortices to stagger
N_e	Number of ensembles
N_s	Number of samples
Q	Spatially integrated (global) heat release
R	Gas constant
Re_D	Reynolds number based on bluff body diameter
S	Local flame area perturbation
St_D	Strouhal number based on bluff body diameter
S_{Mie}	Density ratio estimated from Mie scattering images
T	Temperature
T_{in}	Inlet temperature
T_n	Natural period of oscillation
U_{av}	Average velocity (of bulk and reverse flow)

U_b	Base flow burned gas velocity
U_{lip}	Nominal bluff body lip velocity
U_u	Base flow unburned gas velocity
b^2	Squared bicoherence
c	Hydrodynamic wave propagation speed
c_3	Third order cumulant
f	frequency
f_{BVK}	von Kármán vortex shedding frequency
f_f	Forcing frequency
f_g	Predicted global mode frequency
f_{KH}	Kelvin-Helmholtz frequency
f_n	Natural or measured global mode frequency
f_r	Response frequency
f_{sample}	Sampling frequency
k	wavenumber
k_0	absolute wavenumber
$\dot{m}_{lip}$	Mass flowrate entering combustor
p	Pressure
q	Local heat release amplitude at f_f
q^-	Heat release amplitude of lower flame branch
q^+	Heat release amplitude of upper flame branch
r_f	Correleation coefficient between time signal and sinusoid
$r_{U,L}$	Correlation coefficient between upper and lower flame edge displacement
r_t	Threshold correlation coefficient value
t	time

u	stream-wise (axial) velocity
$\vec{u}$	velocity vector
v	cross-stream (transverse) velocity
w	out of page (spanwise) velocity
x	stream-wise (axial) coordinate
x_{AI}	Axial position of peak absolute instability
y	cross-stream (transverse) coordinate
Δf_{Lock}	Frequency range for frequency locking
$\Delta\varphi$	Degree of stagger of vortices or flame edge
Ω	Out-of page vorticity component
$\vec{\Omega}$	Vorticity vector
α	confinement parameter
β	Base flow backflow ratio
γ	Specific heat ratio
δ_u	Transverse position of velocity discontinuity
δ_ρ	Transverse position of density discontinuity
ζ	Flame edge position
ζ_{FWHM}	Full width at half max of chemiluminescence profile of one flame branch
θ	Momentum thickness
λ_C	Convective wavelength
η'	Fluctuating component of transverse position of hydrodynamic interface
ψ	Stream function
ρ	Density
ρ_{lip}	Density of gas entering combustor
$\underline{\underline{\tau}}$	Viscous stress tensor
$\tau_{n,j}$	j^{th} noisy event

$\tau_{s,i}$ ith sinuous event

ϕ Equivalence ratio

φ_L Lower flame branch displacement phase

φ_U Upper flame branch displacement phase

φ_{v+} Transverse velocity phase at y/D = +0.3

φ_{v-} Transverse velocity phase at y/D = -0.3

ω Radial frequency

ω_0 Absolute frequency

ω_g Global mode frequency

Operations

$(\ )_0$ Time-averaged component

$(\ )_L$ Lower flame branch

$(\ )_U$ Upper flame branch

$(\ )_b$ Burned gas quantity

$(\ )_{,i}$ Imaginary component of complex quantity

$(\ )_{,r}$ Real component of complex quantity

$(\ )^*$ Complex conjugate

$(\ )'_{rms}$ Root mean square of quantity

$(\ )_u$ Unburned gas quantity

$(\ )'$ Fluctuating component

$(\hat{\ })$ Fourier transform

$(\ )^+$ Quantity on upper side of interface

$(\ )^-$ Quantity on lower side of interface

SUMMARY

Combustion instability plagues the combustion community in a wide range of applications. This un-solved problem is especially prevalent and expensive in aerospace propulsion and ground power generation. The challenges associated with understanding and predicting combustion instability lie in the flame response to the acoustic field. One of the more complicated flame response mechanisms is the velocity coupled flame response, where the flame responds dynamically to the acoustic velocity as well as the vortically induced velocity field excited by the acoustics. This vortically induced, or hydrodynamic, velocity field holds critical importance to the flame response but is computationally expensive to predict, often requiring high fidelity CFD computations. Furthermore, its behavior can be a strong function of the numerous flow parameters that change over the operability map of a combustor.

This research focuses on a nominally two dimensional bluff body combustor, which has rich hydrodynamic stability behavior with a manageable number of stability parameters. The work focuses first on experimentally characterizing the dynamical flow and flame behavior. Next, the research shifts focus toward hydrodynamic stability theory, using it to explain the physical phenomena observed in the experimental work. Additionally, the hydrodynamic stability work shows how the use of simple, model analysis can identify the important stability parameters and elucidate their governing physical roles. Finally, the research explores the forced response of the flow and flame while systematically varying the underlying hydrodynamic stability characteristics. In the case of longitudinal combustion instability of highly preheated bluff body

combustors, it shows that conditions where an acoustic mode frequency equals the hydrodynamic global mode frequency are not especially dangerous from a combustion instability standpoint, and may actually have a reduced heat release response. This demonstrates the very non-intuitive role that the natural hydrodynamic flow stability plays in the forced heat release response of the flame.

For the fluid mechanics community, this work contributes to the detailed understanding of both unforced and forced bluff body combustor dynamics, and shows how each is influenced by the underlying hydrodynamics. In particular, it emphasizes the role of the density-shear layer offset, and shows how its extreme sensitivity leads to complicated flow dynamics. For the flow-combustor community as a whole, the work reviews a pre-existing method to obtain the important flow stability parameters, and demonstrates a novel way to link those parameters to the governing flow physics. For the combustion instability community, this thesis emphasizes the importance of the hydrodynamic stability characteristics of the flow, and concludes by offering a paradigm for consideration of the hydrodynamics in a combustion instability problem.

CHAPTER 1. INTRODUCTION

1.1 Bluff Body Combustors

The technological setting of this thesis is bluff body combustors. Bluff body combustors are prevalent in industrial and aerospace applications; for example, bluff body combustors are a popular method for flame stabilization in simple duct burners. The work is motivated by understanding the role of hydrodynamics in the combustion instability of these and other systems. Before discussing the details of the background and motivation for this work, which come in the next chapter, it is helpful to introduce the basics of bluff body flames. Therefore, this chapter provides a very brief introduction to bluff body flames and the problem of combustion instability. The details and literature review associated with these concepts are provided in Chapter 2, *Background and Motivation*.

The bulk flow speed in combustors is typically much greater than the flame speed. This necessitates a method for anchoring the flame so that the flame is not blown off and exhausted from the combustor. In premixed combustors, this is done by creating a location in the combustor where the flame speed and the flow speed are equal. This can be accomplished aerodynamically by placing a blunt object in the flow, known as a bluff body or a flameholder, which forms a wake in the flow. This wake serves the purpose of locally slowing the gas so that the flame becomes anchored immediately behind the bluff body; from this anchoring location, the flame propagates freely into the unburned reactant mixture. For a bluff body which spans a rectangular channel, this tends to create a nominally two-dimensional "V" shaped flame, like the one illustrated in Figure 1-1.

Compare this to an actual time-averaged chemiluminescence image from the current work in Figure 1-2a.

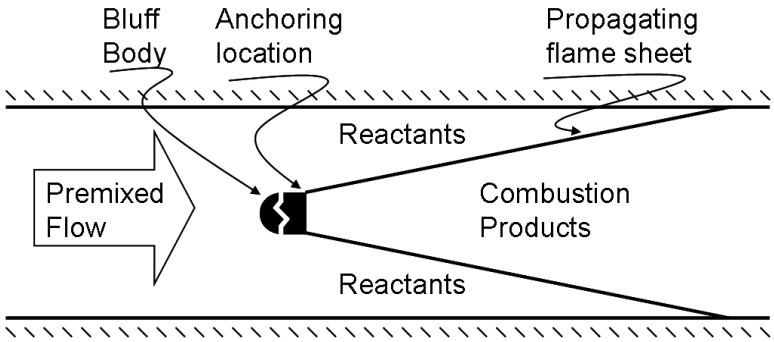

Figure 1-1. Notional cartoon of bluff body stabilized flame

a) **b)**

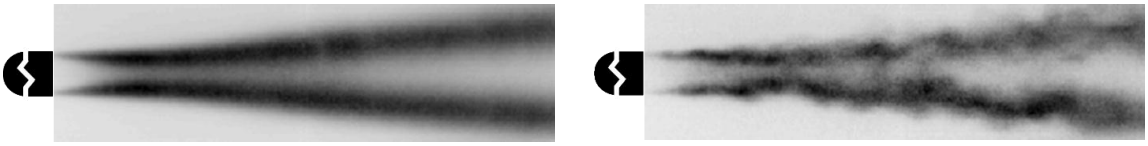

Figure 1-2. Line of sight chemiluminescence flame images showing a) a time-averaged flame image and b) an instantaneous flame image (1/5000th second exposure)

While the bluff body flame stabilization ideas discussed above are conceptually simple, the details of the fluid dynamics in the high Reynolds number wake of a bluff body can complicate the picture. As will be investigated in detail throughout the thesis, acoustic waves and coherent structures born from hydrodynamic instabilities (as well as broadband turbulence) can disturb the flame front from the nominal V shape in Figure 1-1, leading to a temporally evolving, wrinkled flame. This is illustrated above in Figure 1-2b, which shows an instantaneous flame image.

1.2 Combustion Instability in Bluff Body Combustors

Bluff body combustors of industrial interest usually involve significant heat release confined inside a hard-walled duct. Therefore, they are prone to resonant coupling between the duct acoustic modes and the unsteady heat release of combustion. This is a thermoacoustic instability, known specifically as combustion instability, which can cause severe damage to hardware, heat transfer issues, and even blowout of the flame. Additionally, combustion instability is an expensive, unsolved issue in rockets and the lean premixed combustors used in ground power generating gas turbines. Although these systems typically do not employ bluff body combustors, the relative simplicity of planar bluff body flows facilitates the detailed study of many key processes involved in the combustion instability phenomenon.

As mentioned above, combustion instability involves a coupling between acoustic oscillations and the oscillatory heat release of the flame. This self excited feedback loop therefore relies on the response of the flame to the acoustic field. The mechanisms by which the acoustic motions can influence the flame dynamics are numerous. One such mechanism is through hydrodynamic motions in the wake of the bluff body that are excited by the acoustic field. As such, combustion instability is sensitive to hydrodynamic flow stability characteristics. Therefore, the hydrodynamic stability of reacting bluff body wakes and its impact on the flame response to acoustic forcing is the focus of this thesis.

1.3 Research Topics

This effort has four objectives, which are detailed at the end of Chapter 2, *Background and Motivation*, and categorized here as follows. The first objective is the experimental

exploration of hydrodynamic instabilities in reacting bluff body wakes. The second objective is the direct comparison of the experimentally observed unsteady flame and flow features to hydrodynamic stability calculations. The third objective is the use of hydrodynamic stability analysis to identify the key parameters and physical processes that govern the flow stability. The fourth objective is application of the first three objectives to combustion instability by experimentally observing the flame response to acoustic forcing while varying the background hydrodynamic stability characteristics.

CHAPTER 2. BACKGROUND AND MOTIVATION

2.1 Nonreacting Bluff Body Literature

The concepts in this chapter lay a critical foundation for the work presented in this thesis. The chapter begins with a review of un-forced, non-reacting bluff body wakes. This includes the identification of time-averaged wake features, as well as the unsteady, large-scale coherent structures found in these flows. The chapter then shifts focus to the bluff body hydrodynamic stability literature. These hydrodynamics concepts are useful for understanding the final three topics of the chapter: reacting wakes, acoustically forced wakes, and combustion instability.

The unsteady flow fields of reacting bluff body wakes are often dominated by large scale coherent structures, embedded upon a background of acoustic waves and broadband fine scale turbulence. These large scale structures play important roles in such processes as combustion instabilities [1-5], mixing and entrainment, flashback, and blowoff [1], and they arise because of underlying hydrodynamic instabilities of the flow field [2]. There are two key flow features downstream of the bluff body in high Reynolds number flows; these include the separating free shear layers [3] and the wake, both of which strongly influence the flame. Flow visualization of a typical non-reacting bluff body flowfield is shown in Figure 2-1. The separated shear layer is *convectively* unstable due to the Kelvin-Helmholtz mechanism for $Re_D >\sim 1200$ [4], leading to shear layer rollup into tightly concentrated vorticity. This induces a flow field that wraps the flame around these regions of concentrated vorticity [5]. In most practical configurations, the flame lies nearly parallel to the flow and, thus, almost directly in the bluff body shear layer for

high velocity flows. Small perturbations in convectively unstable flows are amplified as they convect downstream, but not locally at their source locations. In other words, convectively unstable flows have positive temporal growth rates for one or more disturbance wavelengths with nonzero group velocity, but all disturbances of zero group velocity are damped. These flows are disturbance amplifiers [6-8].

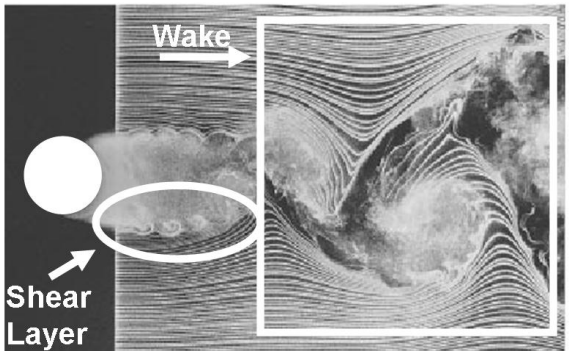

Figure 2-1. Visualization of flow past a bluff body at *Re* = 10,000, reproduced from Prasad and Williamson [4]

The time averaged bluff body flowfield has one major feature, the recirculation zone, which is represented in Figure 2-2 by streamlines from a PIV measurement. In non-reacting flows, this recirculation zone typically hosts a large pocket of absolute instability. This results in a globally unstable wake characterized by large scale, asymmetric rollup of the wake into staggered vortical structures [9]. The key distinction from a convectively unstable flow is that an absolutely unstable flow profile leads to amplification of some disturbances of zero group velocity. Therefore, the associated global instability features a flow exhibiting intrinsic oscillations at a global mode frequency [6-8]. In bluff body wakes, this instability is often referred to as the Von Karman vortex street, and has a characteristic frequency [4] of

$$f_{bvk} = St_D \frac{U_{lip}}{D} \tag{2.1}$$

where St_D is the Strouhal number. For circular cylinders, St_D is independent of Reynolds number ($St_D = 0.21$) in the turbulent shear layer, laminar boundary layer regime, $\sim 1000 < Re_D < \sim 200,000$ [10]. Above $Re_D = \sim 200,000$, the boundary layer starts to transition to turbulence and there are some indications that this Strouhal number value changes [11-12]. The concepts of convective, absolute, and global instability mentioned in the above paragraphs are discussed in significantly more detail below in section 2.2, *Hydrodynamic Stability Analysis of Planar Wake Flows*.

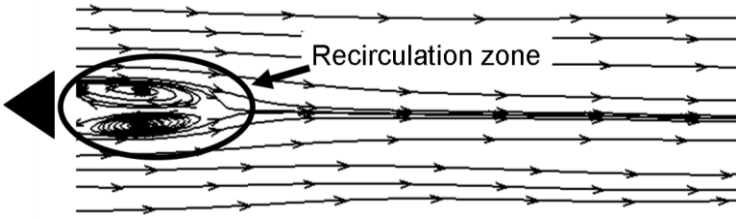

Figure 2-2. Streamlines and vectors measured using PIV, illustrating the time-averaged bluff body flowfield

Bluff body shape also influences the Strouhal number for the Von Karman vortex street [13]. In particular, St_D is lower for "bluffer" bodies, i.e., those with higher drag and wider wakes [14]. For example, $St_D \sim 0.18$ for a 90 degree "v-gutter" and drops to 0.13 for a sharp edge, vertical flat plate [15]. Roshko [14, 16] suggests that St_D fundamentally scales with the wake width and, therefore, care must be applied in inferring Strouhal numbers from one bluff body shape to another. For example, flow separation is retarded for circular bluff bodies when the boundary layer transitions to

turbulence, implying a reduction in wake width and turbulent vortex roll-up [17]. In contrast, the flow separation point often does not move in bluff bodies with sharp trailing edges.

2.2 Hydrodynamic Stability Analysis of Planar Wake Flows

This chapter now shifts focus to hydrodynamic stability theory with application to planar wake flows. The concepts discussed here serve as background for the reacting and forced wake phenomena introduced at the end of this chapter. The discussion begins with local, spatio-temporal stability analysis. Spatio-temporal stability analysis was first used in the context of stratified wake and jet flows by Yu and Monkewitz [18]. More recently, Juniper et al. [19] have developed a significant computational framework for this type of analysis, with application to wakes, jets, and swirling jets. This work has been especially useful for determining the role of confinement in the hydrodynamic stability of wake flows.

Local, spatio-temporal stability analysis is used to distinguish between absolutely and convectively unstable regions in the flow. In general, a flow that temporally amplifies a disturbance of any single wavelength is temporally unstable. If the group velocities of all temporally amplified disturbances are nonzero, the flow is convectively unstable. Physically, this means that while the envelope of the packet of disturbance waves is growing in time, it is being convected away from its point of origin in the lab-fixed reference frame. Thus, a particular location in a convectively unstable flow will exhibit oscillations only if perturbations are continuously fed to the instability. Thus, these flows behave as disturbance amplifiers.

Absolute instability is purely a local concept, meaning that it describes flow profiles in a nominally parallel flow, for example at a fixed axial position. The distinction between absolute and convective instability depends on the long-time behavior of the flow dynamics in the lab-fixed reference frame after a finite-duration perturbation. The instability is absolute if any temporally amplified wavelength has a zero group velocity. Physically, this represents the situation when the disturbance envelope grows temporally while remaining at the location of its inception. These types of flows are self-excited, meaning that they continue to oscillate in the lab-fixed reference frame once they are perturbed. Unlike a convectively unstable flow, oscillations persist without continuous excitation. If a sufficiently large "pocket" of absolute instability exists, this region may serve as a wave-maker which drives a global instability. Global instability occurs when the self-excited oscillations permeate the entire flow, creating a temporally growing and oscillating spatial pattern known as the global mode. Note that global instability describes the physical embodiment of the instability, while absolute instability is a local construct which describes a local flow profile.

As mentioned above, the local stability analysis is concerned with flow profiles, typically at fixed axial positions. As such, the analysis of a given flow involves the analyses of many slices of the flow, each at a unique axial position. The inputs to the analysis include the Reynolds number and the base flow, which consists of mean velocity and density profiles. The general analysis procedure involves the solution of a dispersion relation, which is an equation or family of equations that relate the wavenumber and frequency of harmonic flow disturbance oscillations. Solution of the dispersion relation results in a complex eigenvalue, which is the unknown frequency or wavenumber, and an

eigenvector, which provides the mode shape of the flow disturbances. If a real frequency is used to solve the dispersion relation, the resulting complex wavenumber is the solution to a spatial stability problem. This complex wavenumber contains the wavenumber of the disturbance as well as the spatial growth rate. If a real wavenumber is input, a temporal stability analysis is performed where the dispersion relation is solved for the complex frequency. The complex frequency contains information on the temporal frequency and growth rate. In a spatio-temporal stability analysis, the frequency and wavenumber may both be complex simultaneously. This analysis is used to identify the temporal frequency, temporal growth rate, and complex wavenumber corresponding to a wave packet with zero group velocity. These are known as the absolute frequency, absolute growth rate, and absolute wavenumber, respectively. Generally, if an unstable global mode exists, its frequency will be close to the absolute frequencies from the region of absolute instability.

The implications of the global/convective instability distinction above are particularly significant in thermoacoustic instability problems, where vortical structures excited by acoustic waves play important roles in the feedback mechanism [20]. The convectively unstable system is quite sensitive to acoustic excitation [21] and tends to amplify them. In contrast, the absolutely unstable system is an oscillator – it exhibits intrinsic, self-excited oscillations and does not require external disturbances to persist. In such a self-excited system, the limit cycle behavior may remain independent of the external forcing, unless the amplitude is high enough that the phenomenon of "lock-in" occurs [13, 22]. In one case, low amplitude acoustic excitation will induce a proportional response while

in the other it may not. In turn, this has important implications on which type of flow instabilities can be involved in linear combustion instability mechanisms.

The baseline flow stability characteristics of the two-dimensional wake can be altered by heating the fluid in the wake [16-18, 23-24], by addition of a splitter plate [3], and through base bleeding/blowing, to name several examples. Of most interest to this study are wake density ratio effects (due to heating, for example). It has been shown that a sufficiently hot wake relative to the free stream eliminates the absolute instability of the wake, so that the flow's dynamics are then controlled by the convectively unstable shear layers. This suggests that simulating combustion instabilities in simplified lab combustors with high density ratios may lead to completely different acoustic-hydrodynamic coupling processes than what may be actually occurring in the low flame density ratio application of interest. For example, Yu and Monkewitz [18] performed parallel stability analyses of variable density wakes, characterized by an outer flow with a density, ρ_u, and time-averaged velocity, U_u, and wake region with density ρ_b and velocity U_b (see Figure 2-3). For an inviscid flow with a step jump in properties between the two fluids, they showed that the absolute stability boundary depends upon density ratio between the outer flow and the wake, as well as the ratio of reverse flow velocity in the wake to outer flow velocity, β, defined below:

$$\beta(x) = -\frac{U_b(x)}{U_u(x)} \tag{2.2}$$

The convective/absolute stability boundary predicted by their analysis is plotted in Figure 2-3. For the purpose of this study, only the sinuous (asymmetric) mode stability boundary is plotted, as it is consistently less stable in wakes than the varicose

(symmetric) mode [18]. The figure shows that absolute instability is promoted with lower density ratios, ρ_u/ρ_b, and higher wake reverse flow velocities. For the reacting mixtures considered in this study, the density ratios plotted in the figure are also essentially identical to the flame temperature ratio, T_b/T_u. Similar stability calculations have also been performed using more realistic velocity and density ratio profiles, such as hyperbolic tangent profiles, and incorporating viscous effects [25]. A major topic in this thesis is to study the effects of the flame upon the absolute and convective instability characteristics of the wake (Huerre and Monkewitz 1990; Anderson et al. 1996; Godreche and Manneville 1998; Schmid and Henningson 2001). Therefore, the velocity and density profiles shown in Figure 2-3a provide a model of particular interest, since they approximate the flowfield downstream of a bluff body flameholder.

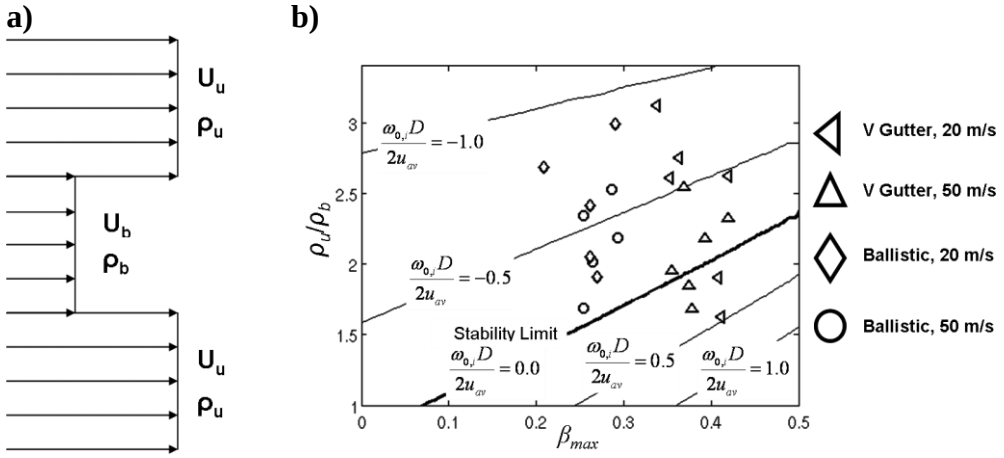

Figure 2-3. a) Flow geometry used for the local parallel stability analysis, and b) tested conditions overlaid onto stability map obtained from local parallel stability analysis for the wake's sinuous mode [18]

2.3 Reacting Bluff Body Literature

The previous section focused on the general hydrodynamic wake stability literature, and identified the density ratio as an important parameter. A significant density ratio appears in the reacting wake of a flameholder. In these flows, the fluid density drops across each of the two flame branches (see Figure 1-1 in Chapter 1, *Introduction*), creating a density profile reminiscent of the model shown in Figure 2-3a. Thus, reacting bluff body wakes can have significantly different stability characteristics than nonreacting wakes.

A variety of prior studies have noted fundamental differences in the dynamic character of the flame and/or flow field at different velocity and fuel/air ratio conditions [26-27], particularly under near blowoff conditions [33-39] or in flames utilizing highly preheated reactants [23, 28-29]. Near blowoff, the flame exhibits substantially increased levels of fluctuations in position, due to local extinction on the flame [30-34], as well as large amplitude sinuous motions of the flow field which resemble the Von Karman vortex street. Hertzberg et al. [30] and Anderson and Hertzberg [35] appear to have first used convective and absolute instability notions to explain various structural features in the flame/flow field, such as vortex shedding and near blowoff flame dynamics.

The first systematic demonstration showing the effects of flame density ratio in combusting flows was presented by Erickson et al. [23] and is reproduced in Figure 2-4. Their results show that a large sinuous flow feature gradually grows in prominence as density ratio across the flame is decreased below values of approximately 2-3. This observation is quite significant as it demonstrates that the dominant fluid mechanics in a lab burner with non-preheated reactants, which has a “high” density ratio, can be very

different from those of a facility with highly preheated reactants, such as many combustion applications. For example, stoichiometric methane air flames with reactant temperatures of 300 and 1000 K have density ratios of 7.5 and 2.6, respectively.

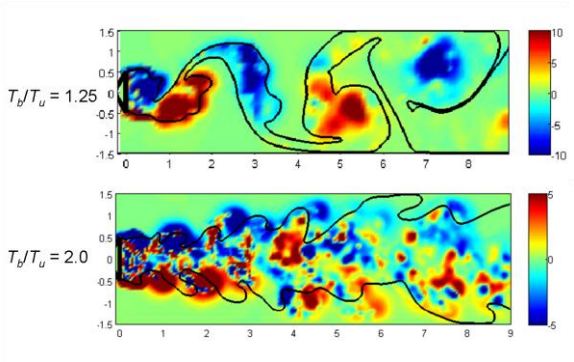

Figure 2-4. Computationally predicted vorticity field and instantaneous flame edge for two flame temperature ratios, reproduced from Erickson et al. [23]

There have been no parallel experimental studies that have systematically studied flame density ratio effects on unsteady flow/flame features. The reason for this is that obtaining a stable (i.e., one that is not near blowoff) flame over a range of density ratios, particularly low density ratios, is quite difficult. Flames propagating into room temperature reactants will blowoff at density ratios much higher than where the phenomenon of interest occurs. For example, a methane/air flame at an equivalence ratio of $\phi = 0.6$ and $T = 300\,\mathrm{K}$ has a density ratio of $\rho_u / \rho_b = 5.6$. Increasing the equivalence ratio to $\phi = 1.0$ leads to a density ratio of 7.5. This density ratio variation of ~25% is all that is possible over the typical range of experimentally accessible fuel/air ratios over which a stable flame can be achieved when fueled with reactants at standard temperature and pressure. In contrast, in a gas turbine combustor with a combustor inlet temperature

of 800K [36] and equivalence ratio of 0.6, the flame temperature ratio is 2.6 for a methane-air flame. Similarly, high efficiency recuperated cycles or reheat cycles may have inlet temperatures of 1000K-1100K [36-37], leading to temperature ratios of ~2.

2.4 Forced Response of Hydrodynamically Unstable Flows

2.4.1 *Convectively Unstable Flows*

As discussed above, high density ratio bluff body flows, like those in most lab scale burners, are convectively unstable. These flows respond strongly to longitudinal acoustic forcing [5, 38-40]. With or without forcing, each shear layer rolls up into concentrated regions of vorticity, which pair as they convect downstream. Vortex pairing [38] occurs when the concentrated vorticity from two adjacent vortices merges into a new, single structure. This occurs due to mutual induction of the two vortices. A vortex pairing event is associated with a halving of the vortex passing frequency.

For a shear layer in the presence of harmonic forcing, the pairing process is adjusted so that vortices pass at the forcing frequency. For example, a train of vortices passing at three times the forcing frequency will tend to merge three at a time to match the forcing frequency. If the forcing frequency is much larger than the vortex passage frequency, a phenomenon called "collective interaction" occurs. In this case, a large number of vortices are spatially localized and merged into one, much larger vortex. In a forced, convectively unstable wake, the two shear layers evolve independently, with structures passing at the forcing frequency due to the vortex pairing/collective interaction processes.

2.4.2 *Globally Unstable Flows*

Low density ratio bluff body flames, as found in many highly preheated industrial applications, tend to be globally unstable. The forced excitation of globally unstable bluff body flows involves the interaction of the two convectively unstable shear layers, which leads to interesting nonlinear phenomena, such as frequency locking [39-44]. Frequency locking occurs through the vortex rollup, pairing, and shedding processes. A detailed summary of these vortex dynamics is presented by Lieuwen [45]. For the bluff body wake, the global mode manifests itself as sinuous rollup of the wake into the Von Karman vortex street. When such flows are forced at low amplitudes, the wake is generally not receptive to the forcing and continues to oscillate at its global mode frequency, f_n, as it does in the unforced case. However, the wake dynamics can be forced to oscillate at the external excitation frequency at sufficient forcing amplitudes. This process is referred to as frequency locking. The amplitude required for frequency locking is a function of the relative values of the forcing and global mode frequencies, f_f and f_n, respectively. Similarly, frequency locking may be achieved over a wider range of forcing frequencies with increased forcing amplitude. A conceptual lock-in map is presented in Figure 2-5, where f_r denotes the response frequency of the wake.

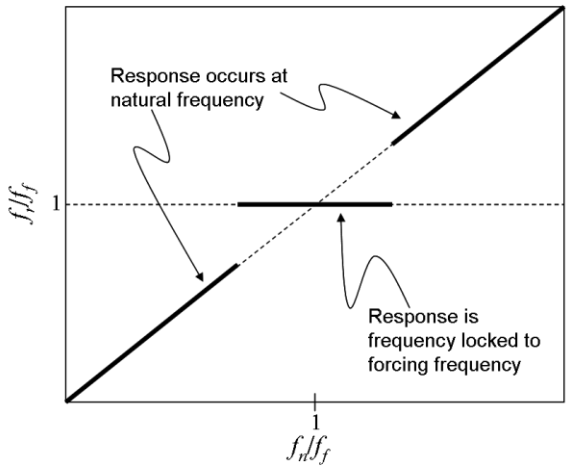

Figure 2-5. Conceptual lock-in map demonstrating the range of offset between the forcing frequency and natural frequency that results in frequency locking.

In an unforced wake, vortices in the shear layers continue pairing as they convect downstream, growing in size and reducing their passage frequency. The vortex pairing causes growth of the shear layers, which eventually grow sufficiently large to interact with one another. The mutual interaction of the vorticity in the two layers leads to instability, manifested as the staggering of vorticity into a sinuous wake pattern [46]. This motion leads to collection of the small shear layer structures into much larger vortices, which pass through the wake at the global mode frequency.

A harmonically forced bluff body flowfield is more complicated than a single shear layer, particularly in the reacting case where it can be either convectively or globally unstable. Multiple scenarios are possible:

(1) If the wake is globally stable, but convectively unstable, axial excitation leads to rollup of the two shear layers, which remain symmetrically spaced across the flow centerline

(2) If a globally unstable wake is subjected to strong harmonic forcing, but is forced at a frequency far from the global mode frequency, the forcing competes with the global mode. Axial forcing drives collective interaction, leading to large scale structures which pass at the forcing frequency, but remain symmetrically spaced across the flow centerline. Simultaneously, the wake tries to amplify the global mode, which competes for the shear generated vorticity and rolls up large structures alternately at the global mode frequency. As will be shown later in this paper, a bimodal spectrum is common in this situation, with responses at both the forcing frequency and the global mode frequency. This bimodal behavior has been observed previously in frequency locking studies of nonreacting, forced wakes [44].

(3) If the excitation frequency is close to the global mode frequency and/or of sufficient amplitude, then the global mode locks into the forcing.

To date, this frequency locking phenomenon has not been investigated systematically in a reacting bluff body flowfield, whose global instability frequency and growth rate are themselves parameters. A related investigation has been performed for thermoacoustically unstable, reacting flows. Here, Chakravarthy et al. investigated the relationship between the dominant acoustic frequency and the vortex shedding frequency in a combustor undergoing natural oscillations [47] and found that the dominant oscillation frequency locked into the vortex shedding frequency.

2.5 Combustion Instability

The work in this thesis is motivated by combustion instabilities. Therefore, this section will provide brief background on this matter, only to introduce where this work fits into the big picture of combustion instabilities. Combustion instability is a resonant

coupling between the acoustic field inside the combustor and the unsteady heat release of the combustion process. The unsteady heat release of combustion is a direct monopole sound source, and is relatively well understood. The effect of the acoustic field on the combustion process can take place through many paths and is not as well understood.

In general, the acoustic field may perturb the heat release of combustion through pressure, entropy, equivalence ratio, or velocity fluctuations. A thorough review of the numerous coupling mechanisms is provided by Lieuwen [48]. Flame response to velocity fluctuations is known as a velocity coupled flame response. The velocity coupled flame response stems from the unsteady velocity fields of the acoustic motions themselves, and the acoustically excited hydrodynamic response. This thesis focuses on understanding the latter; namely, the coupling between the acoustic field and hydrodynamic behavior, and the resulting implications on the unsteady heat release of the flame. This mechanism was shown to be of significant importance in the context of transversely forced bluff body flames [49]. The above general picture of the velocity coupled flame response is sketched in the flow chart in Figure 2-6, with emphasis on the focus of the current work.

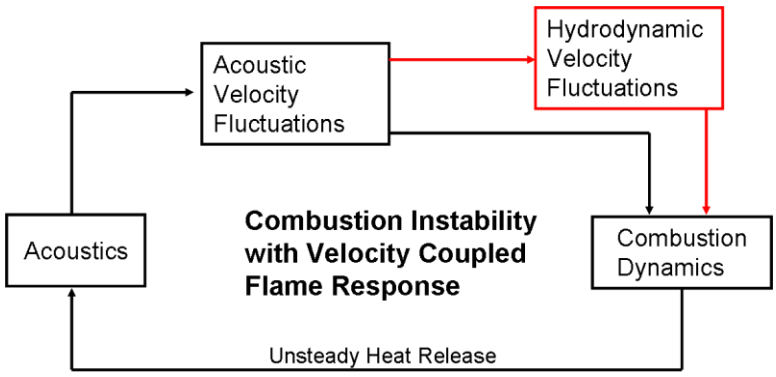

Figure 2-6. Diagram of the combustion instability feedback loop through a velocity coupled flame response. This work focuses on the red branch.

2.6 Study Objectives

The four objectives of this study which were briefly identified at the end of Chapter 1, *Introduction* are the following. The first is to experimentally characterize the unsteady flow evolution as the flame density ratio is monotonically varied in the vicinity of the predicted hydrodynamic stability limit. To do this, it is necessary to highly preheat the reactants to obtain flames that are stable (i.e., well removed from blowoff), yet of low density ratio. This was accomplished by developing a vitiated facility, which has two air injection locations to allow independent control of the mass flowrates and equivalence ratios in the vitiator and test section combustors. Such a facility is able to achieve broad ranges of flame density ratio, and has substantial flexibility in operating conditions. This facility is detailed in Chapter 3, *Experimental Facility and Design of Experiments*, and the results of this experiment are discussed in Chapter 5, *Experimental Results: Unforced Flame and Flow Dynamics* and Chapter 7, *Intermittency of Limit Cycle Events*.

The second study objective is to compare the empirical results from the first objective to the results of local stability theory. The goal of this comparison is to verify that the

key stability parameters have been identified to describe the absolute/convective stability characteristics of reacting wakes. In particular, the work should determine if the density ratio and backflow ratio have the same measured effect as theory would suggest they do. The results will show that they do, but that an additional parameter is important: the spatial offset between the mean density and velocity gradients. These comparisons will also lead to conclusions about the utility of stability analysis of model flow profiles, as well as stability analysis of the full time-averaged flow. This objective is discussed in the first half of Chapter 6, *Local Hydrodynamic Stability Analysis*.

The third study objective is to determine the vortical processes that govern the flow stability, and how they themselves are controlled by the identified stability parameters. This work will draw physical links between the flow stability parameters and the predicted/observed flow stability. The results will show that deriving such physical meaning is a useful strength of the model stability analysis. This objective is explored in the second half of Chapter 6, *Local Hydrodynamic Stability Analysis*.

The fourth study objective is to experimentally determine the effects of the hydrodynamic stability on the velocity-coupled flame response. This final objective relates the previous three objectives to the bluff body combustion instability problem. Results will reveal non-intuitive conclusions about the unsteady heat release of a globally unstable bluff body combustor that is longitudinally acoustically forced at the global mode frequency. These results appear in Chapter 8, *Experimental Results: forced Flame and Flow Dynamics*.

CHAPTER 3. EXPERIMENTAL FACILITY AND DESIGN OF EXPERIMENTS

This chapter describes experimental facility and the experiments that were selected to accomplish the research goals outlined at the end of Chapter 2, *Background and Motivation*. All of the research goals are centralized around the hydrodynamics of combusting bluff body wakes. More specifically, the experimental work shall investigate the hydrodynamic stability characteristics of this flow, and the effect of the hydrodynamics on the flame response to longitudinal acoustic forcing. In order to study both the hydrodynamic characteristics and the flame response behavior, diagnostics should quantify the unsteady flow field, the unsteady flame position, and the unsteady heat release of combustion. Therefore, the experimental facility is an optically accessible bluff body combustor with very flexible operating conditions, thus allowing parametric studies of the hydrodynamic stability characteristics. This experimental facility and the design of experiments are detailed next.

3.1 Experimental Facility

3.1.1 *Desired Performance*

As mentioned above, the two-dimensional bluff body combustor facility must provide control over the hydrodynamic stability characteristics of the flow. These stability characteristics include both the growth rate and the frequency of the global mode. In Chapter 2, *Background and Motivation*, the density ratio across the flame, ρ_u/ρ_b, and

backflow ratio, β, were identified as important parameters governing the absolute growth rate (and presumably the global mode growth rate) in the wake.

The density ratio across the flame may be varied by either adjusting the equivalence ratio or the reactant temperature. As covered in Chapter 2, *Background and Motivation*, the density ratio range for convective/absolute instability transition in a burning wake often occurs in the range $\rho_u/\rho_b \sim 2-3$. For room temperature reactants, this would occur at an equivalence ratio much leaner than lean blowoff for a methane/air bluff body flame. Therefore, it is necessary to highly preheat the reactants to obtain flames that are stable (ie, well removed from blowoff), yet of low density ratio. For this reason, the selected experimental facility should provide control over the level of preheat and the equivalence ratio in the test section.

Chapter 2, *Background and Motivation* also provided a discussion of the global mode frequency in nonreacting wakes, f_{BVK}. The global mode frequency typically occurs at a fixed Strouhal number for a given bluff body shape, and therefore scales with bluff body lip velocity. Therefore, the selected experimental facility should allow control of the bluff body lip velocity at fixed ρ_u/ρ_b so that the global mode frequency can be varied. Results from this work will demonstrate that the global mode frequency in reacting wakes does in fact follow a Strouhal number scaling over the density ratios tested.

The primary diagnostics chosen are particle image velocimetry (PIV) to make the flowfield measurements and high speed chemiluminescence to make the flame dynamics and unsteady chemiluminescence measurements. Details on these techniques are provided in Chapter 4, *Instrumentation and Diagnostic Techniques*. Both of these

diagnostics techniques require substantial optical access to the test section combustor. Therefore, all four rectangular walls of this combustor are made of quartz.

3.1.2 *Design of Facility*

Independent control of the global mode growth rate and frequency necessitates independent control over the level of preheat, the test section equivalence ratio, and the bluff body lip velocity. This was accomplished by developing a facility capable of vitiating the flow, with independent control of the equivalence ratios of the two burners. Such a facility is able to achieve broad ranges of flame density ratio. In order for the density ratio and the lip velocity to be varied independently also requires a second, separately controlled air injection source. The ability to control two independent air flows and two independent fuel/air ratios leads to substantial flexibility in operating conditions.

The facility, shown in Figure 3-1, consists of two premixed, methane-air combustors in series. The figure identifies the various components, which are detailed from Figure 3-3 through Figure 3-16 to allow simulation or reconstruction of the experiments. The first combustor is used to vitiate the flow. The second, bluff body stabilized combustor consists of a rectangular section with a bluff body spanning the width of the combustor, creating a nominally 2D flow. The aspect ratio of bluff body height to chamber width is 0.15. This combustor has quartz windows for optical access from all four sides. Two different bluff bodies were used in the test section: a 2D ballistic shape (shown in Figure 3-17a), and a v-gutter (shown in Figure 3-17b). From here on, the 2D ballistic shape will be referred to as the ballistic bluff body.

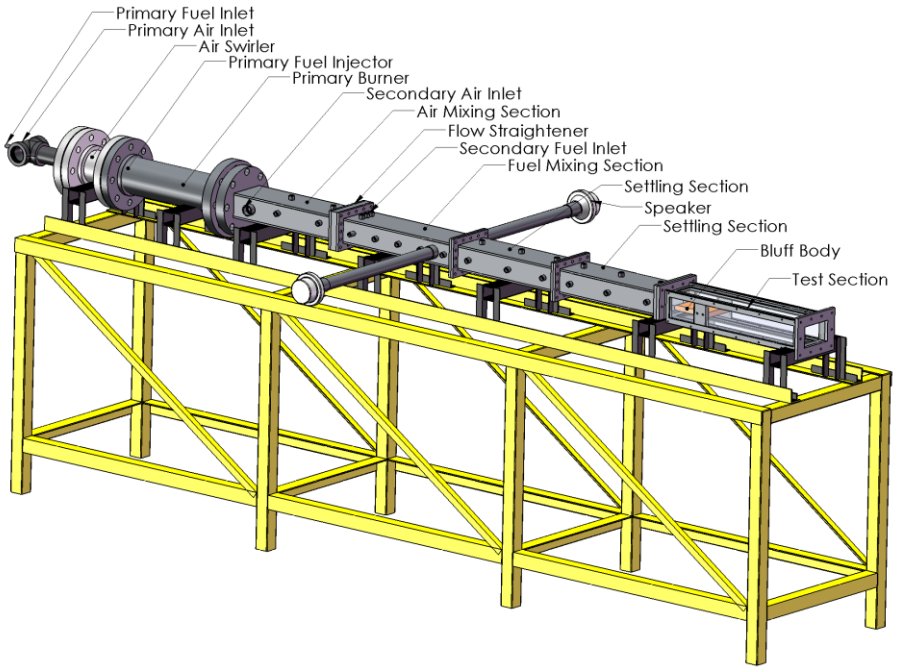

Figure 3-1. Drawing of the experimental facility, showing layout of the various components which are detailed next

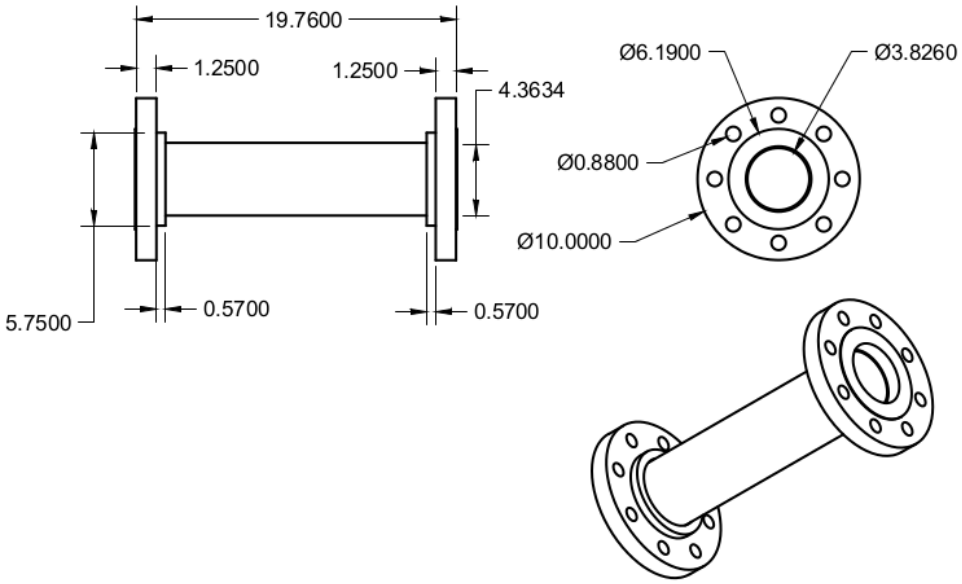

Figure 3-2. Schematic of the primary burner (vitiator), dimensions in inches

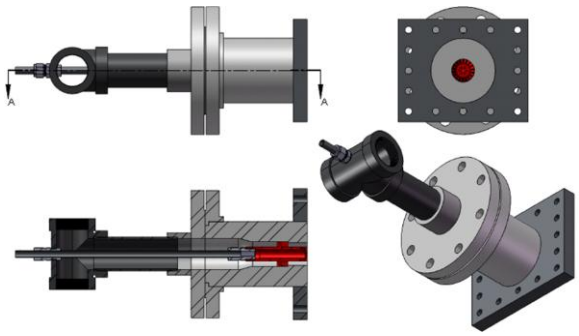

Figure 3-3. Drawing of the vitiator swirler assembly

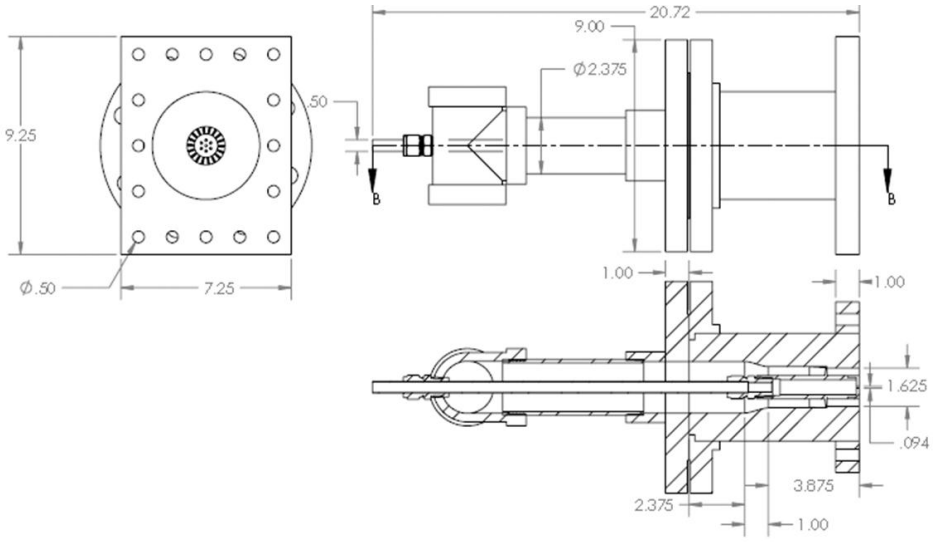

Figure 3-4. Schematic of the vitiator swirler assembly, dimensions in inches

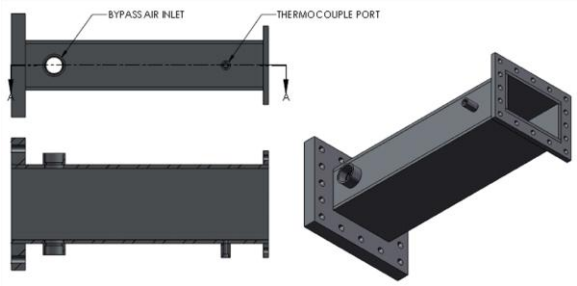

Figure 3-5. Drawing of the air dilution section

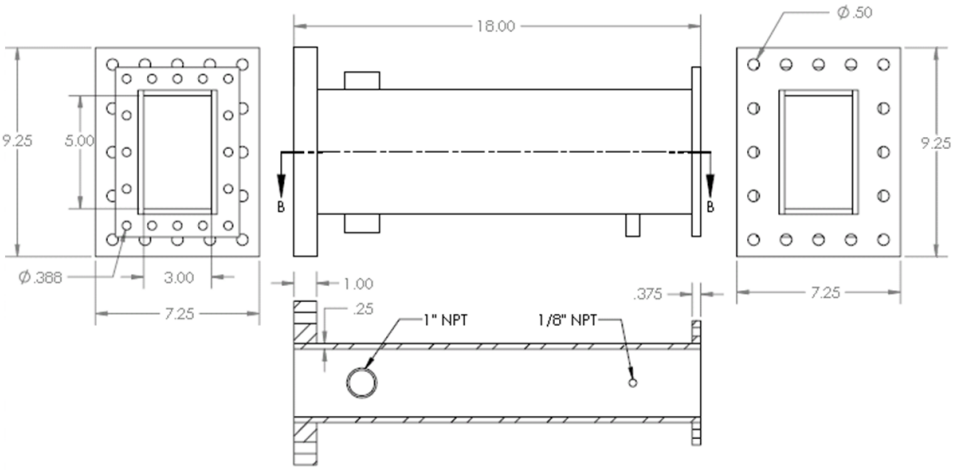

Figure 3-6. Schematic of the air dilution section, dimensions in inches

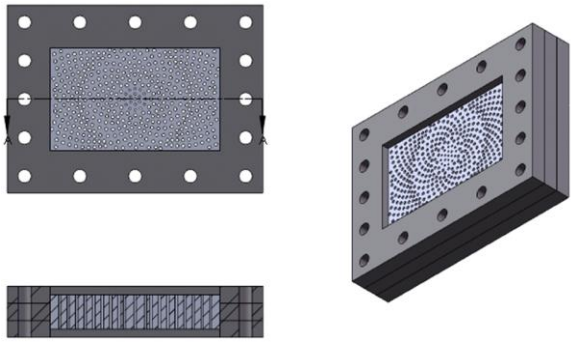

Figure 3-7. Drawing of the flow straightener

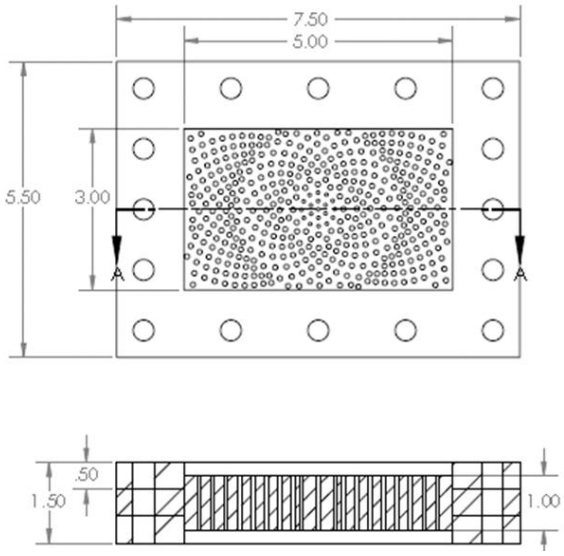

Figure 3-8. Schematic of the flow straightener, dimensions in inches

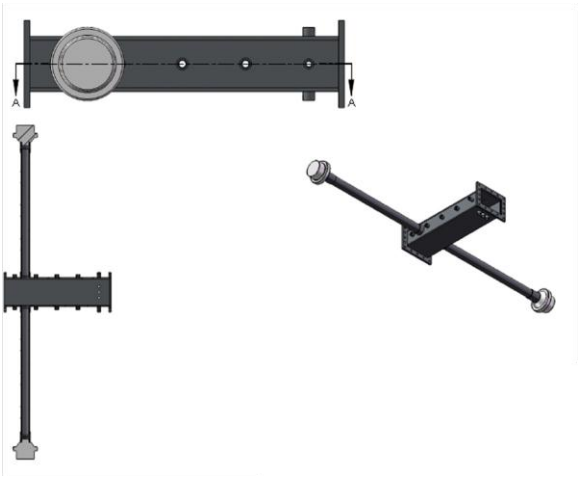

Figure 3-9. Drawing of the fuel mixing and acoustic forcing section

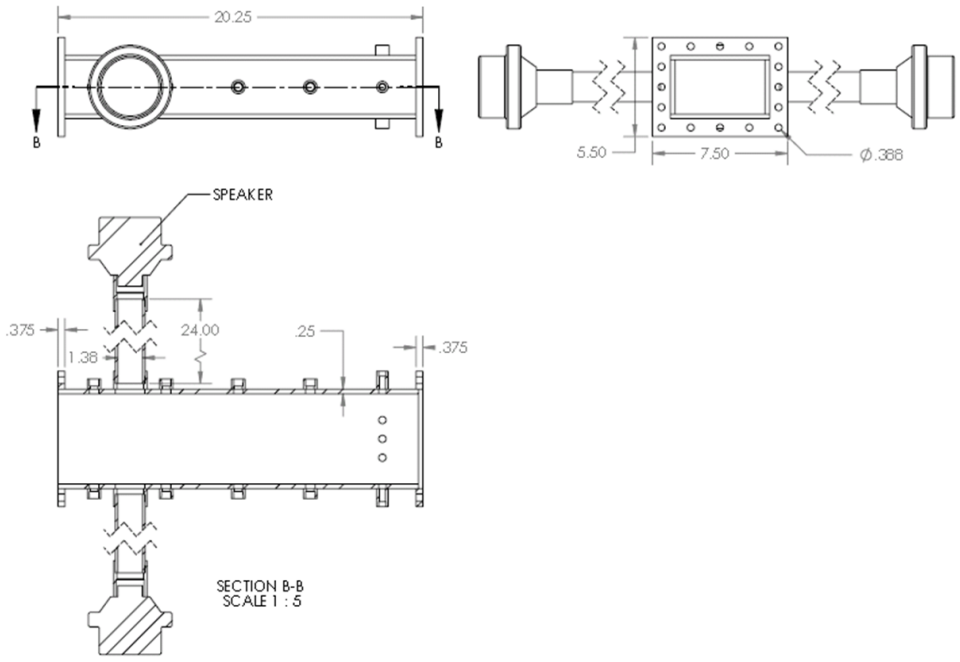

Figure 3-10. Schematic of the fuel mixing and acoustic forcing section, dimensions in inches

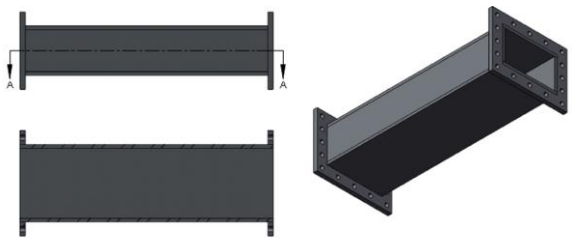

Figure 3-11. Drawing of the first flow settling section

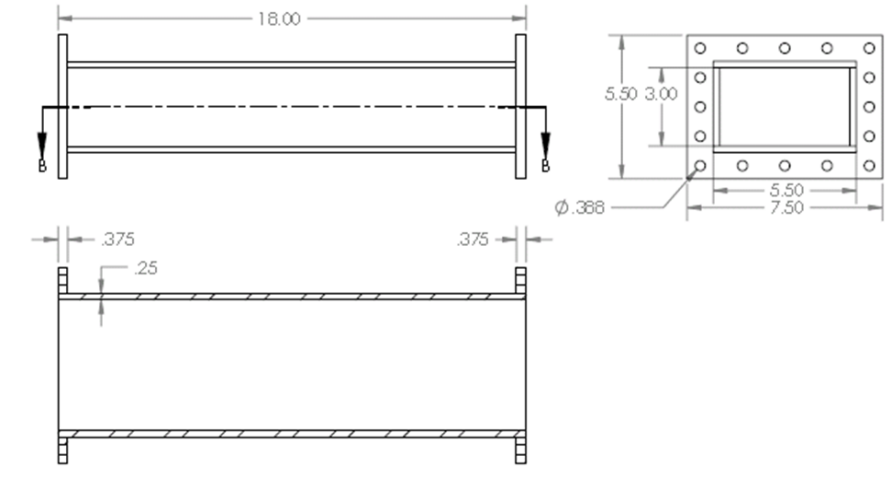

Figure 3-12. Schematic of the first flow settling section, dimensions in inches

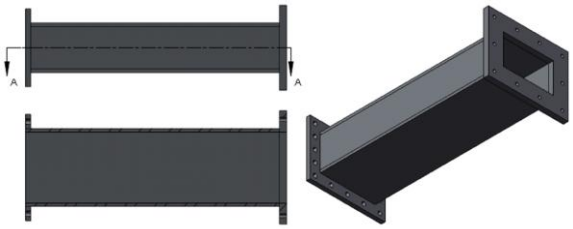

Figure 3-13. Drawing of the second flow settling section

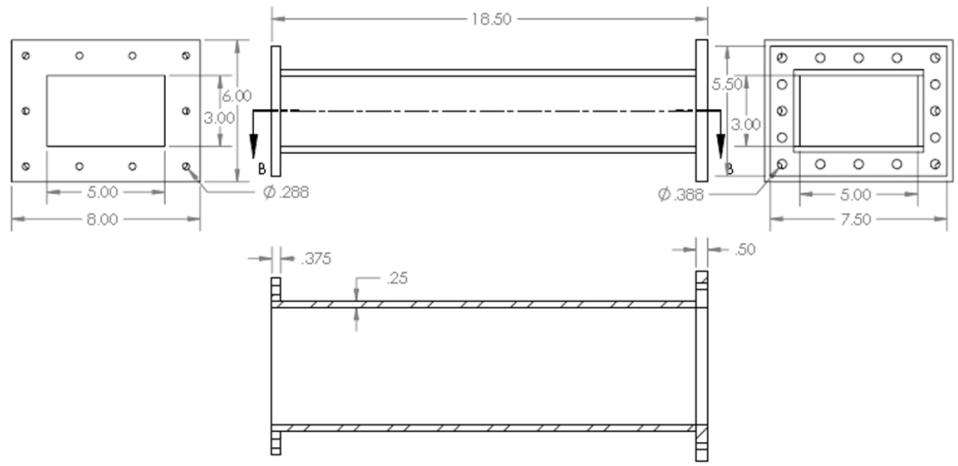

Figure 3-14. Schematic of the second flow settling section

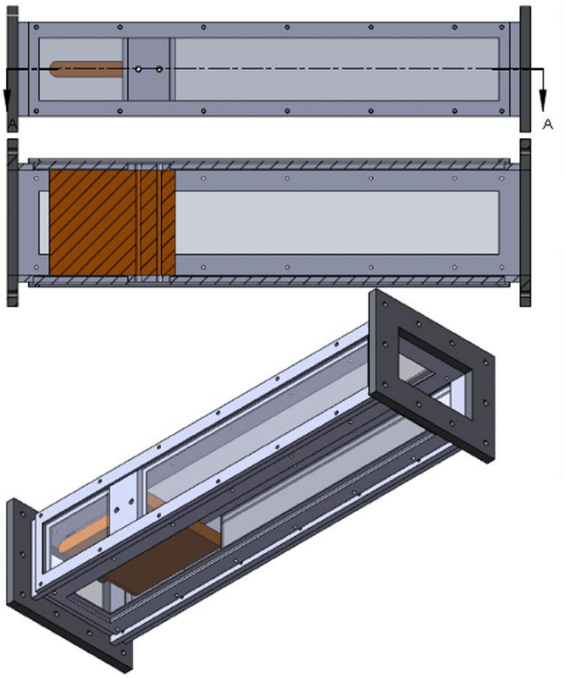

Figure 3-15. Drawing of the test section with ballistic bluff body installed

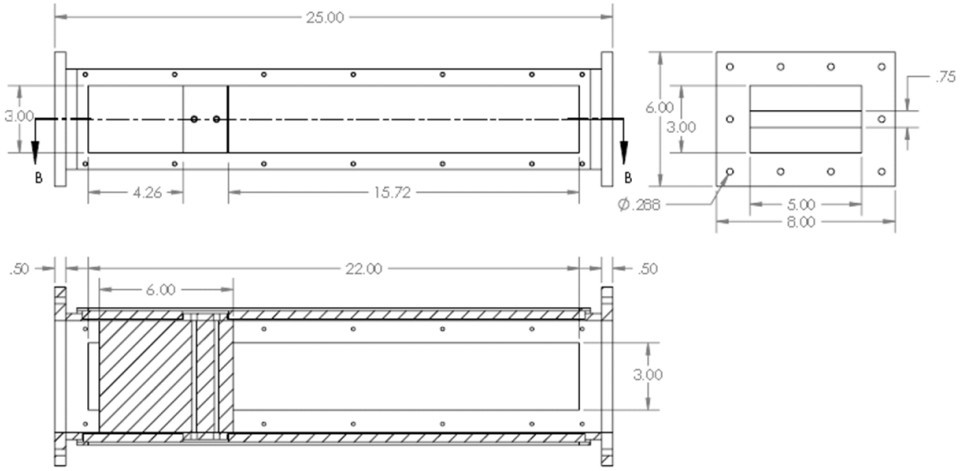

Figure 3-16. Schematic of the test section with ballistic bluff body installed, dimensions in inches

a) **b)**

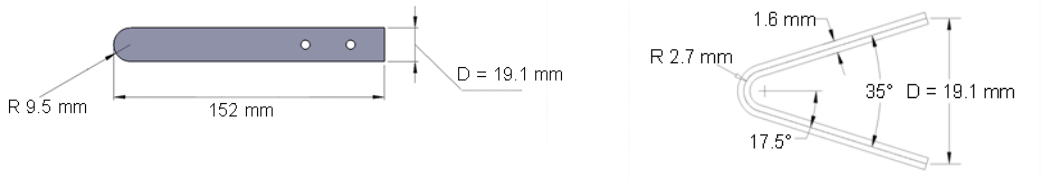

Figure 3-17. Schematics of bluff bodies, a) ballistic, b) v-gutter

The rig operates as a blow-down facility using the 2500 psi air supply in the Ben T. Zinn Combustion Lab at the Georgia Institute of Technology. Upstream of the control valves and instrumentation, the air supply is regulated down to 150 psi. Primary air and fuel were premixed upstream of the vitiator. Secondary air and fuel were plumbed into the rig and premixed in a 1.4 m long settling section aft of the vitiator, and upstream of the test section. Fuel is inserted from a manifold of eight injectors, each of which penetrates 2.5 cm into the flow; three injectors pass through the top wall, three through the bottom wall, and 1 injector passes through each side wall. Using absorption spectroscopy, the natural gas concentration was analyzed as a function of position on the test section inlet plane, and was uniform within ±10%; uniform equivalence ratio was assumed and the effects of nonuniform equivalence ratio [53-55] were not considered.

In order to study flame response to acoustic forcing, the facility was constructed such that the test section could be longitudinally acoustically forced. Transverse forcing was not part of this work, although it has received attention in a parallel study [49-50]. The forcing tone was created with a function generator, and was introduced by two loudspeakers, which were mounted to tubes that entered the combustor several meters upstream of the test section.

3.2 Background Flow Noise

For the conditions reported in this thesis, the background flow noise of the rig (due to acoustics and turbulence, for example) was insignificant compared to the limit cycling behavior of interest. To demonstrate this, Figure 3-18 shows axial velocity spectra for several velocities and density ratios. In the figures, a small hexagram hovers above the global mode frequency. The spectra show that when present, the global mode is responsible for the dominant axial velocity oscillations in the combustor.

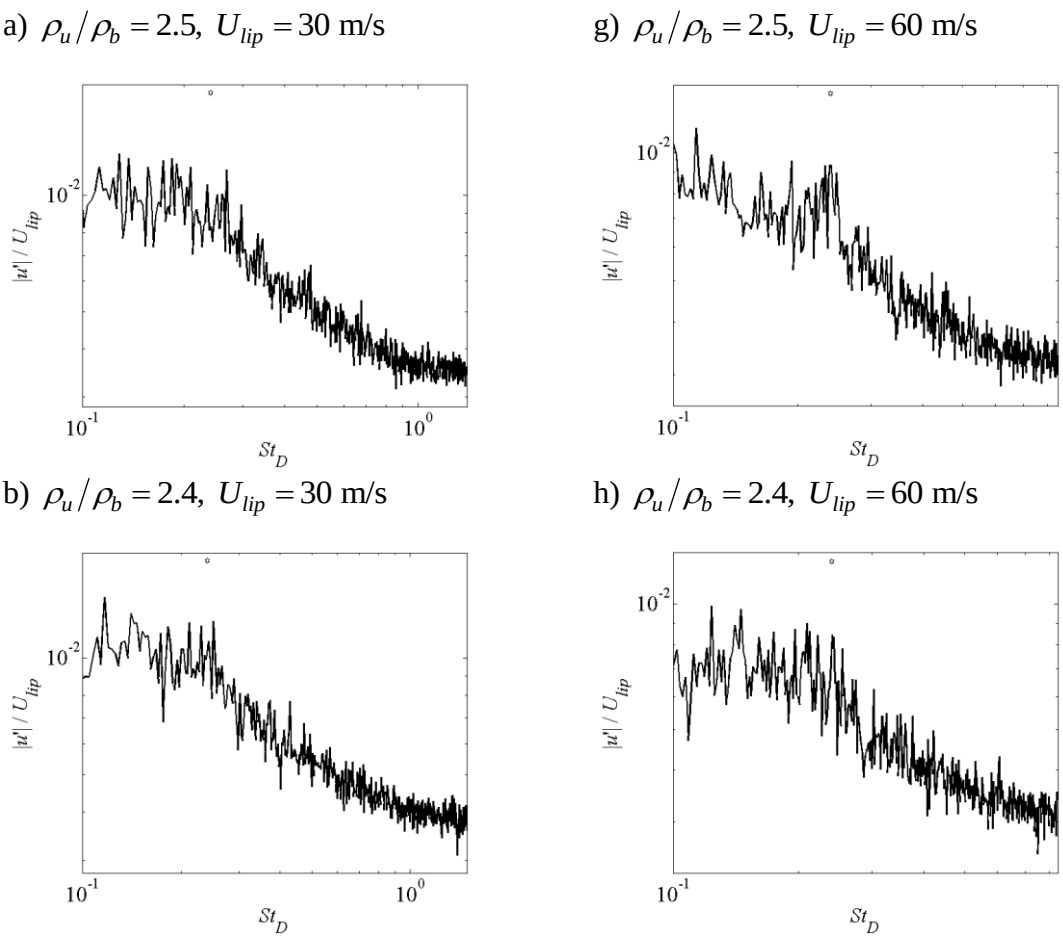

Figure 3-18. Axial velocity spectra, showing the dominance of the hydrodynamic limit cycle behavior over the background acoustics. Results are shown for many combinations of density ratio and velocity, with conditions shown above each plot.

c) $\rho_u/\rho_b = 2.2,\ U_{lip} = 30$ m/s

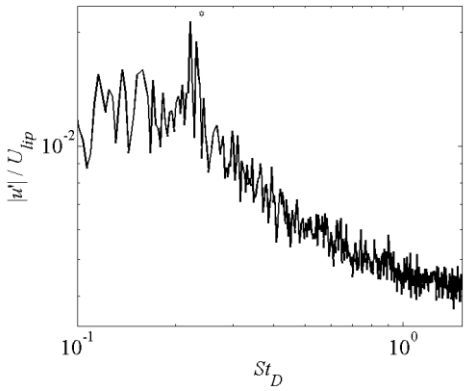

i) $\rho_u/\rho_b = 2.2,\ U_{lip} = 60$ m/s

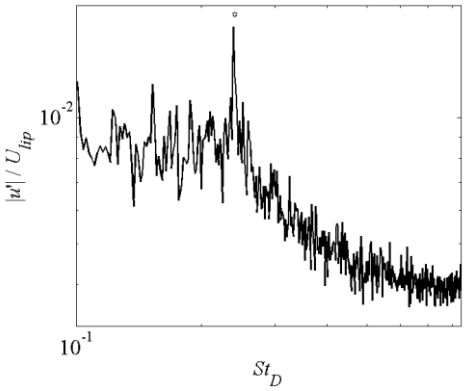

d) $\rho_u/\rho_b = 2.0,\ U_{lip} = 30$ m/s

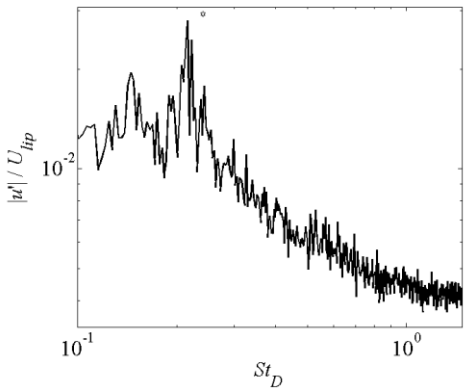

j) $\rho_u/\rho_b = 2.0,\ U_{lip} = 60$ m/s

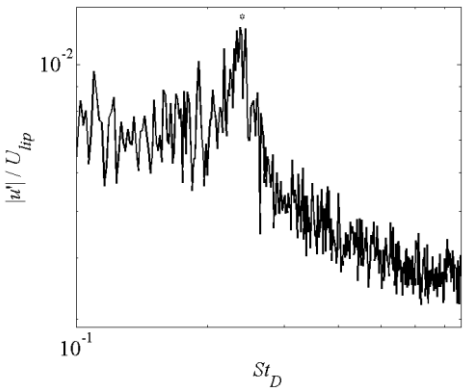

e) $\rho_u/\rho_b = 1.9,\ U_{lip} = 30$ m/s

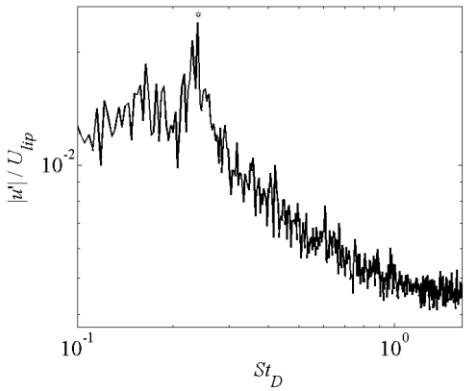

k) $\rho_u/\rho_b = 1.9,\ U_{lip} = 60$ m/s

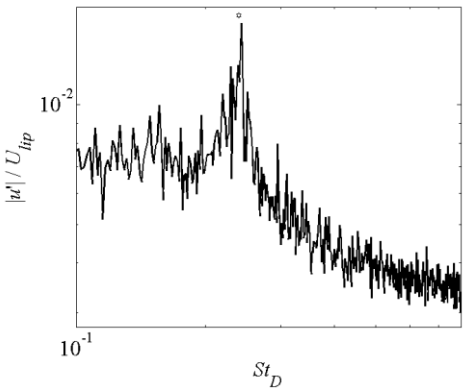

Figure 3-18 continued

f) $\rho_u/\rho_b = 1.7,\ U_{lip} = 30$ m/s

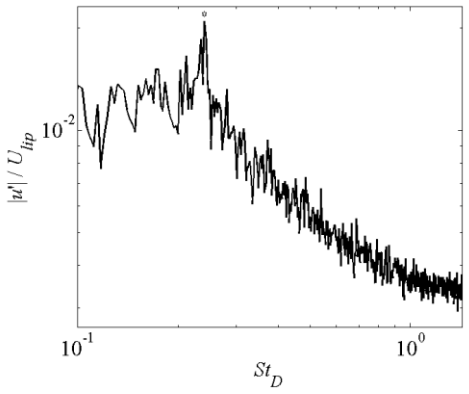

l) $\rho_u/\rho_b = 1.7,\ U_{lip} = 60$ m/s

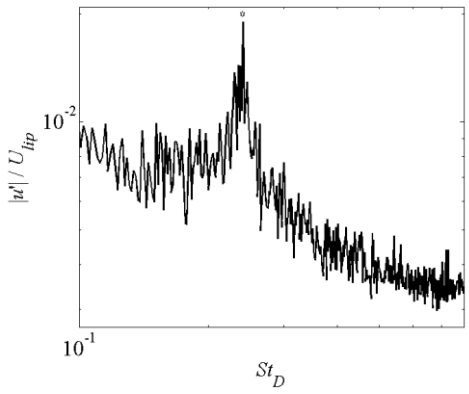

Figure 3-18 continued

At a density ratio of $\rho_u/\rho_b = 1.7$ and lip velocity of $U_{lip} = 65$ m/s, the vitiator begins to become unstable. This is detected audibly by a very faint "hum." Figure 3-19 shows the axial velocity spectrum for this case, which has a significant peak associated with the acoustics of the vitiator instability. Conditions like this, with significant background acoustics, were not included in this study.

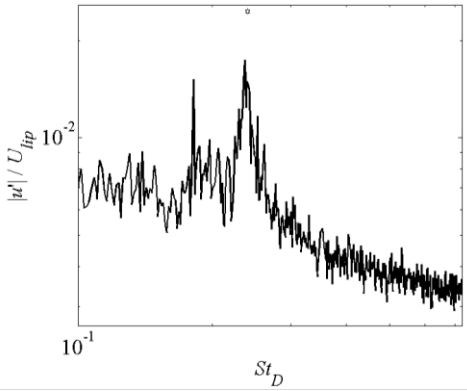

Figure 3-19. Axial velocity spectra for $\rho_u/\rho_b = 1.7$, $U_{lip} = 50$ m/s, showing a case with significant background acoustics stemming from combustion instability in the vitiator

3.3 Two-Dimensionality

This work assumes a two-dimensional flame and flowfield. In reality, three-dimensionality is introduced by turbulence, secondary instabilities, and end-wall effects. The high speed chemiluminescence measurement is a line-of-sight measurement, and therefore captures the effects of three-dimensionality. In order to demonstrate the downstream growth of three-dimensional effects, the full width at half maximum of the luminosity of one flame branch was instantaneously measured at each axial position, and then temporally averaged. This quantity is normalized by its value at the flame attachment point, where three-dimensional effects are expected to be weakest. The result, defined as ζ_{FWHM}, is shown in Figure 3-20 for several density ratios and velocities, showing the growth in the apparent flame thickness as three-dimensional effects develop with downstream position. The first observation is that three-dimensional effects seem to grow more quickly for low velocity cases, and high density ratio cases. The second observation is that in the wavemaker region, three dimensional effects have only grown such that the apparent flame thickness has roughly doubled (to be contrasted with a factor of as much as 7 for locations farther downstream). Chapter 6, *Local Hydrodynamic Stability Analysis* will show that this region, located between one and two bluff body diameters downstream for this flow, is the most important region for hydrodynamic stability predictions.

a) $\rho_u/\rho_b = 2.5,\ U_{lip} = 30$ m/s

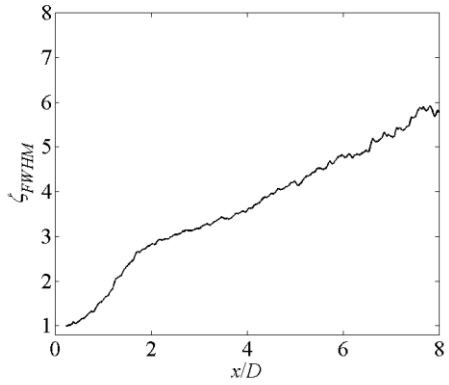

b) $\rho_u/\rho_b = 2.4,\ U_{lip} = 30$ m/s

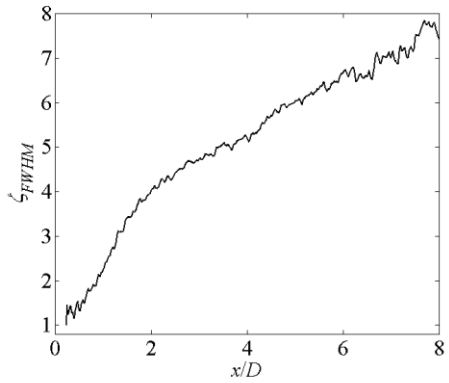

c) $\rho_u/\rho_b = 2.2,\ U_{lip} = 30$ m/s

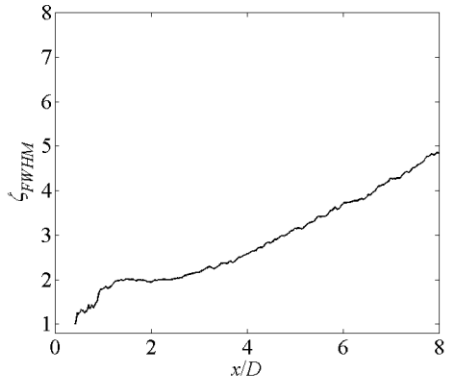

g) $\rho_u/\rho_b = 2.5,\ U_{lip} = 60$ m/s

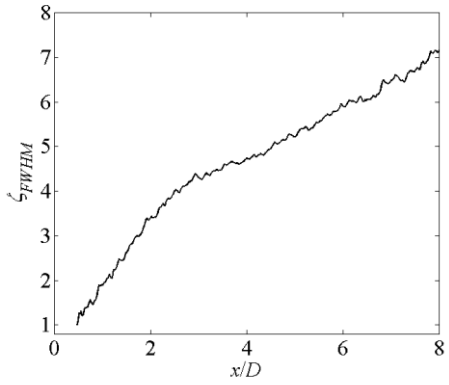

h) $\rho_u/\rho_b = 2.4,\ U_{lip} = 60$ m/s

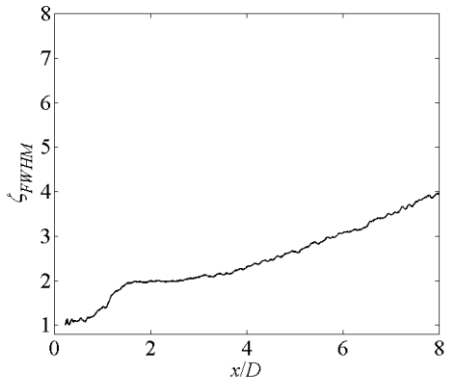

i) $\rho_u/\rho_b = 2.2,\ U_{lip} = 60$ m/s

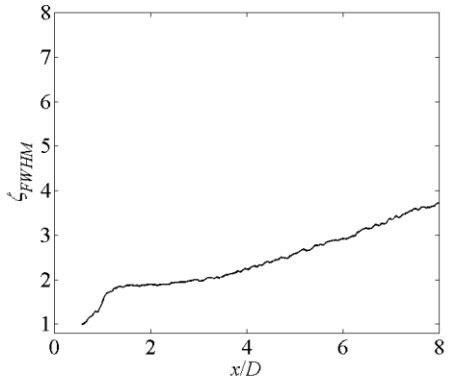

Figure 3-20. Indication of three dimensionality of the line of sight integrated chemiluminescence for several test conditions. Conditions are indicated above each plot.

d) $\rho_u/\rho_b = 2.0,\ U_{lip} = 30$ m/s

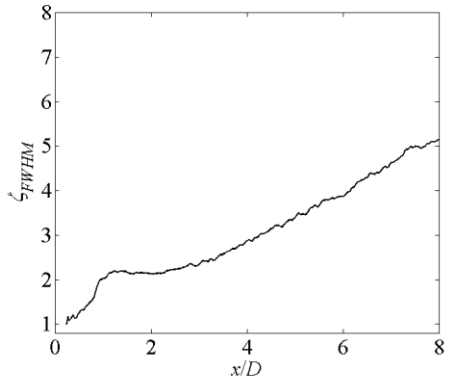

j) $\rho_u/\rho_b = 2.0,\ U_{lip} = 60$ m/s

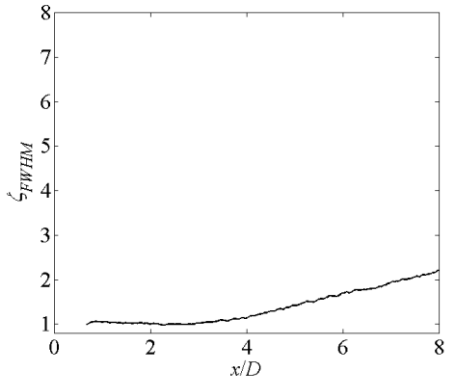

e) $\rho_u/\rho_b = 1.9,\ U_{lip} = 30$ m/s

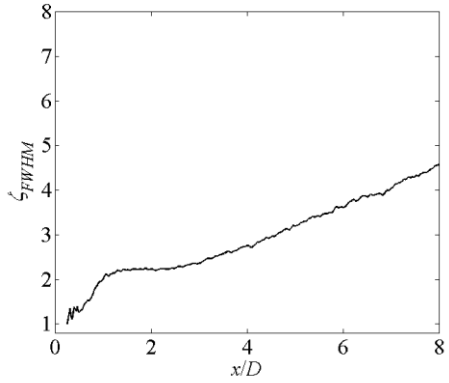

k) $\rho_u/\rho_b = 1.9,\ U_{lip} = 60$ m/s

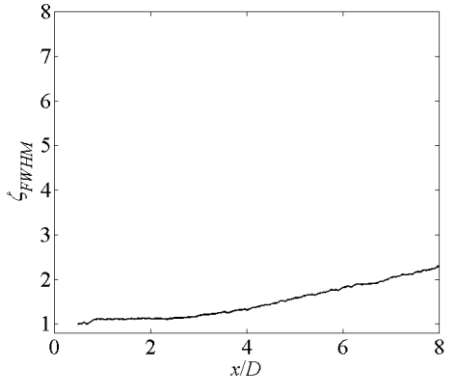

f) $\rho_u/\rho_b = 1.7,\ U_{lip} = 30$ m/s

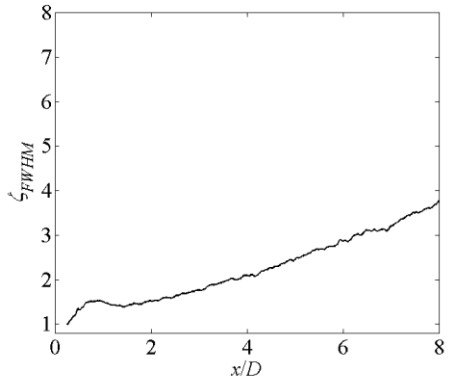

l) $\rho_u/\rho_b = 1.7,\ U_{lip} = 60$ m/s

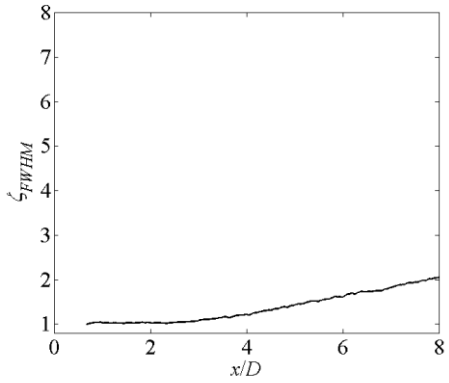

Figure 3-20 continued

3.4 Design of Experiments

Two sets of experiments were performed, an unforced study and a forced study. Both experiments measured the flame and flow dynamics using high speed chemiluminescence and time resolved PIV, respectively. This section describes the design of the test matrices for these experiments.

3.4.1 *Test Matrix for Unforced Experiments*

The purpose of the unforced study was to experimentally characterize the hydrodynamic stability of the reacting wake in the vicinity of the global mode stability limit. Test matrix design was motivated by the stability map from the analysis of Yu and Monkewitz [18], shown in Figure 3-21, which parameterizes the flow stability in terms of a backflow ratio and a density ratio. The backflow ratio (defined in Chapter 2, *Background and Motivation*) is a convenient measure of the shear. Additionally, the density ratio used in this thesis is the inverse of the density ratio used by Yu and Monkewitz (where they use *S*), so that it will remain greater than 1.

The test matrix was laid out as follows. For each of the two bluff bodies shown in Figure 3-17, a density ratio sweep was performed at a fixed bluff body lip velocity of 50 m/s, and again at 20 m/s. Density ratio was swept from $\rho_u/\rho_b = 1.7$ to 2.5 for PIV measurements and from $\rho_u/\rho_b = 1.7$ to 3.2 for high speed chemiluminescence measurements. The systematic density ratio sweeps were meant to study the density ratio as a parameter influencing the hydrodynamic global instability growth rate. Likewise, the two different bluff body geometries allowed testing of two different backflow ratio parameters. The two different lip velocities allow application of Strouhal scaling to

confirm the hydrodynamic rather than acoustic nature of the observed dynamics. The PIV measurement was conducted over a narrower range of density ratios because at density ratios greater than 2.5, insufficient seeding density was present in the low density combustion products to make good velocity measurements in the products. This limited range of density ratio was acceptable, because the phenomena of interest occurred at and below $\rho_u/\rho_b = 2.5$ as evidenced by the chemiluminescence measurements. This problem could be overcome by increased overall seeding density; however, such attempts led to rapid accumulation of seed particles on the windows, obscuring successful image capture.

The actual conditions tested in the unforced PIV experiments are overlaid on the stability map, where the backflow ratio $\beta_{\max}$ is determined from the maximum value of β (which itself varies axially). Note that the v-gutter provides larger reverse flow than the ballistic bluff body. Contours of constant $\omega_{0,i}D/(2U_{av})$ are provided as well, and correspond to the absolute spatio-temporal growth rate as computed from density and velocity measurements in conjunction with linear stability theory. These theoretical values are calculated with a model stability analysis assuming top hat density and velocity profiles, parallel flow, and high Reynolds number. While this simplified, model stability analysis is useful for parameterizing the stability problem and designing the test matrix, a detailed local stability analysis is performed to compare stability theory results to experimental observations. The stability analysis details and results are discussed later in Chapter 6, *Local Hydrodynamic Stability Analysis*.

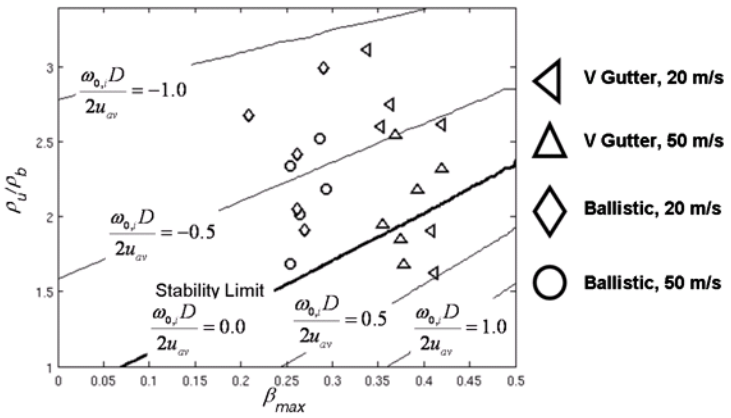

Figure 3-21. Tested conditions overlaid onto stability map obtained from 2D parallel flow stability analysis for the sinuous wake mode.

3.4.2 *Test Matrix for Forced Experiments*

The forced experiments were conducted to investigate the interaction of the hydrodynamics with the acoustic forcing, over a range of hydrodynamic global mode growth rates and frequencies. Therefore, the test matrix design was based off of the test matrix from the unforced experiments, where hydrodynamic stability characteristics were systematically varied. In the forced experiments, only the ballistic bluff body was studied. The density ratio was varied over the range $\rho_u/\rho_b = 1.7$ to 2.5 to modulate the global mode growth rate. For each density ratio, the lip velocity was varied from 20 to 70 m/s in order to vary the global mode frequency.

For every combination of density ratio and lip velocity, the flow was first set to the conditions of interest and an unforced test was conducted. Then, without adjusting any valves, a longitudinally acoustically forced test was conducted. This procedure allowed measurement of the true global mode frequency, without influence from forcing, and ensured that the density ratio and lip velocity did not drift between the unforced and forced cases due to error introduced by manually adjusting valves and reading gauges. In

order to mitigate drifts in the global mode frequency due to thermal transients, the rig was "warmed up" before each series of measurements at a given density ratio and lip velocity. Most conditions were tested with only an unforced and a forced case, however forcing amplitude sweeps were performed at density ratios of $\rho_u/\rho_b = 1.7$ and 2.0.

The forcing amplitude was quantified by A_f, which is the ratio of the acoustic particle displacement amplitude to the bluff body diameter. The strongest forcing corresponded to a particle displacement amplitude of 0.5 mm, or $A_f = 0.02$. Displacement based forcing amplitudes were used to make the data comparable to the early literature, where the bluff body was physically displaced. An amplitude of $A_f = 0.02$ corresponds to roughly 3% of the bluff body lip velocity for $U_{lip} = 50$ m/s. For $\rho_u/\rho_b = 1.9$, 2.2, 2.4, and 2.5, forcing amplitudes of $A_f = 0$ and 0.02 were used. For $\rho_u/\rho_b = 1.7$ and 2.0, forcing amplitude sweeps were conducted with $A_f = 0$, 0.005, 0.01, 0.015, and 0.02. This test matrix for forced experiments resulted in a large database of PIV and high speed chemiluminescence data each with 182 cases.

The forcing frequency is held fixed at 515 Hz for all experiments, since the combustor has a longitudinal acoustic mode at this frequency. Although this response will change somewhat with temperature, the response peak is broad enough that the effect is not too pronounced. Over the range of conditions tested, there is not a significant change in the acoustic response of the rig at 515 Hz.

For the acoustically forced cases, sampling was performed such that spectral leakage from the forcing frequency would be negligible. This ensures that measurements of dynamics at the global mode frequency are not contaminated artificially by spectral

energy leaking from the forcing frequency, even when the two frequencies are close. This was accomplished by setting the forcing frequency, sampling frequency, number of samples, and number of ensembles such that Eq. (3.1) was satisfied [51]. In the equation, N_e represents the number of ensembles for spectral averaging; this is not necessarily the same as the total number of ensembles, which may be increased further by spatial averaging. In essence, this equation ensures that an integer number of cycles of the forced response are sampled. N_s represents the total number of samples, not the number of samples per ensemble, and j is any integer. For example, in this study $f_f = 515$, $N_e = 4$, $f_{sample} = 5000$ Hz, and $N_s = 4000$, which corresponds to $j = 103$ cycles per ensemble (or 412 cycles for the entire data record).

$$f_f = jN_e f_{sample} / N_s \tag{3.1}$$

3.4.3 *General Test Matrix Considerations*

Bluff body lip velocity was calculated using the formula $U_{lip} = \dot{m}_{lip} / \left(\rho_{lip} A_{lip} \right)$, which is an average axial flow velocity. The density for the lip velocity calculation was determined from the temperature measured just before the test section and the gas composition of the secondary air and fuel adiabatically mixed with the equilibrium vitiated gas. An equilibrium gas solver was then used to calculate the adiabatic density ratio across the test section flame. The area, A_{lip}, is the cross-sectional area of the flow at the plane of the bluff body trailing edge. The flame density ratio, ρ_u / ρ_b, is defined as the ratio of the density entering the test section to the density of the post flame gases in the test section.

In terms of the lip velocity and density ratio, the operating map of the combustor is limited by combustion instability, blowoff, and thermal constraints. The bluff body lip velocity is limited to a range of roughly 20 m/s to 70 m/s because of combustion instability in the vitiator at low and high flowrates and conditions of interest. The lower limit of the density ratio occurs when the vitiator flame is "hot," the test section flame is "cold," and the test section flowrate is not much greater than the vitiator flowrate. This is not as simple as running the vitiator at stoichiometric fuel air ratio, adding a small secondary air flow, and running the test section as lean as possible. This is because the vitiator cannot be run near stoichiometric without significant secondary air injection due to melting of the downstream flow straightener. This significant air addition does not facilitate low density ratios because of the decreased temperature and increased mass flow entering the test section. Typically the vitiator was run at an equivalence ratio between 0.7 and 0.8 where the secondary air addition was not driven by cooling needs. The lean blowout limit of the test section flame was generally close to $\phi = 0.55$ for the typical oxygen content of the vitiated flow. Furthermore, great care was taken to stay well away from blowoff boundaries, where additional flame dynamics can occur [1, 52-53]. The test section equivalence ratio was kept in the range $\phi = 0.70 - 0.75$. In light of all of these considerations, the density ratio was limited to $\rho_u / \rho_b \geq 1.7$.

It is the independent control of the primary and secondary air and fuel supplies that allows the flame density ratio and bluff body lip velocity to be varied independently in the test section. For example, if a density ratio sweep is desired at a fixed bluff body lip velocity, the secondary air flowrate can be varied. Increasing the secondary air flowrate raises the mass flowrate through the test section combustor, but reduces the temperature

entering the test section (and hence raises the density at the bluff body lip). In terms of bluff body lip velocity, these two effects roughly balance one another. In terms of flame density ratio, the reduced inlet temperature leads to higher flame density ratio. The primary air and fuel flowrates as well as the secondary fuel flowrate may then be tweaked to ensure the desired lip velocity.

Samples of the design parameters used to achieve a constant lip velocity density ratio sweep are presented next. Figure 3-22 plots the experimental air flowrates and equivalence ratios from the ballistic bluff body at 50 m/s. The figure demonstrates how air flowrates and equivalence ratios in the two burners may be adjusted so that the density ratio can be swept while lip velocity is held constant. For the reasons discussed above, the secondary air flowrate is the key control parameter for a density ratio sweep at constant velocity.

a) b)

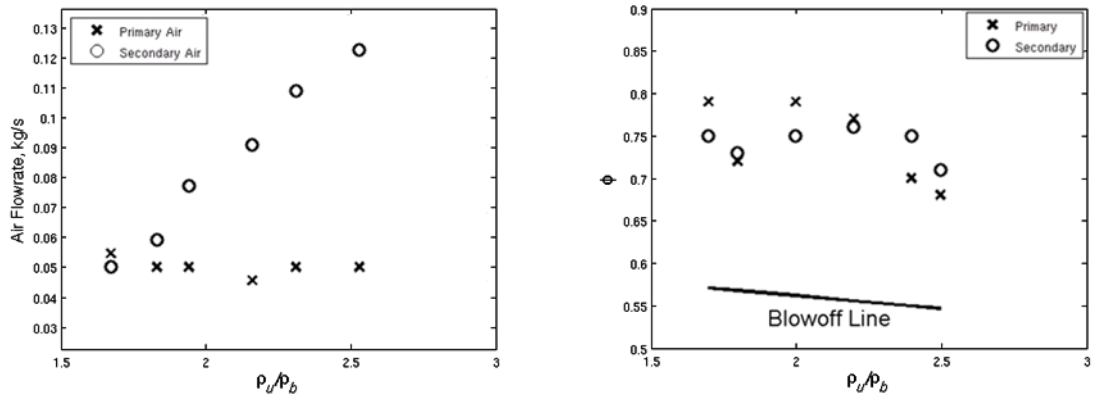

Figure 3-22. Experimental design parameters for ballistic bluff body at U_{lip} = 50 m/s, showing a) primary and secondary air flowrates and b) the equivalence ratios in both combustors

A lip velocity sweep at constant density ratio is much simpler. To achieve this, all four flowrates are multiplied by the same factor to alter the total mass flow and therefore multiply the bluff body lip velocity by that factor. This process maintains the same stoichiometry in the two burners and hence the test section inlet temperature and the flame density ratio.

CHAPTER 4. INSTRUMENTATION AND DIAGNOSTIC TECHNIQUES

This chapter details the instrumentation installed in the facility and the diagnostic techniques used in the experimental work. The two primary diagnostic techniques were particle image velocimetry (PIV) and chemiluminescence imaging. Time-resolved PIV was used to measure the mean and unsteady velocity and vorticity fields. High speed chemiluminescence was used to capture the mean and fluctuating flame position and to estimate the flame's unsteady heat release. In addition to these techniques, laser Doppler velocimetry (LDV) was used to resolve the boundary layer at the bluff body lip, and Mie scattering was used to obtain planar flame position measurements synchronized with the PIV measurements.

4.1 Flow Instrumentation

Mass flowrates for the primary and secondary air and fuel were measured across calibrated knife-edge orifice plates using the static upstream pressure and the differential pressure across the plate, measured with Omega PX209 solid state pressure transducers and Omega PX771A differential pressure transmitters, respectively. The temperature just upstream of the test section (after addition of secondary air and fuel) was measured by a type K thermocouple and an Omega TX13 Transmitter. Values were recorded once every second for ten seconds, and then averaged. Typical measured gas temperatures entering the test section were 25-30% lower than the calculated adiabatic temperature, as might be expected due to heat loss in the settling section. The flame density ratio was estimated from an equilibrium solution for the adiabatic flame temperature, using the

measured approach flow temperature and using a gas composition determined from an adiabatic mixing calculation of the secondary air, fuel, and equilibrium vitiated gas.

Uncertainty in the density ratio was estimated from the Mie scattering images taken during the PIV measurements. The density ratio was estimated by measuring the intensity summed over a 140 pixel region on each side of the flame, for several images. The ratio of the intensity in the unburned region to that in the burned region was defined as S_{Mie}. The mean and 95% confidence intervals of S_{Mie} are plotted in Figure 4-1 against the density ratio defined above, ρ_u/ρ_b. A one-to-one line is shown to aid comparison.

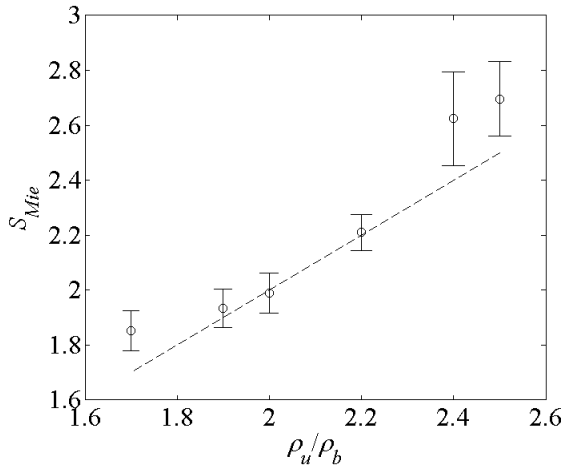

Figure 4-1. Density ratio uncertainty estimated from Mie scattering images

For the 50 m/s cases, the uncertainty in measured gas flowrates and the resulting temperature and density ratios was about 2%. For the 20 m/s cases, uncertainty was about 4% for the measured gas flowrates, and about 10% for the temperature and density ratios. Uncertainties are bounded by worst case combinations of maximum and

minimum flowrates and thermocouple readings for a given test. Uncertainty in thermocouple readings was less than 1%.

4.2 Particle Image Velocimetry

The high speed, time-resolved PIV measurements were obtained with a LaVision Flowmaster Planar Time Resolved system. The laser system is a Litron LDY303He Nd:YLF system with a laser wavelength of 527 nm, pulse duration of 10 ns, and 5 mJ/pulse pulse energy. Each of the two lasers in the system has a maximum 10 kHz repetition rate. Images were captured using the Photron High Speed Star 6 camera.

The flow was seeded with 5 μm Al_2O_3 particles. This ceramic material was chosen due to its durability in reacting flows and its high refractive index [54]. This particle size was chosen because it is large enough to resist accumulation on and clouding of the test section windows, although accumulation was still somewhat troublesome. Also, this particle size has a sufficiently small Stokes number to accurately track the flow at the frequencies of interest. Following the work by Mei [55], the Stokes number calculated for this flow and seed particle combination was 0.015. This Stokes number is based on 5 μm seeding particles, with environmental kinematic viscosity of $3x10^{-4}$ m^2/s, and oscillation frequency of 850 Hz (roughly the highest global mode frequency encountered). The high temperature and corresponding high viscosity in the test section facilitate the use of such a particle. This Stokes number is comfortably below the cutoff Stokes number for solid particles in air [55], which is in the range of .02-.04 and would correspond to a frequency of at least 1500 Hz.

The DaVis 7.2 software from LaVision was used to process the PIV data, performing background subtraction and then calculating the velocity fields. All velocity calculations

were performed using the LaVision multi-pass method; this consisted of a single pass with 64x64 pixel interrogation windows and 50% overlap between interrogation windows, followed by 2 passes with 32x32 pixel interrogation windows and 50% overlap between the interrogation windows. The next two sections provide details on the PIV measurements that are specific to either the unforced or forced experiments. A typical instantaneous velocity field measured with PIV is shown in Figure 4-2. Note that boxes around velocity fields are not meant to indicate the locations of the channel walls. The PIV measurement did not reach close enough to the channel walls to capture their boundary layers.

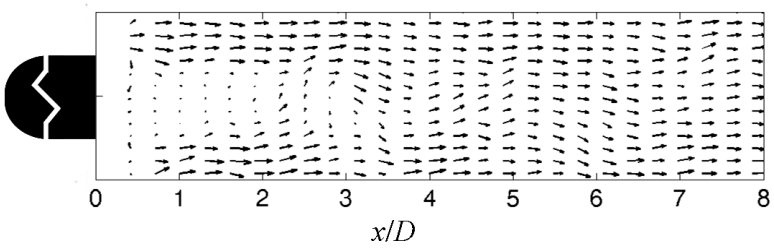

Figure 4-2. Typical instantaneous velocity field from PIV measurement. This measurement was taken with the ballistic bluff body at 20 m/s, $\rho_u/\rho_b = 1.9$

4.2.1 *Unforced Experiments*

For the unforced experiments, the camera was operated with a pixel resolution of 640x448. A total of 2000 PIV image pairs was taken at a frame rate of 10 kHz with 12 μs between images for a given pair. A BG-28 optical filter was placed in front of the camera for removal of red and infrared radiation during reacting tests. The filter transmission exceeds 10% for wavelengths between 340 and 630 nm, and peaks at 82% transmission at 450 nm.

Post-processing on the velocity vectors was performed with the DaVis 7 software, as follows. For 50 m/s cases, any velocity vector with an axial component outside of the ±90 m/s range or a transverse component outside of the ±45 m/s range was discarded. For 20 m/s cases, the accepted range of axial velocities was ±36 m/s and for transverse velocities was ±18 m/s. Furthermore, any velocity vector whose velocimetry calculation had a peak correlation coefficient less than 0.2 was discarded, as were neighboring vectors whose ratio of difference to average velocity magnitude was greater than 20 percent of the rms of the nearest neighbors.

Studies were performed with two fields of view and corresponding resolutions. The larger field captured a region of the combustor that was nominally 250 mm long in the axial direction and 80 mm wide in the transverse direction. This field of view had a velocity field resolution of 4.8 mm per pixel using a 50 mm lens at f/1.8. The smaller field of view captured a region in the combustor that was 100 mm x 80 mm, and had a velocity field resolution of 3.0 mm per pixel using an 85mm lens at f/2.8. The spatial resolution of the mie scattering images is 16 times greater than the corresponding velocity field resolution, due to the use of 32x32 pixel interrogation windows and 50% overlap in the velocimetry calculation.

4.2.2 *Acoustically Forced Experiments*

For the forced experiments, the camera was again operated with a pixel resolution of 640x448, but this time with image pairs being acquired at a frame rate of 5 kHz. The reason for the reduced sampling rate was to capture a greater number of cycles of the forced response than what could be acquired at the maximum 10 kHz.. This increases the frequency bin resolution of the ensuing fast Fourier transforms, at the expense of a lower

Nyquist frequency. A 55 mm Nikon lens was mounted to the camera and operated at f/5.6. A 527/20 nm BrightLine single-band bandpass optical filter (Part number FF01-527/20-25) was placed in front of the camera in order to capture only light originating from the laser (particularly, for removal of red, blue, and infrared radiation associated with combustion). The filter pass-band is centered at 527nm and has greater than 93% transmission between 517 and 437nm. This filter was an upgrade from the one used in the unforced experiments, and provided significantly more transmission of laser light. Consequently, the reason for the reduced aperture was to avoid saturating the camera.

Post-processing on the velocity vectors was performed with the DaVis 7 software, as follows. Any velocity vector with an axial component outside of the ±90 m/s range or a transverse component outside of the ±45 m/s range was discarded. Furthermore, any velocity vector whose velocimetry calculation had a peak correlation coefficient less than 0.2 was discarded, as were neighboring vectors whose ratio of difference to average velocity magnitude was greater than 20 percent of the rms of the nearest neighbors.

All studies from the forced experiments were performed with a single field of view. The field of view covered a region of the combustor that was roughly 160 mm long in the axial direction and 80 mm wide in the transverse direction, with to a velocity field resolution of 2.84 mm per pixel. The spatial resolution of the corresponding Mie scattering images is 16 times greater, due to the use of 32x32 pixel interrogation windows and 50% overlap in the velocimetry calculation.

4.3 High Speed Chemiluminescence

The next two sections discuss the methodology used to capture high speed chemiluminescence images for both the unforced and forced experiments. While

chemiluminescence provides a useful estimation of the unsteady heat release of the flame [56], it also captures the space-time evolution of the flame position. The flame position was quantified from edge detection, by normalizing the chemiluminescence intensity at each axial position, binarizing the resulting image according to an intensity threshold, and then extracting the longest two interfaces in the binarized image.

4.3.1 *Unforced Experiments*

For the unforced experiments, high speed chemiluminescence imaging was performed with a Photron Fastcam SA3 camera. The flame was imaged through a BG-28 filter, which is characterized in the discussion of the unforced experiments above in section 4.2, *Particle Image Velocimetry*.

Acquisition parameters were set up as follows. A total of 8029 images were captured for each test at a 3000 Hz frame rate and 512 x 256 pixel resolution. The camera was operated continuously such that the exposure time was $1/3000^{th}$ s. The flame was imaged from the bluff body trailing edge to approximately nine bluff body diameters downstream, with a spatial resolution of about 0.42 mm/pixel. A typical flame image from this set of experiments is shown in Figure 4-3.

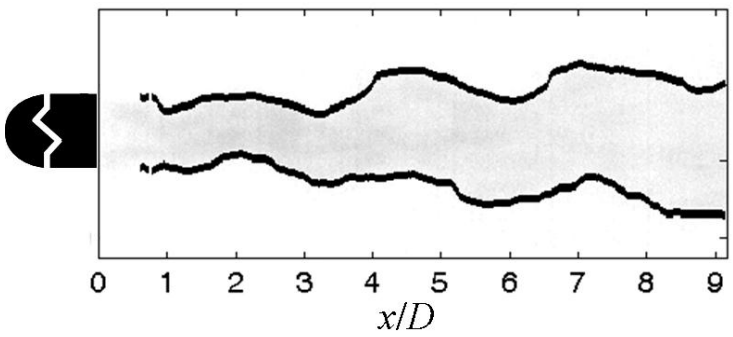

Figure 4-3. Typical flame image from the unforced experiments with edge tracking overlaid. This image was taken with the ballistic bluff body at 50 m/s, $\rho_u/\rho_b = 1.7$

4.3.2 *Acoustically Forced Experiments*

Due to equipment upgrade, a different camera and filter were used for the acoustically forced cases. Images were captured with a NAC Memrecam GX-3 camera with a 135 mm lens and an intensifier. The camera was operated at a 5000 Hz frame rate with a total of 4000 images stored in each run. The selection of frame-rate and number of images captured is explained in Chapter 3, *Experimental Facility and Design of Experiments*. The exposure time was 1/5000 seconds. Shorter exposure times were investigated, but produced qualitatively similar images and required more intensifier gain. The lens aperture was wide open at f/2.8. The flame was imaged through a 434/17 nm BrightLine single-band bandpass filter for chemiluminescence imaging. The filter has a pass band centered at 434 nm, with 90% transmission between 425.5nm and 442.5 nm.

The camera was operated at a 384 x 768 pixel resolution. The resolution for these measurements was roughly 0.4 mm per pixel. Thus, the field of view included the entire channel height, and an axial domain $15D$ downstream of the bluff body. A typical flame image from this set of experiments is shown in Figure 4-4.

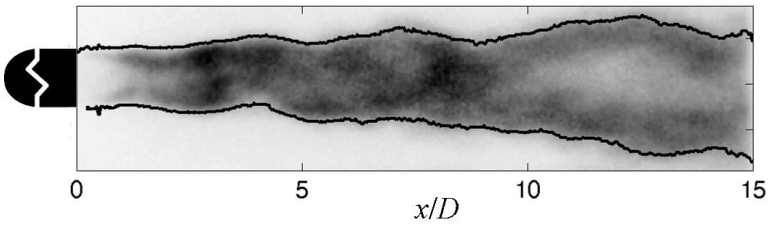

Figure 4-4. Typical flame image from the forced experiments with edge tracking overlaid. This image was taken with the ballistic bluff body at $\rho_u/\rho_b = 1.7$, a natural to forced frequency ratio of $f_n/f_f = 1.1$, and a forcing amplitude of $A_f = .005$

4.4 Laser Doppler Velocimetry

Two-component Laser Doppler Velocimetry (LDV) was used to measure the boundary layer thickness at the trailing edge of the bluff body. Seeding material consisted of 5 μm aluminum oxide, whose frequency response characteristics were discussed previously. For each measurement volume, data acquisition was limited to either 30 seconds or 5000 counts, whichever came first. The acquisition channel used for axial velocity measurements used a laser wavelength of 514.5 nm, a fringe spacing of 7.9196 μm, a beam waist of 70.19 μm, and a Bragg cell frequency of 40 MHz. The resulting low and high velocity limits were -24 m/s and 119 m/s, respectively. The acquisition channel used to measure the transverse velocity used a laser wavelength of 488 nm, a fringe spacing of 7.5117 μm, a beam waist of 66.57 μm, and a Bragg cell frequency of 40 MHz. For this channel, the low and high velocity limits were -68 m/s and 68 m/s. Both channels had a focal length of 300 mm, a beam separation of 19.5 mm, a beam diameter of 2.8 mm, and used a 20 MHz high pass filter.

4.5 Mie Scattering

Flame edge tracking was performed on the mie scattering images from PIV. Details on the acquisition of these images can be found in the above sections. It should be noted that Mie scattering was not the primary method for obtaining flame location information. It is, however, the only flame location measurement available that is synchronized with the PIV measurement. Although flame edge detection generally works quite well with these types of mie scattering images, it is difficult at the low flame density ratios of interest in this work. Additionally, edge detection in Mie scattering images is often more computationally expensive and of lower spatial resolution than edge detection from

chemiluminescence. It is for these reasons, in addition to the desire to estimate heat release oscillations, that chemiluminescence flame imaging was performed.

Flame edge detection on the Mie scattering images was performed as follows. First, a maximum filter was used between the two Mie scattering images of a given pair. This was done to superimpose the particles from the two images and increase the particle count. Next, a minimum filtered image from the two pairs was subtracted, which served as a rudimentary background subtraction to remove reflections and artifacts from fogged quartz. The resulting image was median filtered with 10 pixel by 10 pixel windows. This had the effect of "smearing" the reflected light from particles nearly continuously in the denser regions of reactant gas. Next, the intensity at each axial position was normalized by the maximum value in order to remove effects due to non-uniform laser sheet intensity. Finally, the image was binarized according to a threshold intensity, and the longest interface in the binary field was extracted as the instantaneous flame edge. This process was only performed on a single flame edge (the upper edge) due to its computational expense. The computational expense primarily stems from the median filter. A typical pair of Mie scattering images superimposed on each other with flame edge detection overlaid is shown in Figure 4-5a.

In addition, the time averaged density field was determined from the flame edge detection. The instantaneous density was then specified as a binary field having either the burned or unburned value. These instantaneous values were then averaged at each location to obtain the temporally averaged density field. The key assumption behind this procedure is that the flame is very thin relative to bluff body diameter, which is well satisfied for this problem, as verified by detailed chemical kinetic calculations of an

unstretched, premixed flame (using GRI 3.0) showing that the estimated flame thickness is roughly 2% of the bluff body diameter. A typical mean density field resulting from this method is shown in Figure 4-5b.

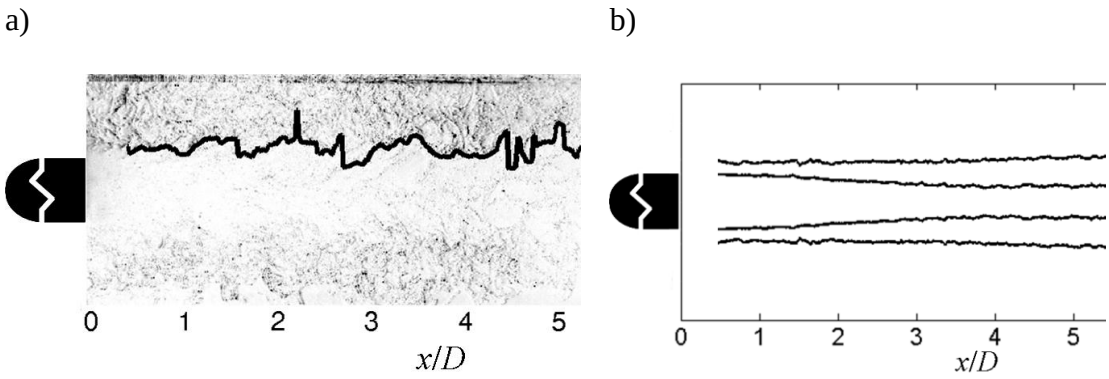

Figure 4-5. a) Flame edge tracking overlaid on a typical mie scattering image and b) resulting mean density field with $(\rho-\rho_b)/(\rho_u-\rho_b)=0.1,\ 0.9$ contours. Mean density field is a reflection from the upper flame branch about the flow centerline. Conditions were $\rho_u/\rho_b=2.5$, $U_{lip}=50$ m/s, unforced.

CHAPTER 5. EXPERIMENTAL RESULTS: UNFORCED FLAME AND FLOW DYNAMICS

This chapter discusses results of the unforced experiments. In these experiments, the flow stability characteristics were altered by varying density ratio, bluff body lip velocity, and bluff body shape. The chapter begins with a description of the time averaged inflow conditions and velocity field. The time averaged velocity field is used to approximate the base flow in Chapter 6, *Local Hydrodynamic Stability Analysis*, and the inflow conditions are needed for computational simulations of this flow. The chapter next shifts attention to the unsteady flame and flow dynamics, focusing on experimental characterization of the flow stability characteristics and identification of the important hydrodynamic stability parameters.

5.1 Mean Flowfield Characteristics

This section summarizes the time averaged flow characteristics and inflow conditions. These data are useful as inputs for flow stability or computational predictions. First is a presentation of LDV-based measurements of the inflow velocity, specifically the boundary layer at the bluff body lip. Next is a presentation of PIV-based measurements of the time averaged and fluctuating root mean square (rms) velocity field characteristics. Several important flow parameters are then extracted from these data, including recirculation zone length, location and value of peak reverse flow velocity in the wake, and the dependencies of these quantities upon flame density ratio and bluff body lip velocity. All of these base flow features have important implications on flow stability characteristics.

Consider first the inflow conditions. Two dimensional LDV measurements were obtained at the bluff body trailing edge by scanning the flow transversely in steps of 0.1 mm, as shown in Figure 5-1. Supplemental data are presented in *Appendix A*. LDV was selected for this measurement because it is well suited to fine spatial resolution, and has less trouble than PIV with laser light reflecting from the bluff body. The velocity components measured were the axial velocity, u, and the transverse velocity, v. These data show that the separating boundary layer approaches the freestream velocity at a distance of about 1 mm from the flameholder. The momentum thickness was calculated with the relation:

$$\theta = \int_{y/D=0}^{y/D=2} \left\{ \frac{1}{4} - \left(\frac{U - U_{av}}{|\Delta U|} \right)^2 \right\} dy \tag{5.1}$$

yielding $\theta = 0.14$ and $\theta = 0.10$ mm for $\rho_u / \rho_b = 1.7$ and $\rho_u / \rho_b = 2.5$, respectively, for the v-gutter at $U_{lip} = 50\,\text{m/s}$. This leads to a most-amplified frequency for the Kelvin Helmholtz instability in the shear layers of $f_{KH} = 12$ kHz and $f_{KH} = 21$ kHz respectively using the relation [57]

$$f_{KH} = 0.032 \frac{U_{lip}}{\theta} \tag{5.2}$$

These high frequency shear layer dynamics cannot be temporally resolved by the 10 kHz PIV system. The lower density ratio case has a thicker boundary layer since the reactant temperature (and therefore viscosity) for low density ratio cases is higher than that for high density ratio cases. In comparison to the v-gutter, the momentum thickness at the ballistic bluff body trailing edge was somewhat higher, as would be expected because of the boundary layer's longer development length in this case. For most cases,

the momentum thickness at the trailing edge of the ballistic bluff body was 1.7 times that of the v-gutter. Measured momentum thickness values and estimated f_{KH} values are presented in Table 1 for both bluff bodies.

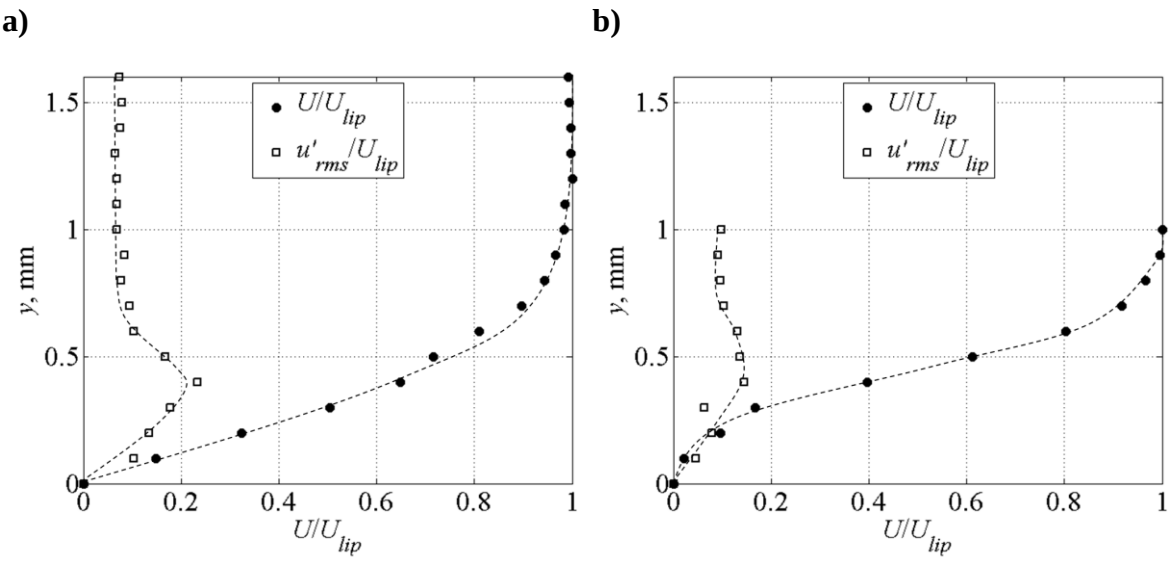

Figure 5-1. Boundary layer profiles for the v-gutter at $U_{lip} = 50$ m/s, and a density ratio of a) $\rho_u/\rho_b = 1.7$ and b) $\rho_u/\rho_b = 2.5$, showing point of inflection

Table 1. Measured momentum thickness and estimated Kelvin Helmholtz frequency, as well as outer flow turbulence intensity, for both bluff bodies and several flow conditions

Bluff Body	U_{lip} (m/s)	ρ_u/ρ_b	u'_{rms}/U_{lip}	θ (mm)	f_{KH} (Hz)
V-gutter	50	1.7	0.08	0.14	12000
V-gutter	50	2.5	0.10	0.09	21000
V-gutter	20	1.9	0.15	0.15	5300
V-gutter	20	3.2	0.15	0.20	4600
Ballistic	50	1.7	0.16	0.25	5900
Ballistic	50	2.5	0.13	0.15	12000
Ballistic	20	1.9	0.22	0.26	2200
Ballistic	20	3.2	0.23	0.16	4300

Returning to Figure 5-1, note the differences in the near wall velocity profile in the high and low density ratio cases. This is due to heat transfer from the hot bluff body to the boundary layer. In the high temperature ratio case, the v-gutter becomes very hot with respect to the much cooler reactant temperature; therefore there is heat conduction from the flame holder to the reactant gas. This is a destabilizing effect [58], and leads to a point of inflection profile (as evidenced by the data in Figure 5-1b). However, no boundary layer separation was observed, as shown by the data in the figure. The profiles for the high density ratio case are "clipped" at 1 millimeter because of thermal expansion of the v-gutter in the transverse direction (again, because the flameholder becomes very hot for this case), which obscured the first $1/2$ millimeter of the transverse scan. The rig is restrained such that axial thermal expansion is not a concern.

The measured turbulence intensity, approximated from the rms axial velocity $u'_{rms}(y)$ and rms transverse velocity $v'_{rms}(y)$ is plotted as a function of transverse position in Figure 5-2. Inflow turbulence intensity, $I_{turb} = \sqrt{(u'_{rms})^2 + (v'_{rms})^2}\,/U_{lip}$, was about 9% in

the outer flow and ranged from roughly 15 percent to 25 percent in the boundary layers for the v-gutter at $U_{lip} = 50$ m/s.

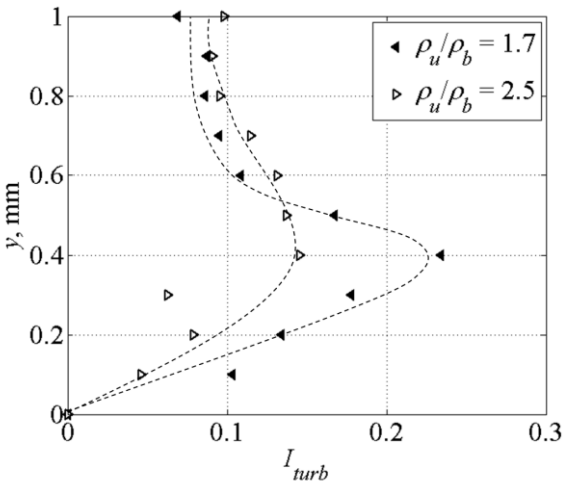

Figure 5-2. LDV measurement of the turbulence intensity at the bluff body trailing edge, as a function of transverse position, for the v-gutter at $U_{lip} = 50$ m/s.

Consider next the time averaged flow features downstream of the bluff body. A typical flow field is shown in Figure 5-3, illustrating the expected high velocity outer flow and wake region behind the bluff body, which transitions from negative to positive velocity at nearly three bluff body diameters downstream. The time averaged density field for a low density ratio case is plotted in Figure 5-4.

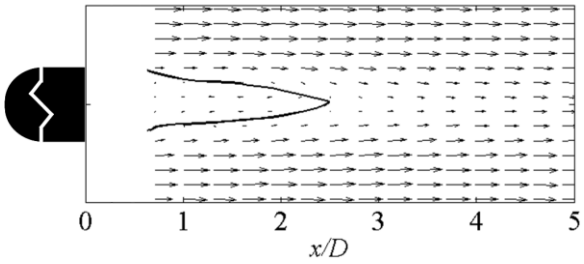

Figure 5-3. Illustration of the time averaged bluff body flowfield, showing region of reverse flow in the wake (shown for ballistic bluff body at $U_{lip} = 50$ m/s, $\rho_u/\rho_b = 2.5$); Black line dividing backflow and forward flow regions indicates contour of zero axial velocity.

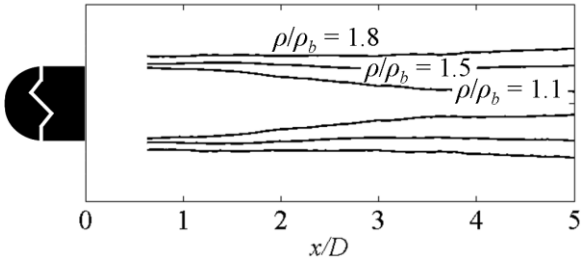

Figure 5-4. Contours of the reacting bluff body mean density field determined from Mie scattering images, shown for ballistic bluff body at $U_{lip} = 50$ m/s, $\rho_u/\rho_b = 1.9$

Figure 5-5 plots streamlines in the wake of the v-gutter for several representative cases; the top half of each image represents a 50 m/s case, and the bottom half of each image represents a 20 m/s case for the same density ratio. These plots show that the v-gutter wake has a significant time-averaged transverse velocity component, especially in the bluff body nearfield. The plots also show an increase of recirculation zone length, L_r, with increasing density ratio, and also that L_r is relatively insensitive to velocity (but slightly longer for higher velocity). Both observations are quantified later.

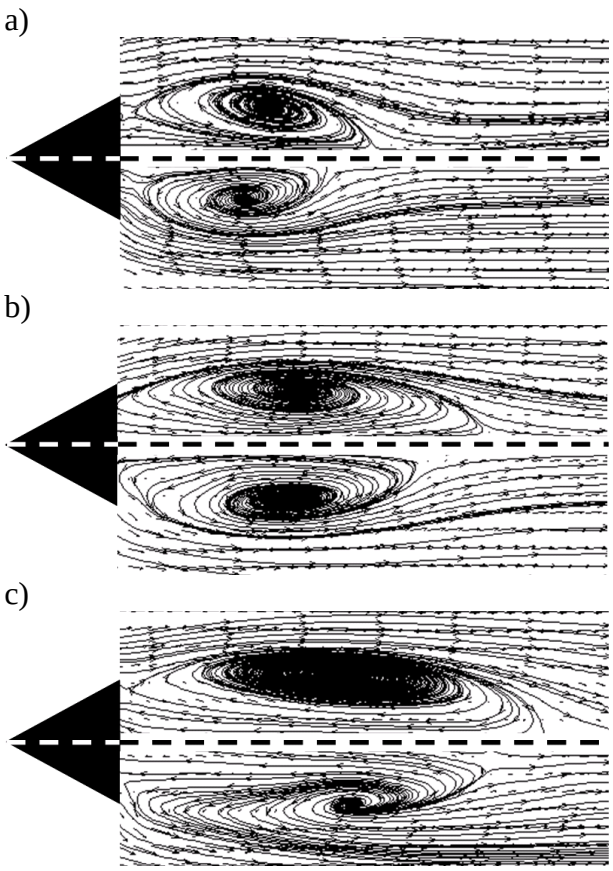

Figure 5-5. Time-averaged streamlines and velocity vector fields for the v-gutter at several density ratios; top half of each image is from a $U_{lip} = 50$ m/s test, bottom half of each image is from a $U_{lip} = 20$ m/s test. Density ratios shown are a) $\rho_u/\rho_b = 1.0$, b) $\rho_u/\rho_b = 1.7$ and c) $\rho_u/\rho_b = 2.5$

Figure 5-6 plots the dependence of the time-averaged axial flow field along axial and transverse cuts. Start with Figure 5-6a, which plots the axial variation of the velocity at two transverse locations, corresponding to the bluff body centerline and one half diameter beyond the bluff body lip. The figure illustrates how the reverse flow in the recirculation zone evolves with axial position, reaching a maximum reverse flow velocity at a location denoted as $L_{\max}$ which is typically about 1.5 bluff body diameters downstream. The

recirculation zone length, L_r, is also indicated on the figure. The transverse profiles of axial velocity are shown in Figure 5-6b. These transverse profiles of axial velocity, taken at fixed axial positions, illustrate the recirculation zone and wake profile characteristics. The corresponding mean density profiles are overlaid. Note that the density gradient region is slightly thinner than, although comparable to, the shear layer thickness at a given axial position. Note also that the point of inflection of the average density profile is located near that for the velocity. In general, near the bluff body the flame tends to sit slightly closer to the flow centerline than the shear layer point of inflection ("inboard" of the shear layer), whereas farther downstream the flame tends to sit farther from the flow centerline ("outboard" of the shear layer) due to its propagation into the reactants.

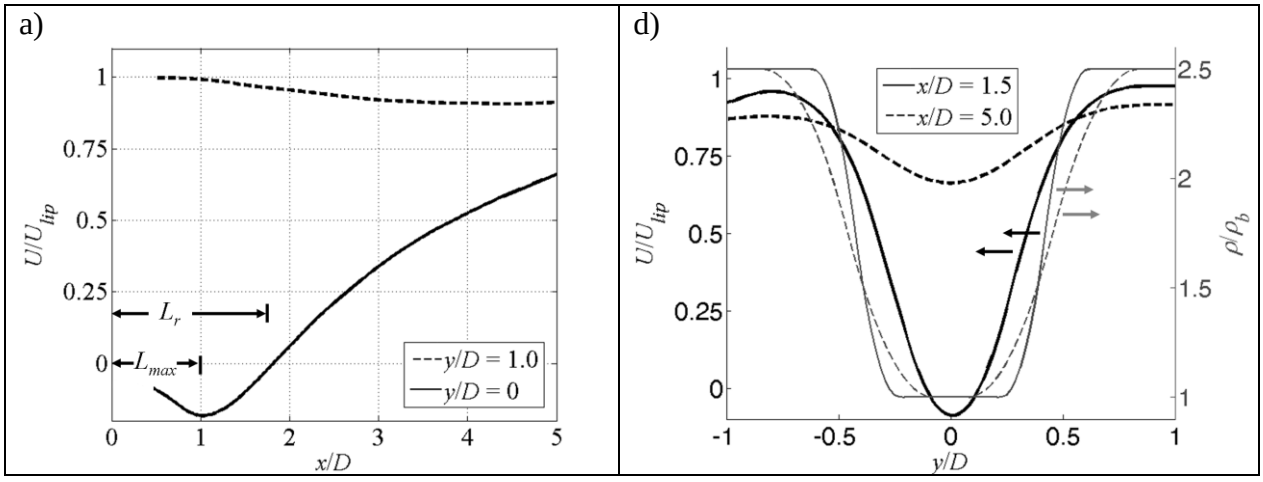

Figure 5-6. Mean axial velocity and density profiles, showing a) axial profiles & b) transverse profiles for the ballistic bluff body at $U_{lip} = 50$ m/s, $\rho_u/\rho_b = 2.5$. Arrows indicate which axis of ordinates belongs to which dataset.

The effects of density ratio on the recirculation zone characteristics are illustrated in Figure 5-7 and Figure 5-8. These plots show that the recirculation zone length generally increases with density ratio. This seems to be consistent with the idea that recirculation

zone length increases as large-scale vortex shedding is suppressed [3, 5, 59]. Furthermore, the magnitude and location of peak reverse velocity also increase with density ratio. These latter parameters have important implications on the hydrodynamic global mode growth rate, and location of the pocket of absolute instability (the wavemaker for the global mode). These points will be discussed in significantly more detail in Chapter 6, *Local Hydrodynamic Stability Analysis*. When reviewing the time averaged velocity field characteristics, it is important to remember that these data are obtained under "limit cycle" conditions for the globally unstable cases. Therefore, the reverse flow velocities and recirculation zone geometry are presumably impacted by the global instability of the flow under the lower density ratio conditions. This influence of the flow instability on the time-averaged flowfield should be kept in mind when considering the time-averaged flowfield to be the base flow for a hydrodynamic stability calculation. Finally, the data in Figure 5-8 show a relatively weak dependence of recirculation zone characteristics on velocity, consistent with previous observations [60].

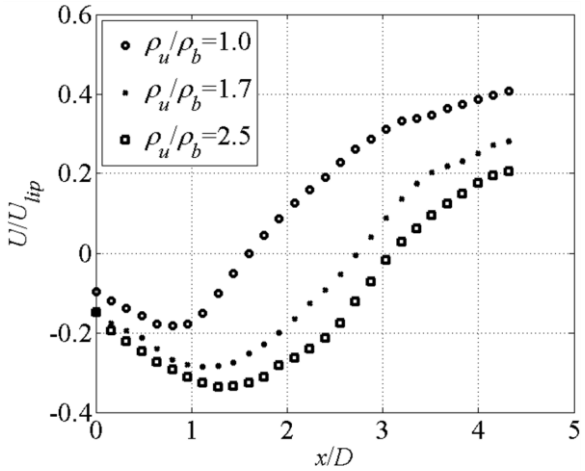

Figure 5-7. Centerline time-averaged axial velocity for the v-gutter at various density ratios and $U_{lip} = 50$ m/s.

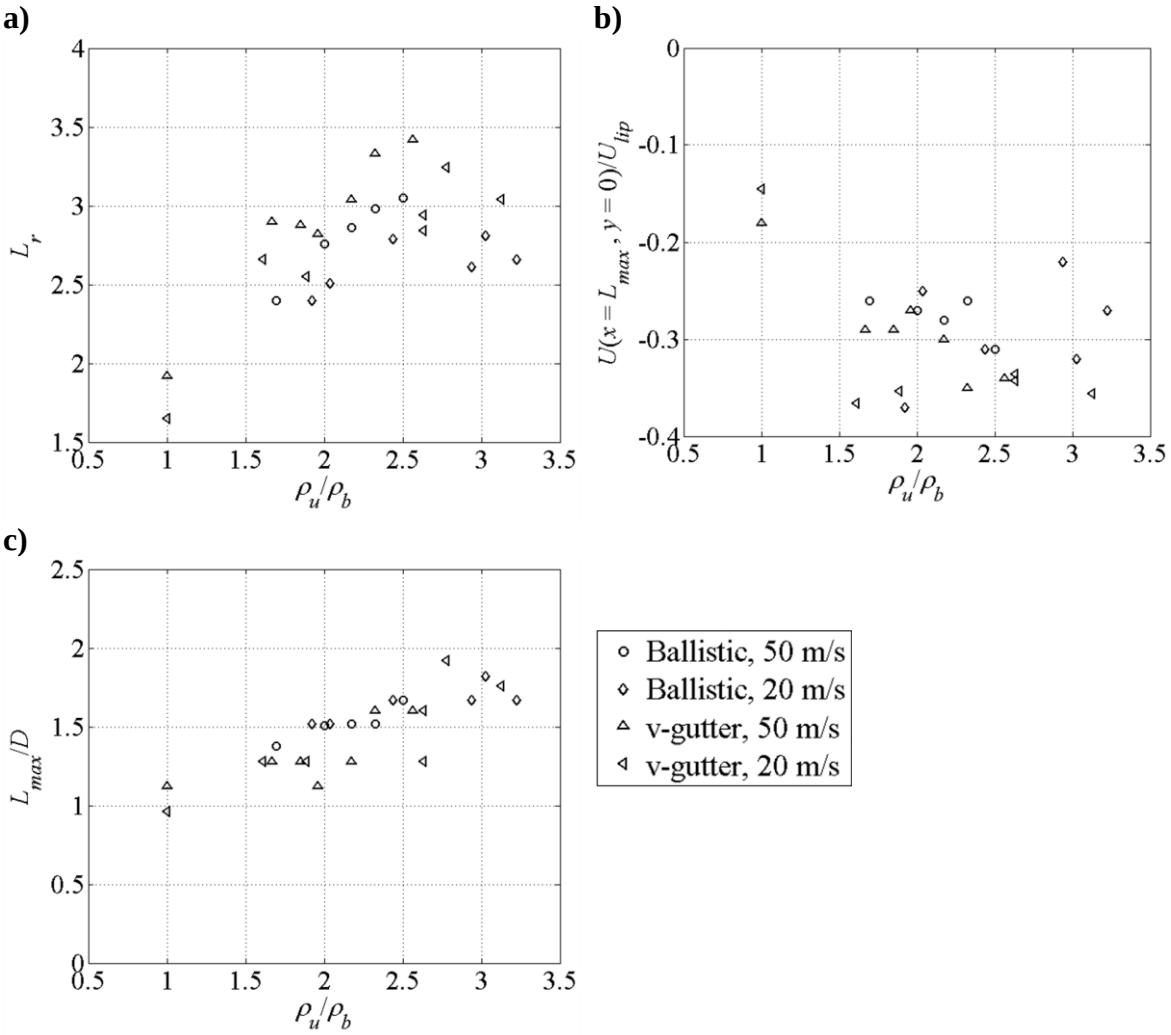

Figure 5-8. Dependence of the recirculation zone geometry on the density ratio, showing a) the recirculation zone length, b) the peak backflow velocity and c) the axial location of peak backflow velocity.

5.2 Unsteady Flowfield Characteristics

This section describes key dynamical characteristics of the flame and flow dynamics. In order to present a qualitative picture of the flow first, Figure 5-9 illustrates typical instantaneous streamlines and flame images from low and high density ratio flames. The flame images show clear, spatially sinuous undulations at low density ratios which largely disappear at higher density ratios. This is supplemented in *Appendix A*, which

shows time-sequences of flame images from a range of density ratios. These observations are in agreement with previous experiments [61] and computations [23] reviewed in the Background section.

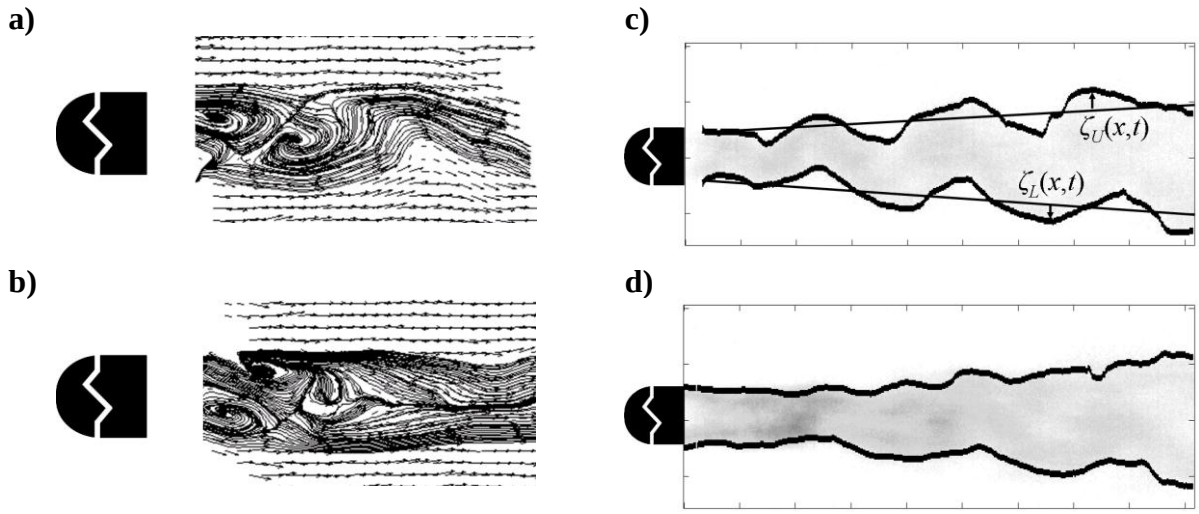

Figure 5-9. Typical instantaneous visualizations of flame and flow structure for the ballistic bluff body with $U_{lip} = 50$ m/s at two density ratios, showing a) streamlines at $\rho_u/\rho_b = 1.7$, b) streamlines at $\rho_u/\rho_b = 2.4$, c) flame with edge tracking at $\rho_u/\rho_b = 1.7$ and d) flame with edge tracking at $\rho_u/\rho_b = 2.4$

Flame dynamics were quantified using the transverse positions of the top and bottom flame branch edges, $\zeta_U(x,t)$ and $\zeta_L(x,t)$, as functions of axial position and time, as shown in Figure 5-9c. For brevity, the flame edge position is shortened to $\zeta(x,t)$ if there is no need to distinguish between the two flame branches. The flame position measurements resulted in time series for edge positions along both flame branches at each axial position. These time series are Fourier transformed to determine their temporal spectra, given by $\hat{\zeta}_U(x,f)$ and $\hat{\zeta}_L(x,f)$.

PIV data were used for corresponding analysis of flowfield dynamics. PIV data shown in this section were taken from the transverse velocity along the combustor centerline, $v(x, y = 0, t)$ whose Fourier transform is given by $\hat{v}(x, y = 0, f)$. The next section summarizes the key results obtained from analysis of the time series and spectra of both flame and flow dynamics as functions of flame density ratio.

5.2.1 *Spectral Analysis*

Figure 5-10 presents the flame and flow spectra at their axial positions of peak magnitude, for three density ratios, as functions of Strouhal number, $St_D = fD/U_{lip}$. Figure 5-10a shows this result for the upper flame edge. At the highest density ratio shown, $\rho_u/\rho_b = 2.4$, spectral energy is broadly distributed across all frequencies, with a small peak at $St_D \sim 0.24$. As the density ratio is decreased to 2.0, a clear feature appears centered near $St_D = 0.24$. As the density ratio is further decreased to 1.7, the response at $St_D = 0.24$ becomes more narrowband and prominent. Figure 5-10b shows spectra of the unsteady transverse velocity for the same flow conditions, and demonstrates that the flow similarly exhibits a growing narrowband spectral feature at $St_D = 0.24$.

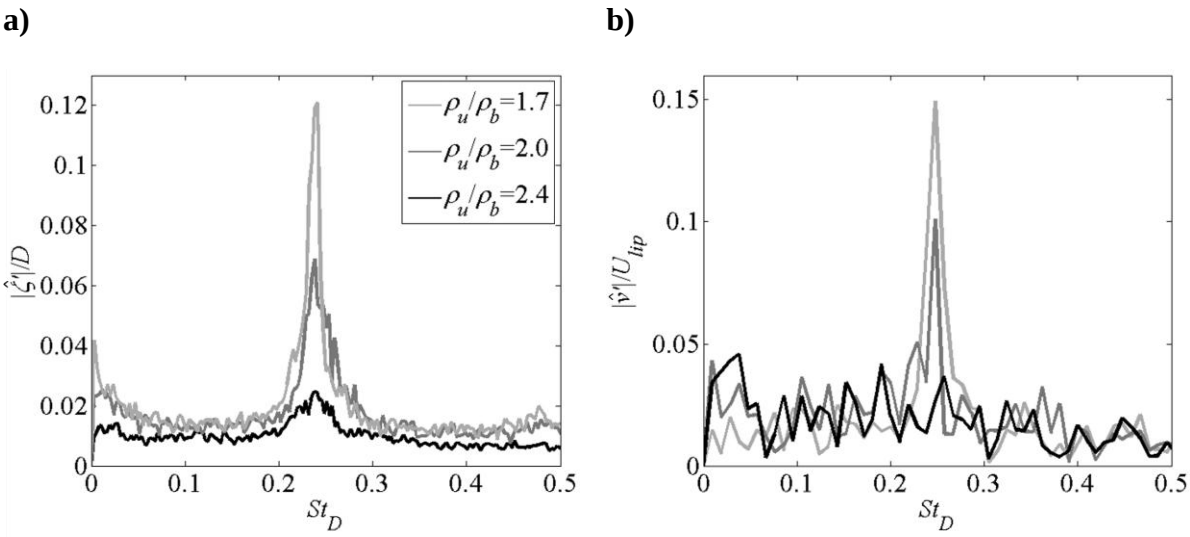

Figure 5-10. Spectra for ballistic bluff body at $U_{lip} = 50$ m/s at the axial position of peak response for a) upper flame edge displacement and b) centerline transverse unsteady velocity magnitude

The spatial evolutions of the velocity and flame displacement spectra are summarized in Figure 5-11. The top two figures correspond to the lowest density ratio, $\rho_u/\rho_b = 1.7$. Both figures show a strong narrowband peak at $St_D = 0.24$ for the low density ratio case, whose magnitude varies non-monotonically with axial location. These flame spectra envelope results are typical of those measured in flames forced by narrowband acoustic disturbances and reflect the additional effect of flame anchoring and kinematic restoration [62]. Results for the higher density ratio values of 2.0 and 2.4 are shown in the 2nd and 3rd rows, respectively, illustrating a decrease in amplitude of the narrowband response feature. The envelopes of the spatial evolution of the responses at $St_D = 0.24$ are overlaid in Figure 5-12 for ease of comparison between the various density ratios. Notice that the flame response and the flow response are related, as would be expected. The peak flame response occurs a few bluff body diameters downstream of the peak

centerline flow response, and a "stronger" flow response results in a stronger flame response. A comprehensive overview of this data is presented in *Appendix A.*

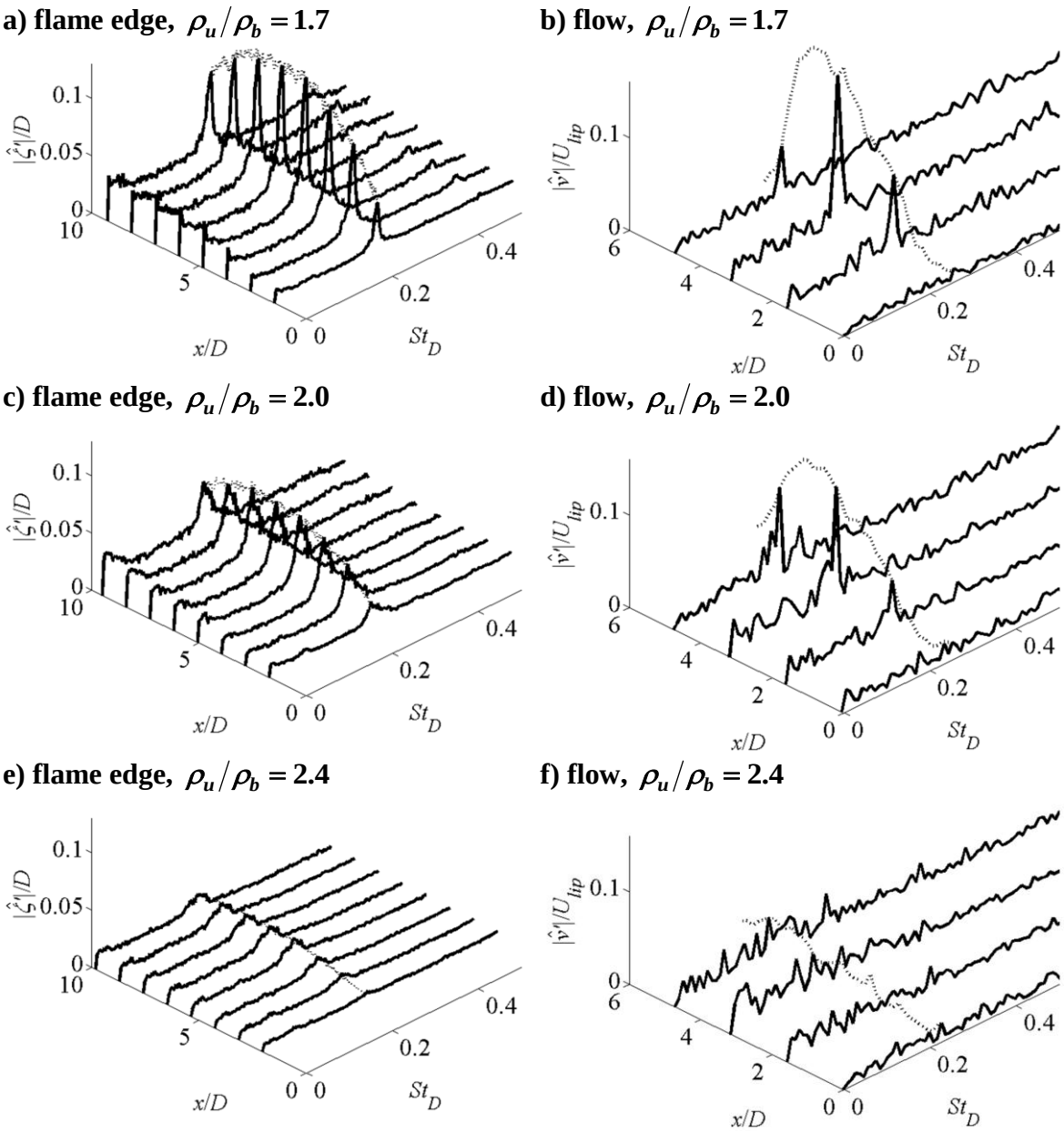

Figure 5-11. Spectra for the ballistic bluff body at $U_{lip} = 50$ m/s, as a function of axial position. Left and right images correspond to flame and flow spectra, respectively. Images ordered top to bottom with increasing density ratio, $\rho_u/\rho_b = 1.7$, 2.0, and 2.4.

a) **b)**

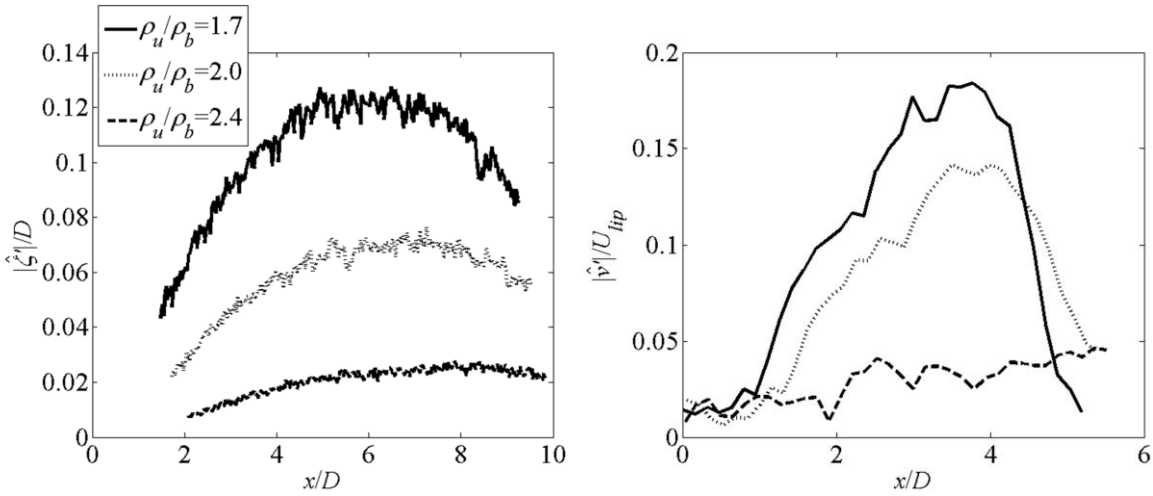

Figure 5-12. Axial profiles of a) the flame and b) the flow, showing the response at $St_D = 0.24$ for the ballistic bluff body at $U_{lip} = 50$ m/s

In order to focus on the characteristics near the frequency of peak response, the integrated power under the spectral peak between Strouhal numbers of 0.20 and 0.28 is computed as a function of density ratio. This energy is converted to an rms square of the signal at the response frequency by use of Parseval's theorem, using the relation below that relates the rms of the time series $s(t)$ of duration T and spectrum $\hat{s}(f)$,

$$s_{rms} = \sqrt{\frac{1}{T}\int |\hat{s}(f)|^2 \, df} \tag{5.3}$$

These rms values are presented in Figure 5-13 for both the flame and the fluctuating velocity. The flame data in Figure 5-13 show that the unsteady flame displacement rms has a value of roughly 4% of the bluff body diameter over the $2.4 < \rho_u/\rho_b < 3.4$ range. Below a value of $\rho_u/\rho_b = 2.4$, the response gradually increases to 18% at $\rho_u/\rho_b = 1.7$. Similar behavior is shown by the velocity data. This plot also indicates that the transition

in flow and flame characteristics is not an abrupt bifurcation with change in density ratio, but a more gradual increase in narrowband response as the density ratio decreases. Spectral energies for other bluff body/velocity combinations are included in *Appendix A.*

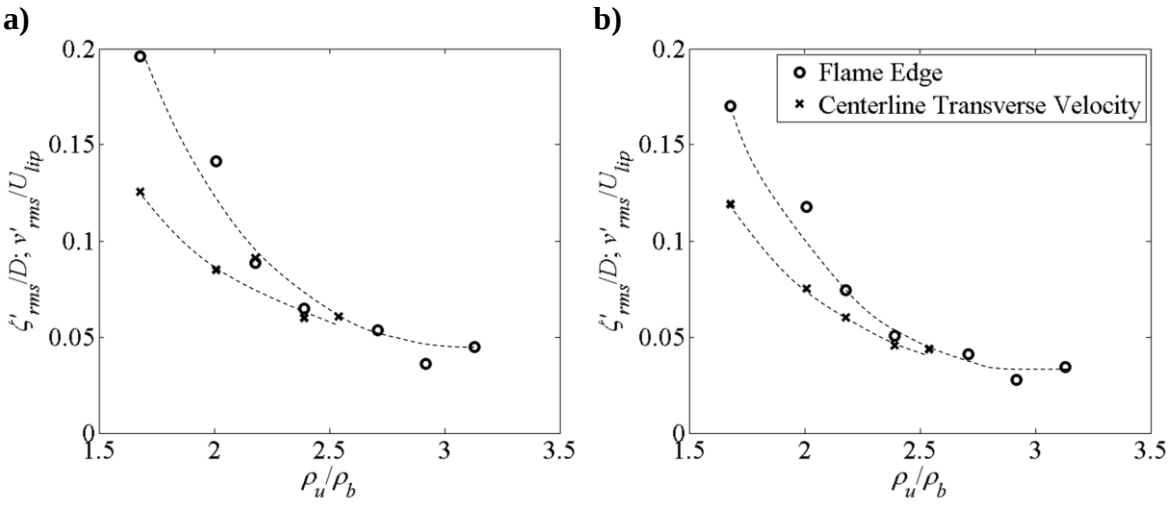

Figure 5-13. Dependence of narrowband spectral energy ($0.20 < St_D < 0.28$) upon density ratio for ballistic bluff body at $U_{lip} = 50$ m/s, expressed as rms flame edge displacement averaged over both flame branches, and rms centerline transverse velocity. Measurement was taken at a) the axial position of peak response and b) $x/D = 3.5$

5.2.2 *Correlation Analysis*

The correlation coefficient between the two flame branches, $r_{U,L}$ (defined below), provides important information on the scale and/or correlation between the underlying flow structures perturbing them.

$$r_{U,L}(x) = \frac{\left\langle \zeta_U(x,t)\zeta_L(x,t)\right\rangle}{\sqrt{\left\langle \left[\zeta_U(x,t)\right]^2\right\rangle\left\langle \left[\zeta_L(x,t)\right]^2\right\rangle}} \tag{5.4}$$

Note that negative and positive correlation coefficients imply asymmetric and symmetric flame wrinkling, respectively (take note of the sign convention for ζ_U and ζ_L in Figure 5-9c). Furthermore, a nearly zero correlation coefficient implies that the flame branches are disturbed by uncorrelated structures with a scale much smaller than their transverse separation distance. The dependence of the correlation coefficient upon ρ_u/ρ_b is plotted in Figure 5-14, showing that the correlation coefficients are near zero or positive, for $\rho_u/\rho_b >\sim 2.5$. The correlation coefficient monotonically decreases towards values of $r_{U,L} \sim -0.6$, indicative of growing correlation and asymmetric motion with decreasing flame density ratio.

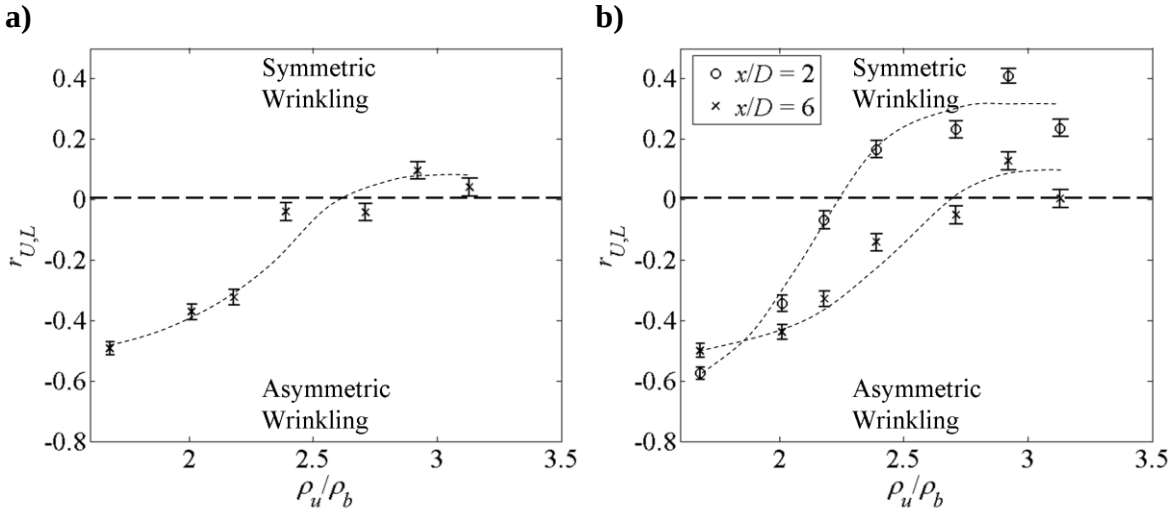

Figure 5-14. Correlation coefficient between top and bottom flame edge position for ballistic bluff body at $U_{lip} = 50$ m/s. Measurement was taken at a) the axial position of peak response and b) $x/D = 2.0$ and 6.0

5.3 Closing Remarks

To summarize these dynamical data, Figure 5-13 shows that there is a gradual increase in spectral energy at the asymmetric vortex shedding frequency as density ratio is decreased. Figure 5-14 shows a gradual increase in asymmetry and correlation between the two flame branches for decreasing ρ_u/ρ_b, suggesting the appearance of large structures in the wake. The very narrowband spectral nature of the flow in Figure 5-10 suggests that the flow evolves to a limit-cycling, globally unstable flow at low density ratios. Simultaneously, the limit cycle amplitude of the global mode grows gradually and monotonically with decreases in density ratio for $\rho_u/\rho_b < 2.4$. This latter result is significant, as it shows that the flow does not abruptly bifurcate to the globally unstable state below some threshold density ratio. A first look at this result suggests that the amplitude of the limit cycle monotonically increases with decreasing density ratio. While this is certainly true in a time averaged sense, Chapter 7, *Intermittency of Limit Cycle Events* will show that a better description of the phenomenon comes from time-localized analysis. The results there will show that this behavior arises due to an intermittent transition of the flow between two states. The next chapter will compare the observations from this chapter to results derived from local, parallel stability analyses using the time averaged, unforced PIV measurements as the base flow.

CHAPTER 6. LOCAL HYDRODYNAMIC STABILITY ANALYSIS

The previous chapter discussed unsteady flame and flow characteristics as density ratio was varied. It was shown that low flame density ratios promoted a sinuous, limit cycling behavior in the wake, while at high density ratios this motion was suppressed. In this chapter, local, spatio-temporal, hydrodynamic stability analysis is used to describe these observations, and to find the key parameters governing the hydrodynamic stability of premixed, reacting wakes. Stability analysis is useful for such parameter studies due to its lack of computational expense when compared to computational fluid dynamics. Two general types of stability analysis will be reviewed: analysis of model base flow profiles with a single equation dispersion relation, and a spectral analysis of the full base flow profiles. These will be referred to as the model stability analysis and the detailed stability analysis, respectively. This chapter will show that both have their merits. Stability analysis of the full base flow profiles can give accurate predictions for quantities such as the expected global mode frequency, the direct and adjoint global mode shapes, and the structural sensitivity of the wake. The model stability analysis offers extensive computational savings and rich, easy to access physical insight on the stability parameters and base flow features.

As mentioned in Chapter 2, *Background and Motivation*, the test conditions for the unforced experiments (shown previously in Chapter 5, *Experimental Results: Unforced Flame and Flow Dynamics*) were motivated by the stability analysis of Yu and Monkewitz [18]. Figure 6-1 overlays those test conditions on a contour map showing the absolute growth rates predicted by their parallel, local stability analysis. The figure

demonstrates the resultant range of predicted absolute growth rates tested near the stability limit (where $\omega_{0,i} D / 2U_{av} = 0$), which was the goal of the test matrix design.

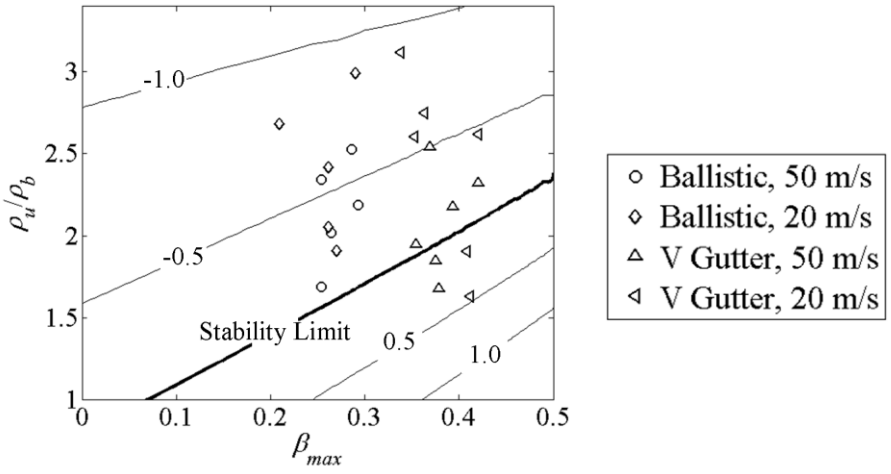

Figure 6-1. Contour map of predicted absolute growth rate, $\frac{\omega_{0,i} D}{2U_{av}}$, as a function of backflow ratio and density ratio [18]. Contour values are labeled on plot. Test conditions from the unforced experiments are overlaid.

6.1 Parallel Flow Assumption

The stability analyses discussed in this chapter implement the parallel flow assumption. To quantify the degree to which the velocity field deviates from parallel flow, xx plots contours of the absolute value of the mean velocity vector angles. In this convention, zero degrees indicates purely axial velocity, and 90 degrees indicates purely transverse velocity. The parallel flow assumption implies a purely axial mean velocity field. Note that this assumption holds well throughout the flow, except at the ends of the recirculation bubble. In spite of the deviation from parallel flow, this chapter will show that parallel stability analysis makes useful predictions for this flow.

a)

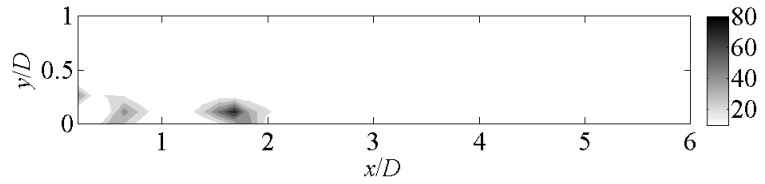

b)

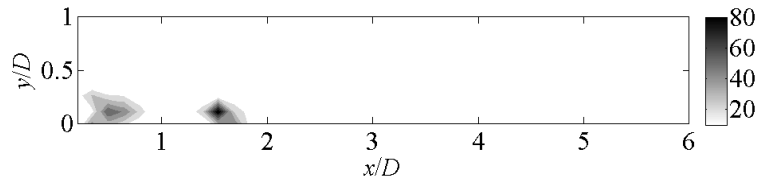

c)

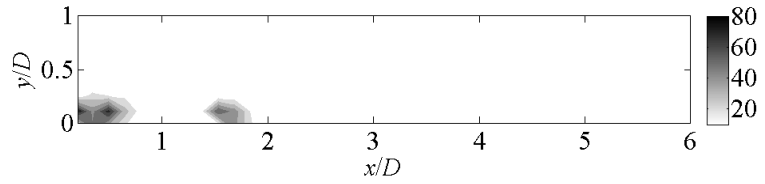

d)

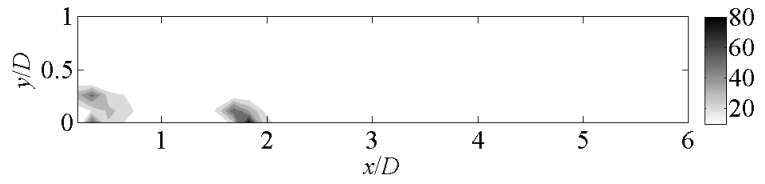

e)

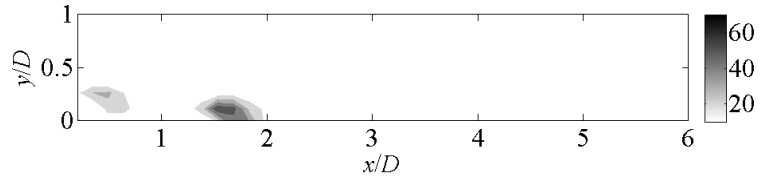

f)

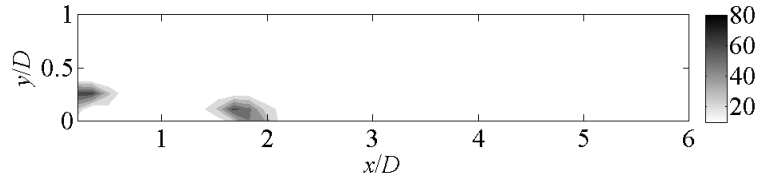

Figure 6-2. Contours of velocity vector angles, in degrees, quantifying degree to which flow is parallel for $U_{lip} = 30$ m/s and a) $\rho_u/\rho_b = 1.7$, b) $\rho_u/\rho_b = 1.9$, c) $\rho_u/\rho_b = 2.0$, d) $\rho_u/\rho_b = 2.2$, e) $\rho_u/\rho_b = 2.4$, and f) $\rho_u/\rho_b = 2.5$

6.2 Model Local Stability Analysis Procedure

The model stability analysis discussed in this chapter stems from the analysis of Yu and Monkewitz [18], whose result is shown above in Figure 6-1. This analysis is a local, parallel stability analysis that assumes top hat velocity and density profiles (see Figure 6-3), and reduces to a single-equation dispersion relation which can be solved analytically. From here on, all such analyses will be referred to as model stability analyses. The analysis leads to a dispersion relation which is a function of the backflow ratio, the density ratio, and the hydrodynamic symmetry (i.e., sinuous vs varicose mode shape). In order to plot the experimental test conditions on the stability map as shown in Figure 6-1, knowledge of the backflow ratio and density ratio was required for each condition. The centerline and freestream axial velocity fields obtained from PIV data were used to calculate the velocities needed to quantify the backflow ratio, $\beta(x)$. The density ratio was obtained as discussed in Chapter 4, *Instrumentation and Diagnostic Techniques*. Although this stability analysis treats both sinuous and varicose modes, results are only shown for the sinuous mode since it is always the most absolutely unstable mode in this flow.

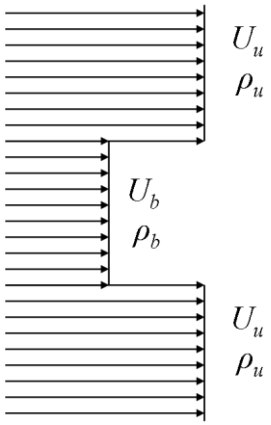

Figure 6-3. Velocity and density profiles used in the model, local, parallel stability analysis.

It will be useful at this point to define several characteristic velocities to relate the experimentally measured flow profiles to the model profile shown in Figure 6-3. The backflow ratio, defined in Chapter 2, *Background and Motivation*, is the ratio of reverse flow velocity in the wake to outer flow velocity, $\beta(x) = -U_b(x)/U_u(x)$. The average velocity is defined as the average velocity between the inner and outer streams, $U_{av} = (U_u + U_b)/2$, and is a function of axial position. Finally, a velocity difference is defined as $\Delta U = U_u - U_b$.

The stability prediction procedure is as follows. The measured local backflow ratio (corresponding to a flow profile at a given axial position) and density ratio were inserted into the inviscid dispersion relation from Yu and Monkewitz [18] for a large grid of complex wavenumbers, k, in order to map complex frequency, $\omega = \omega_r + i\omega_i$, onto the complex k-plane. Saddle points were located on the resulting Riemann surface and verified to be valid k^+/k^- pinch points [21] (which identifies them as "valid saddle points"). The growth rate at the most elevated valid saddle point corresponded to a

predicted, local, absolute spatio-temporal growth rate, $\omega_{0,i}$. This process was then repeated at each axial position, for each test condition.

6.3 Detailed local stability analysis procedures

In addition to the above described model analysis, a detailed analysis was performed which took the measured mean velocity and density profiles as inputs. This analysis uses a software tool developed by Matthew Juniper [19, 63]. The absolute growth rate, $\omega_{0,i}$, and absolute wavenumber, k_0, were calculated at each axial station by performing a spatio-temporal stability analysis on the time-averaged velocity and density profiles. The linearized, low Mach number Navier-Stokes equations were reduced to three ODEs in three primitive variables (u, v, p), which were solved using Chebyshev spectral methods on Gauss-Lobatto spaced gridpoints. The procedure is described in previous work performed at Cambridge University [19, 64-65]. As in the model analysis, saddle points were found in the complex k-plane and verified to be valid k^+/k^- pinch points [21]. The valid saddle point with the highest absolute growth rate was labeled the dominant saddle point. If the absolute growth rate of this saddle point is greater than zero then this slice of the flow is absolutely unstable.

The choice to use an incompressible, three equation analysis (for both the model and detailed studies) is well justified by comparison to a compressible, five equation stability analysis. A fully compressible (without low Mach number assumption) five equation analysis (in u, v, w, p, T) was performed for some cases and was verified to very nearly match the incompressible analysis. The solution scheme for the compressible analysis was the same as the general procedure above, with the addition of the spanwise (with

respect to the bluff body) momentum equation and the energy equation. A specific heat ratio of $\gamma = 1.3$ and gas constant of $R = 298\ \mathrm{J/(KgK)}$ were specified, along with a base flow temperature profile (calculated from the base flow density, the mean atmospheric pressure, and the gas constant). A comparison between the five equation compressible and three equation incompressible predictions is shown in Figure 6-4, showing unperceivable differences.

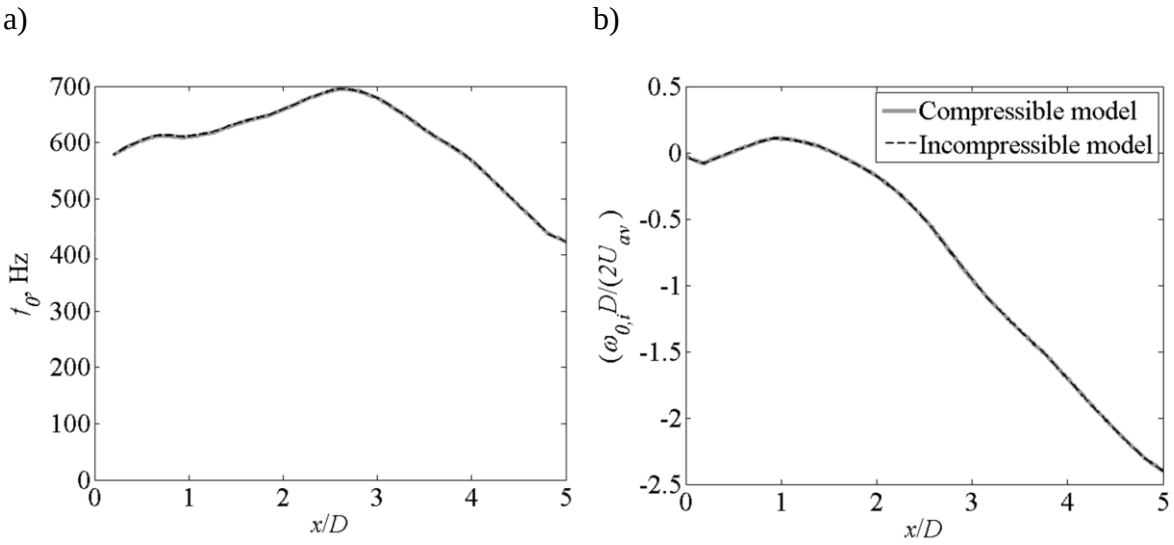

Figure 6-4. Comparison of compressible and incompressible detailed, local, spatio-temporal stability analyses for $\rho_u/\rho_b = 2.4$, $U_{lip} = 50$ m/s, showing a) absolute frequency and b) absolute growth rate

6.4 Comparison of measured flow dynamics to stability predictions

The global mode frequency measured with PIV is compared to the local absolute frequency, $f_0(x/D) = \dfrac{\omega_{0,r}(x/D)}{2\pi}$, for both the model and detailed stability analyses in Figure 6-5a. The horizontal line indicates the measured global mode frequency. The curves that vary with axial position indicate the absolute frequency. Figure 6-5b shows

the corresponding absolute growth rates to help identify the most amplified region and to further compare the two analyses. Figure 6-5 draws attention to three important observations. The first observation is that in the vicinity of the absolute instability pocket, the detailed stability analysis predicts absolute frequencies that are very close to the measured global mode frequency. The second observation is that the model stability analysis predicts frequencies that do not have such a good quantitative comparison. This is due to the infinitely thin shear layer used in the model, which introduces quantitative error. The third observation is that the model stability analysis predicts a much lower absolute growth rate, the reason for which is discussed later. Despite its quantitative shortcomings, this section will show that the model stability analysis is successful at capturing qualitative stability trends, and thus the roles of the stability parameters. The end of this chapter will show that the model stability analysis provides a simple, tractable, physical interpretation of the key stability parameters and base flow features.

a) b)

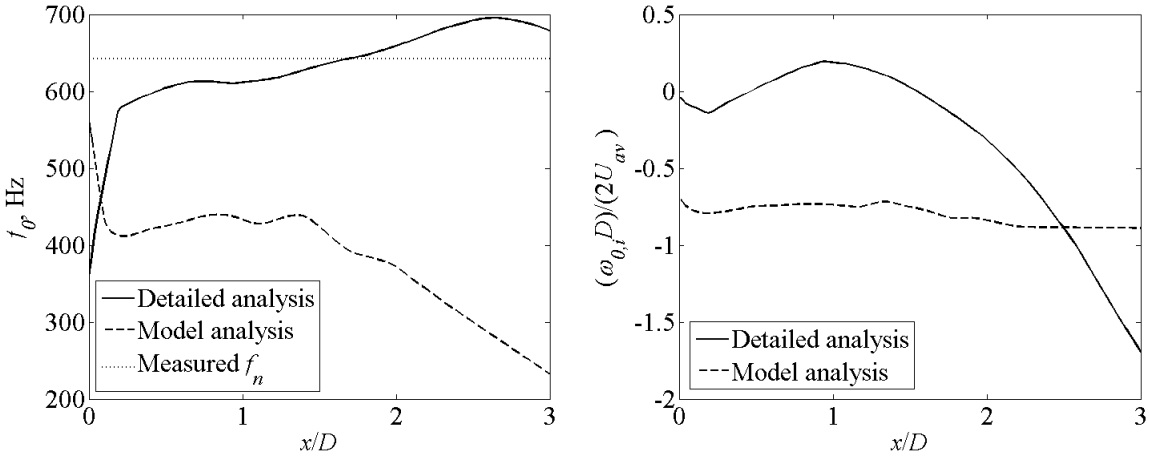

Figure 6-5. Comparison of the detailed and model stability analyses, zoomed in on the most amplified region, showing a) frequency and b) growth rate. The measured global mode frequency, f_n, is overlaid as a horizontal line in part (a). Conditions were ballistic bluff body, $\rho_u/\rho_b = 2.4$, $U_{lip} = 50$ m/s.

Isocontours of the nondimensional absolute growth rate, $\omega_{0,i}D/(2U_{av})$, are presented in Figure 6-6. This figure plots calculated absolute growth rate contours as functions of axial position and density ratio for both bluff bodies at lip velocities of 50 m/s and 20 m/s. Each of these plots was compiled from the measured velocity fields (and hence $\beta(x)$) of tests at several density ratios and a given bluff body and lip velocity. The plots show that regions of largest local absolute instability, $\omega_{0,i}D/(2U_{av}) > 0$, occur at low density ratios and at axial positions of roughly $x/D \sim 3/2$ near where the reverse flow velocity is highest. The spatial extent of these predicted absolute instability pockets grows with decreasing density ratio. Note that the absolute instability region does not start immediately aft of the bluff body, because of the low backflow velocities immediately downstream of the bluff body.

a) Detailed result, ballistic bluff body at 50 m/s

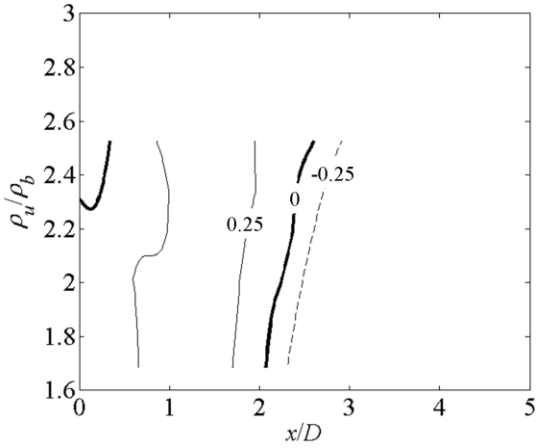

b) Model result, ballistic bluff body at 50 m/s

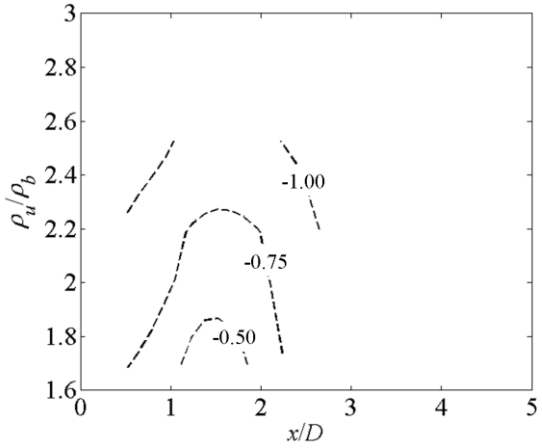

c) Detailed result, ballistic bluff body at 20 m/s

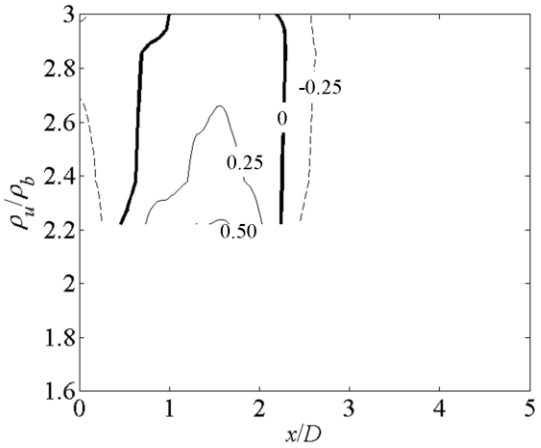

d) Model result, ballistic bluff body at 20 m/s

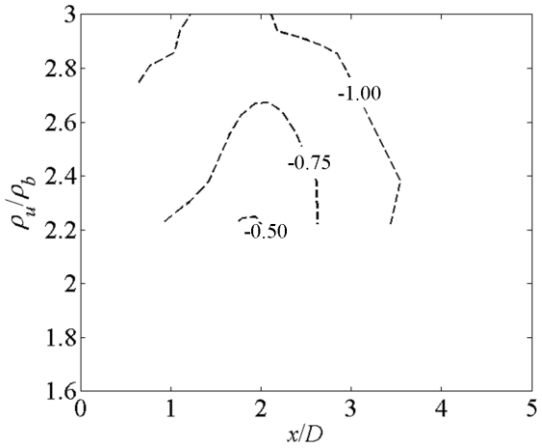

e) Detailed result, v-gutter at 50 m/s

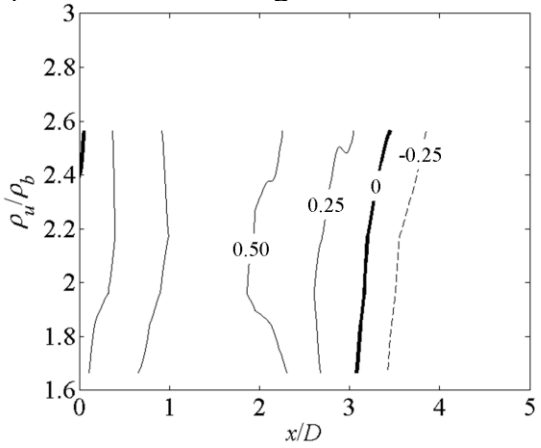

f) Model result, v-gutter at 50 m/s

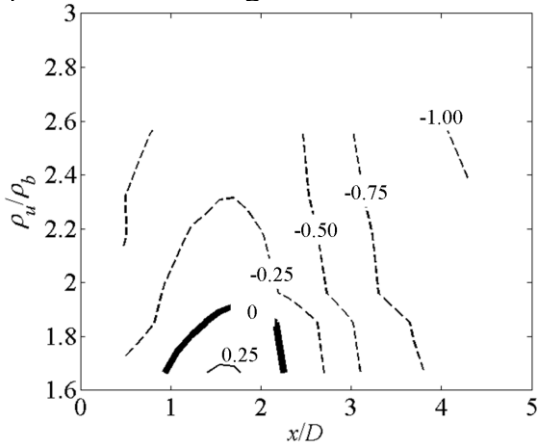

Figure 6-6. $\omega_{0,i}D/(2U_{av})$ contour maps vs axial position and density ratio, for a&b) ballistic bluff body at U_{lip} = 50 m/s, c&d) ballistic bluff body at U_{lip} = 20 m/s, e&f) v-gutter at U_{lip} = 50 m/s, g&h) v-gutter at U_{lip} = 20 m/s. First column shows detailed analysis result, second column shows model analysis result

g) Detailed result, v-gutter at 20 m/s **h) Model result, v-gutter at 20 m/s**

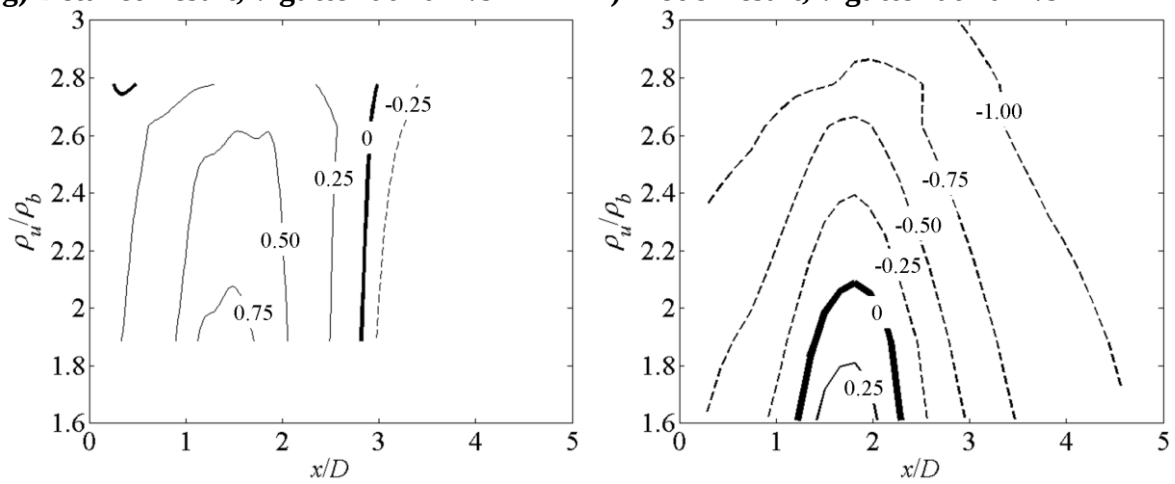

Figure 6-6 continued

Note that the predictions obtained from the model profile shown in Figure 6-6 and the calculations obtained from the actual measured profiles are qualitatively similar. However, a key quantitative difference between the two is the larger growth rates, and the prediction of absolute instability for a much broader range of density ratios, obtained from the computed results that used the measured profiles. For example, consider Figure 6-6c and Figure 6-6d, showing local absolute stability results for the ballistic bluff body at 20 m/s. At a density ratio of $\rho_u/\rho_b = 2.6$, the model analysis solution predicts the flow to be convectively unstable at all spatial positions using the simple profile, while the flow is predicted to have a pocket of absolute instability with the detailed computation.

Figure 6-7 plots the measured axial dependence of the centerline velocity fluctuations at $St_D = 0.24$. The axial coordinate is referenced to the location of maximum absolute growth rate, x_{AI} (obtained from Figure 6-6), which for the simple top hat profile corresponds to the location of maximum backflow ratio. Both plots show that, for a

range of conditions, growth of the narrowband $St_D \sim 0.24$ fluctuations begins at approximately the same location, within roughly a half of the bluff body diameter of one another, and that this location is centered near the peak in absolute growth rate at $x - x_{AI} \sim 0$ for the detailed stability analysis. The peak absolute growth rate in the model analysis occurs slightly farther upstream, such that narrowband velocity fluctuations begin to grow at $\left(x - x_{AI}\right)/D \sim -0.5$. Once the oscillations are initiated in the pocket of absolute instability, the structure associated with this mode continues to grow spatially as it passes through the downstream convectively unstable region.

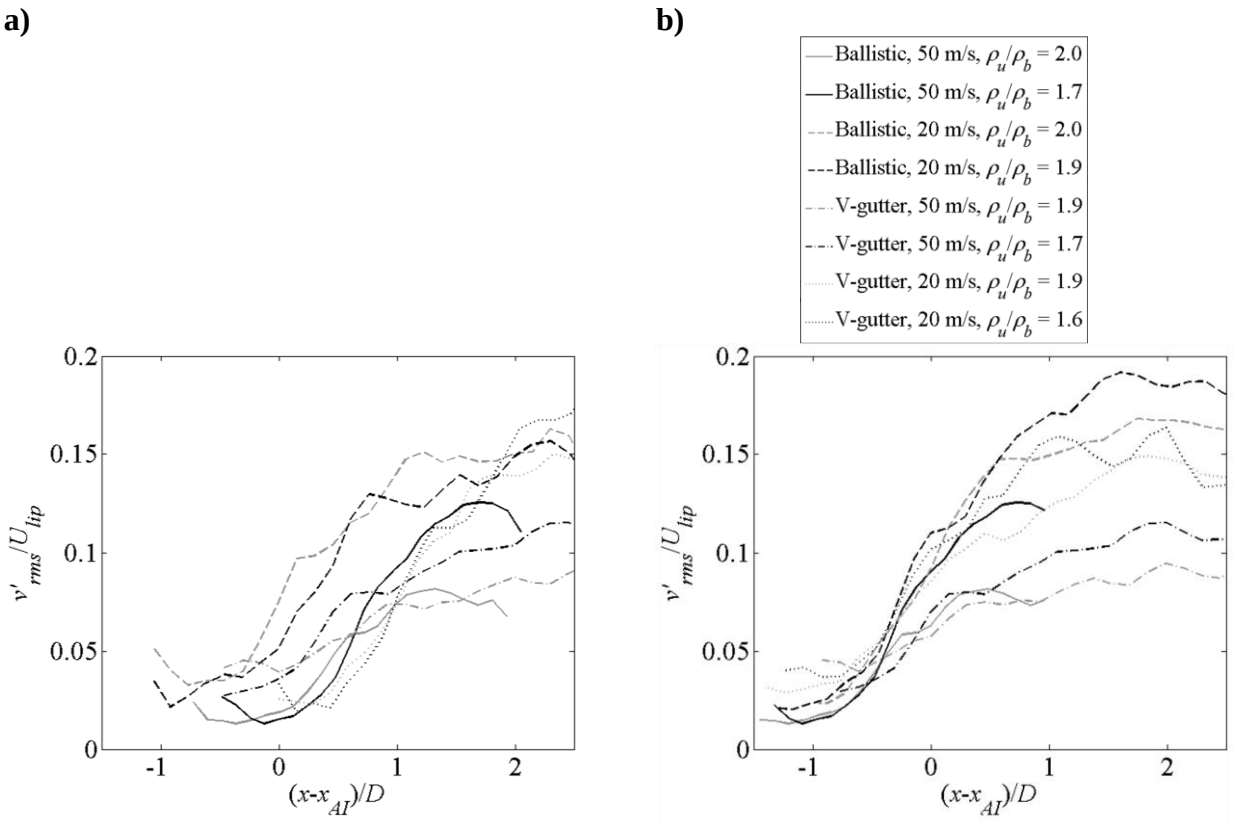

Figure 6-7. v'_{rms} at St_D~0.24 vs distance downstream from the predicted location of maximum absolute growth rate for several test conditions showing a) detailed analysis result, b) model analysis result

The detailed stability analysis can also provide some useful insight into the location of the wavemaker, and the region of greatest sensitivity to passive forcing. These results were obtained using numerical tools written by Matthew Juniper [3-4, 7]. In short, these results are obtained by considering all of the local analyses (for each axial position) and extrapolating the complex absolute frequency into the complex axial position plane. A valid saddle point of $\omega_0(x_r, x_i)$ is located and determined to correspond to the global mode frequency, ω_g, and growth rate, and identifies the wavemaker location. All local analyses downstream of this location are forced at ω_g assuming downstream wave propagation (using the k^+ branch), and all local analyses upstream are forced at ω_g assuming upstream wave propagation (using the k^- branch). This constitutes a numerical "stitching" together of the local analyses to form the global mode, and the results of this process are the direct and adjoint global modes.

The global mode shape was obtained from the PIV measurement by conditionally averaging the transverse velocity. Averages were conditioned as follows. First, a sine fit was performed on a local portion of the velocity signal with duration of twice the global mode period. Next, this sine fitting procedure was repeated while shifting through the signal. Finally, the velocity average was conditioned on the phase of these sine fits. The result is shown in Figure 6-8a, and compared to the direct global mode shape from stability analysis in Figure 6-8b. Note the excellent agreement of the axial wavelength. Figure 6-8c shows the magnitude of the adjoint global mode for axial velocity fluctuations (chosen because the forced experiments use axial forcing). Figure 6-9 plots the global mode frequency prediction vs. the measured global mode frequency and shows close comparison. The adjoint global mode identifies the spatial locations that are most

sensitive (most receptive) to passive forcing, which for this flow is the shear layers near the bluff body trailing edge. Figure 6-8d shows the magnitude of the maximum energy of the overlap between the direct and adjoint global modes. Physically, this captures a closed loop forcing between the direct and adjoint global modes (ie, where the fluctuations are greatest vs where the flow is most sensitive to them), and it identifies the region with the greatest structural sensitivity. In other words, it identifies the location of the wavemaker, which in this case is strongest at about $x = 1.5D$ and essentially covers the recirculation zone. This is the region that would have to be "disrupted" in order for such a disruption to have the greatest impact on the global mode. A comprehensive set of these computations is presented in *Appendix B.* The appendix utilizes data taken over the wide range of velocities and densities from the unforced cases of the acoustically forced test matrix.

a)

b)

c)

d)

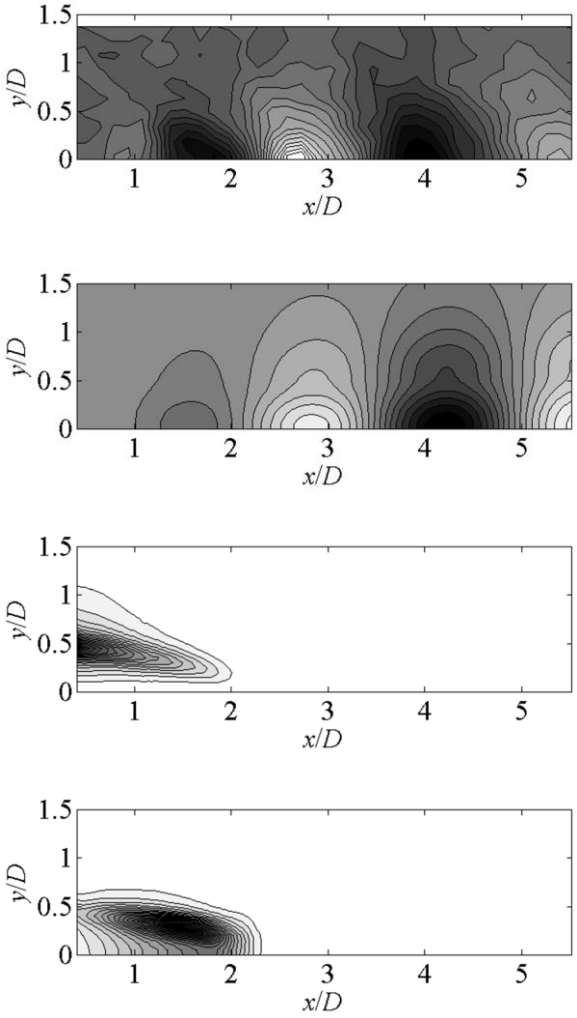

Figure 6-8. Comparison of a) Measured global mode shape from conditionally averaged transverse velocity, b) direct global mode shape (transverse velocity) from detailed stability analysis, c) magnitude of adjoint global mode (axial velocity) from detailed stability analysis, d) magnitude of maximum energy of overlap of direct and adjoint global modes

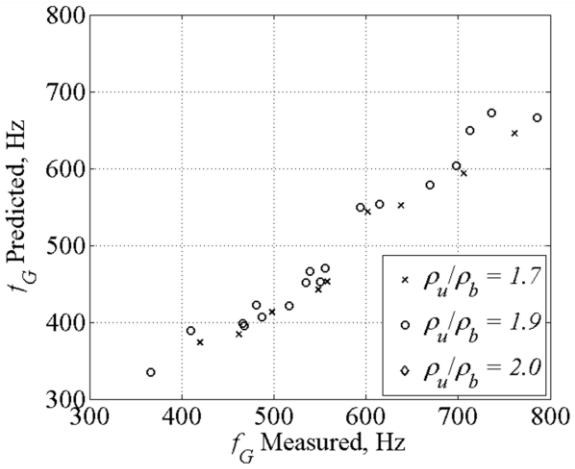

Figure 6-9. Comparison of predicted and global mode frequency for three density ratios, over the range of lip velocities tested

It should be emphasized that the parallel stability analysis assumes a "quiescent" base state; i.e., one without coherent or turbulent fluctuations. When the system is globally unstable, large vortices are alternately shed from the bluff body. Measurements are obtained under finite amplitude, limit cycle conditions where these cause the time averaged profiles to differ from the true base flow. Therefore, while quantitative variations between this type of stability analysis and these data should be expected, the general agreement between model and data shown above illustrate that the key physical processes are nonetheless captured.

6.5 Flame-Shear Layer Offset

The differences between the model and detailed stability analyses are largely due to two important simplifications of the geometry used for the model stability analysis: (1) co-located base flow density and velocity discontinuities and (2) an infinite domain. For high Reynolds number wake flows, confinement destabilizes the sinuous mode in wake flows such as these, as discussed by Rees and Juniper [65]. Further effects which

influence the stability prediction and are not accounted for by the simplified analysis, such as no slip boundary conditions, finite Reynolds number, and global vs. local results, are detailed by Juniper et al. [19]. In addition, the absolute instability growth rate is a very sensitive function of the relative locations of the gradients in density and velocity. In order to illustrate this point, the simple model flow profile shown in Figure 6-3 was generalized to include confinement and non co-located density and velocity jumps (see Figure 6-11). This analysis is summarized below, which provides the generalized dispersion relation for the sinuous mode. Figure 6-10 plots the dependence of the density ratio of the absolute/convective instability transition upon the density-velocity jump offset, $\delta_\rho - \delta_u$. These results are shown at a fixed backflow of $\beta = 0.25$ and are shown both with and without confinement. The velocity jump is located at a distance (from the centerline) corresponding to the bluff body half width, and the confinement was chosen to match the experimental facility. The plot shows the strong destabilizing effects of non-colocated density and shear layers, as well as confinement. For example, begin with co-located velocity and density jumps for the unconfined case. If the velocity jump location is held fixed, and the density jump is shifted away from (outside of) the flow centerline by 10% of its original position, then the density ratio for the AI/CI transition increases by 50%, from about 1.6 to 2.4. Adding confinement on top of this further shifts the density ratio for the AI/CI transition to about 2.7.

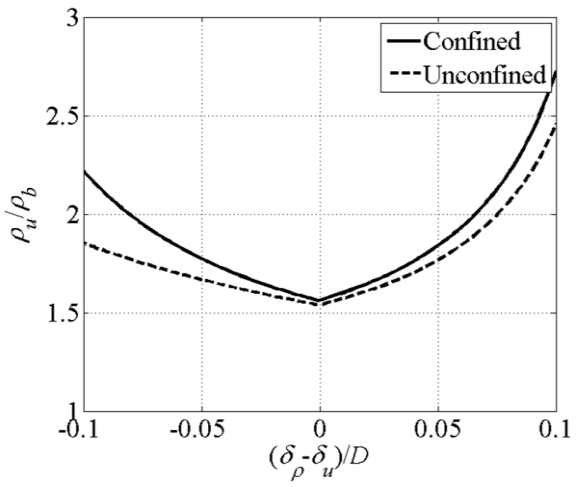

Figure 6-10. Stability limit as a function of the density-velocity jump offset, for a constant backflow ratio of $\beta = 0.25$, a velocity jump located at the bluff body half width ($\delta_u/D = 0.5$), and for the confined case a geometry of $H/D = 2$.

The basic trends in Figure 6-10 (i.e., that a shift in the relative positions of velocity and density gradients away from one another, in either direction, is destabilizing), can be understood from the two limiting cases. If the density layers are moved far outboard of the shear layers, the wake and its shear layers essentially sit in a uniform density fluid, and the stability boundary tends toward that of the iso-density case. The same result may be expected if the density layers are moved inboard to the flow centerline; in this case, the density ratio becomes an increasingly irrelevant quantity since the inner density region becomes pinched into a progressively thinner slab along the centerline, and again the wake effectively sits in a uniform density fluid. Indeed, it can be shown that the dispersion relation shown next limits to the uniform density case in these two extremes.

The dispersion relation for the confined, sinuous wake mode with non-colocated density and shear layers and rigid walls at $y = \pm H$, when the density layer is closer to the flow centerline than the shear layer, is

$$\frac{\rho_b}{\rho_u}\left\{\frac{e^{k\left(\delta_\rho-\delta_u\right)}\left[1+\alpha\frac{\left(U_u-c\right)^2}{\left(U_b-c\right)^2}\right]+e^{k\left(\delta_u-\delta_\rho\right)}\left[1-\alpha\frac{\left(U_u-c\right)^2}{\left(U_b-c\right)^2}\right]}{e^{k\left(\delta_\rho-\delta_u\right)}\left[1+\alpha\frac{\left(U_u-c\right)^2}{\left(U_b-c\right)^2}\right]-e^{k\left(\delta_u-\delta_\rho\right)}\left[1-\alpha\frac{\left(U_u-c\right)^2}{\left(U_b-c\right)^2}\right]}\right\}=\frac{e^{k\delta_\rho}+e^{-k\delta_\rho}}{e^{k\delta_\rho}-e^{-k\delta_\rho}} \tag{6.1}$$

where α is a confinement parameter defined by

$$\alpha=\frac{e^{k\delta_u}+e^{2kH}e^{-k\delta_u}}{e^{k\delta_u}-e^{2kH}e^{-k\delta_u}} \tag{6.2}$$

The dispersion relation for when the shear layer is closer to the flow centerline than the density layer is

$$\frac{\left(U_u-c\right)^2}{\left(U_b-c\right)^2}\left[\frac{\left(\frac{\rho_b}{\rho_u}+\alpha\right)e^{k\left(\delta_u-\delta_\rho\right)}-\left(\frac{\rho_b}{\rho_u}-\alpha\right)e^{k\left(\delta_\rho-\delta_u\right)}}{\left(\frac{\rho_b}{\rho_u}+\alpha\right)e^{k\left(\delta_u-\delta_\rho\right)}+\left(\frac{\rho_b}{\rho_u}-\alpha\right)e^{k\left(\delta_\rho-\delta_u\right)}}\right]=\frac{e^{k\delta_u}-e^{-k\delta_u}}{e^{k\delta_u}+e^{-k\delta_u}} \tag{6.3}$$

where α is defined by

$$\alpha=\frac{e^{k\delta_\rho}+e^{2kH}e^{-k\delta_\rho}}{e^{k\delta_\rho}-e^{2kH}e^{-k\delta_\rho}} \tag{6.4}$$

The geometry used in these equations is provided in Figure 6-11. This geometry was assumed symmetric about the bluff body centerline, which is shown at the bottom of the figure. In the limiting case of $H\to\infty$ ($\alpha\to -1$) and $\delta_u=\delta_\rho$, these dispersion relations simplify to the unconfined result of Yu and Monkewitz [18] and Huerre and Monkewitz [21].

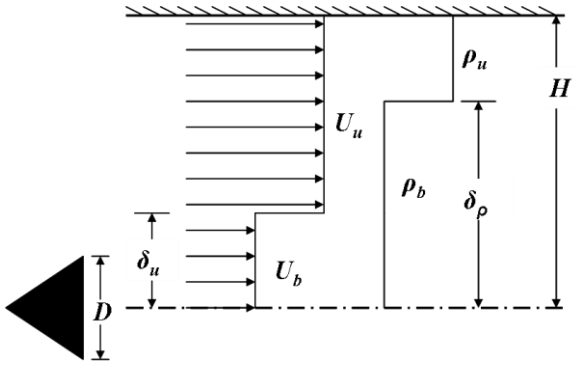

Figure 6-11. Geometry governing the dispersion relations in Eq. (6.1) and Eq. (6.3), for the sinuous wake mode with non-colocated density and shear layers

Having shown that the basic trends shown in Figure 6-10 can be understood from limiting cases, this work next investigates the significant sensitivity of the stability boundary to even very small changes in relative locations of the gradients. This point is both predicted by the analysis and borne out by the comparisons between the measurements and the two different stability calculations. The important effect of non-colocation of density and shear layers was observed in the stability analysis of low density jets with co-flow by Raynal et al. [66]. The effect of non-colocated density and shear layers on flow stability has also been observed previously in DNS of a variable density jet flow [67], showing that a small degree of misalignment materially changes the flow stability characteristics. It should be noted that because that study investigated low density ratio jets, this misalignment was a stabilizing effect, in contrast to the destabilizing effect it has in these low density ratio wakes. Similar observations on the hydrodynamic stability sensitivity to this misalignment have been observed experimentally in the context of shear layers [68].

Figure 6-12a plots the solution to the non-colocated dispersion relation over a range of density ratios and levels of non-colocation for the model stability analysis. Figure 6-12b

mimics this study with the detailed stability analysis. This comparison captures the quantitative differences between the two stability analyses that cannot be attributed to non-colocation effects. Note that both analyses show a significant sensitivity to the degree of non-colocation, although for large values of $\left(\delta_\rho - \delta_u\right)/\delta_u$ (when the density layer is approaching the confining wall) there are slight differences. This may be due to the fact that the model analysis is inviscid, while the detailed analysis captures a boundary layer in the fluctuating velocity at the wall. Such an effect will only be significant when the near wall fluctuating velocity is significant, like when base flow features are located near the wall.

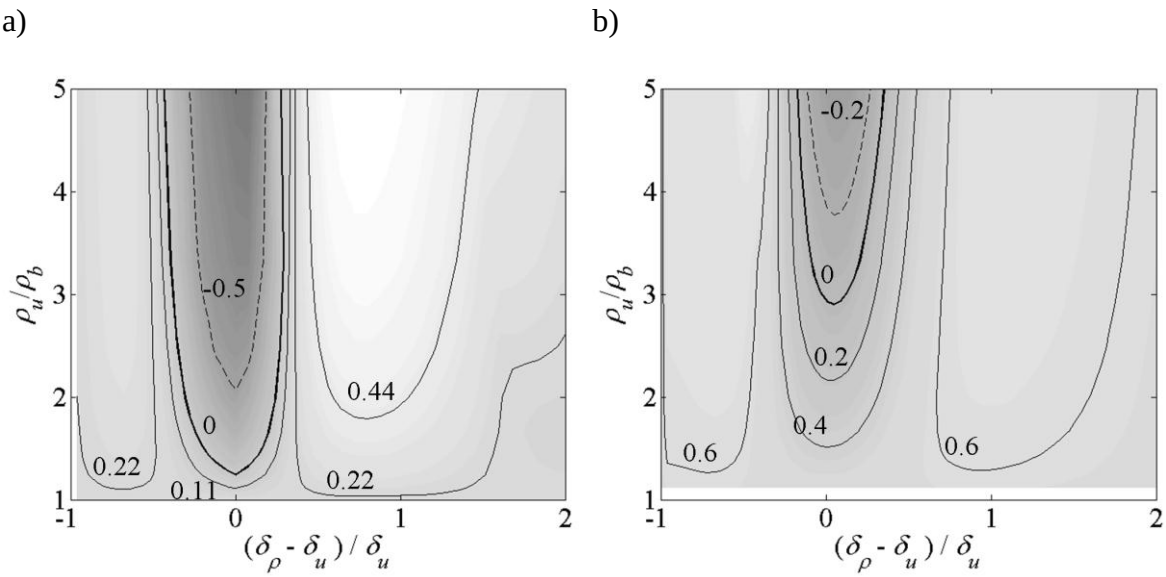

Figure 6-12. Contours of $\omega_{0,i} D/\left(2U_{av}\right)$ for $\beta = 0.15$ from the a) model stability analysis and b) detailed stability analysis

For both 2-D jets and wakes, the global stability of the system is crucially affected by the nature of the interactions between the two shear layers. In particular, the two shear

layers which would be nominally convectively unstable in isolation, interact with each other to cause global instability for the wake problem. The spatial variations in density can influence these interactions through two processes which are shown in the vorticity equation below: baroclinic torque and gas expansion.

$$\frac{D\vec{\Omega}}{Dt} = -\underbrace{\left(\nabla\cdot\vec{u}\right)\vec{\Omega}}_{\text{gas expansion}} + \underbrace{\left(\vec{\Omega}\cdot\nabla\right)\vec{u}}_{\text{vortex stretching \& bending}} + \underbrace{\frac{\nabla\rho\times\nabla p}{\rho^2}}_{\text{baroclinic torque}} + \underbrace{\nabla\times\left(\frac{\nabla\cdot\underline{\underline{\tau}}}{\rho}\right)}_{\text{viscous diffusion}} \tag{6.5}$$

Gas expansion reduces vorticity magnitudes, and consequently weakens the degree of interactions between the two shear layers. Therefore, it has a stabilizing effect on the system. In addition, vorticity is created through baroclinic torque, which also modifies the strength of the vorticity in the two shear layers. Moreover, the baroclinic mechanism is only active in regions with simultaneously misaligned pressure and density gradients; for the linearized analysis presented here, this is due to the mean density gradient in the transverse direction interacting with the fluctuating pressure gradient in the axial direction.

In reacting flows, this degree of misalignment between the time averaged density and velocity gradients will be a strong function of the turbulent burning velocity, which controls the time averaged speed at which the flame propagates into the unburned mixture and, thus, moves out of the shear layer. For example, increasing laminar burning velocity or turbulence intensity will act to increase turbulent burning velocity and, hence, alter the relative locations of velocity and density gradients. The importance of this effect as a result of varying preheat temperature has been observed by Erickson and

Soteriou [69], who suggested that the resulting variations in wake structure that were observed were due in part to the flame moving away from the shear layer. This observation also suggests an explanation for why the transition in wake structure has been observed at different density ratio ranges in different experimental facilities. For example, the wake stability boundary has been observed within the density ratio range $3.2 \le \rho_u/\rho_b \le 5.6$ [70], $1.25 \le \rho_u/\rho_b \le 2.0$ [71], and $1.7 \le \rho_u/\rho_b \le 2.4$ (current study). Each of these facilities has different operating conditions, fuels and Reynolds numbers, and as a result likely has significantly different offsets between the density and shear layers. Even for a single backflow ratio, Figure 6-10 shows the wide range of values that the stability limit could have in terms of density ratio, if the mean flame position moves only a tenth of the bluff body diameter. In addition, with different bluff body geometries, these facilities may have different maximum backflow ratios.

6.6 Stability Analysis and the Vorticity Equation: The Vorticity Budget

Up to this point, this chapter has shown that the model stability analysis of this flow does not necessarily quantify the flow stability characteristics successfully. It is, however, useful for verifying the key stability parameters and determining their influences on the flow stability characteristics. Therefore, the model stability analysis holds clues on *why* the parameters have such influences. This motivates a study to read these clues, namely to identify the relationships between key physics, the stability parameters, and the instability growth rate. The rest of this chapter is dedicated to such an effort, the result of which is named the "vorticity budget."

6.6.1 *Relationship Between the Vorticity Equation and the Rayleigh Equation*

Previously, the vorticity equation was introduced along with a brief discussion of some of the terms, and their relevance to the wake stability. This section derives the Rayleigh equation and the governing equation for the model stability analysis from the vorticity equation. Each of the terms of the vorticity equation is "tagged" so that it may be tracked through the derivation. This helps identify the physical processes that are captured in the stability analysis. The process begins with the vorticity equation, Eq. (6.5), which is repeated below with a coefficient (letters A through E) added in front of each term. These added coefficients are the tags that will be used to track the terms throughout the derivation.

$$A\frac{D\vec{\Omega}}{Dt} = -\underbrace{B\left(\nabla\cdot\vec{u}\right)\vec{\Omega}}_{\text{gas expansion}} + \underbrace{C\left(\vec{\Omega}\cdot\nabla\right)\vec{u}}_{\text{vortex stretching \& bending}} + \underbrace{D\frac{\nabla\rho\times\nabla p}{\rho^2}}_{\text{baroclinic torque}} + \underbrace{E\left\{\nabla\times\left(\frac{\nabla\cdot\overline{\overline{\tau}}}{\rho}\right)\right\}}_{\text{viscous diffusion}} \tag{6.6}$$

For a two-dimensional inviscid flow in the *x-y* plane, there is no vortex stretching or bending, and Eq. (6.6) reduces to:

$$A\frac{\partial\Omega}{\partial t} + Au\frac{\partial\Omega}{\partial x} + Av\frac{\partial\Omega}{\partial y} = -B\Omega\left(\nabla\cdot\vec{u}\right) + D\frac{\nabla\rho\times\nabla p}{\rho^2} \tag{6.7}$$

where Ω represents the out of page vorticity component (in the z direction). Note that the absence of vortex stretching and bending highlights a weakness of the two-dimensionality assumption, since streamwise vorticity due to secondary instabilities is known to occur in bluff body wakes [72]. Decomposing the vorticity, velocity, density, and pressure into mean and fluctuating components, linearizing and assuming parallel base flow leads to:

$$A\frac{\partial\Omega'}{\partial t}+Au_0\frac{\partial\Omega'}{\partial x}+Av'\frac{d\Omega_0}{dy}=-B\Omega_0\left(\nabla\cdot\vec{u}'\right)+D\frac{\nabla\rho'\times\nabla p_0}{\rho_0^2}+D\frac{\nabla\rho_0\times\nabla p'}{\rho_0^2} \quad (6.8)$$

Zero mean pressure gradient is assumed for this analysis. Under the assumptions of the Rayleigh equation (namely linear in flow perturbations, inviscid flow, and parallel base flow), the Reynolds Averaged Navier Stokes (RANS) equations are satisfied with with this assumption due to the absence of viscosity, Reynold's stress, and mean flow acceleration. Hence, the zero mean pressure gradient assumption is consistent with the other assumptions, and one of the baroclinic terms is eliminated:

$$A\frac{\partial\Omega'}{\partial t}+Au_0\frac{\partial\Omega'}{\partial x}+Av'\frac{d\Omega_0}{dy}=-B\Omega_0\left(\nabla\cdot\vec{u}'\right)+D\frac{\nabla\rho_0\times\nabla p'}{\rho_0^2} \quad (6.9)$$

Finally, the cross product in the remaining baroclinic term can be simplified due to the 2D flow and parallel flow assumptions. Expanding the cross product and expressing mean vorticity in terms of the 2D, parallel base flow velocity leads to:

$$A\frac{\partial\Omega'}{\partial t}+Au_0\frac{\partial\Omega'}{\partial x}-Av'\frac{d^2u_0}{dy^2}=B\frac{du_0}{dy}\left(\nabla\cdot\vec{u}'\right)-D\frac{1}{\rho_0^2}\frac{\partial p'}{\partial x}\frac{d\rho_0}{dy} \quad (6.10)$$

This vorticity budget analysis will probe the fluid dynamics inside the infinitely thin base flow discontinuities, which include a density jump. Assuming zero mass accumulation at the discontinuity leads to:

$$\frac{\partial\rho}{\partial t}=0 \quad (6.11)$$

From the continuity equation:

$$\nabla\cdot\left(\rho\vec{u}\right)=0 \quad (6.12)$$

Under the assumption of parallel base flow, and with Eq. (6.11) in mind, Eq. (6.12) is linearized to

$$\rho_0 \nabla \cdot (\vec{u}') + v' \frac{d\rho_0}{dy} = 0 \tag{6.13}$$

It is now convenient to express Eq. (6.10) in terms of a density weighted fluctuating stream function, ψ', such that Eq. (6.13) is satisfied:

$$u' = \frac{1}{\rho_0}\frac{\partial \psi'}{\partial y},\ v' = -\frac{1}{\rho_0}\frac{\partial \psi'}{\partial x},\ \Omega' = -\frac{1}{\rho_0}\nabla^2\psi' + \frac{1}{\rho_0^2}\frac{d\rho_0}{dy}\frac{\partial \psi_1}{\partial y} \tag{6.14}$$

Inserting Eq. (6.14) into Eq. (6.10) leads to:

$$\begin{aligned} A\frac{\partial}{\partial t}\left(-\frac{1}{\rho_0}\nabla^2\psi' + \frac{1}{\rho_0^2}\frac{d\rho_0}{dy}\frac{\partial \psi_1}{\partial y}\right) + Au_0\frac{\partial}{\partial x}\left(-\frac{1}{\rho_0}\nabla^2\psi' + \frac{1}{\rho_0^2}\frac{d\rho_0}{dy}\frac{\partial \psi_1}{\partial y}\right) + \\ + A\frac{1}{\rho_0}\frac{\partial \psi'}{\partial x}\frac{d^2u_0}{dy^2} = B\frac{du_0}{dy}(\nabla \cdot \vec{u}') - D\frac{1}{\rho_0^2}\frac{\partial p'}{\partial x}\frac{d\rho_0}{dy} \end{aligned} \tag{6.15}$$

Next, the fluctuating flow variables are expanded in normal modes as

$$\{\psi', p'\} = \{\hat{\psi}(y), \hat{p}(y)\} e^{-i(\omega t - kx)} \tag{6.16}$$

Plugging in this expansion and using the canonical relationship $k = \omega/c$, Eq. (6.15) can be rearranged into a form of the Rayleigh equation [73] including the effect of nonuniform mean density:

$$A(u_0 - c)\left(\frac{1}{\rho_0}\nabla^2\hat{\psi} - \frac{1}{\rho_0^2}\frac{d\rho_0}{dy}\frac{d\hat{\psi}}{dy}\right) - A\frac{1}{\rho_0}\hat{\psi}\frac{d^2u_0}{dy^2} = B\frac{du_0}{dy}\hat{\psi}\frac{d(1/\rho_0)}{dy} + D\frac{\hat{p}}{\rho_0^2}\frac{d\rho_0}{dy} \tag{6.17}$$

Eq. (6.17) allows each term in the Rayleigh equation to be related to rotational phenomena from the vorticity equation. If the base flow velocity and density profiles are tophat profiles (as in the simple models described throughout this chapter), then their

spatial derivatives are everywhere zero (except at the jump discontinuities associated with the shear layer and flame). Hence, Eq. (6.17) simplifies to

$$\frac{d^2\hat{\psi}}{dy^2} - k^2\hat{\psi} = 0 \tag{6.18}$$

with jump conditions for particle displacement and pressure [73] at the base flow discontinuities. This second order, linear ODE is the same equation used in the analysis of Yu and Monkewitz (although in their work it is written in terms of pressure, and is derived from the continuity, Navier Stokes, virial equation of state, and the energy equations) [18]. It is valid only for discontinuous step profiles of velocity and density, for high Reynolds number, for parallel base flows, and for incompressible flows. It is also the governing equation used to derive all model analysis dispersion relations in this work. Note that where the base flow velocity and density profiles are spatially uniform, Eq. (6.18) is equivalent to $\hat{\Omega}(y) = 0$. Therefore, the unsteady velocity field is irrotational everywhere except at the base flow discontinuities.

It is immediately evident that Eq. (6.18) captures only the "A" term from the vorticity equation, which is the substantial derivative of the vorticity. This governing equation contains no vorticity sources or sinks. However, unsteady vorticity and its sources (and sinks) may be present at the base flow discontinuities (in both velocity and density) where the right hand side of Eq. (6.17) is nonzero. Therefore, these physics are captured through the jump conditions at the base flow discontinuities.

6.6.2 *Jump Conditions*

As utilized in the stability analysis of Yu and Monkewitz [18] and outlined in Godreche [73], the jump conditions require continuity of unsteady particle displacement and unsteady pressure. However, the stability analysis of Yu and Monkewitz [18] was interested only in the fluid dynamics of the top-hat slabs of fluid, and not in the dynamics inside of the infinitely thin discontinuities, and hence used the standard, zero dilatation stream function and its associated jump conditions. Therefore, this section re-derives the jump conditions under the same assumptions as the previous section, using the density weighted stream function.

6.6.2.1 *Particle Displacement*

The derivation of the particle displacement jump condition begins by defining an interface that fluctuates in the transverse direction about a fixed transverse position, y_0, with amplitude η':

$$y = y_0 + \eta'(x,t) \tag{6.19}$$

By definition, the material derivative of this interface position is the transverse velocity. Under this consideration, Eq. (6.19) is linearized to:

$$v_1 = \frac{\partial \eta'}{\partial t} + u_0 \frac{\partial \eta}{\partial x} \tag{6.20}$$

Using the normal modes expansion in Eq. (6.16), inserting the density weighted stream function, the particle displacement is:

$$\eta' = \frac{-\psi'}{\rho_0 (u_0 - c)} \tag{6.21}$$

This quantity shall be constant across the base flow discontinuity.

6.6.2.2 *Pressure*

The unsteady pressure is derived from the inviscid, axial momentum equation. Under the assumptions of this analysis, the linearized axial momentum equation is:

$$\rho_0 \frac{\partial u_1}{\partial t} + \rho_0 u_0 \frac{\partial u_1}{\partial x} + \rho_0 v_1 \frac{du_0}{dy} = -\frac{\partial p_1}{\partial x} \tag{6.22}$$

Inserting the density weighted stream function and applying the normal modes decomposition from Eq. (6.16), this becomes:

$$p' = \psi' \frac{du_0}{dy} - \left(u_0 - c\right) \frac{\partial \psi'}{\partial y} \tag{6.23}$$

Like the particle displacement, this quantity shall be constant across the base flow discontinuities.

6.6.3 *Integrated Vorticity at Base Flow Discontinuities*

The velocity jump in the shear layer and the density jump across the flame are clearly linked to the jump conditions, but their physical influences on the unsteady vorticity and the hydrodynamic stability are not immediately clear. Furthermore, it is not apparent how the offset between the shear layer and the density jump physically enters the stability analysis. The irrotational, hydrodynamic velocity field is induced by unsteady vortex sheets that partition the flow at the base flow discontinuities. Therefore, the physics of the base flow discontinuities may be described in terms of their unsteady vorticity. This requires integrating the vorticity equation across the base flow discontinuities, identifying the contributing terms, and expressing them in terms of quantities that are available in the

stability analysis (in this case, the unsteady pressure). The rest of this chapter is dedicated to such an effort.

The top-hat nature of the modeled velocity and density fields presents a challenge when quantifying the right hand side of Eq. (6.17). This is because the mean velocity and density are discontinuous; their derivatives in the transverse spatial direction are Dirac delta functions. Since these quantities enter directly into the unsteady vorticity, the vorticity and its sources are expected to be composed of Dirac delta functions. This motivates integration of the unsteady vorticity equation across the base flow discontinuities, which allows identification and quantification of the active terms in Eq. (6.17) at each base flow discontinuity. Although it cannot identify which terms are active, Stokes' theorem provides a way to quantify the unsteady vorticity, and is used to validate the integral method.

The analysis begins with the vorticity equation, starting from its form in Eq. (6.17). Here, the left hand side is written in terms of vorticity instead of the stream function.

$$\left(u_0 - c\right)\Omega' = -\frac{1}{\rho_0}\hat{\psi}\frac{d^2u_0}{dy^2} - \frac{du_0}{dy}\hat{\psi}\frac{d\left(1/\rho_0\right)}{dy} - \frac{\hat{p}}{\rho_0^2}\frac{d\rho_0}{dy} \tag{6.24}$$

This equation may be rearranged to take the following form, which will be integrated across the base flow discontinuities:

$$\Omega' = -\frac{1}{\rho_0\left(u_0 - c\right)}\hat{\psi}\frac{d^2u_0}{dy^2} - \frac{\hat{\psi}}{\left(u_0 - c\right)}\frac{du_0}{dy}\frac{d\left(1/\rho_0\right)}{dy} - \frac{\hat{p}}{\rho_0^2\left(u_0 - c\right)}\frac{d\rho_0}{dy} \tag{6.25}$$

The right hand side of Eq. (6.25) has three terms which govern the local unsteady vorticity. From the term tracking in the previous section, these are identified as follows. From left to right, the first term is conversion of mean vorticity to unsteady vorticity by

transport due to the unsteady velocity. This will be referred to as the shear-associated vorticity. The second and third terms are strictly source/sink terms, and are due to dilatation and baroclinic torque, respectively.

6.6.3.1 *Shear-associated vorticity*

This section integrates the first term on the right hand side of Eq. (6.25) across the base flow discontinuities:

$$\int_{jump} \Omega_{\left(\substack{shear- \\ associated}\right)} dy = -\int_{jump} \frac{\psi'}{\rho_0 \left(u_0 - c\right)} \frac{d^2 u_0}{dy^2} dy \tag{6.26}$$

The second order derivative in Eq. (6.26) is problematic for integration, and can be dealt with using integration by parts:

$$\int_{jump} \Omega_{\left(\substack{shear- \\ associated}\right)} dy = -\frac{\psi'}{\rho_0 \left(u_0 - c\right)} \frac{du_0}{dy}\bigg|_{jump} + \int_{jump} \frac{d}{dy}\left(\frac{\psi'}{\rho_0 \left(u_0 - c\right)}\right) \frac{du_0}{dy} dy \tag{6.27}$$

The first term on the right hand side of Eq. (6.27) is zero, since it is evaluated at its end-points (which can reach into the top-hat velocity profile where $\partial u_0 / \partial y = 0$). Expanding the derivative in the other term and re-grouping the resulting terms allows Eq. (6.27) to be rewritten as follows:

$$\begin{aligned} \int_{jump} \Omega_{\left(\substack{shear- \\ associated}\right)} dy = & \int_{jump} \frac{1}{\rho_0 \left(u_0 - c\right)^2} \left\{ -\psi' \frac{du_0}{dy} + \left(u_0 - c\right) \frac{d\psi'}{dy} \right\} \frac{du_0}{dy} dy \\ & + \int_{jump} \frac{\psi'}{\left(u_0 - c\right)} \frac{d}{dy}\left(\frac{1}{\rho_0}\right) \frac{du_0}{dy} dy \end{aligned} \tag{6.28}$$

This is very convenient, since all fluctuating quantities in the first term can be written in terms of the unsteady pressure, and the unsteady quantities in the second term can be written in terms of the particle displacement:

$$\int_{jump} \Omega_{\left(\substack{shear-\\associated}\right)} dy = \int_{jump} \frac{p'}{\rho_0 \left(u_0 - c\right)^2} \frac{du_0}{dy} dy - \int_{jump} \eta' \rho_0 \frac{d}{dy}\left(\frac{1}{\rho_0}\right) \frac{du_0}{dy} dy \qquad (6.29)$$

Recall that this analysis is concerned with infinitely thin regions, across which the pressure and particle displacement must be continuous. Therefore, in the limit of zero density layer or shear layer thickness, these quantities are constant across the jump. Applying this logic, and consolidating the base flow velocity and its derivative, Eq. (6.29) is rewritten as:

$$\int_{jump} \Omega_{\left(\substack{shear-\\associated}\right)} dy = -p' \int_{jump} \frac{1}{\rho_0} \frac{d}{dy}\left(\frac{1}{\left(u_0 - c\right)}\right) dy - \eta' \int_{jump} \rho_0 \frac{d}{dy}\left(\frac{1}{\rho_0}\right) \frac{du_0}{dy} dy \qquad (6.30)$$

The first term on the right hand side of Eq. (6.29) is evaluated using quadrature, by taking the limit of a linearly varying velocity layer. The discontinuity geometry may be conveniently approximated according to Figure 6-13. Thus, the derivative in Eq. (6.30) becomes a constant quantity and may be taken outside the integral. Applying quadrature to the remaining integral quantity leads to:

$$\int_{\text{jump}} \hat{\Omega} dy = \frac{\hat{p}}{2}\left(\frac{1}{u_0^+ - c} - \frac{1}{u_0^- - c}\right)\left(\frac{1}{\rho_0^+} + \frac{1}{\rho_0^-}\right) - \eta' \int_{jump} \rho_0 \frac{d}{dy}\left(\frac{1}{\rho_0}\right) \frac{du_0}{dy} dy \qquad (6.31)$$

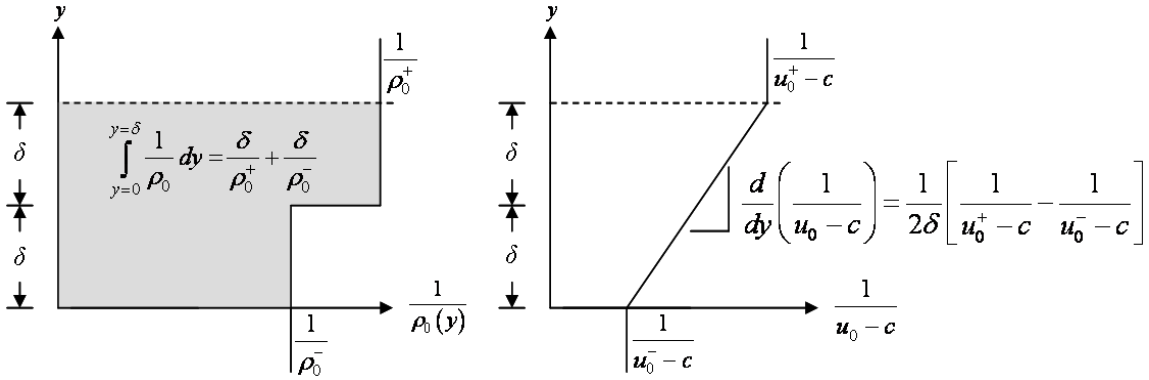

Figure 6-13. Schematic of geometry for integrating shear-associated vorticity

The second term on the right hand side of Eq. (6.31) integrates to infinity if there are simultaneous density and velocity jumps; otherwise, it is zero. The next section will show, however, that this component of the shear-associated vorticity is exactly balanced by the unsteady dilatation.

6.6.3.2 *Dilatation*

This section integrates the second term on the right hand side of Eq. (6.25) across the base flow discontinuities:

$$\int_{jump} \Omega_{dilatation} dy = \int_{jump} -\psi' \frac{1}{(u_0 - c)} \frac{du_0}{dy} \frac{d}{dy}\left(\frac{1}{\rho_0}\right) dy \tag{6.32}$$

This can be expressed in a cleaner form by substituting the particle displacement, and taking it outside the integral (as justified in section 6.6.3.1, *Shear-associated vorticity*):

$$\int_{jump} \Omega_{dilatation} dy = \eta' \int_{jump} \rho_0 \frac{d}{dy}\left(\frac{1}{\rho_0}\right) \frac{du_0}{dy} dy \tag{6.33}$$

This term is nonzero only when there are simultaneous velocity and density discontinuities. This is easily explained physically, since the first order contribution of dilatation to the unsteady vorticity is due only to unsteady dilatation of the mean vorticity (this is evident from a return to the linearized vorticity equation, Eq. (6.8)). Unsteady dilatation occurs due to unsteady velocity across the mean density jump, and mean vorticity exists only at the mean velocity jump. When these two discontinuities are co-located, Eq. (6.33) is nonzero and integrates to infinity. It is exactly balanced, however, by the second term on the right hand side of the shear associated vorticity in Eq. (6.31).

In other words, co-location of the density and shear layers leads to a nonzero and infinite dilatation, which is counteracted by part of the shear associated vorticity.

As a closing commentary on the dilatation contribution to the unsteady vorticity, note that the dilatation is only due to unsteady dilatation of the mean vorticity. Mean dilatation of the unsteady vorticity, which is perhaps a more familiar vorticity sink from the viewpoint of flow across a flame, does not exist in the framework of this parallel flow model since it does not accommodate mean flow across the density jump.

6.6.3.3 *Baroclinic Production*

This section integrates the last term of Eq. (6.25) across the base flow discontinuities:

$$\int_{jump} \Omega_{baroclinic} dy = -\int_{jump} p_1 \frac{1}{(u_0 - c)} \frac{1}{\rho_0^2} \frac{d\rho_0}{dy} dy \tag{6.34}$$

The pressure can be taken outside the integral since it is a constant quantity across the jump, and the mean density and its derivative can be consolidated:

$$\int_{jump} \Omega_{baroclinic} dy = p_1 \int_{jump} \frac{1}{(u_0 - c)} \frac{d}{dy}\left(\frac{1}{\rho_0}\right) dy \tag{6.35}$$

Like the shear-associated vorticity, quadrature is used to evaluate the integral, this time taking the limit of a linearly varying density layer. In this case, it is convenient to approximate the discontinuity geometry according to Figure 6-14. The derivative in Eq. (6.35) becomes a constant quantity and may be taken outside the integral. Evaluating the remaining integral with quadrature gives:

$$\int_{\substack{\text{base flow} \\ \text{discontinuity}}} \hat{\Omega} dy = \frac{\hat{p}}{2}\left(\frac{1}{\rho_0^+} - \frac{1}{\rho_0^-}\right)\left(\frac{1}{u_0^+ - c} + \frac{1}{u_0^- - c}\right) \tag{6.36}$$

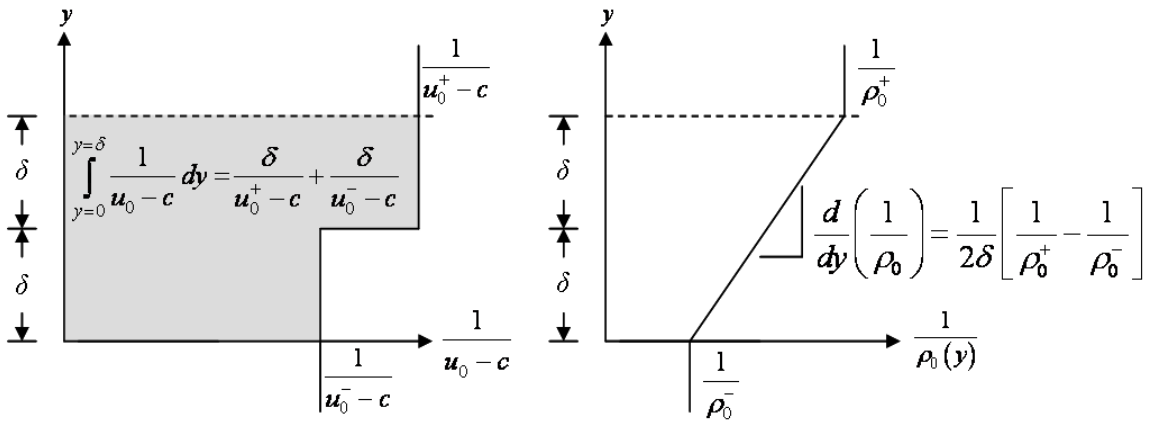

Figure 6-14. Schematic of geometry used for quadrature of the density layer

6.6.4 *Stokes' Theorem*

The previous three sections have identified and quantified the physical sources of unsteady vorticity at the base flow discontinuities. Stokes' theorem provides a simple way to verify these quantifications (although it cannot identify which vortical terms are active). The unsteady vorticity sheets at the base flow discontinuities induce potential velocity fields in the surrounding flow. Stokes' theorem relates the circulation of these velocity fields to the vortex sheet strength. This analysis begins with Stokes' theorem,

$$\oint \vec{v}' \cdot d\vec{s} = \iint_A \left(\nabla \times \vec{v}'\right) dA \tag{6.37}$$

where $\vec{s}$ is the local unit tangent to the closed line integration path, and A is the domain enclosed by that path. In this section, the "primes" will be dropped from unsteady velocities and stream functions to avoid cluttered notation; base flow velocities will retain the subscript zero. For a 2D flow, Eq. (6.37) is simply

$$\oint \vec{v} \cdot d\vec{s} = \iint_A \Omega dA \tag{6.38}$$

where Ω is the unsteady out of page component of vorticity. Applying this to a velocity field which is discontinuous in the transverse direction, such that the line integration path encloses a differential fluid element spanning the discontinuity (see Figure 6-15), leads to:

$$\int_{y=-\delta}^{y=0} v^- dy + \int_{y=0}^{y=\delta} v^+ dy + \int_{x=\Delta x}^{x=0} u^+ dx + \int_{y=\delta}^{y=0} v^+ dy + \int_{y=0}^{y=-\delta} v^- dy + \int_{x=0}^{x=\Delta x} u^- dx = \int_{y=-\delta}^{y=\delta} \int_{x=0}^{x=\Delta x} \Omega' dx dy \quad (6.39)$$

Higher order terms, associated with the axial variation of the velocity, have been discarded in Eq. (6.39). This equation reduces to:

$$\int_{x=0}^{x=\Delta x} u^- dx - \int_{x=0}^{x=\Delta x} u^+ dx = \int_{y=-\delta}^{y=\delta} \int_{x=0}^{x=\Delta x} \Omega' dx dy \quad (6.40)$$

Equation (6.40) may be rewritten in terms of the density weighted stream function (Eq. (6.14)):

$$\int_{x=0}^{x=\Delta x} \frac{1}{\rho_0^-} \frac{\partial \psi^-}{\partial y} dx - \int_{x=0}^{x=\Delta x} \frac{1}{\rho_0^+} \frac{\partial \psi^+}{\partial y} dx = \int_{y=-\delta}^{y=\delta} \int_{x=0}^{x=\Delta x} \Omega' dx dy \quad (6.41)$$

Finally, taking the limit as $\Delta x \to 0$,

$$\Delta x \frac{1}{\rho_0^-} \frac{\partial \psi^-}{\partial y} - \Delta x \frac{1}{\rho_0^+} \frac{\partial \psi^+}{\partial y} = \Delta x \int_{y=-\delta}^{y=\delta} \Omega' dy \quad (6.42)$$

Expanding in normal modes (as in Eq. (6.16)), this simplifies to:

$$\int_{y=-\delta}^{y=\delta} \hat{\Omega} dy = \frac{1}{\rho_0^-} \frac{d\hat{\psi}^-}{dy} - \frac{1}{\rho_0^+} \frac{d\hat{\psi}^+}{dy} \quad (6.43)$$

Thus, Eq. (6.43) provides the integrated vorticity at discontinuities in the unsteady velocity field (which, in this analysis, must occur at discontinuities in the base flow).

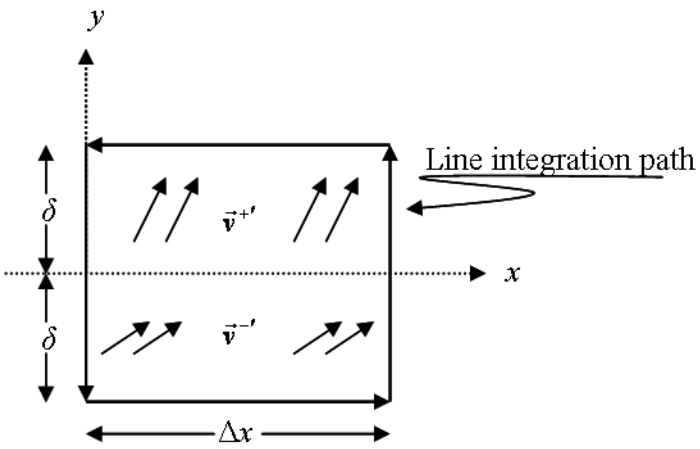

Figure 6-15. Integration path enclosing a discontinuity in the unsteady velocity field.

Stokes' theorem is expected to provide the total integrated vorticity (ie, the sum of vorticity due to the shear-associated term, the dilatation, and the baroclinic term). Adding these integrated vorticity contributions (from Eq. (6.31), Eq. (6.33), and Eq. (6.36)) and cancelling opposing terms gives:

$$\int_{\text{jump}} \hat{\Omega} dy = \hat{p}\left(\frac{1}{u_0^+ - c}\right)\left(\frac{1}{\rho_0^+}\right) - \hat{p}\left(\frac{1}{u_0^- - c}\right)\left(\frac{1}{\rho_0^-}\right) \tag{6.44}$$

Keeping in mind the equation for the unsteady pressure (Eq. (6.23)), this is:

$$\int_{\text{jump}} \hat{\Omega} dy = \frac{1}{\rho_0^-}\frac{\partial \hat{\psi}^-}{\partial y} - \frac{1}{\rho_0^+}\frac{\partial \hat{\psi}^+}{\partial y} \tag{6.45}$$

which is equivalent to the result from Stokes' hypothesis in Eq. (6.43).

Previously, it was shown that the flow is irrotational outside of the base flow discontinuities. The previous sections have shown that integrating the vorticity equation across the base flow discontinuities identifies and quantifies three active vorticity terms: shear-associated vorticity due to transport of the mean vorticity by the unsteady velocity, dilatation due to unsteady dilatation of the mean vorticity, and baroclinic torque due to

the unsteady axial pressure gradient interacting with the mean density gradient from the flame. The backflow ratio parameter directly controls the shear-associated vorticity, and the density ratio parameter directly controls the baroclinic torque. When the two layers are co-located, the backflow ratio and density ratio both contribute to an additional shear associated vorticity and a nonzero dilatation a; these two contributions infinite, but exactly cancel. When considering the direct influences of the various stability parameters, however, it is important to keep in mind that each vorticity sheet is influenced by the induced velocity of the other.

The previous sections showed that the dilatation is only nonzero when density and shear layers are colocated, is infinite in this case, and is always exactly balanced by one term in the shear-associated vorticity. In the next section, the quantifications of the shear associated vorticity and the baroclinic vorticity production derived above are compared to the predicted instability growth rates over a broad parameter range. For the remainder of this chapter, the shear-associated vorticity will include the dilatation to remain non-singular when the two layers are colocated.

6.6.5 *Vorticity Budget Results*

The previous sections derived expressions for the unsteady shear-associated vorticity, dilatation, and baroclinic production, in terms of the base flow properties and unsteady pressure and particle displacement (which can easily be extracted from the stability analysis). This section will show a strong relationship between the relative values of these vorticity terms and the predicted stability characteristics. The relative contribution of these terms to the total unsteady vorticity is referred to here as the "vorticity budget."

As mentioned in the previous section, the remaining analysis will lump together the shear associated vorticity and the dilatation, so that they remain non-singular for co-located layers. The shear-associated vorticity and baroclinic vorticity production may augment or inhibit each other depending on their relative phases. In order to consider a vorticity "budget," it is convenient to define a total vorticity, $\Omega_{total} = |\Omega_{baroclinic}| + |\Omega_{shear}|$, which is the sum of the magnitudes of the shear-associated and baroclinic vorticity. Figure 6-16 shows the relative magnitudes and phases of baroclinic and shear-associated vorticity terms when the density ratio is held constant, and the degree of non-colocation is varied. The figure shows that this parameter has a significant influence on the relative phases of the two terms. As the two layers move away from one another, the phases of the baroclinic and shear-associated vorticity become more aligned. Thus, non-colocation of the two layers moves the two vorticity sources in-phase with one another. Figure 6-16 shows that this effect is especially pronounced when the density layer is outboard of the shear layer. This is reflected in the corresponding growth rates in Figure 6-12a, which indicates much greater destabilization when the density layer moves outboard instead of inboard. Jumps in the plots (other than when the shear layer moves across the density interface) occur when two pinch point saddles (saddles in the Riemann surface of $\omega(k_r, k_i)$) exchange dominance.

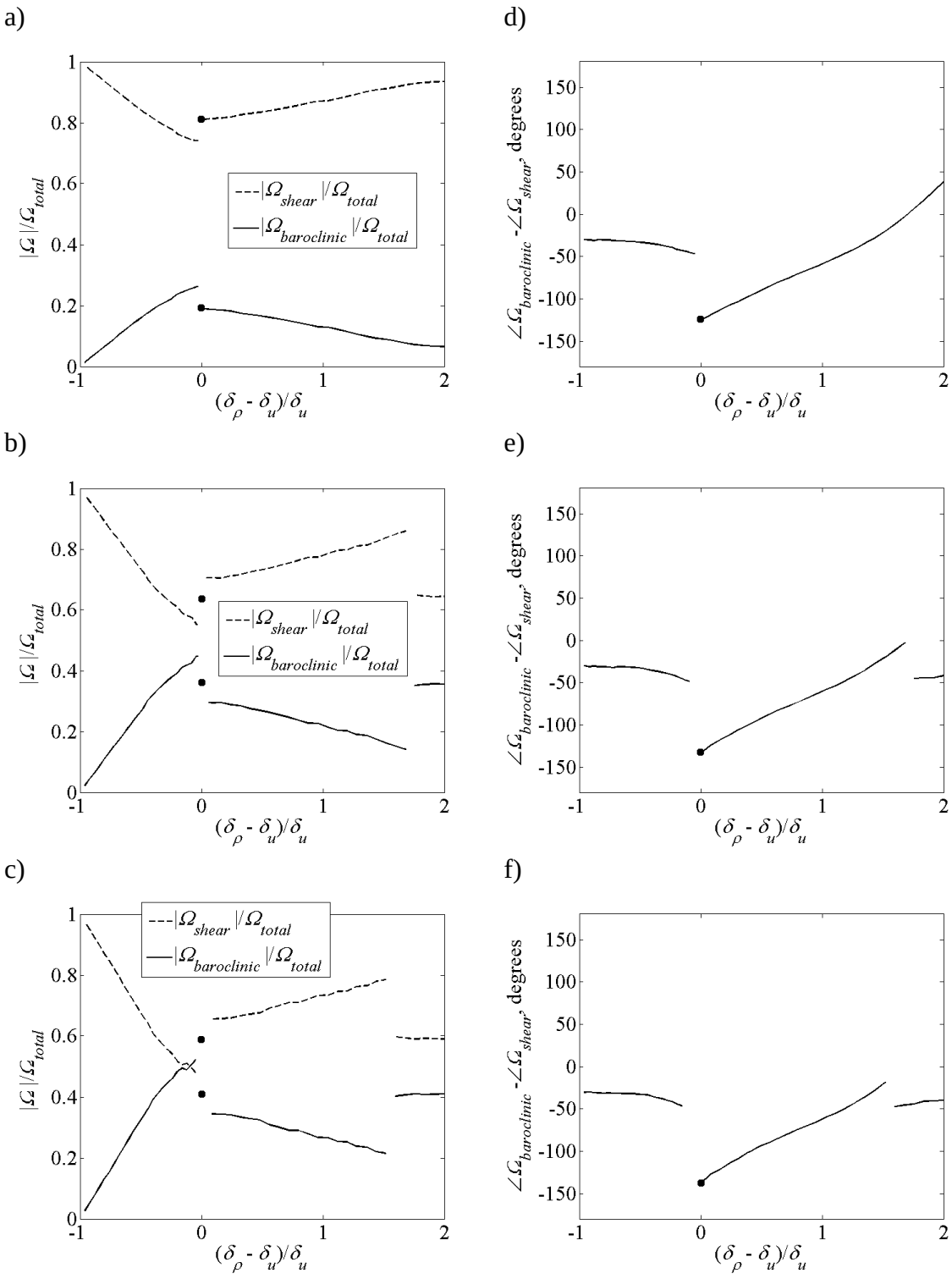

Figure 6-16. Comparison of magnitudes of the shear-associated and baroclinic vorticity (left column) and phase difference between the two terms for $\rho_u/\rho_b = 1.4,\ 2.0,$ and 2.5 (top to bottom)

Figure 6-17 shows the relative magnitudes and phases when the degree of non-colocation is held fixed and the density ratio is varied. The figure shows that the density ratio primarily influences the relative magnitude of the baroclinic vorticity and has little influence on the phase. Higher density ratios lead directly to greater baroclinic vorticity generation. In general, when the two vorticity terms are out of phase, this effect is stabilizing as the baroclinic vorticity balances the shear associated vorticity (over the range of density ratios studied, baroclinic vorticity is lower magnitude than shear-associated vorticity). Likewise, when the two vorticity terms are very nearly in-phase (i.e. the density layer is far outboard of the shear layer), increasing the density ratio can actually become destabilizing (see again Figure 6-12a).

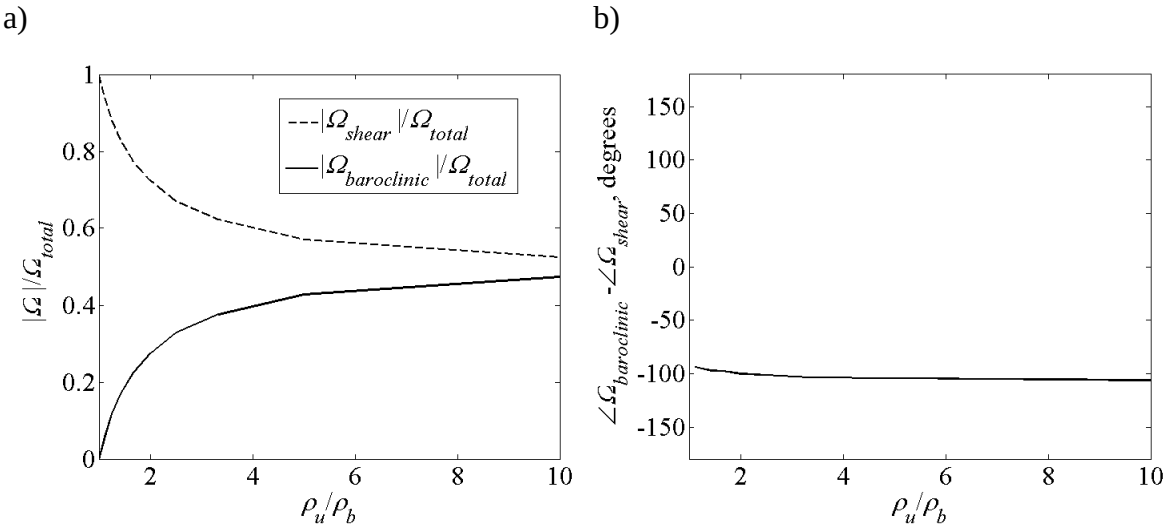

Figure 6-17. Relative a) magnitudes and b) phases of the baroclinic and shear associated vorticity during a density ratio sweep, for $\left(\delta_\rho - \delta_u\right)/\delta_u = 0.2$

If the total vorticity in one half plane ($0 < y < H$), denoted $\Omega_{\substack{half \\ plane}}$, is equal to the instantaneous sum of the baroclinic and shear-associated vorticity,

$$\left|\hat{\Omega}_{\substack{half \\ plane}}\right| \sin\left(\omega_{0,r}t + \angle\hat{\Omega}_{\substack{half- \\ plane}}\right) = \left|\hat{\Omega}_{baroclinic}\right| \sin\left(\omega_{0,r}t + \angle\hat{\Omega}_{baroclinic}\right) + \left|\hat{\Omega}_{shear}\right| \sin\left(\omega_{0,r}t + \angle\hat{\Omega}_{shear}\right) \tag{6.46}$$

then the amplitude of this summed vorticity may be determined by summing the two harmonic, like-frequency, phase shifted, vorticities according to Eq. (6.47):

$$\left|\hat{\Omega}_{\substack{half \\ plane}}\right| = \sqrt{\left|\hat{\Omega}_{baroclinic}\right|^2 + \left|\hat{\Omega}_{shear}\right|^2 + 2\left|\hat{\Omega}_{baroclinic}\right|\left|\hat{\Omega}_{shear}\right| \cos\left(\angle\hat{\Omega}_{baroclinic} - \angle\hat{\Omega}_{shear}\right)} \tag{6.47}$$

This analysis was performed such that the stream function eigenfunction is normalized by its complex amplitude in the outer layer, and the result is plotted in Figure 6-18. Note the valley of small total vorticity amplitude when the flame and shear layer are colocated, which is reminiscent of the valley of small $\omega_{0,i}$ in Figure 6-12a.

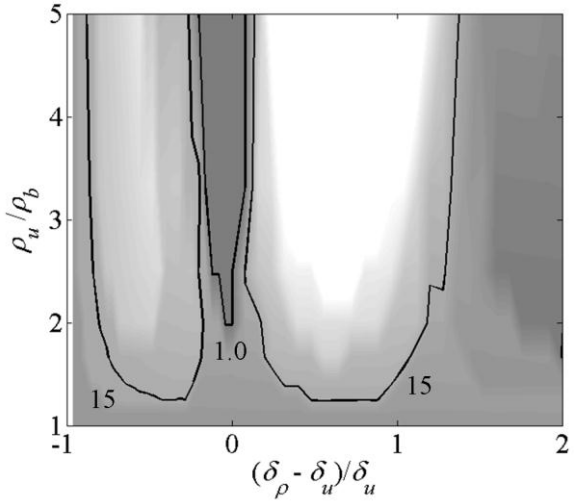

Figure 6-18. Isocontours of the total unsteady vorticity amplitude, $\left|\Omega_{\substack{half \\ plane}}\right|$

It is important to keep the boundary conditions in mind. For the sinuous mode, the flow centerline requires zero unsteady axial velocity, and the confining wall requires zero unsteady transverse velocity. These boundary conditions can be satisfied with the method of images. In this sense, each vortex sheet has a like-signed mirror image across the flow centerline. Likewise, each vorticity sheet has an opposite-signed mirror image across the confining walls. This leads to an infinite series of sources on each side of the flow centerline. The present analysis has shown, however, that analysis of a single half of the flow, without considering the image sources, can significantly enhance physical understanding of the role of the stability parameters. Studies of highly confined flows would likely benefit from modeling some image sources near the wall.

This section has shown that the flow stability characteristics have a strong dependence on the vorticity budget, which is dominated by the shear-associated vorticity and the baroclinic vorticity production. When the density jump and shear layer are colocated, the integrated dilatation becomes nonzero and singular, and is exactly balanced by part of the integrated shear associated vorticity. Under the assumptions of this analysis, shear-associated vorticity is produced by transport of mean vorticity by the unsteady velocity, baroclinic vorticity production is due only to the unsteady axial pressure gradient acting on the mean density gradient, and dilatation is due to unsteady dilatation of the mean vorticity.

6.7 Closing Remarks

This chapter began with a classical model stability analysis. Data from the unforced experiments were compared to the classical analysis, and then to a higher fidelity analysis. Both analyses showed the same qualitative trends and demonstrated a good

parameterization of the stability problem, although quantitative differences were identified. Both types of stability analysis have their merits. The detailed analysis results in a good quantitative description of the frequency and flow stability, and offers considerable computational savings over a global stability or CFD analysis. The model stability analysis does not make such a good quantitative prediction. However, it offers further computational savings, exhibits the correct qualitative trends, and allows easy identification of the important stability parameters and their physical roles. Therefore, it is a useful tool for determining the key flow stability parameters and how they physically influence the flow stability. An improved model analysis dispersion relation was presented, which included the effects of confinement (which had been investigated already by Rees and Juniper [65]) and non co-location of the density and velocity jumps, which is a contribution of this work. This analysis showed that the degree of non-colocation primarily affects the flow stability by influencing the relative phasing of the baroclinic and shear-associated vortex sheets.

CHAPTER 7. INTERMITTENCY OF LIMIT CYCLE EVENTS

This chapter builds on the discussion from Chapter 5, *Experimental Results: Unforced Flame and Flow Dynamics*. It has been postponed until this point in the manuscript because it draws from the results in Chapter 6, *Local Hydrodynamic Stability Analysis*. Additionally, it is a major finding of this work and thus deserves its own chapter. Chapter 5, *Experimental Results: Unforced Flame and Flow Dynamics* concluded that the flow stability characteristics do not bifurcate sharply as the density ratio is varied; rather, the limit cycle amplitude of the sinuous mode appears to grow gradually and monotonically as this parameter is reduced. This chapter justifies the statement that a better description of this behavior requires time-local analysis of the unsteady flame and flow dynamics.

7.1 Time-local Description

Chapter 5, *Experimental Results: Unforced Flame and Flow Dynamics* showed that there is a gradual increase in spectral energy at the asymmetric vortex shedding frequency as density ratio is decreased. In other words, the flow does not abruptly bifurcate to a globally unstable mode below some threshold density ratio. However, the measures of the flame and flow response illustrated so far are averaged temporal attributes and do not illustrate that the flame dynamics are actually highly intermittent in time. As will be shown next, it appears that rather than characterizing the limit cycle as monotonically growing in amplitude with ρ_u/ρ_b, a better description is that the flow has two possible states (the noise-driven base flow, and a stable limit cycling oscillation) and

intermittently varies between them. The relative fraction of time the flow spends in each state monotonically varies with density ratio. This intermittent character is evident from Figure 7-1, which shows a short sequence of flame images at the same operating condition; the flame has a generally symmetric structure at the beginning of the sequence, and has switched to a sinuous mode by the end. Likewise, Figure 7-2 shows instantaneous vectors and streamlines calculated from PIV measurements at the same conditions. Figure 7-1 and Figure 7-2 show the large scale, asymmetric undulations of the flame/flow in some frames, with more disorganized features in other frames. The intermittent nature of the flame (and flow) is also apparent when observing the measured time signals from high speed video and PIV. For example, in time signals of flame edge displacement (see Figure 7-5a), there are clearly periods of time where the signal is very noisy, but there are also periods of time when the signal appears to be nearly sinusoidal. It should be emphasized that the word "intermittency" is used here in the nonlinear dynamics sense, not to reference the internal or external intermittency phenomena discussed in the turbulent flows literature [74].

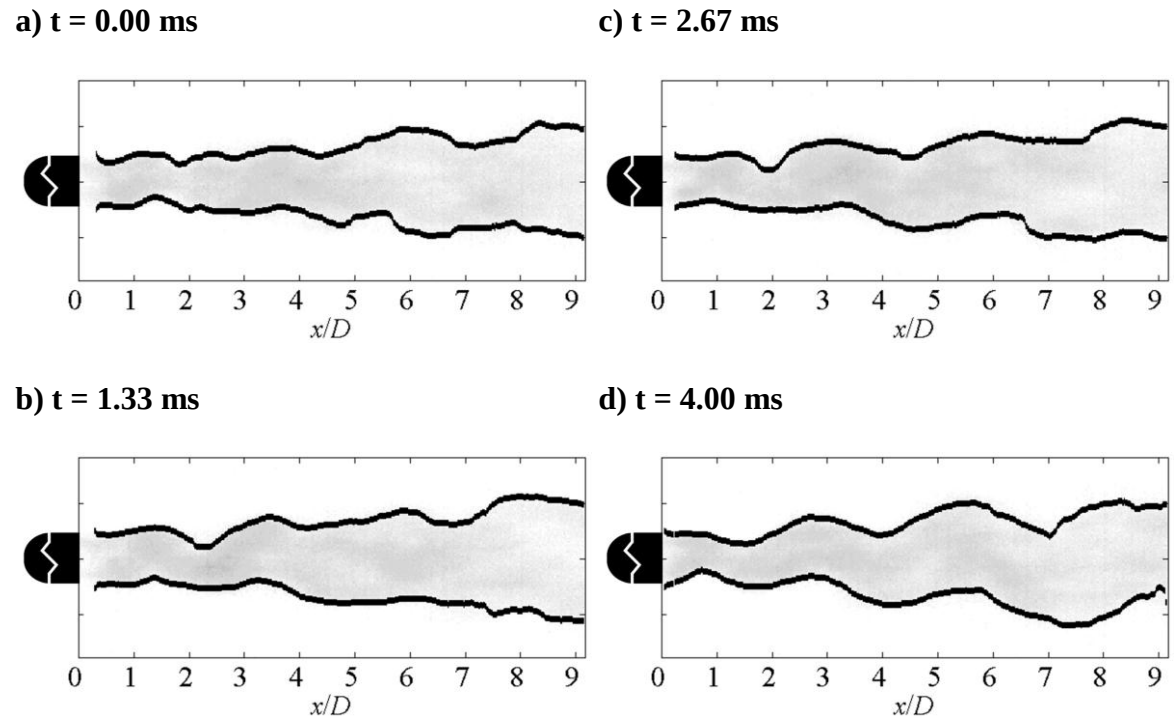

Figure 7-1. Sequence of flame images with edge tracking, demonstrating intermittent flame structure for ballistic bluff body at $U_{lip} = 50$ m/s and $\rho_u / \rho_b = 2.0$

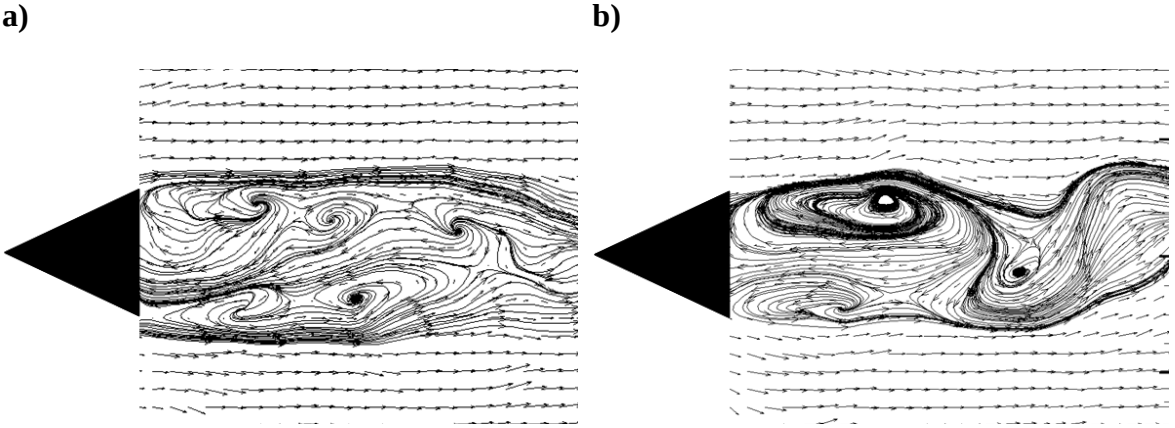

Figure 7-2. Instantaneous velocity vectors and streamlines at two different times but same operating condition for v-gutter at $U_{lip} = 50$ m/s, $\rho_u / \rho_b = 2.0$, showing intermittent character of the wake flow.

7.2 Proper Orthogonal Decomposition

This chapter discusses the intermittent appearance of the sinuous wake mode. Proper orthogonal decomposition (POD) was performed on the PIV data, using the DAVIS 7.2 software, to determine if any other significant modes were present. The POD analysis revealed that the only coherent, non-noisy mode was the sinuous mode. A series of the first 8 POD modes is shown in Figure 7-3 for a low density ratio case. These first eight modes collectively contain 48% of the total energy of the POD. The figure is arranged so that the mode number increases from one to eight from top to bottom, with energy decreasing as mode number increases. The left column shows the spatial modes, and the right column shows the spectrum of the corresponding time coefficients. Modes 2 and 3 show the sinuous mode, oscillating periodically at the global mode frequency. These modes are spatially shifted from one another by half of the axial wavelength and temporally shifted by 90° of the global mode cycle, and both are required to reconstruct the global mode. This pairing phenomenon will be present in the POD discussion in Chapter 8, *Experimental Results: forced Flame and Flow Dynamics*. The other modes shown are noisy and incoherent. This is representative of the POD result from other unforced cases. Results from other density ratios and lip velocities are shown in Figure 7-4, showing only the pair of coherent modes. Note that the global mode becomes difficult to detect as density ratio increases.

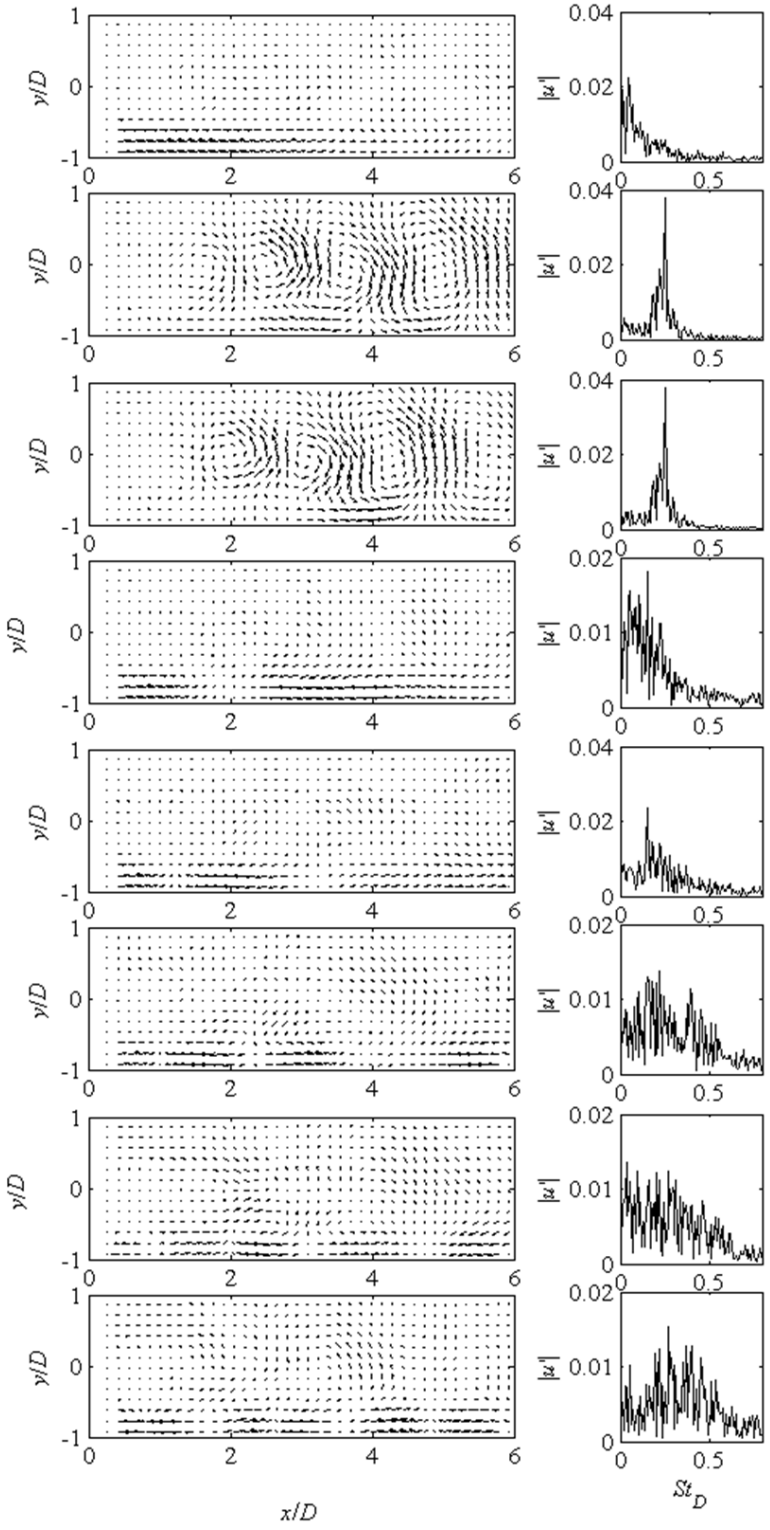

Figure 7-3. First ten POD modes for $\rho_u/\rho_b = 1.7$, $U_{lip} = 30$ m/s

a)

b)

c)

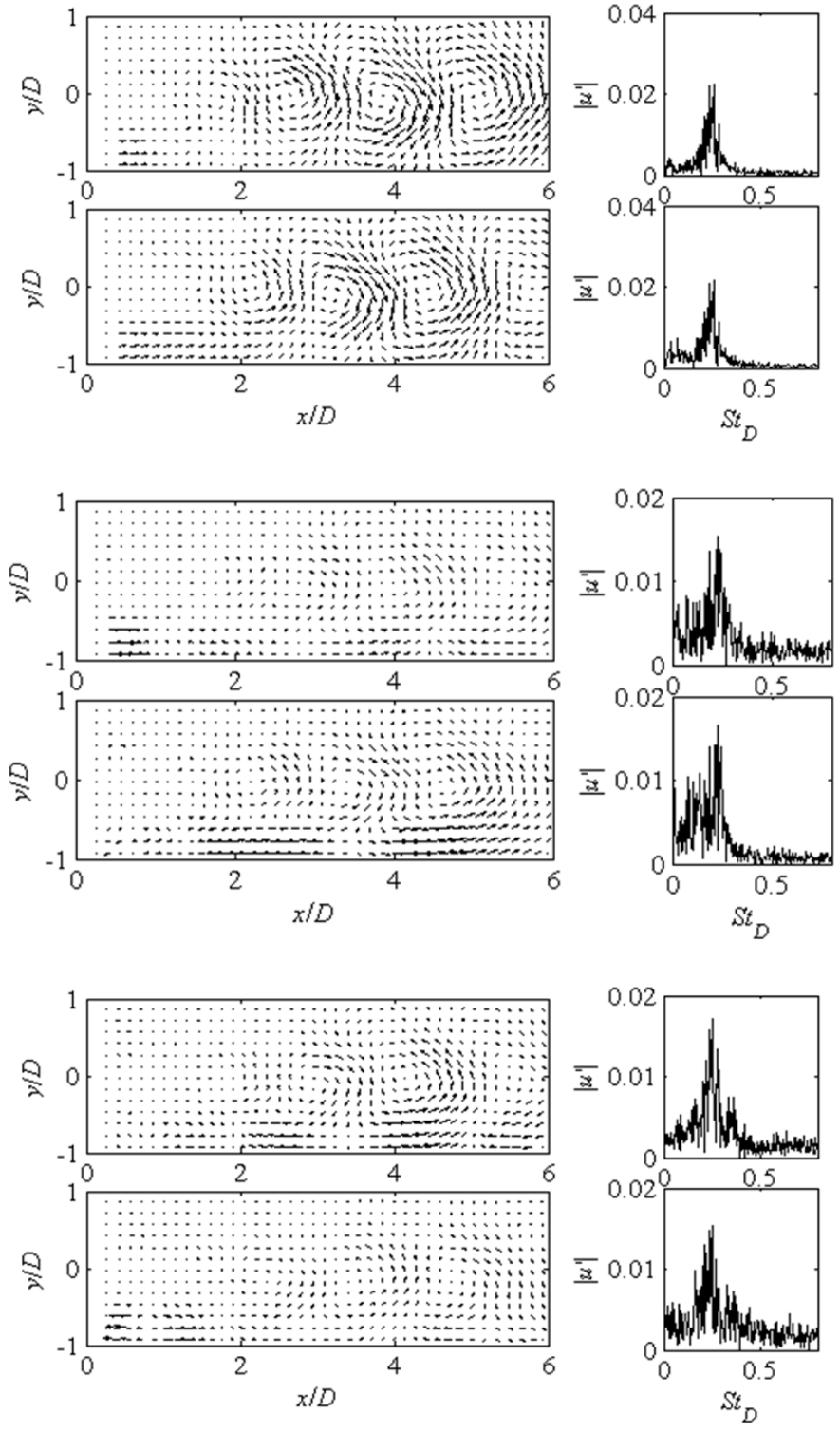

Figure 7-4. POD modes contributing to the global mode for $U_{lip} = 50$ m/s and a) $\rho_u/\rho_b = 1.7$, b) $\rho_u/\rho_b = 1.9$, and c) $\rho_u/\rho_b = 2.0$

7.3 Statistical distribution of periodic events

Analysis of various time windows of a given data set show that the flame and flow behavior erratically changes between apparently random oscillations over a certain time interval, τ_n, to highly periodic oscillations over another time interval, τ_s. To quantify these observations, these intervals are be indexed such that $\tau_{n,j}$ represents the j^{th} noisy event, and $\tau_{s,i}$ represents the i^{th} sinusoidal event. Figure 7-5 illustrates these characteristic times using flame edge data. The duration of these two time intervals is a strong function of density ratio. Although these different behaviors appear erratically, they can be statistically characterized. It is now convenient to define a time period, $T_n = 1/f_n$, which is the period of the limit cycle behavior. As a method to quantify this intermittency, the time series were locally fit to a sinusoidal fluctuation with a fixed frequency of $f_n = 0.24U_{lip}/D$ over a $2T_n$ window, providing an amplitude $Z(x)$ and phase $\Psi(x)$. Within each two period window, a correlation coefficient, r_f (defined below), was calculated between the sine fit and the actual data, providing a measure of the goodness of fit.

$$r_f(x) = \frac{\left\langle \zeta_U(x,t) Z(x) \sin\left(2\pi f_n t + \Psi(x)\right)\right\rangle}{\sqrt{\left\langle \left(\zeta_U(x,t)\right)^2 \right\rangle \left\langle \left(Z(x)\sin\left(2\pi f_n t + \Psi(x)\right)\right)^2 \right\rangle}} \tag{7.1}$$

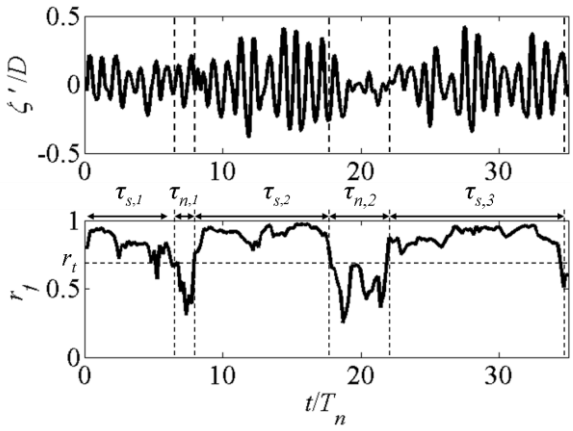

Figure 7-5. Top) Time signal of flame edge motion for $U_{lip} = 50$ m/s, $\rho_u/\rho_b = 2.0$, partitioned (and labeled accordingly) into sinusoidal times and noisy times; Bottom) r_f, defining when each time signal is approximately sinusoidal according to a threshold value, r_t

Figure 7-6 shows a sample of flame displacement time signals for many density ratios, with the resulting r_f below each one. Figure 7-7 shows the same for the transverse velocity. The figures illustrate that for lower density ratio cases, the signal spends a significant fraction of time between $r_f = 0.9-1.0$ for flame edge displacement (slightly less for the unsteady transverse velocity), but also has certain periods of time where it drops to values well below 0.5. In contrast, the results at higher density ratios ($\rho_u/\rho_b = 2.4$ and above) show substantially more time with low correlation coefficients.

a) $\rho_u/\rho_b = 1.7$

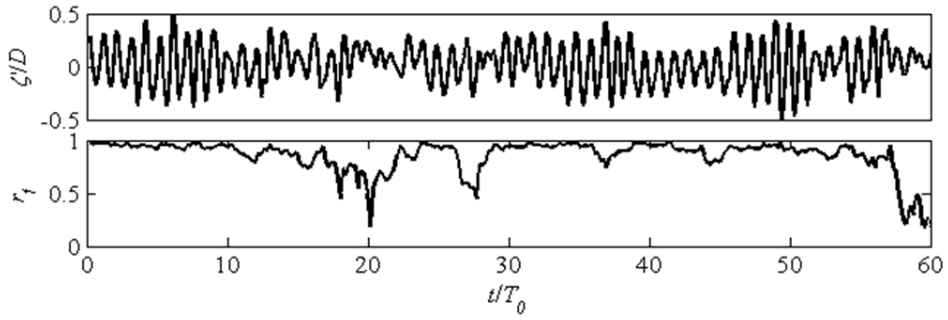

b) $\rho_u/\rho_b = 2.0$

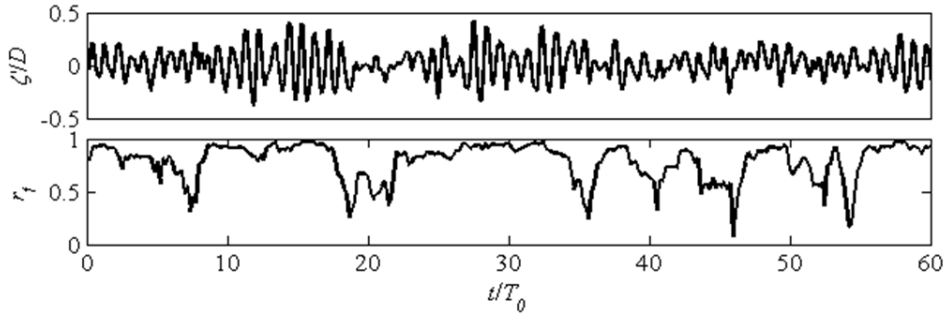

c) $\rho_u/\rho_b = 2.2$

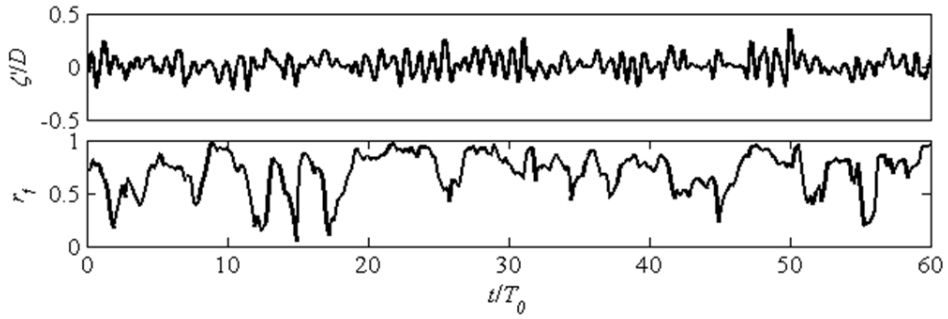

d) $\rho_u/\rho_b = 2.4$

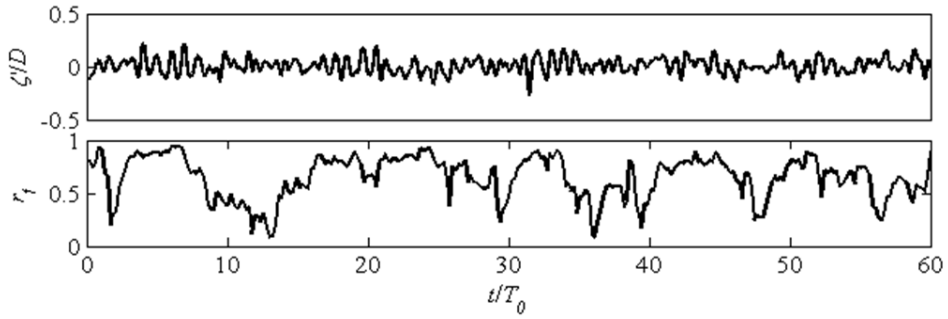

Figure 7-6. Sample of flame edge displacement signal and corresponding fit correlation coefficient for a) $\rho_u/\rho_b = 1.7$, b) $\rho_u/\rho_b = 2.0$, c) $\rho_u/\rho_b = 2.2$, d) $\rho_u/\rho_b = 2.4$, e) $\rho_u/\rho_b = 2.7$, f) $\rho_u/\rho_b = 2.9$, g) $\rho_u/\rho_b = 3.1$

e) $\rho_u/\rho_b = 2.7$

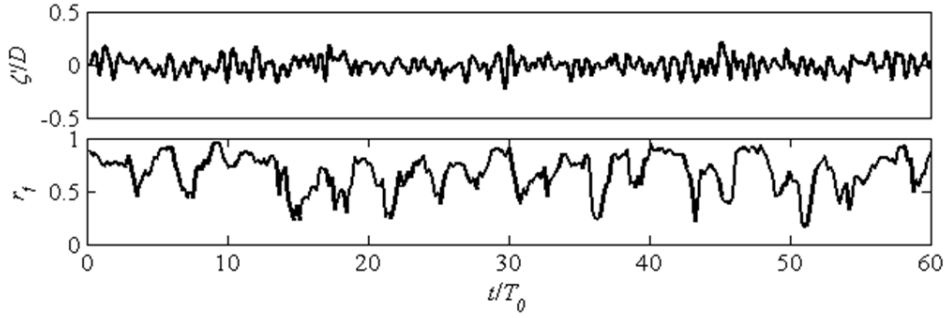

f) $\rho_u/\rho_b = 2.9$

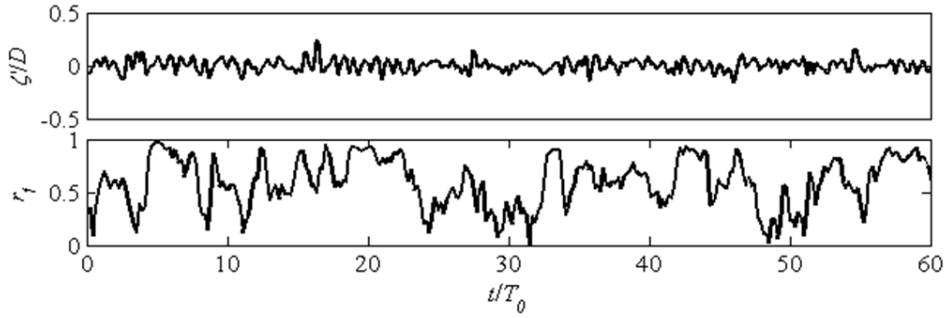

g) $\rho_u/\rho_b = 3.1$

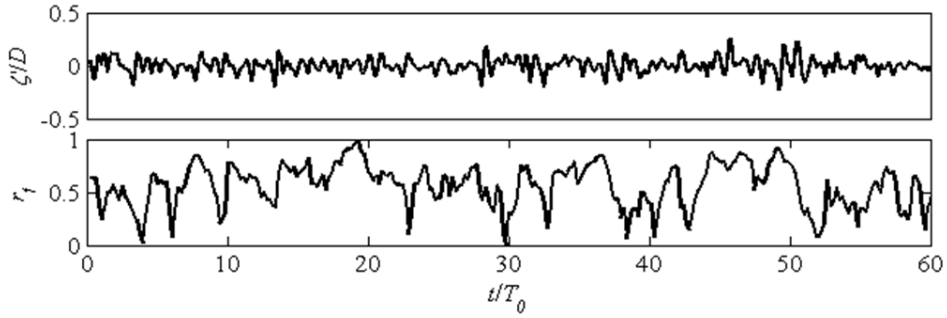

Figure 7-6 continued

a) $\rho_u/\rho_b = 1.7$

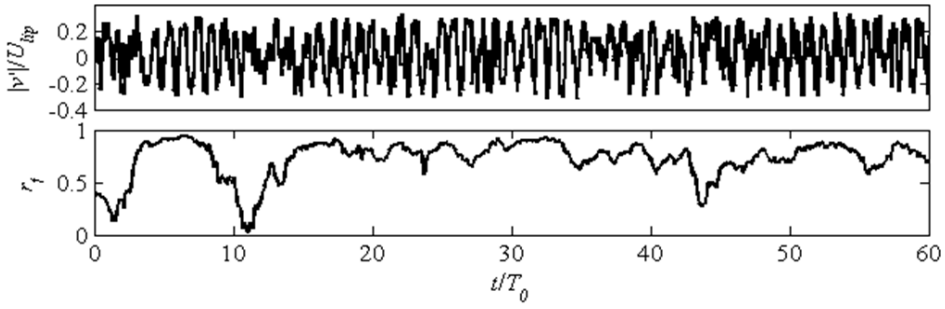

b) $\rho_u/\rho_b = 2.0$

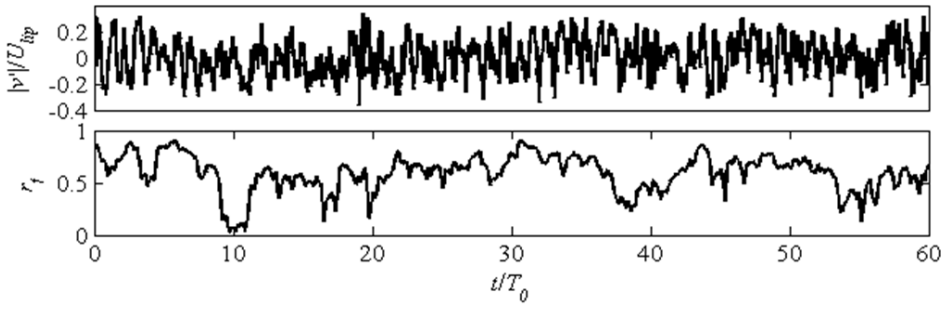

c) $\rho_u/\rho_b = 2.2$

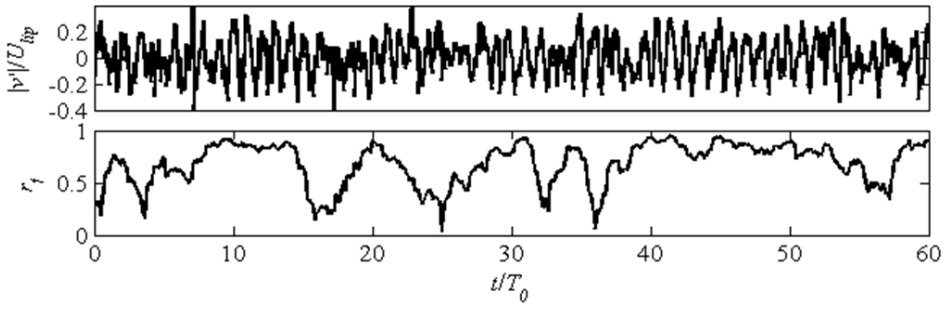

d) $\rho_u/\rho_b = 2.4$

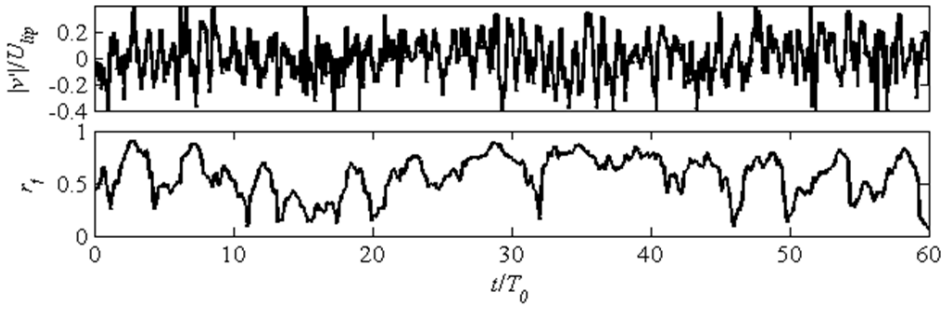

Figure 7-7. Sample of transverse velocity signal and corresponding fit correlation coefficient for a) $\rho_u/\rho_b = 1.7$, b) $\rho_u/\rho_b = 2.0$, c) $\rho_u/\rho_b = 2.2$, d) $\rho_u/\rho_b = 2.4$, e) $\rho_u/\rho_b = 2.5$

e) $\rho_u/\rho_b = 2.5$

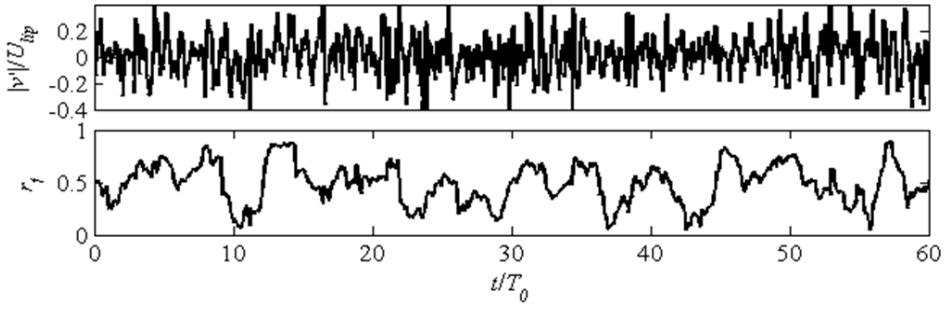

Figure 7-7 continued

The fraction of time, F, that this correlation coefficient, r_f, exceeds a specified threshold value, r_t, was computed at each spatial location and density ratio. Here, F will be termed the intermittency factor. Figure 7-8 plots typical results for the density ratio dependence of the intermittency factor at two threshold values, $r_t = 0.5$ and 0.8. Notice the similarities between the spectral energy plot, (see Figure 5-13 of Chapter 5, *Experimental Results: Unforced Flame and Flow Dynamics*), and the intermittency plot, Figure 7-8. Figure 7-9 shows a similar result, plotting the axial dependence of the intermittency factor for several density ratios.

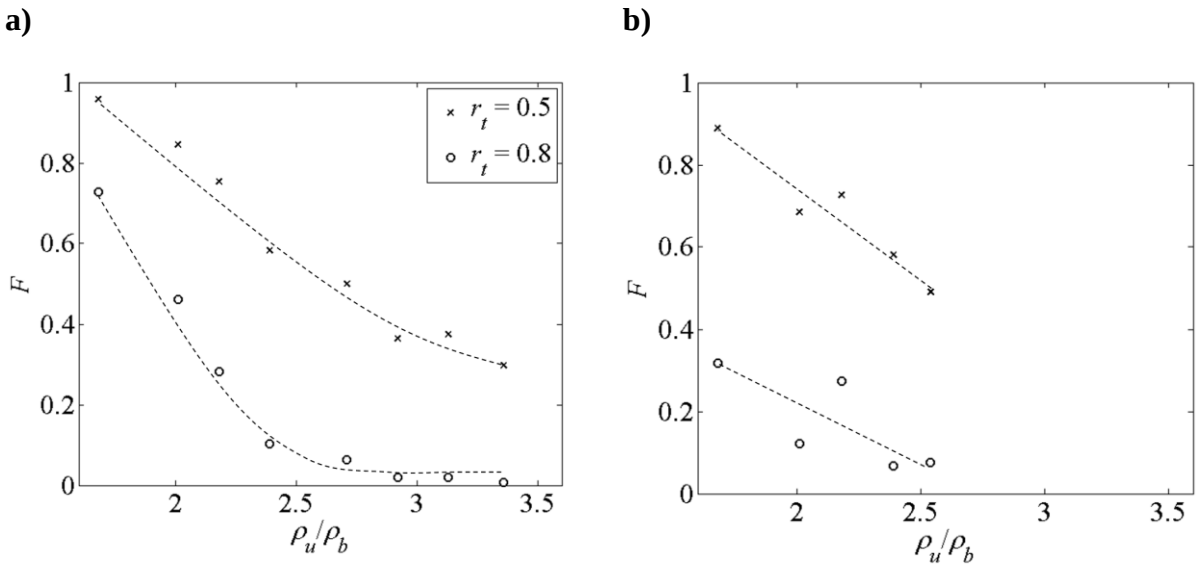

Figure 7-8. Intermittency factor for ballistic bluff body at $U_{lip} = 50$ m/s, $x/D = 3.5$ for a) flame edge and b) centerline transverse unsteady velocity. Results for two threshold values are presented.

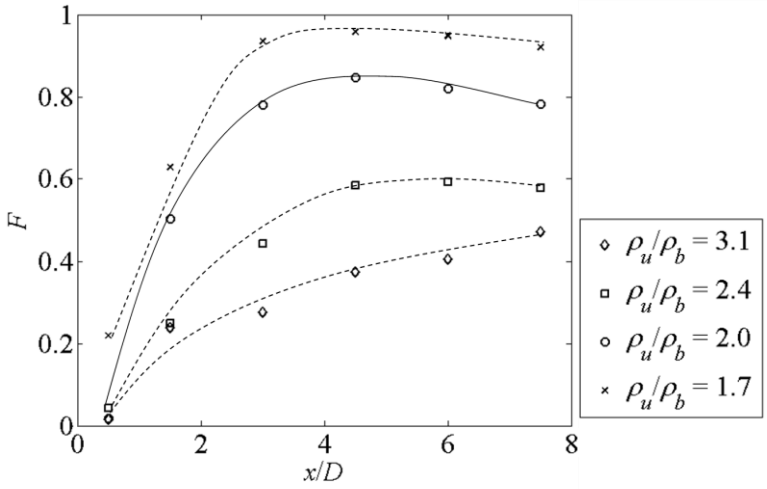

Figure 7-9. Axial dependence of the intermittency factor for ballistic bluff body flame edge at $U_{lip} = 50$ m/s

These data clearly show that the rise in narrowband energy is associated with an increased fraction of time that the flow spends in a limit-cycling state, manifested by

asymmetric structures with length scales of the order of the bluff body diameter. However, the growth in amplitude with decreasing density ratio shown in Chapter 5, *Experimental Results: Unforced Flame and Flow Dynamics* is not only due to intermittency effects, but also a rise in limit cycle amplitude during the time instants when the flow exhibits highly periodic character. This point is quantified by the conditional amplitude of the sinusoidal fits averaged over the time intervals when $r_f > r_t$, denoted by $\zeta'_{rms}\left(r_f > r_t\right)$ in Figure 7-10. The figure shows that the monotonic increase in narrowband spectral energy is not only due to changes in intermittency characteristics, but also because of a rise in limit cycle amplitude of the sinusoidal configuration as density ratio decreases. This is clearly evident in the time signals of flame edge motion presented in Figure 7-6, where a doubling of the amplitude of the sinusoidal parts of the time signal is observed when decreasing the density ratio from $\rho_u/\rho_b = 2.4$ to $\rho_u/\rho_b = 1.7$.

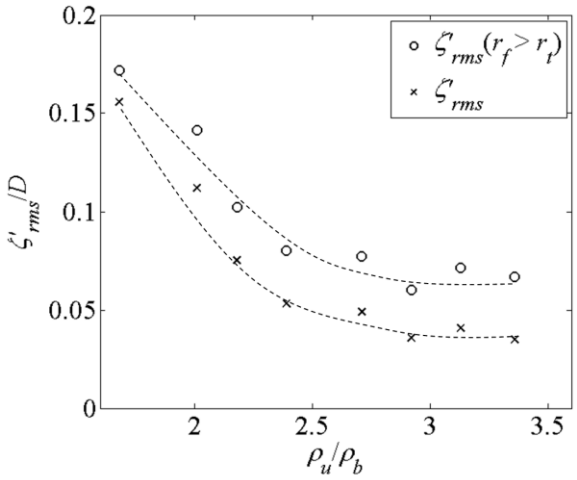

Figure 7-10. Effect of density ratio and intermittency on flame limit cycle amplitude for ballistic bluff body at $U_{lip} = 50$ m/s, $x/D = 3.5$

As introduced previously, the time intervals of the "sinusoidal" and "random" bursts in the flame edge time series were determined, and were named τ_s and τ_n, respectively. These were obtained by traversing through the correlation coefficient time series, and recording the time between crossings of the correlation coefficient threshold as shown in Figure 7-5. Time spent above the threshold was associated with sinusoidal bursts, and time below the threshold was associated with random bursts. Thus, event durations were accumulated for both sinusoidal and random bursts. The probability density functions (pdfs) of the sinusoidal event durations, τ_s, are shown in Figure 7-11a and correlate well to exponential distributions, $\text{pdf}\left(\tau > 0, \lambda\right) = \lambda e^{-\lambda\tau}$, where λ is a constant often referred to as the "rate parameter". The pdfs were fit to exponential pdfs using MATLAB's expdf() function, and the result is shown in Figure 7-11b. Qualitatively, the pdfs of τ_s reveal that as density ratio decreases, longer duration sinusoidal events become increasingly common (an increasingly large fraction of events have large τ_s). Although an exponential distribution provided the best fit to these pdfs (compared to lognormal, Poisson, and normal pdf fits), τ_s and τ_n also correlated well to lognormal distributions. Lognormal behavior of intermittent fluid phenomena is not uncommon. Kolmogorov [75] suggested that the interval between intermittent "bursts" in a turbulent boundary layer is distributed lognormally, a prediction that has also been experimentally observed [76]. Likewise, turbulence intensity in atmospheric boundary layers is distributed log-normally [77]. Intermittency is also present in other aspects of bluff body flows, such as Rai's [78] observations of shear layer amplification rates.

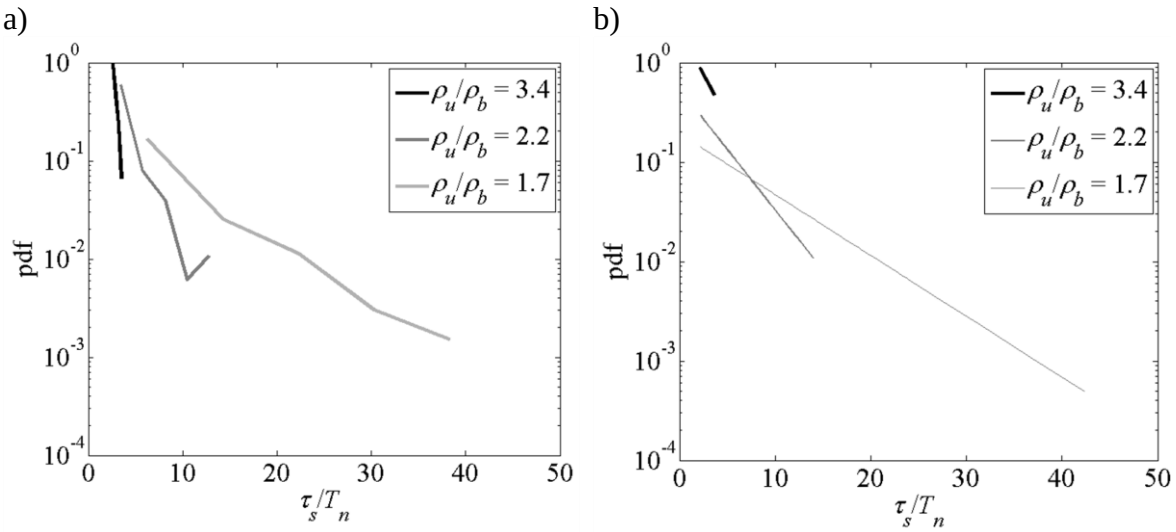

Figure 7-11. pdfs of the duration of sinusoidal bursts for several density ratios, showing a) raw data and b) fits to exponential pdfs.

The average durations of these "sinusoidal" time intervals, $\langle \tau_{s,i} \rangle$, normalized by the limit cycle period, are plotted against density ratio in Figure 7-12 using two different window sizes. This result shows that $\langle \tau_{s,i} \rangle$ increases monotonically with decreasing density ratio. The figure shows that at the lowest density ratios, the average duration of the limit cycling behavior occupies as many as 32 periods of the oscillation (depending on selection of r_t), whereas at higher density ratios this behavior persists, on average, for only 2 or 3 periods (hardly more than the window size). This result shows that as density ratio is decreased, the sinuous, narrowband state becomes present for increased durations of time; i.e., the monotonic dependence on density ratio shown in Figure 7-8 is not due to an increased event rate, but an increased event duration. This becomes evident from Figure 7-13a, which presents the pdfs of the event arrival rates; notice that the mean arrival rate first increases and then decreases as density ratio is decreased. In fact, the event rate for sinusoidal intervals becomes very low at low density ratios. This is

because as density ratio decreases and the signal dwells in a sinusoidal configuration for much longer intervals, the event rate necessarily becomes low. This concept is illustrated in Figure 7-14. The pdf's shown in Figure 7-13 correlate very well to a Poisson distribution, although a true Poisson process describes events of zero duration. The MATLAB function poisspdf() was used to fit the data to Poisson distributions, as shown in Figure 7-13b. A comprehensive review of the intermittency statistics, including many more density ratios, is included in *Appendix C*.

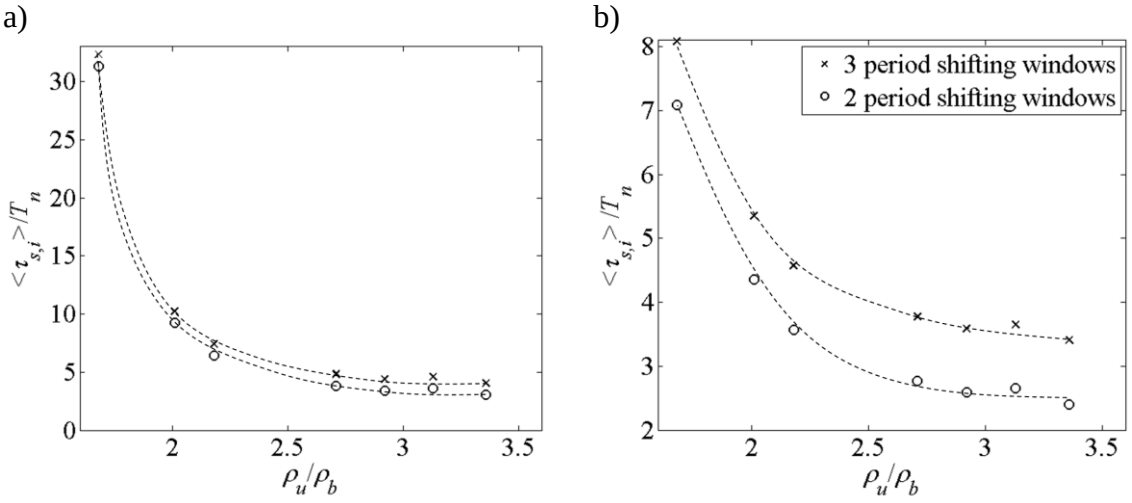

Figure 7-12. Density ratio dependence of $\langle \tau_{s,i} \rangle$ based on a) $r_t = 0.5$ and b) $r_t = 0.8$, at $x/D = 3.5$. Note the different scaling in the axis of ordinates between (a) and (b).

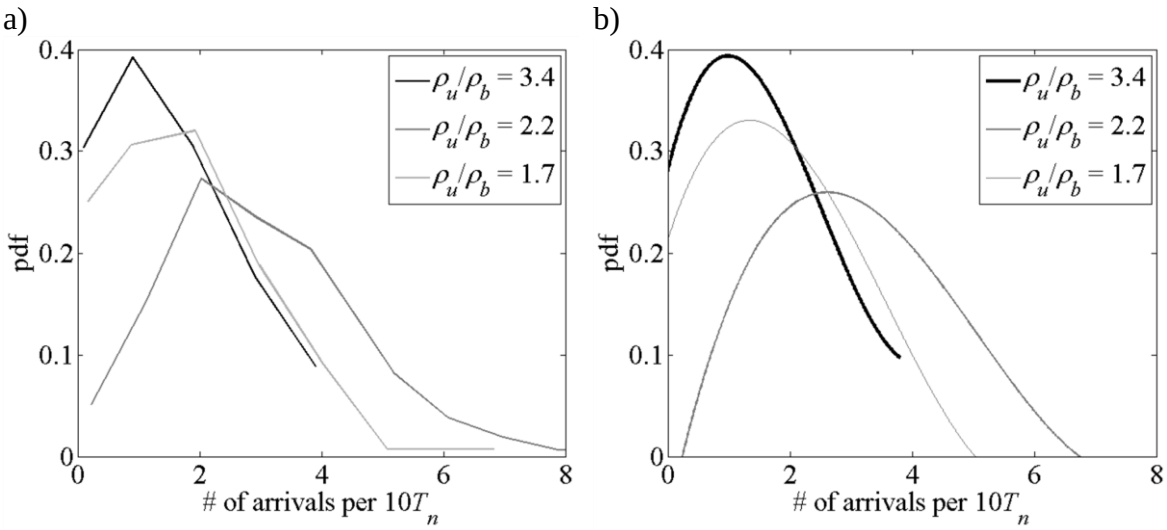

Figure 7-13. Smoothed distributions of the sinusoidal event arrival rate for several density ratios, showing a) raw data and b) fits to Poisson distributions. Data is from the upper flame edge signal for the ballistic bluff body at $U_{lip} = 50$ m/s

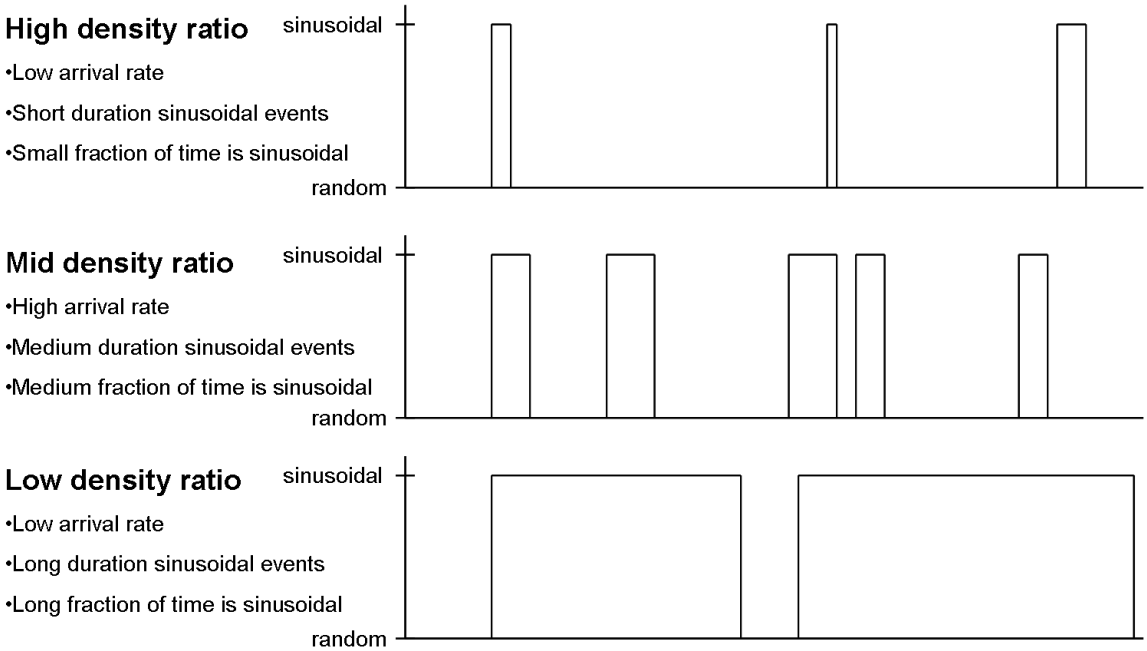

Figure 7-14. Notional chart demonstrating relationship between density ratio and sinusoidal event arrival rate, event duration, and fraction of time that signal is sinusoidal

7.4 Comparison of Intermittency to Local Absolute Growth rate

This section revisits the local stability theory. As alluded to previously, comparison to local stability theory is complicated by the fact that no sharp bifurcation in flow stability actually occurs. In order to compare the stability characteristics of the different geometries and velocities, Figure 7-15 summarizes the data by plotting the maximum $\omega_{0,i}D/(2U_{av})$ for a given test (corresponding to the location of maximum backflow ratio) as a function of the intermittency factor, F. Intermittency factor is quantified here by the fraction of time that $r_f > r_t = 0.5$. The figure shows that there is a good correlation between absolute growth rate and intermittency. Moreover, the slopes of all four data sets are comparable. It is also evident that predicted absolute growth rate values are systematically lower with the ballistic shape than the v-gutter (consistent with the lower backflow ratio for the ballistic shape). These results show that the variation in intermittent characteristics of the flow, namely the intermittency factor, is related to the absolute stability of the base flow.

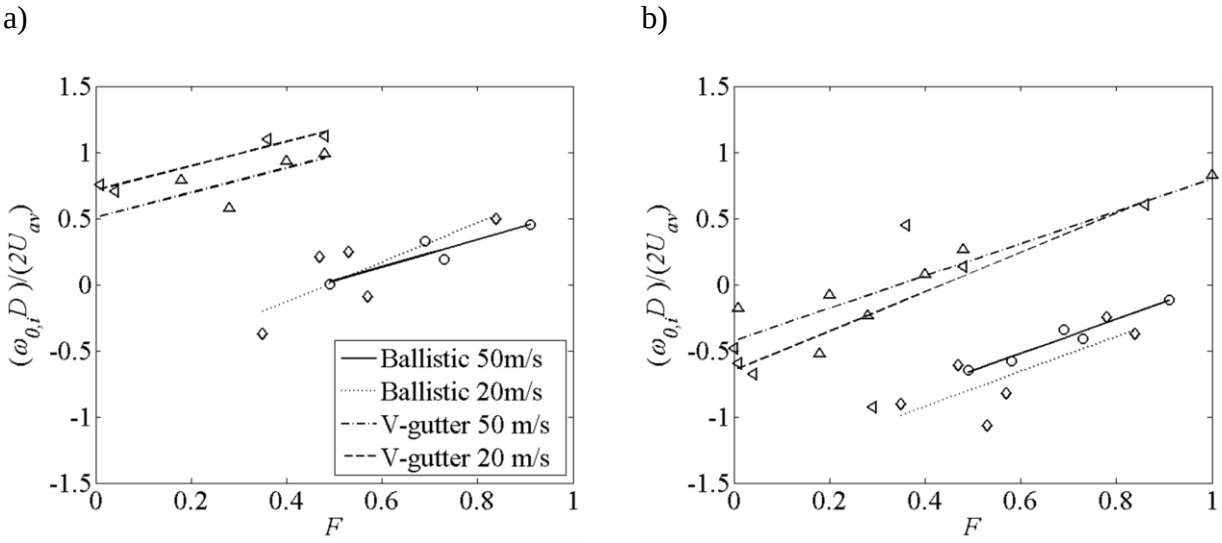

Figure 7-15. Dependence of predicted absolute growth rate upon measured intermittency factor, showing a) detailed result from smoothed data, b) model result from top hat base flow profiles

7.5 Source of intermittency

7.5.1 *General Types of Intermittency*

Intermittent behaviors have been discussed extensively in the context of nonlinear dynamical systems, and may arise from either deterministic or stochastic processes. Hilborn [79] discusses in detail several deterministic sources of intermittency, which include tangent bifurcation intermittency (Type I), Hopf-bifurcation intermittency (Type II), period-doubling intermittency (Type III), and on-off intermittency. For example, the Pomeau-Manneville scenario [80] is a deterministic route to chaos through intermittency; such an intermittency may be present even in a noiseless system.

Stochastic processes associated with either additive or parametric noise may also cause intermittency [81]. For example, consider a bi-stable dynamical system, such as a

system in the vicinity of a subcritical Hopf bifurcation with a stable fixed point and stable limit cycle. In the presence of additive noise, the system may be bumped back and forth between the two stable solutions; the stationary probability density of such a system would have local maxima at values consistent with the locations of the potential wells. For example, Waugh and Juniper [82] demonstrated this phenomenon in the context of the Rijke tube.

Parametric noise can also lead to intermittency in systems with supercritical bifurcations [81]. For example, consider a dynamical system with a single stable solution in the unforced system. Parametric noise can shift the stability boundary, as well as change the number or location of the maxima in the stationary probability density. A qualitative shift in the stationary pdf is thus possible in the context of parametric noise.

7.5.2 *Effects of Additive and Parametric Noise*

The effects of noise may be demonstrated using the Landau equation as a model problem:

$$\frac{dZ}{dt} = \lambda Z - B|Z|^2 Z \tag{7.2}$$

The Landau equation naturally appears in weakly nonlinear stability analyses of wakes [73], and describes the behavior of the complex amplitude Z when the system is in the vicinity of a supercritical Hopf bifurcation. In Eq. (7.2), λ represents how far a stability parameter is from its critical value (for example, how far the Reynolds number or the density ratio is from its value at the onset of vortex shedding), and B is the Landau constant. Eq. (7.2) has an equilibrium point at $Z = 0$ for all λ, which is stable for negative λ. As λ increases past $\lambda = 0$, the $Z = 0$ solution becomes unstable and new

stable solutions appear at $Z = \pm\sqrt{\lambda/B}$. This represents a supercritical Hopf bifurcation, whose bifurcation diagram is shown in Figure 7-16. The following model problem demonstration will consider the case of $Z \in \mathbb{R}$ and $B = 1$.

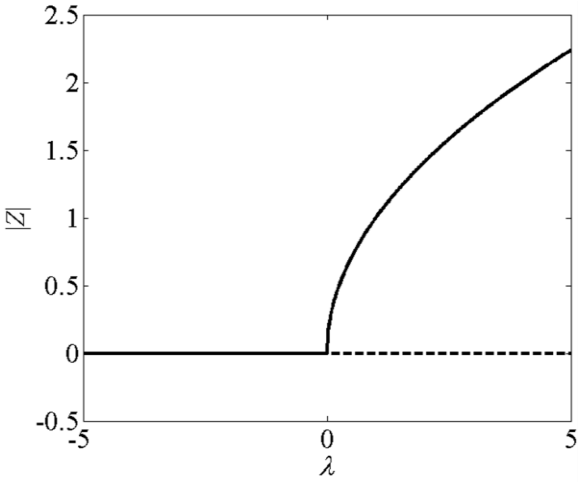

Figure 7-16. Bifurcation diagram showing the supercritical Hopf bifurcation represented by the Landau equation. Solid and dashed lines represent stable and unstable solutions, respectively.

In the presence of noise, the system is stochastic and rather than stable states, it instead has potential wells. The Fokker-Planck equation may be used to find the Stationary pdf of Z, and hence the expected value of Z. Within the framework of Itō calculus, a stochastic differential equation (SDE) may be expressed as

$$dX_t = f\left(X_t\right)dt + \sigma g\left(X_t\right)dW_t \tag{7.3}$$

where X_t is the time-dependent variable of interest, f and g are functions of X_t, σ is the variance of the noise, and W_t represents a Wiener process.

The Landau equation may be subjected to additive white noise and written as an SDE as follows:

$$dZ_t = \left[\lambda Z_t - B\left|Z_t\right|^2 Z_t \right] dt + \sigma dW_t \tag{7.4}$$

Likewise, parametric noise may be added on top of the additive noise, so that the SDE takes the form:

$$dZ_t = \left[\lambda Z_t - B\left|Z_t\right|^2 Z_t \right] dt + \sigma \left[A + Z_t \right] dW_t \tag{7.5}$$

Here, the additive noise is proportional to the constant A, and the parametric noise is proportional to the time-dependent value of Z.

The stationary pdf, P_s, of Eq. (7.3) given by the Fokker Planck equation is:

$$P_s\left(X\right) = Ng^{-1}\left(X\right)\exp\left\{ \frac{2}{\sigma^2}\int_X \frac{f\left(u\right)}{g\left(u\right)}du \right\} \tag{7.6}$$

The stationary pdf for the model with additive noise alone follows from plugging Eq. (7.4) into Eq. (7.3) and applying Eq. (7.6):

$$P_s\left(Z\right) = NZ^{\frac{2\lambda}{\sigma^2}-1}\exp\left\{ -\frac{B}{\sigma^2}A^2 \right\} \tag{7.7}$$

Likewise, the stationary pdf for the model with both additive and multiplicative noise follows from plugging Eq. (7.5) into Eq. (7.3) and applying Eq. (7.6):

$$P_s\left(Z\right) = N\left(Z+A\right)^{\frac{-6A^2B+2\lambda}{\sigma^2}-1}\exp\left\{ \frac{2}{\sigma^2}\left[\frac{A\lambda - A^3B}{Z+A} - \frac{1}{2}B\left(Z+A\right)^2 + 3AB\left(Z+A\right) \right] \right\} \tag{7.8}$$

In Eq. (7.7) and (7.8) N represents the normalizing factor required to satisfy $\int_{-\infty}^{\infty} P_s\left(Z\right)dZ = 1$. The left column of Figure 7-17 shows pdfs of $\left|Z\right|$ under various levels of additive noise. Notice first that the additive noise has the effect of broadening the peak in the pdf. Also, notice what happens when the noise is strong and the limit cycle amplitude is small- there is significant probability density at zero. This is because the

noise extends far enough that the system is being pushed back and forth between opposite phases of its cycle. In the phase plane, it would appear that the noise pushes the system through (or near) the origin, taking a shortcut to the other side of the cycle rather than continuing around at the limit cycle amplitude. Although the system is not bistable, this is somewhat analogous to the bistable system with additive noise that pushes it back and forth between its two potential wells. Finally, note that the peak in the pdf is never moved by the noise. Additive noise, although it may shift the expected value of $|Z|$ (see Figure 7-18a), cannot change the location or number of peaks in the pdf. In other words, additive noise cannot alter the most probable value of $|Z|$.

The right column of Figure 7-17 shows pdfs of $|Z|$ under various levels of parametric noise. A small level of additive noise ($A = 0.1$) has been included to force the system to wander from its stable equilibrium state for negative λ ($Z = 0$ remains a true equilibrium state with the parametric noise alone). The figure show that the parametric noise can have a serious influence on the stationary pdf of $|Z|$. For example, all levels of parametric noise shift the peak in the pdf, altering the most probable value. Furthermore, Figure 7-17d shows that a second peak can be formed in the pdf for $\sigma^2 = 10$, and Figure 7-17e-f show a complete change in the qualitative nature of the pdf for $\sigma^2 = 10$. Figure 7-18b shows the expected value of the system with parametric noise, demonstrating that parametric noise, like additive noise, is capable of "smoothing" the sharp bifurcation that is experienced by the noiseless system.

This section has shown, though, that even very simple sources of parametric noise can cause profound changes in the system behavior. These changes can include qualitative

changes in the stationary probability of the system, which can range from a shift in the most probable state to the creation of new, co-existing most probable states. Parametric noise, therefore, is a prime environment for intermittent behavior, and therefore a plausible source of the behavior of the data shown in Figure 7-10.

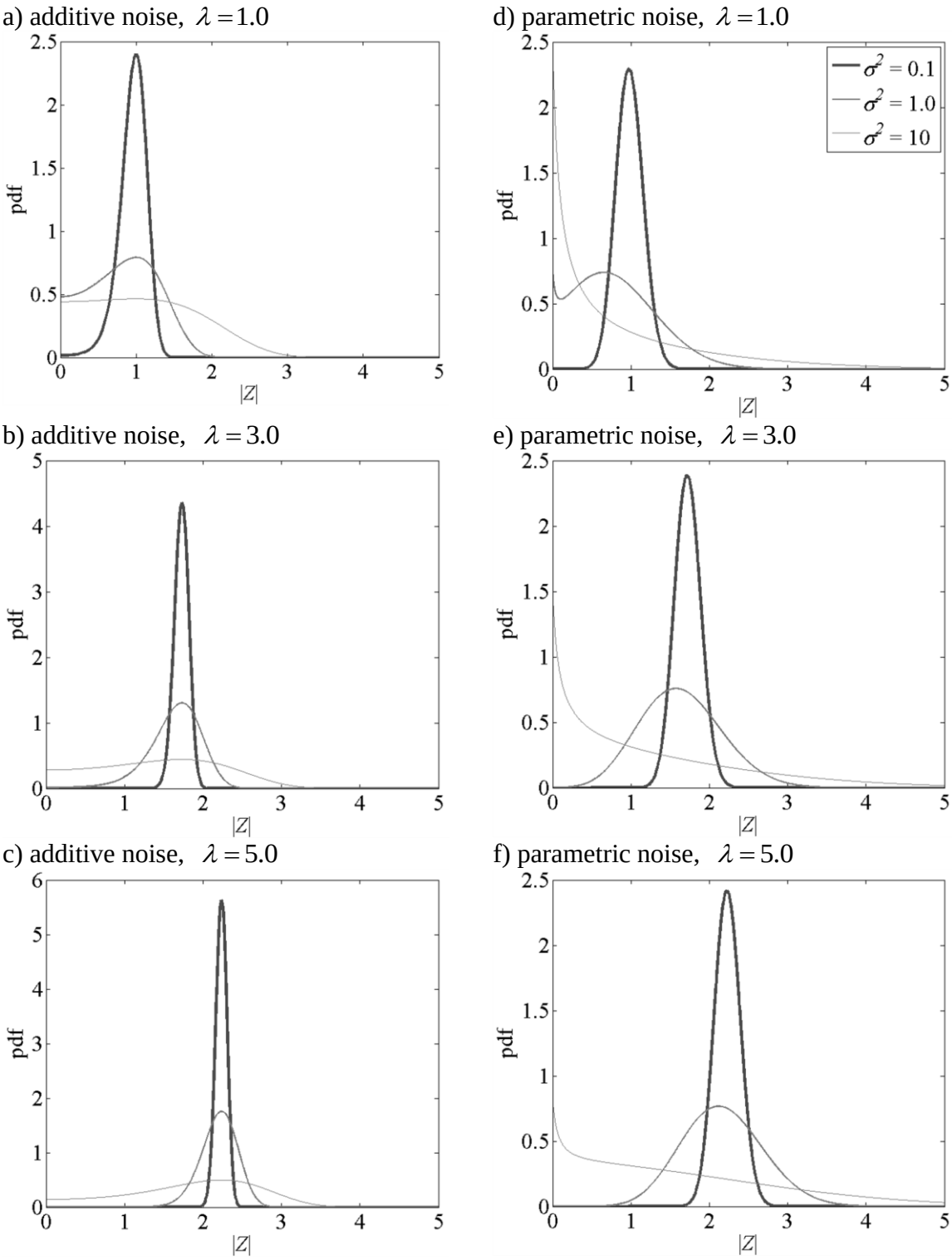

Figure 7-17. Stationary pdfs of the Landau equation subjected to various levels of noise. Left column is for additive noise only, according to Eq. (7.4). Right column is for parametric noise according to Eq. (7.5) with $A = 0.1$. a,d) $\lambda = 1.0$, b,e) $\lambda = 3.0$, c,f) $\lambda = 5.0$.

a) b)

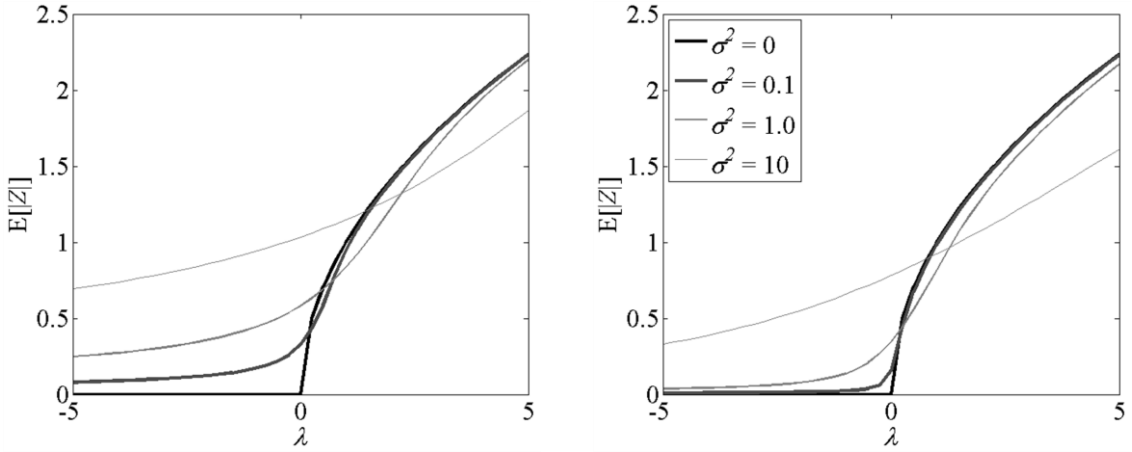

Figure 7-18. Expected value of $|Z|$ for a) additive noise only, according to Eq. (7.4), and b) parametric noise according to Eq. (7.5) with $A = 0.1$

7.5.3 *Intermittency in Low Density Ratio Wakes*

The viscous, iso-density bluff body wake undergoes a super-critical Hopf bifurcation at $\mathrm{Re}_D \approx 35$ [83]. While the author is not aware of theoretical studies that have explored the nature of this bifurcation for non-constant density wakes, analysis of these data suggests that the bifurcation to asymmetric vortex shedding remains supercritical. For example, Figure 7-19 plots the pdf of the amplitude of the flame front oscillations, ζ', obtained from its Hilbert transform, ζ'_H.

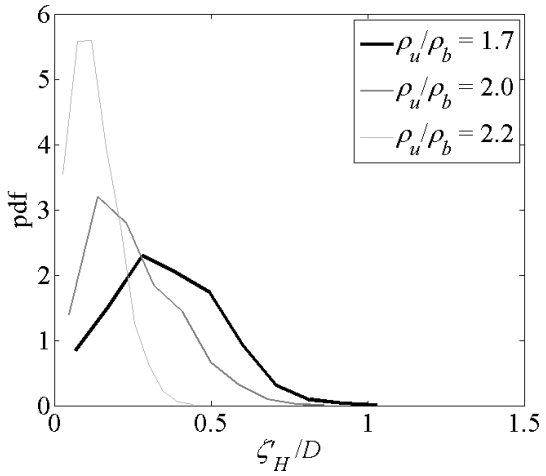

Figure 7-19. Pdf of the envelope of flame edge displacement, shown for several density ratios at $x/D = 4$

This figure does not show any behavior indicative of multiple peaks in the amplitude pdf, which would be suggestive of a bi-stable system. Rather it shows a gradual shift in the peak amplitude to higher values as density ratio is reduced. Thus, these results suggest that the system undergoes a supercritical bifurcation in the presence of parametric background noise. An important remaining question, then, is what is the source of the parametric noise that leads to this intermittent behavior? This section shows next that this is due to random drifts in relative location of the shear layer and flame front.

The influence of the random drift of these two features was illustrated in Chapter 6, *Local Hydrodynamic Stability Analysis*. Recall that the limit cycling behavior was attributed to the hydrodynamic global mode of the wake. The global mode was shown to be generated by a wavemaker region, which is located in the recirculation zone behind the bluff body. Analysis of model stability problems emphasized that the global mode growth rate is highly sensitive to the degree of non-colocation between the density and shear layers, where increased non-colocation of the two layers was shown to be

destabilizing. The sensitivity of the growth rate to this parameter is such that small, relative motion of the shear layer and flame edge within the wave-maker region can lead to stochastic modulation of the global mode amplification rate. For these low density ratio wakes, which are near the hydrodynamic stability limit, this can have the effect of turning the instability off and on.

In order to illustrate this point, Figure 7-20 plots a pdf of the moving average (over a time interval of $3T_n$) of the offset between the flame and the shear layer. The flame edge was obtained by edge-tracking the abrupt change in density in the Mie scattering images, and the shear layer point of inflection was obtained from the PIV measurement. The data for this plot were taken at $x/D = 2.0$, near the peak in absolute growth rate. Two pdfs are presented, one unconditional, and the other conditioned on the value of $r_f > 0.5$ (indicative of periodicity of the flame measurement at the global mode frequency). At this axial position, the mean flame sits inboard of the shear layers (farther downstream, the mean flame propagates outboard of the shear layers). When a high degree of periodicity at the global mode frequency is observed, the flame is preferentially located even farther inboard; i.e., the peak in the pdf of the conditioned offset is more than 50% larger than the unconditioned value. Thus, the most probable offset between the flame and the shear layer is greater when periodic oscillations are observed than the most probable, unconditional offset between these layers.

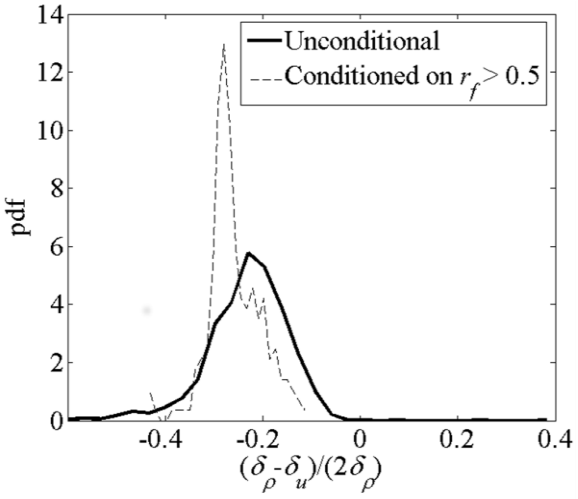

Figure 7-20. Pdf of the unconditioned and conditioned offset between the flame edge and the shear layer.

7.6 Closing Remarks

Chapter 5, *Experimental Results: Unforced Flame and Flow Dynamics* identified a bifurcation in flow structure that occurs as flame density ratio is reduced. This bifurcation manifests itself as the appearance of limit cycling behavior in the flow and flame, characterized by sinuous, narrowband vortex shedding. Spectral techniques identified that the bifurcation in wake structure is not sudden, but very gradual. Using time-local techniques, this chapter showed that in the transitional range of density ratios, the limit cycling behavior is actually highly intermittent in time.

This intermittency was investigated statistically, showing increasing duration of limit cycling events as density ratio is reduced. This leads to an overall greater fraction of time that limit cycling behavior is observed at lower flame density ratios. Several sources of intermittency were discussed, and parametric noise was suggested as the source of this intermittency. The parametric noise source is believed to be the extreme sensitivity of the hydrodynamic instability responsible for the limit cycle behavior to small offsets

between the time averaged flame and shear layer positions, which “breaths” slowly in time. This was supported by showing that the flame-shear layer offset is preferentially large when the limit cycling behavior is strong. This also highlights the important reality that can result from introducing larger Reynolds numbers to sever hydrodynamic sensitivities: small-scale lab burners may simply not capture the phenomena that actually occur in industrial-scale burners.

CHAPTER 8. EXPERIMENTAL RESULTS: FORCED FLAME AND FLOW DYNAMICS

The previous chapters presented an experimental dataset of unforced flame and flow dynamics, and characterization of this flow's hydrodynamics from both experimental and theoretical viewpoints. This chapter discusses a set of experiments conducted with longitudinal acoustic forcing. As discussed in Chapter 3, *Experimental Facility and Design of Experiments*, two main parameters were varied in these experiments: the bluff body lip velocity, and the density ratio. This has the effect of independently varying the global mode frequency and growth rate, respectively. Additionally, for two density ratios, a forcing amplitude sweep was performed. The forcing amplitude, A_f, denotes the ratio of the acoustic particle displacement amplitude to the bluff body diameter. The strongest forcing corresponded to a particle displacement amplitude of 0.5 mm, or $A_f = .02$. A total of 5 forcing amplitudes was used, $A_f = 0, .005, .010, .015,$ and $.020$. Unless otherwise specified, forced results in this thesis correspond to $A_f = .02$.

For chemiluminescence imaging, a few additional tests were performed beyond the test matrix at higher density ratios ($\rho_u/\rho_b = 3.1$ and $\rho_u/\rho_b = 7.0$). These tests could not cover the full range of desired lip velocities, however, because of their low preheat combined with the maximum available air mass flowrate. Such higher density ratio testing was not done for the PIV measurement due to insufficient seed density in the post-flame gases.

To impose an acoustic field allows study of the flame and flow response branches of the combustion instability cycle. This chapter will demonstrate the important interactions

that occur between the forced response and the hydrodynamic global mode oscillations. These interactions will be used to explain the behavior of the forced heat release response of the flame. This behavior includes the important observation that having a longitudinal acoustic mode frequency equal to the natural vortex shedding frequency is not as dangerous as previous notions would suggest- in other words, it does not lead to increased heat release oscillations.

8.1 Forced Response Characteristics: Basic Features

This section briefly introduces the basic forced response characteristics of the flow and flame. Chapter 5, *Experimental Results: Unforced Flame and Flow Dynamics* presented time averaged flow characteristics for the unforced experiments. The effect of forcing on the time averaged flow is minor, and leads to a slight reduction in recirculation zone length. This is consistently observed for all cases, and is illustrated by the streamlines in Figure 8-1. This chapter will therefore focus purely on the dynamics of the forced flame and flow responses.

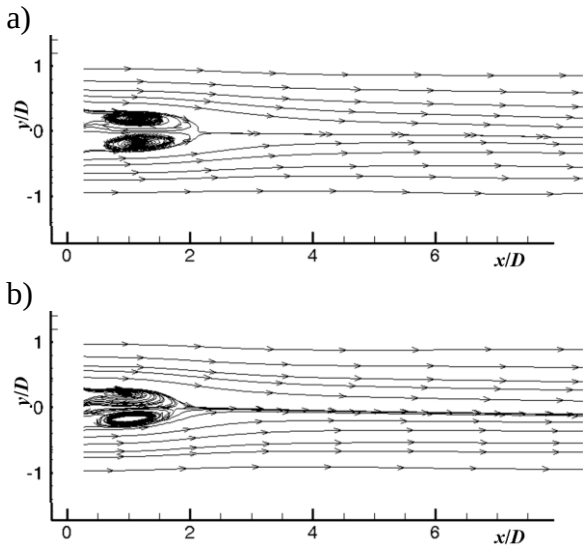

Figure 8-1. Streamlines for $\rho_u/\rho_b = 1.9$, $U_{lip} = 50$ m/s, for a) unforced and b) forced cases

The effect of forcing on the recirculation zone length is summarized in Figure 8-2, which compares L_r between forced and unforced cases for the full range of test conditions measured with PIV. Results from the forced experiments clearly indicate an increase and saturating behavior of the recirculation zone length with bluff body lip velocity. Also, the reduction of recirculation zone length for forced flows is consistently observed over the full range of test conditions. As forcing amplitude is reduced, this effect is diminished. The influence of forcing amplitude on the recirculation zone length is summarized in Figure 8-3 for the two density ratios where forcing amplitude sweeps were performed. The figure emphasizes the reduction of recirculation zone length as forcing amplitude increases.

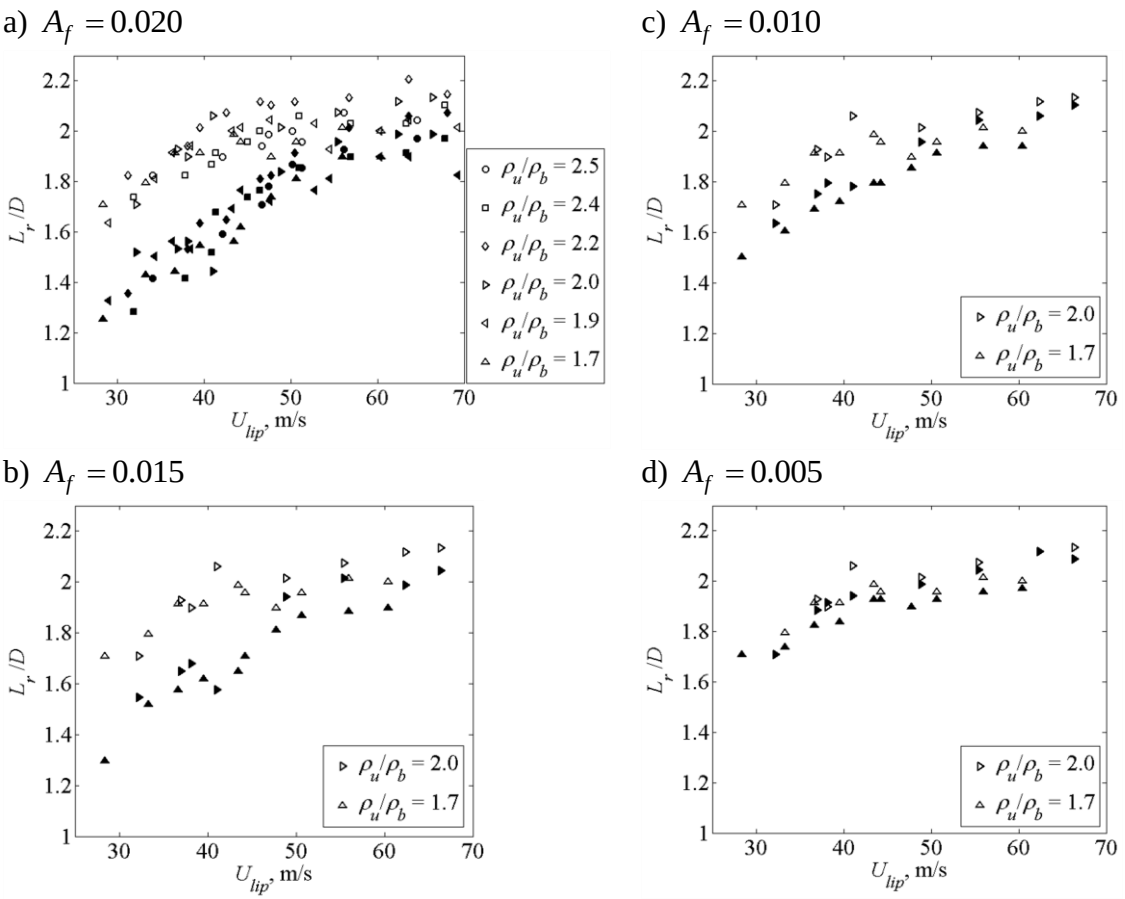

Figure 8-2. Comparison of forced to unforced recirculation zone lengths from PIV measurements of the full range of test conditions. Filled symbols indicated forced flows, unfilled symbols indicated unforced flows. Forcing amplitudes were a) $A_f = 0.020$, b) $A_f = 0.015$, c) $A_f = 0.010$, and d) $A_f = 0.005$

a) b)

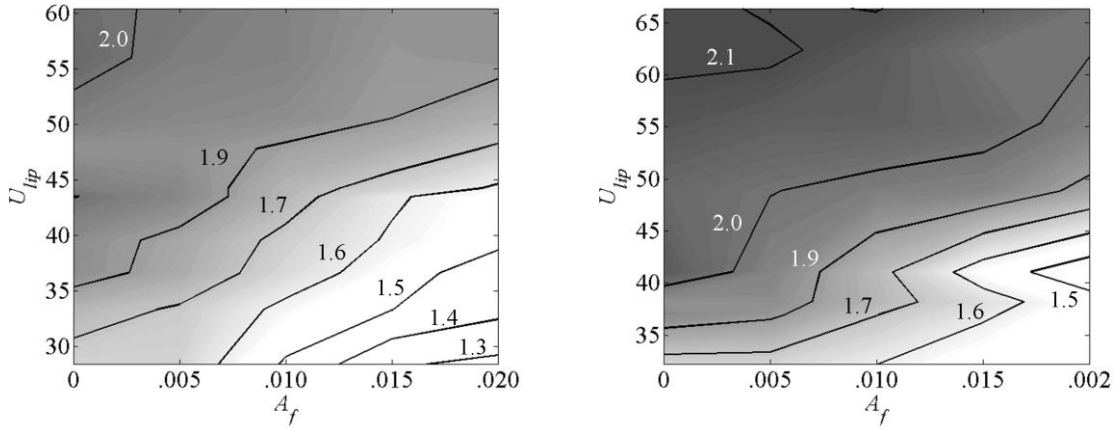

Figure 8-3. Contours of recirculation zone length as a function of forcing amplitude and lip velocity for a) $\rho_u/\rho_b = 1.7$ and b) $\rho_u/\rho_b = 2.0$. Contour levels of L_r/D are labeled on the plots.

External forcing strongly influences the rollup of the separating shear layers and how they subsequently merge and interact to form larger scale structures. In addition, the flame wrinkles in response to the unsteady flow [5, 62, 84]. The change in character of the underlying flow field with density ratio can be clearly seen from the image in Figure 8-4b which shows a forced, globally stable (but convectively unstable) flame; note the manifestation of the symmetric vortices in the flame wrinkling. This is even more pronounced in the forced, un-vitiated ($\rho_u/\rho_b = 7$), flame shown in Figure 8-4a, which would be typical of many non-preheated lab burners. All flame images presented in this chapter have been contrast enhanced for visualization.

The clear change in character of the underlying flow field at $\rho_u/\rho_b = 1.7$ is evident in Figure 8-4f-h, where the flame exhibits a strong sinuous character. As such, low density

ratio flames tend to exhibit an asymmetric structure, even in the presence of symmetric forcing - the vortex staggering mechanism for this is discussed later.

A typical flame edge displacement spectrum for a forced flame is shown in Figure 8-5. Notice that the spectrum has several distinct features. First, note the broad peak at the global mode frequency, $St_D = 0.24$. Next, note the narrowband peak at the forcing frequency, f_f, as well as its harmonics. Many addition flame and velocity spectra are presented in section 8.3, *Forced Response Characteristics: Frequency Effects and Lock-in*.

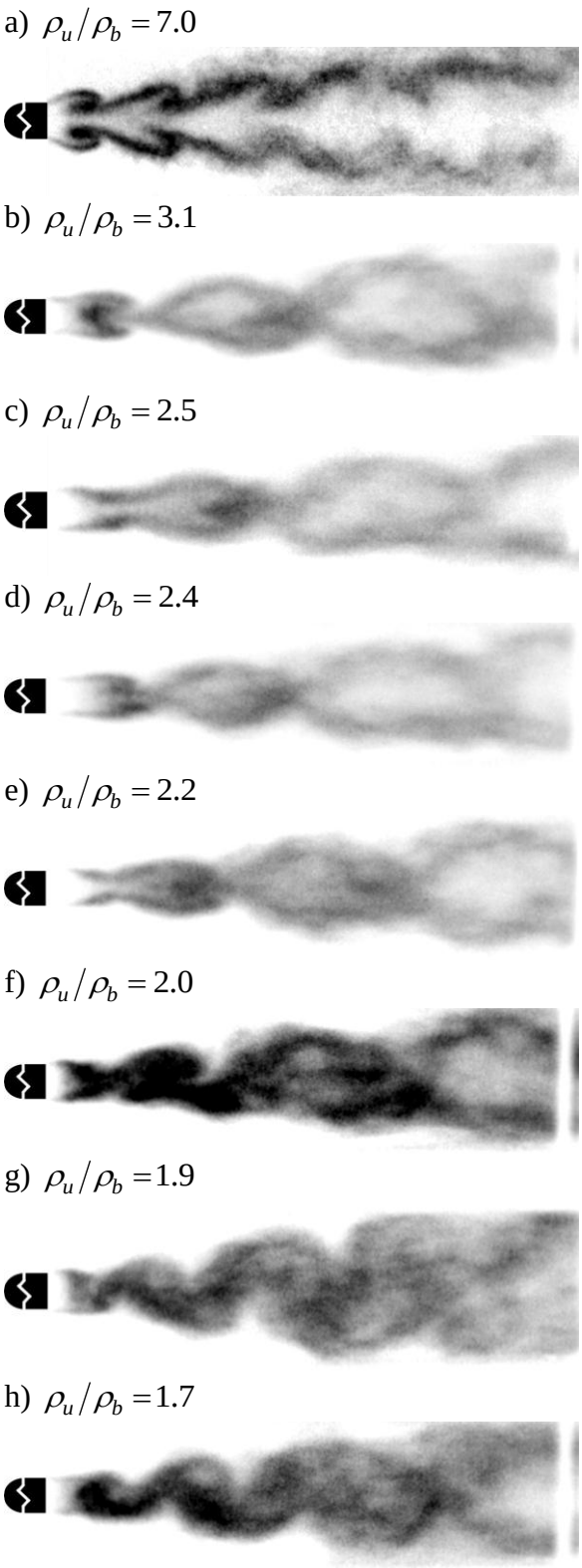

Figure 8-4. Instantaneous chemiluminescence images of forced flames at several density ratios. Density ratios are labeled above each figure.

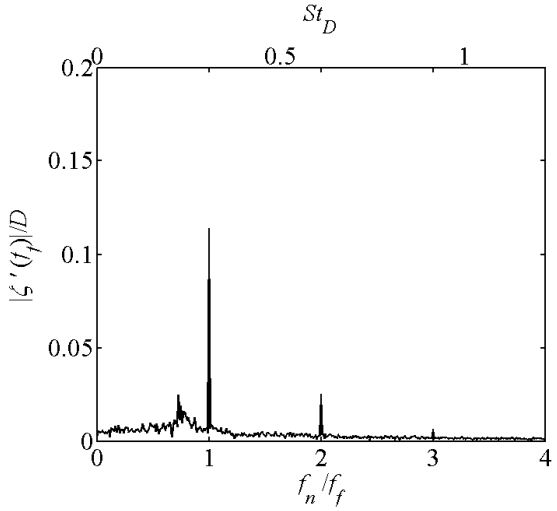

Figure 8-5. Forced flame edge displacement spectrum at $x/D = 3$, $f_n/f_f = 0.8$, $\rho_u/\rho_b = 1.9$

8.2 Forced Response Characteristics: Linear Receptivity to Forcing

Chapter 6, *Local Hydrodynamic Stability Analysis* introduced a linear stability analysis methodology which was shown to successfully capture global stability characteristics. This section extends the linear stability analysis to a spatial stability analysis, and compares the results to the forced flow response measurements. As discussed in Chapter 2, *Background and Motivation*, the spatial stability analysis is performed by solving the hydrodynamic dispersion relation with a known pure real frequency, ω_r, to find the corresponding complex wavenumber, k, and mode shape. The real component of the complex wavenumber gives the axial flow disturbance wavelength, and the imaginary component gives the spatial growth rate. These quantities describe the spatial evolution of a disturbance oscillating at the imposed frequency, ω_r. This solution process is repeated at all axial positions, resulting in a wavenumber dependent on axial position, as

well as complex transverse mode shapes (e.g. $\hat{v}$ for transverse velocity) at each axial position.

Once the spatial stability analysis has been performed at all axial positions, the forced response is reconstructed using the WKBJ approximation. For example, for the spatial stability analysis of transverse velocity fluctuations, this is:

$$v(x,y,t) = \hat{v}(x,y)\exp\left\{-i\left[\omega_r t - \int_0^x k(\xi)\,d\xi\right]\right\} \tag{8.1}$$

where $\hat{v}$ and k are obtained from the dispersion relation for $\omega = \omega_r$. The magnitude of Eq. (8.1) provides an envelope of the forced response magnitude.

The measured transverse velocity magnitude at the forcing frequency is compared to the linear stability result in Figure 8-6 for several density ratios. As shown by the adjoint global mode in Figure 6-8c of Chapter 6, *Local Hydrodynamic Stability Analysis*, the flow is most sensitive to axial velocity forcing in the shear layers, very close to the bluff body trailing edge. This is in contrast to the global mode, which was shown to have its greatest structural sensitivity (and therefore its wavemaker) in the recirculation zone [19]. Unfortunately, for application to spatial stability analysis, the PIV spatial resolution is not fine enough to resolve the thin shear layer near the trailing edge. Therefore, the base flow approximation was interpolated from the 50 m/s LDV measurements at the bluff body lip (discussed in Chapter 5, *Experimental Results: Unforced Flame and Flow Dynamics*), to the PIV measurement at $x/D = 1.0$. Downstream of this location, the PIV data was used. To compare the spatial growth characteristics, the linear stability curve amplitude is matched to the experimental measurement at $x/D = 0$. Note that the agreement is good for small amplitudes, and for high density ratios. Agreement is likely

poor at low density ratios due to nonlinear exchange of energy between the global mode and the forced response, which is discussed later in section 8.4, *Bicoherence*.

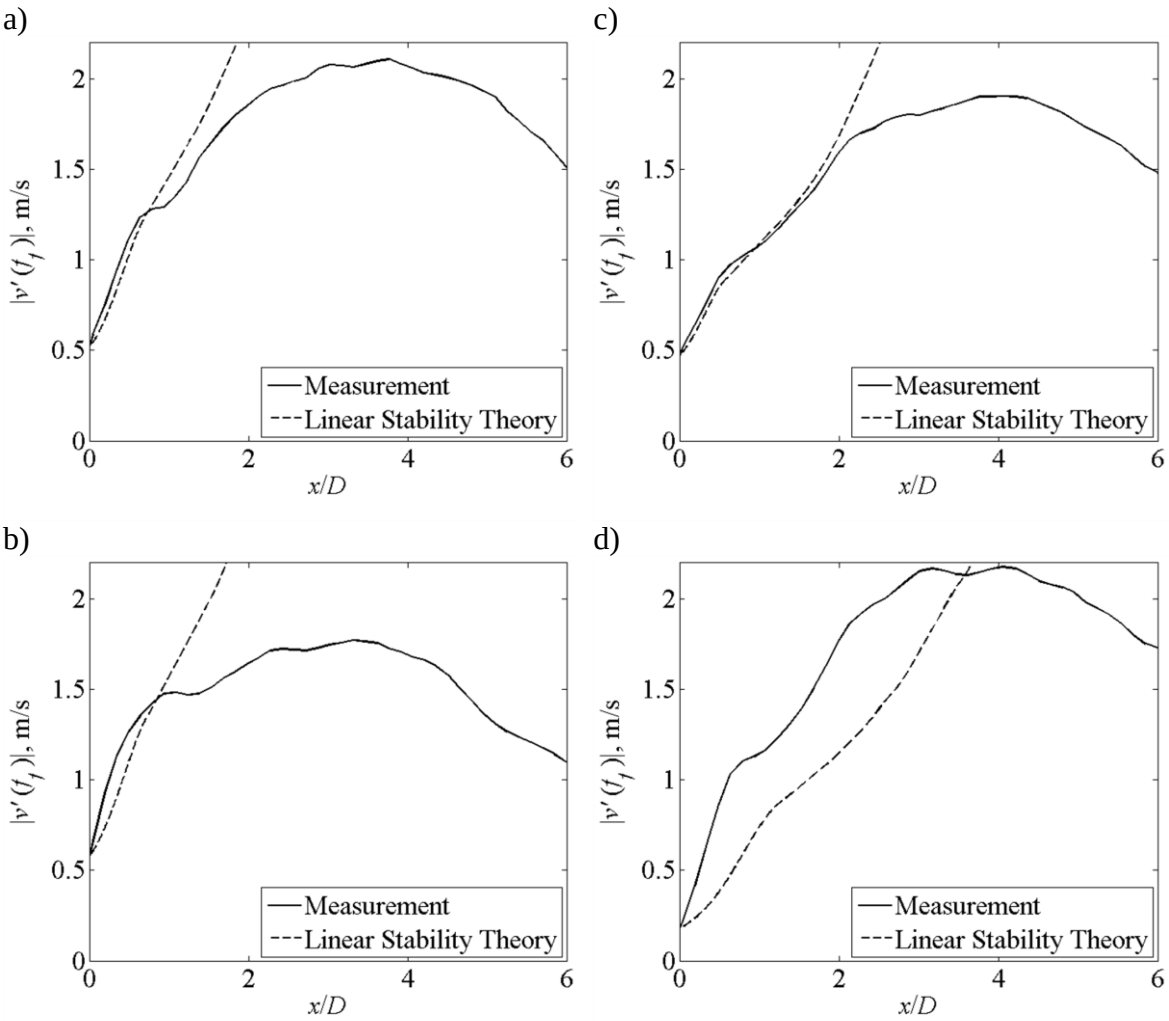

Figure 8-6. Comparison of linear spatial stability analysis to measured transverse velocity fluctuations at $y/D = 0.6$, $A_f = 0.02$, and a) $\rho_u/\rho_b = 2.5$, b) $\rho_u/\rho_b = 2.4$, c) $\rho_u/\rho_b = 2.2$, d) $\rho_u/\rho_b = 1.9$

8.3 Forced Response Characteristics: Frequency Effects and Lock-in

Section 8.1, *Forced Response Characteristics: Basic Features* demonstrated the significant difference in topology of the forced flame response in low and high density

ratio cases. This section further explores the processes leading to these differences, as well as the important role that forcing frequency and amplitude play in these results.

Figure 8-7 through Figure 8-11 present flame and flow spectra where the global mode frequency is swept from $f_n/f_f = 0.8$ to $f_n/f_f = 1.5$. Data from the many cases not shown here are presented in *Appendix D*. Each figure from Figure 8-7 to Figure 8-10 shows a different density ratio, with strong forcing of $A_f = .02$. Figure 8-11 shows a low density ratio ($\rho_u/\rho_b = 1.7$) case with weak forcing ($A_f = .001$), which combines the strongest global mode with the weakest forcing.

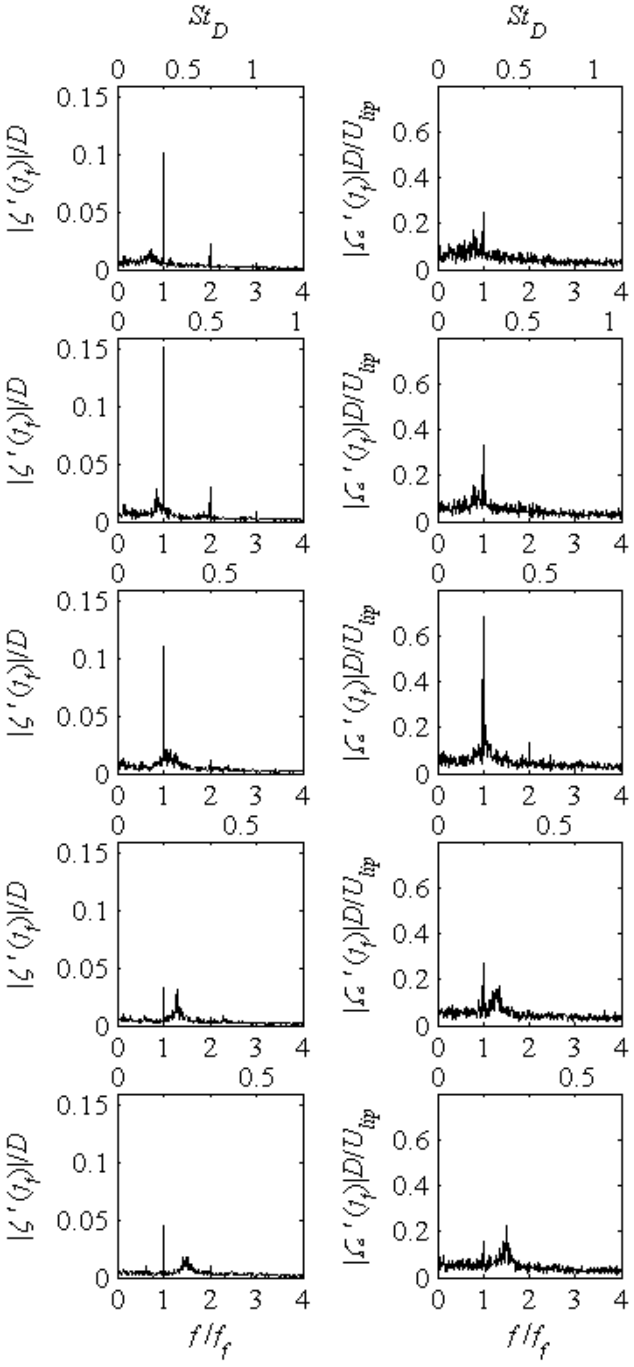

Figure 8-7. Flame displacement (left column) and vorticity (right column) spectra as f_n/f_f is swept through values 0.8, 0.9, 1.1, 1.3, and 1.5 (top to bottom). Conditions are $\rho_u/\rho_b = 1.7$, $A_f = 0.02$, $x/D = 3$.

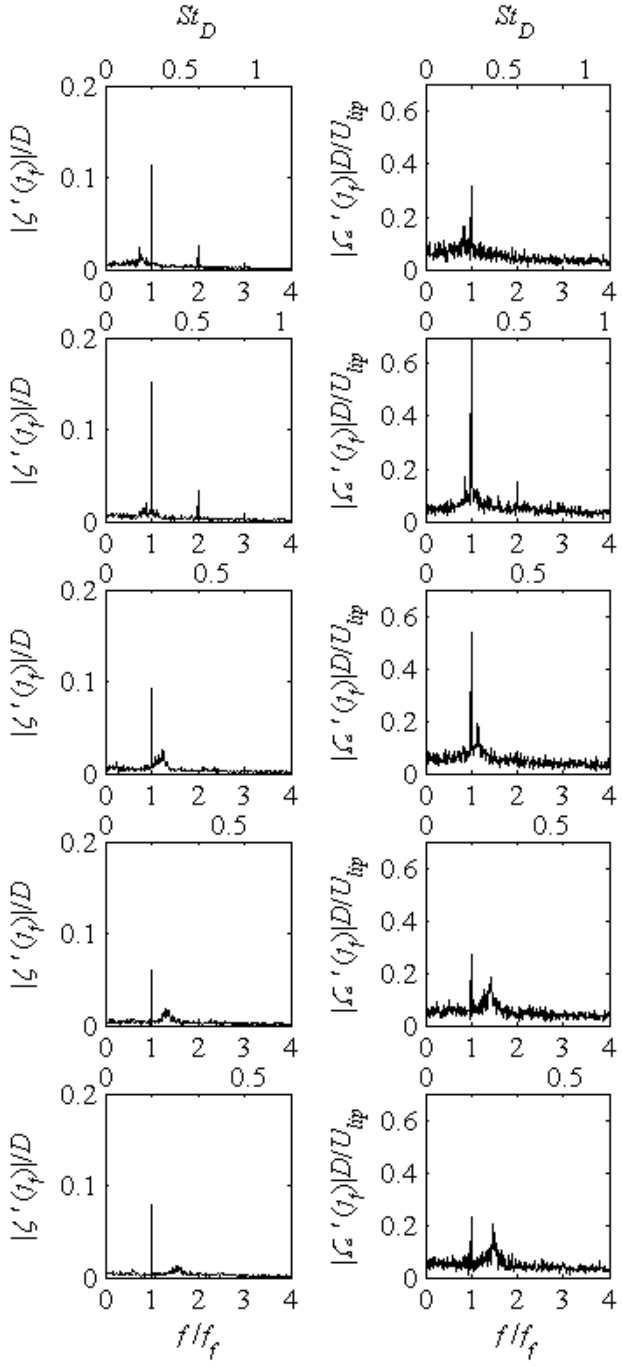

Figure 8-8. Flame displacement (left column) and vorticity (right column) spectra as f_n/f_f is swept through values 0.8, 0.9, 1.1, 1.3, and 1.5 (top to bottom). Conditions are $\rho_u/\rho_b = 1.9$, $A_f = 0.02$, $x/D = 3$.

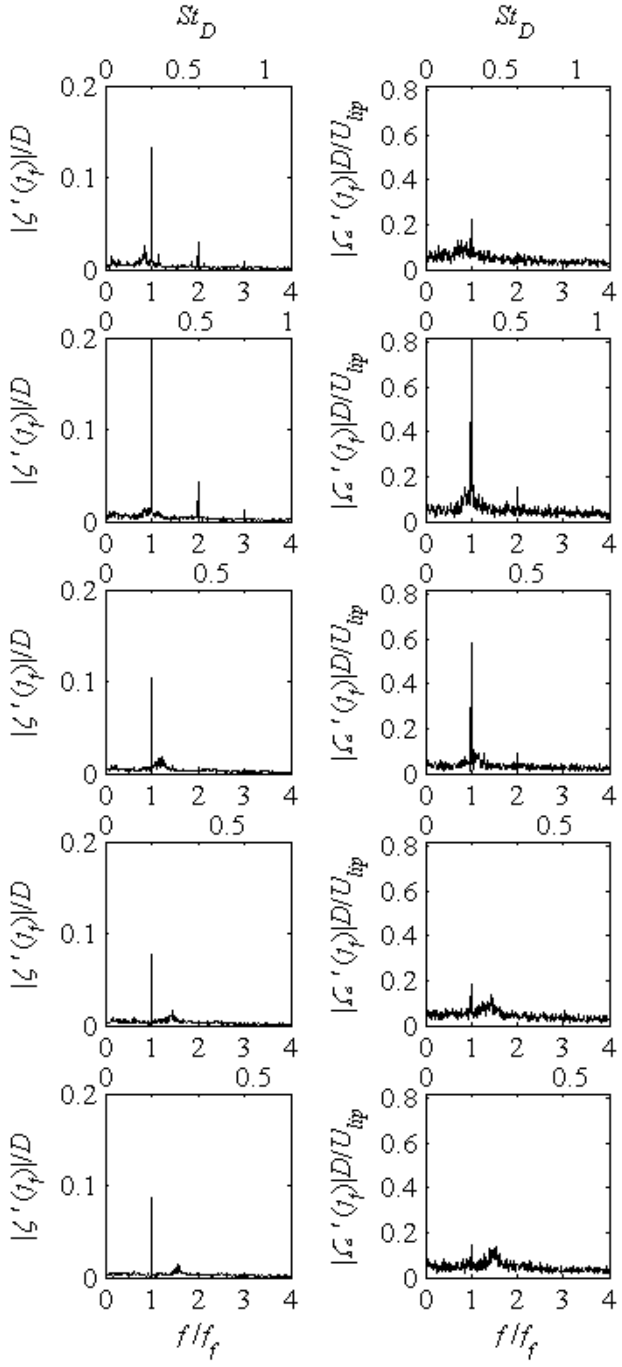

Figure 8-9. Flame displacement (left column) and vorticity (right column) spectra as f_n/f_f is swept through values 0.8, 0.9, 1.1, 1.3, and 1.5 (top to bottom). Conditions are $\rho_u/\rho_b = 2.0$, $A_f = 0.02$, $x/D = 3$.

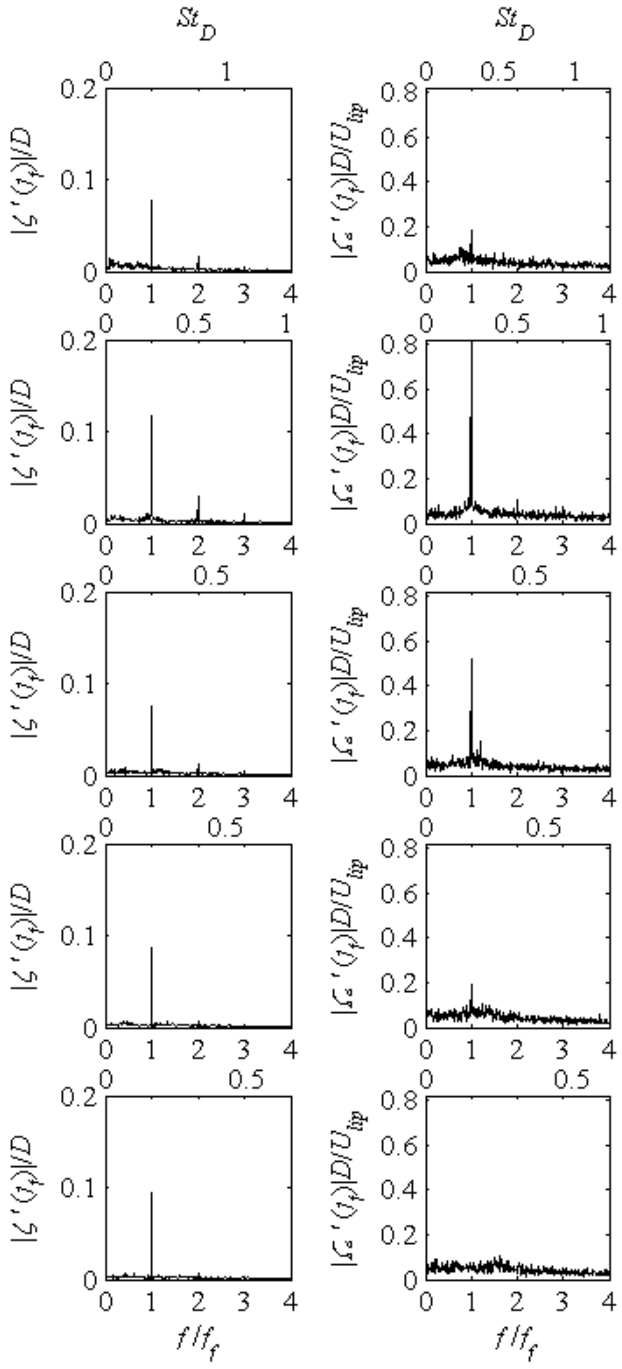

Figure 8-10. Flame displacement (left column) and vorticity (right column) spectra as f_n/f_f is swept through values 0.8, 0.9, 1.1, 1.3, and 1.5 (top to bottom). Conditions are $\rho_u/\rho_b = 2.4$, $A_f = 0.02$, $x/D = 3$.

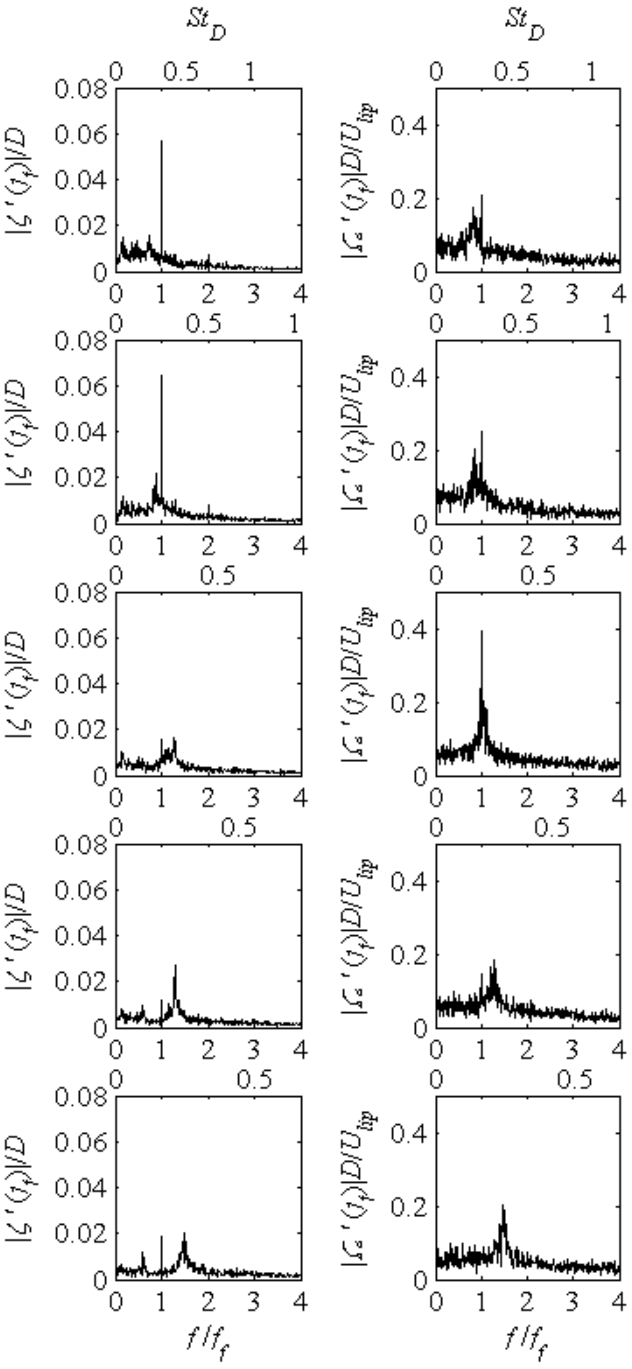

Figure 8-11. Flame displacement (left column) and vorticity (right column) spectra as f_n/f_f is swept through values 0.8, 0.9, 1.1, 1.3, and 1.5 (top to bottom). Conditions are $\rho_u/\rho_b = 1.7$, $A_f = 0.005$, $x/D = 3$.

In the figures above, notice the evolution of the broad peak at $St_D \sim 0.24$ and how it is subsumed by the peak at the forcing frequency. Although the peak at the forcing frequency is taller than the hump about the natural frequency, the broad natural flow response often contains significantly more integrated spectral energy than the narrowband forced response. The relative energy of the forced and natural motions can be quantitatively compared by their root mean square, rms, values, using Parseval's theorem. This expression relates the rms of the time series $s(t)$ of duration T and spectrum $\hat{s}(f)$:

$$s_{rms} = \sqrt{\frac{1}{T}\int_{f^-}^{f^+} |\hat{s}(f)|^2 df} \tag{8.2}$$

The data acquisition parameters were set up such that a frequency bin is located exactly at the forcing frequency, so that $s_{rms} = \left|\hat{s}\left(f = f_f\right)\right| / \sqrt{2}$. The rms of the natural response was obtained by setting the lower and upper integration limits at Strouhal numbers of 0.20 and 0.28. The response frequency, f_r, is defined here as the frequency corresponding to the motions with larger rms values.

Results from a frequency sweep are summarized in Figure 8-12, which shows a lock-in map as quantified by the centerline vorticity. Points lying along the diagonal, $f_r / f_f = f_n / f_f$, line correspond to conditions where the dominant response is at the global mode frequency. Points lying at $f_r / f_f = 1$ line correspond to conditions where the response is locked into the excitation. Figure 8-12b defines the range of frequencies, Δf_{Lock}, over which frequency locking was observed. Lock-in maps from the remaining test cases are presented in *Appendix D*.

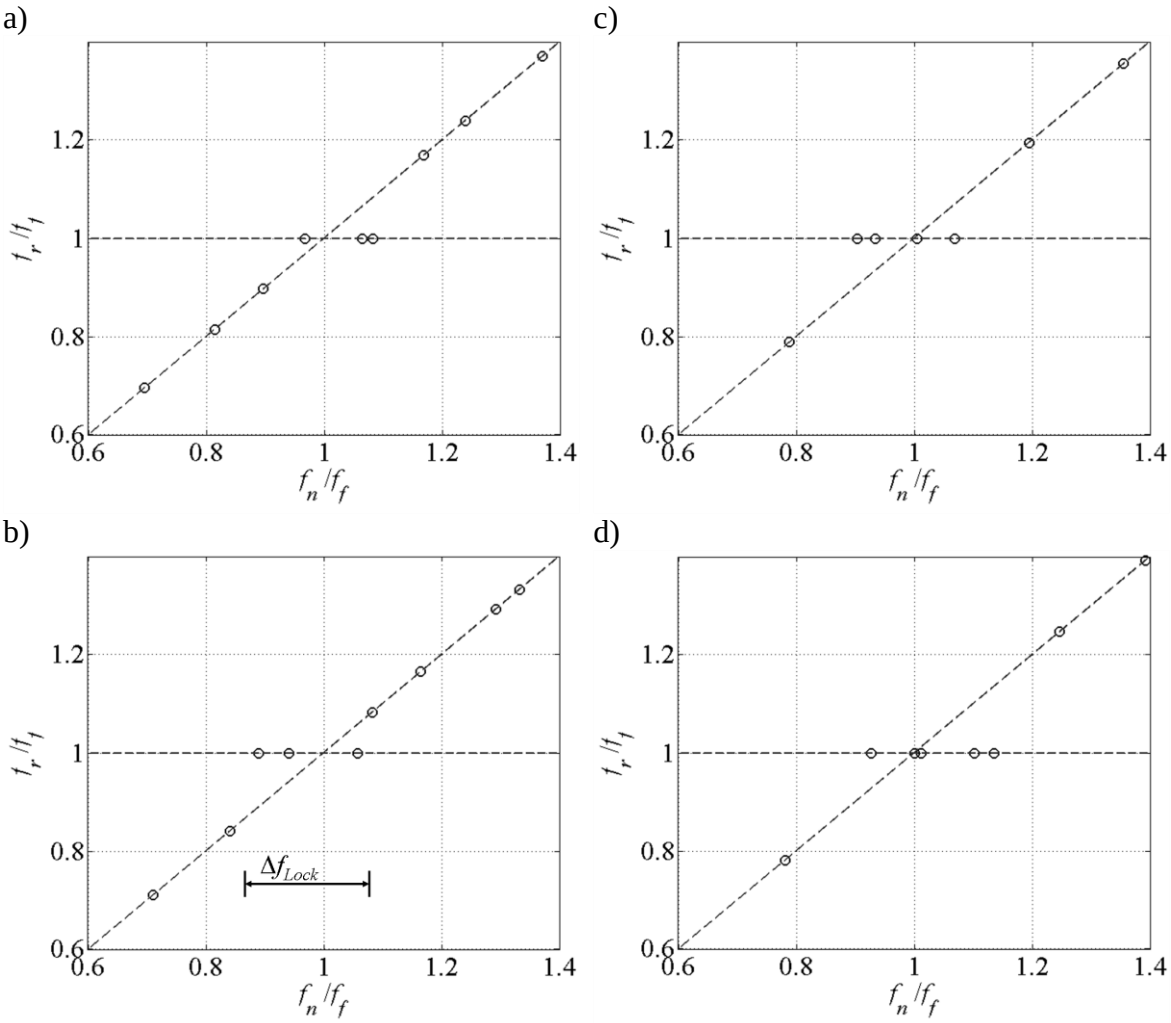

Figure 8-12. Lock-in map from centerline vorticity measured at $x/D = 3$ and $A_f = 0.02$, for a) $\rho_u/\rho_b = 1.7$, b) $\rho_u/\rho_b = 1.9$, c) $\rho_u/\rho_b = 2.0$, d) $\rho_u/\rho_b = 2.4$

As discussed in the background section, the frequency locking range, Δf_{Lock}, is sensitive to the forcing amplitude. This is demonstrated in Figure 8-13a, which plots Δf_{Lock} as a function of A_f. Notice that Δf_{Lock} varies significantly with forcing amplitude, and that a saturating behavior appears at high forcing amplitudes. Also, notice

that Δf_{Lock} appears to be sensitive to density ratio; at $\rho_u/\rho_b = 1.7$, frequency locking is not observed without significant forcing amplitude. The dependence of Δf_{Lock} on ρ_u/ρ_b is quantified in Figure 8-13b, which shows that low density ratios have a narrower frequency locking range. This is expected, and it reinforces the idea that the more globally unstable flow, $\rho_u/\rho_b = 1.7$, is less receptive to external forcing. Hence, higher density ratio wakes are receptive to forcing over a greater range of forcing frequencies.

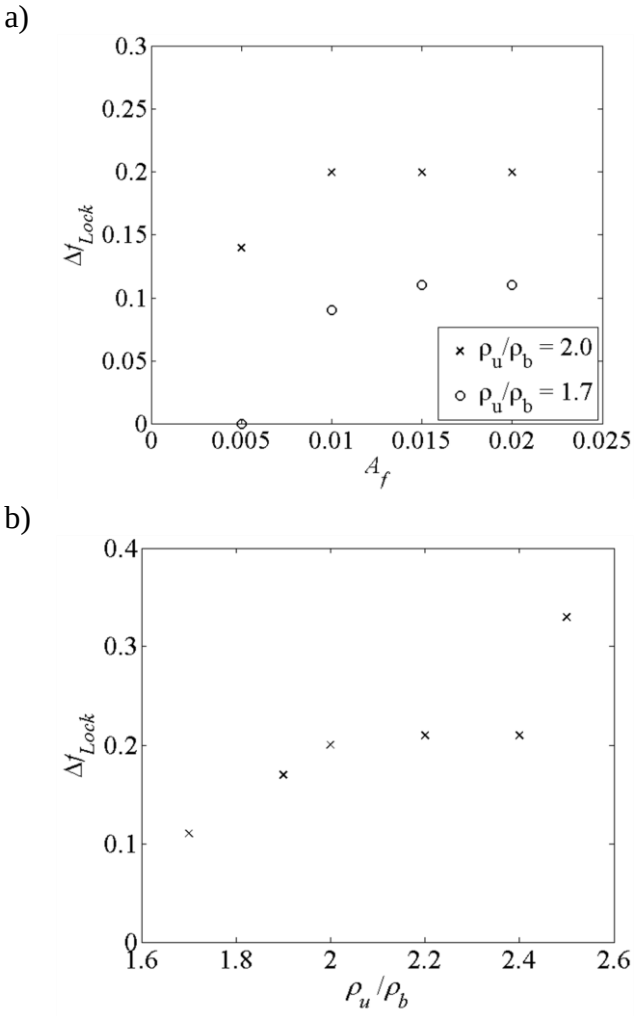

Figure 8-13. Dependence of the frequency locking range on a) forcing amplitude and b) density ratio for $A_f = 0.02$.

8.4 Bicoherence

The previous section showed spectra that exhibit bimodal character, with oscillations at both the global mode and forcing frequencies. Spectra cannot indicate whether the origin of this bimodal behavior is nonlinear, or due to linear superposition of oscillations at the two frequencies. Furthermore, Chapter 7, *Intermittency of Limit Cycle Events* identified intermittent appearance of the global mode. Therefore, if the bimodal behavior is nonlinear, its origin requires further clarification: is it a random switching between global mode oscillation and convectively unstable amplification of the forcing, or is there phase coupling between the forced and global mode oscillations? Higher order spectra can shed light on this issue by identifying phase-coupled, nonlinear interactions between oscillators at different frequencies.

For example, the third order cumulant spectrum, or bispectrum, is defined as:

$$C_3(\omega_1,\omega_2)=\sum_{\tau_1=-\infty}^{\infty}\sum_{\tau_2=-\infty}^{\infty}c_3(\tau_1,\tau_2)\exp\left(-i\left(\omega_1\tau_1+\omega_2\tau_2\right)\right) \tag{8.3}$$

where c_3 is the third order cumulant of a time signal, $s(t)$, and C_3 is its bispectrum. Analyses of the finite duration datasets discussed in this thesis provide an estimation of C_3, and would benefit from a window function applied to c_3. The bispectrum may equivalently be obtained from the FFTs of many ensembles of the signal [85]. This method was used due to its significantly reduced computational expense, so that the bispectrum applied to the discrete datasets studied here is defined as:

$$\hat{B}(f_1,f_2)=\frac{1}{N}\sum_{n=1}^{N}\hat{s}_n(f_1)\hat{s}_n(f_2)\hat{s}_n^*(f_1+f_2) \tag{8.4}$$

Here, $\hat{s}_n(f)$ is the complex Fourier coefficient of the FFT of the n^{th} ensemble of time signal $s(t)$, and $\hat{s}_n^*(f)$ is its complex conjugate. The bispectrum magnitude is significant and nonzero for frequency pairs where quadratic phase coupling occurs between harmonic oscillations at the two paired frequencies [86]. Some intuition for this can be gained from inspecting Eq. (8.4). First, consider the phase differences between $\hat{s}_n(f)$ at f_1, f_2, and $f_1 + f_2$. Observe that the ensemble average operation in Eq. (8.4) drives the magnitude of $\hat{B}$ towards zero if the phase differences vary randomly between $0°$ and $360°$ from ensemble to ensemble. Secondly, notice that this phase coupling is identified between two frequencies and their sum frequency, a necessary attribute of a quadratic nonlinearity. This quadratic phase coupling would not occur for either superposition of, or random switching between, two simple harmonic oscillators.

Like any truncated statistical measure, the bispectrum estimation has variance, and its variance is a strong function of f_1 and f_2. Unfortunately, this variance is large where the bispectrum magnitude tends to be large: at frequency pairs where either $|\hat{s}(f_1)|$, $|\hat{s}(f_2)|$, or both are large, and at frequency pairs harmonically related to peaks in the power spectrum. The variance of the bispectrum estimation is proportional to $p(f_1)\,p(f_2)\,p(f_1+f_2)$ [87], where $p(f)$ is the power spectrum estimation defined as

$$p(f) = \frac{1}{N}\sum_{n=1}^{N} \hat{s}_n(f)\,\hat{s}_n^*(f). \tag{8.5}$$

The bicoherence leverages this proportionality to normalize the bispectrum and provide a more useful measure, and can be defined as

$$b^2(f_1, f_2) = \frac{\hat{B}(f_1, f_2)\hat{B}^*(f_1, f_2)}{p(f_1)p(f_2)p(f_1 + f_2)} \tag{8.6}$$

where b^2 is the squared bicoherence, simply referred to from here on as the bicoherence. Note that there are several accepted definitions of bicoherence, stemming from different normalizations of the bispectrum. Eq. (8.6) essentially provides a measure of skewness of the bispectrum magnitude, and is used by the Higher Order Spectra Toolbox for Matlab [88], HOSA, which was used to compute the bicoherencies in this thesis. For the current work, the HOSA toolbox was used with ensemble lengths (and FFT lengths) of 1000 samples, 99% overlap between ensembles, and Hanning windows. In addition to the ensemble averaging inherent to the bispectrum estimation, the bicoherence was spatially ensemble averaged over 11 points within the region $x/D = 3 \pm 0.1$.

Sample "cuts" of bicoherence of flame edge displacement are shown for an amplitude sweep at low density ratio in the left column of Figure 8-14. These cuts are performed so that one frequency is fixed at the forcing frequency, and the other remains an independent variable. Thus, these plots identify the frequencies with the strongest quadratic phase coupling to the forcing frequency. Notice that the bicoherence is noisy despite the significant ensemble averaging. At higher density ratios, its signal to noise prohibits interpretation.

The left column of Figure 8-14 shows bicoherence, and the right column shows the corresponding spectra (with the same ensemble averaging). Notice from the spectra that this is a bimodal case, with significant response at both the forcing and global mode frequencies. At the lowest forcing amplitude, $A_f = .005$, the spectrum shows response only at these two frequencies and a very faint bump at their sum frequency ($f_n + f_f$), and

the bispectrum shows a response only at the frequency pairing $\left(f_n, f_f\right)$. This suggests that the responses at f_n and f_f are related through quadratic phase-coupling. At $A_f = .01$, the first harmonic of the forcing frequency ($2f_f$) appears in the spectrum, and at $A_f = .02$, its response becomes more prominent. Likewise, there is a growth of the bicoherence at $\left(f_f, f_f\right)$ as forcing amplitude is increased. This suggests that the forced response itself has become strong enough to exhibit quadratic nonlinearity. As forcing amplitude increases, the growth of bicoherence between the forcing frequency and other harmonically relevant frequencies further highlights the complicated, phase coupled nonlinearity that is present during this bimodal behavior.

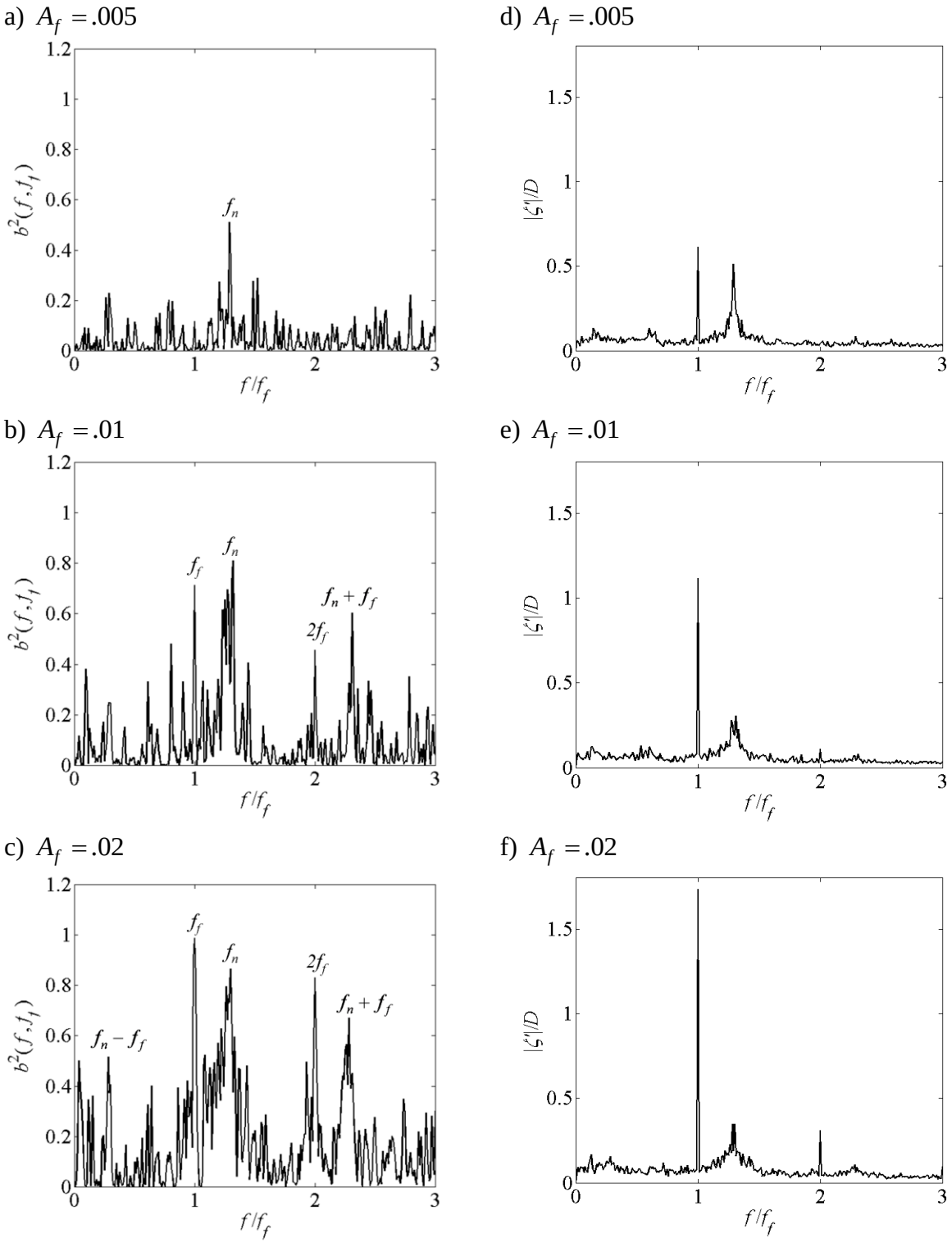

Figure 8-14. Bicoherence (left column) and corresponding spectra (right column) for flame edge displacement during forcing amplitude sweep, at $x/D = 3$, $\rho_u/\rho_b = 1.7$, and $f_n/f_f = 1.25$. Forcing amplitudes are labeled above plots.

A low amplitude frequency sweep is shown in Figure 8-15, again with bicoherence in the left column and spectra in the right column. At all three values of f_n/f_f, there is significant bicoherence at $\left(f_n, f_f\right)$. This continues to show that the responses at f_n and f_f interact through nonlinear phase coupling. Notice, however, that when f_n and f_f are close ($f_n/f_f = 0.8$ and $f_n/f_f = 1.2$), the response in the spectra at f_f becomes strong (strong enough to generate its first harmonic), while the response in the spectra at f_n is weak. Thus, close to frequency locking, there is a strengthening of the forced response at the expense of the natural response in the presence of strong bicoherence. This suggests that frequency locking is associated with a transport of energy between the two responses through quadratic, and probably higher order, nonlinear coupling.

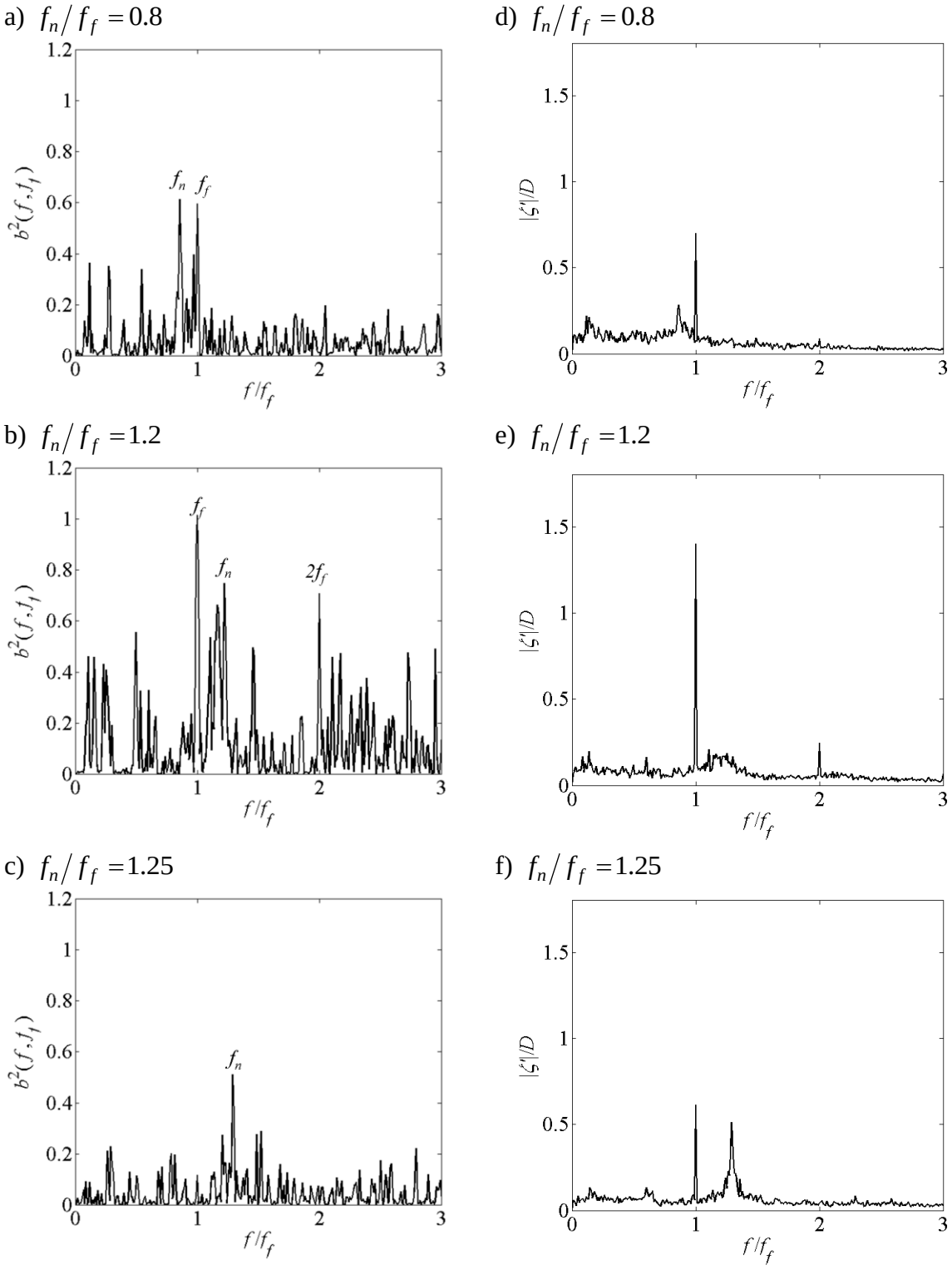

Figure 8-15. Bicoherence (left column) and corresponding spectra (right column) for flame edge displacement during f_n/f_f sweep, at $x/D = 3$, $\rho_u/\rho_b = 1.7$, and $A_f = .001$. Values of f_n/f_f are labeled above plots.

8.5 Forced Response Characteristics: Lock-in Effects Upon Flow Topology

Given that the flow is forced longitudinally, this boundary condition forces symmetric oscillatory conditions at the upper and lower separation points of the bluff body. Frequency locking manifests itself in a fundamental change in the way that vortices in the upper and lower side of the flow are arranged relative to each other.

The two shear layers roll up initially into larger structures that are symmetrically placed on the upper and lower half of the flow. However, these two shear layers interact and their subsequent evolution is strongly controlled by the overall hydrodynamic stability of the flow. In particular, shear layer interaction can lead to staggering of the vortices after some distance, $L_{Stagger}$, which is defined later. The distance required for staggering is primarily a function of the frequency ratio f_n / f_f.

This staggering phenomenon is illustrated in Figure 8-16, which shows phase-averaged iso-vorticity contours at two different values of f_n / f_f. Phase averaging was performed over the forcing period, to identify the structure of the forced response. Although the density ratio is the same for the two cases, note the completely different evolution of vorticity. The left column corresponds to non-frequency locked cases - note how the vorticity iso-contours remain symmetrically placed as far downstream as $x/D = 6$. The right column of Figure 8-16 corresponds to frequency locked cases, showing how the vortices quickly stagger into an antisymmetric configuration for these low density ratio flames.

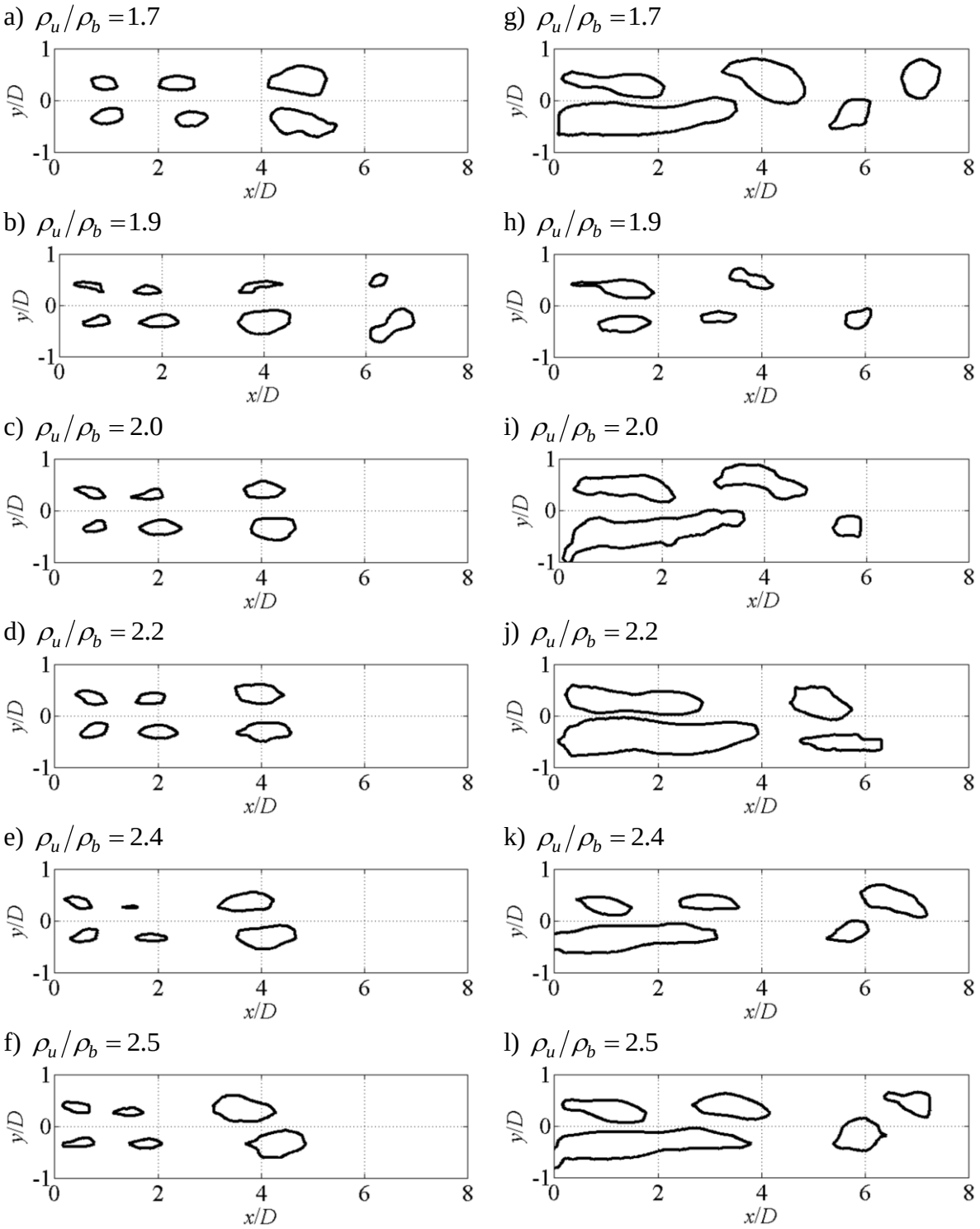

Figure 8-16. Phase averaged vorticity contours for several density ratios forced with $A_f = 0.02$, such that the left column $f_n/f_f = 0.8$ and the right column is $f_n/f_f = 1.1$. Density ratios are labeled above plots.

Figure 8-17 presents flame images at several density ratios and frequencies, revealing a similar phenomenon. Notice the sinuous flame structure in the right column that appears when operating in a frequency-locked condition. Also notice that, although the $\rho_u/\rho_b = 2.5$ flame is not globally unstable, the lightly damped global mode is still receptive to forcing (see how the sinuous flame shape appears even in Figure 8-17g). This is important because the effects of frequency locking will be applicable even to flows whose global mode is lightly damped.

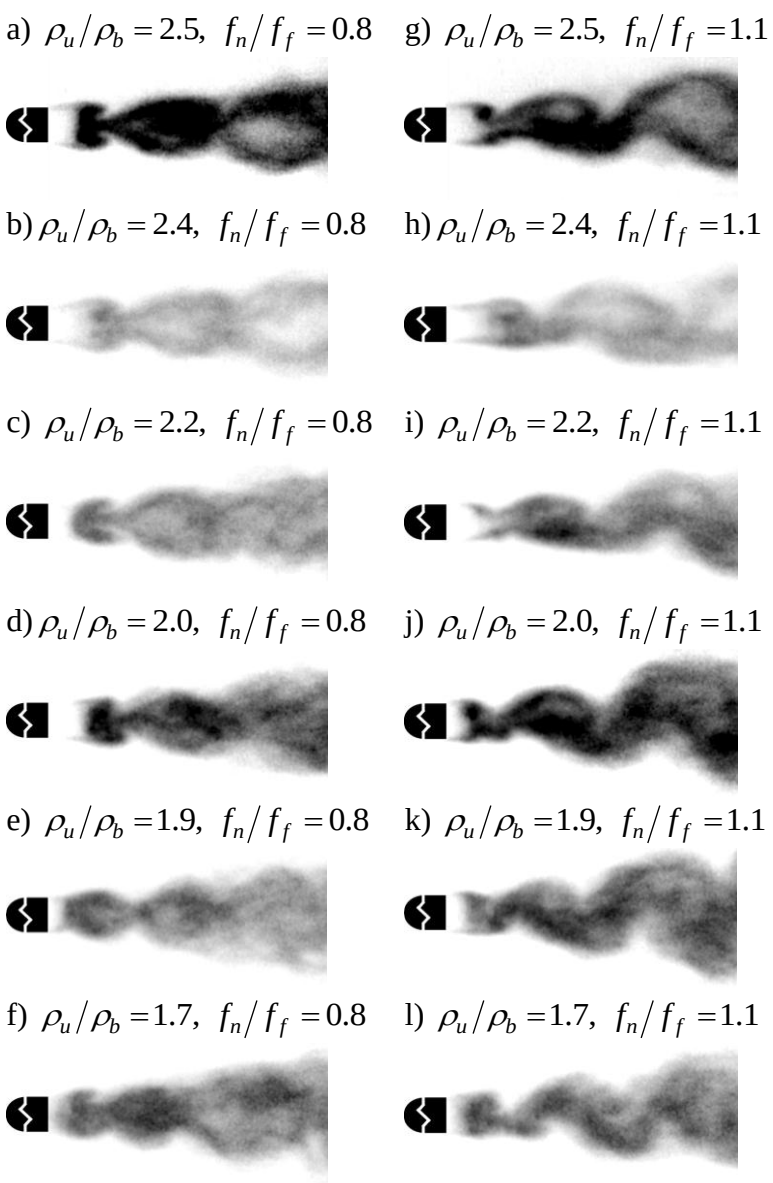

Figure 8-17. Chemiluminescence images of low density ratio flames at several combinations of f_n/f_f and ρ_u/ρ_b (labeled above each figure). The left column shows cases away from lock-in, and the right column shows cases at lock-in.

The axial variation of the transverse velocity phase at the forcing frequency is presented in Figure 8-18. Results are shown for two spatial positions straddling the flow centerline, $y/D = \pm 0.3$. The nearly linear phase roll-off of each curve indicates a nearly constant phase speed. Notice, however, that the two curves are not quite linear, as

indicated by their separation. Their separation is approximately 180° near the bluff body, and decreases to almost zero farther downstream. This is due to the vortex staggering effect, and is described in more detail next.

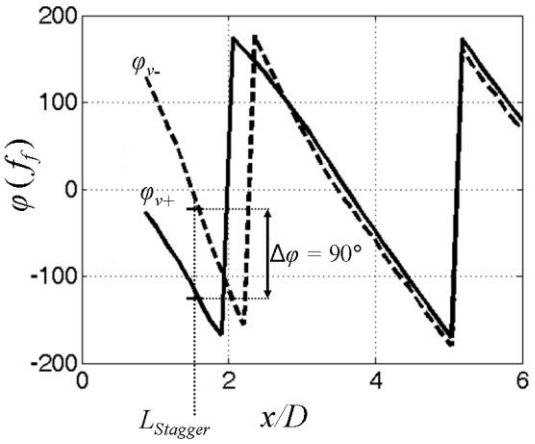

Figure 8-18. Axial dependence of the phase of the transverse velocity from the upper and lower sides of the flow centerline. The phase is at the forcing frequency. Flow conditions were $\rho_u/\rho_b = 1.9$, $f_n/f_f = 1.0$, and $A_f = 0.02$.

Vortex staggering, which is a function of axial position, is quantified by the phase difference between the transverse velocities at $y/D = +0.3$ and $y/D = -0.3$. The phases at these two positions will be denoted $\varphi_{v+}\left(f = f_f\right)$ and $\varphi_{v-}\left(f = f_f\right)$, respectively, and their difference will be denoted $\Delta\varphi$ (as illustrated in Figure 8-18). A phase difference of 180° indicates a varicose structure since, at a given axial position, the transverse velocity has opposite sign on opposing sides of the flow centerline. Likewise, a value of zero indicates sinuous behavior. Figure 8-19 illustrates this phase difference as a function of axial position, for a fixed ρ_u/ρ_b. This shows that in the frequency locking case ($f_n/f_f = 1.1$) the vortices are typically staggered after about two bluff body diameters

downstream. Figure 8-20 shows the stagger length, $L_{Stagger}$, which is defined as the axial location where $\Delta\varphi = 90°$ (see Figure 8-18 for illustration). Note that the stagger lengths are dramatically reduced when $f_n \sim f_f$. Interestingly, ρ_u/ρ_b does not have a significant influence on $L_{Stagger}$. This is apparent in the figure, where stagger lengths overlaid from many density ratios fall virtually onto one curve. This may be due to the fact that the most locally amplified region in this flow, the "wavemaker" region near where the reverse flow velocity peaks, is located at a fixed x/D that is relatively insensitive to density ratio [89].

a) $\rho_u/\rho_b = 1.7$

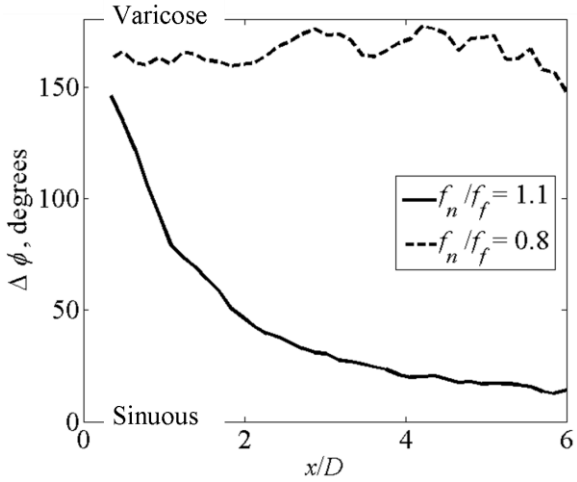

c) $\rho_u/\rho_b = 2.0$

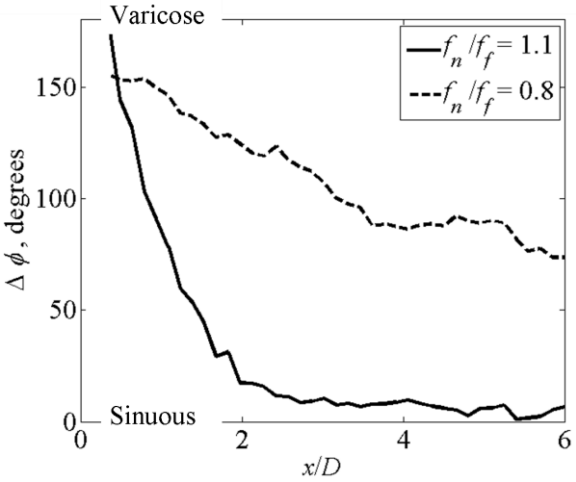

b) $\rho_u/\rho_b = 1.9$

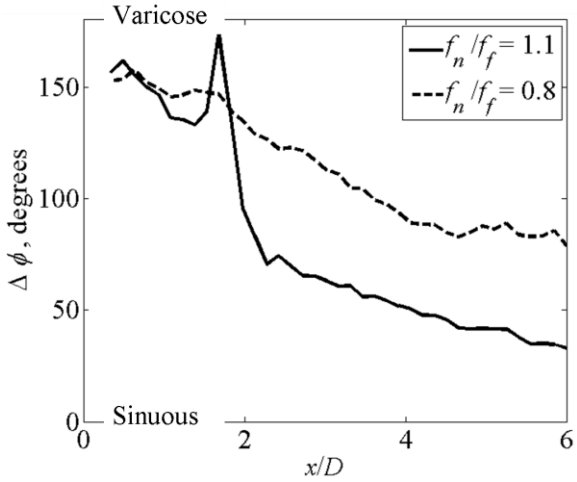

d) $\rho_u/\rho_b = 2.4$

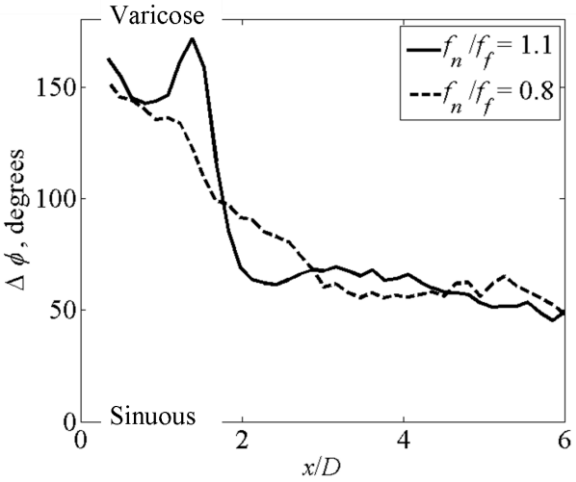

Figure 8-19. Degree of stagger for two values of f_n/f_f at several density ratios (labeled above plots) and $A_f = 0.02$

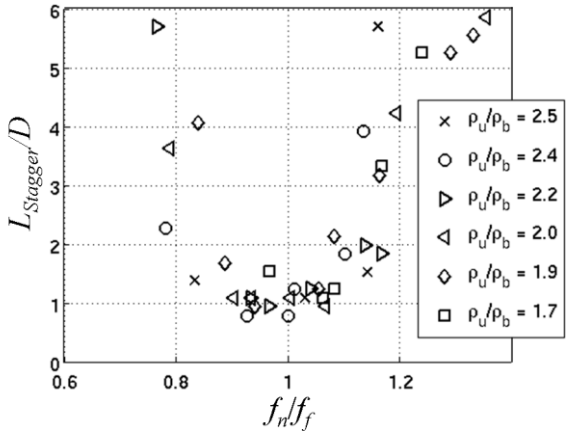

Figure 8-20. Stagger length for all density ratios at $A_f = 0.02$

8.6 Proper Orthogonal Decomposition

Proper orthogonal decomposition (POD) was performed using the DAVIS 7.2 software. For low density ratio cases with large forcing amplitude, the natural sinuous mode, the forced varicose mode, and the vortex staggering effect are all well captured (many noisy and incoherent modes are also present). The first six modes are shown in the figures below for a sweep of f_n/f_f. The figure is arranged so that the mode number increases from one to six from top to bottom, with energy decreasing as mode number increases. For the cases shown, the first six modes contain between 42% and 54% of the total POD energy. The left column shows the spatial modes, and the right column the spectra of their corresponding time coefficients. The pairing of modes is discussed in the POD discussion of the unforced results in section 7.2, *Proper Orthogonal Decomposition*. Figure 8-21 shows a non-frequency locked at $f_n/f_f = 0.8$, primarily

showing the varicose structure responding at the forcing frequency with a hint of vortex staggering. Figure 8-22 shows the result for $f_n/f_f = 1.0$, revealing a predominantly sinuous response at the overlapping forcing/global mode frequency. Figure 8-23 shows the frequency-locked case of $f_n/f_f = 1.1$, and shows a partially staggered structure responding at both the forcing and global mode frequency. Finally, Figure 8-24 shows another non-frequency locked case at $f_n/f_f = 1.2$, which clearly shows the varicose response peaking at the forcing frequency and the sinuous response peaking at the global mode frequency.

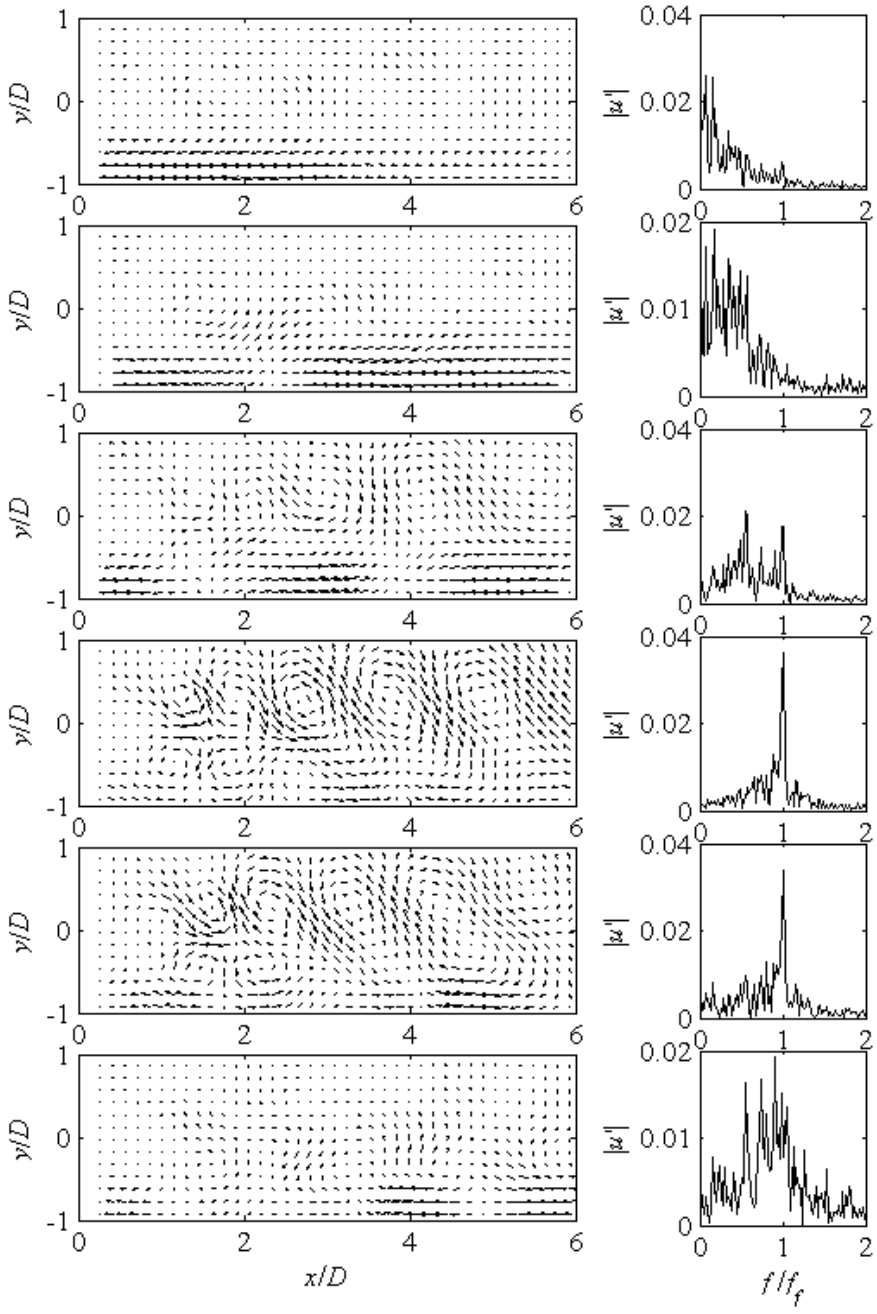

Figure 8-21. First six POD modes for $\rho_u/\rho_b = 1.7$, $A_f = 0.02$, $f_n/f_f = 0.8$

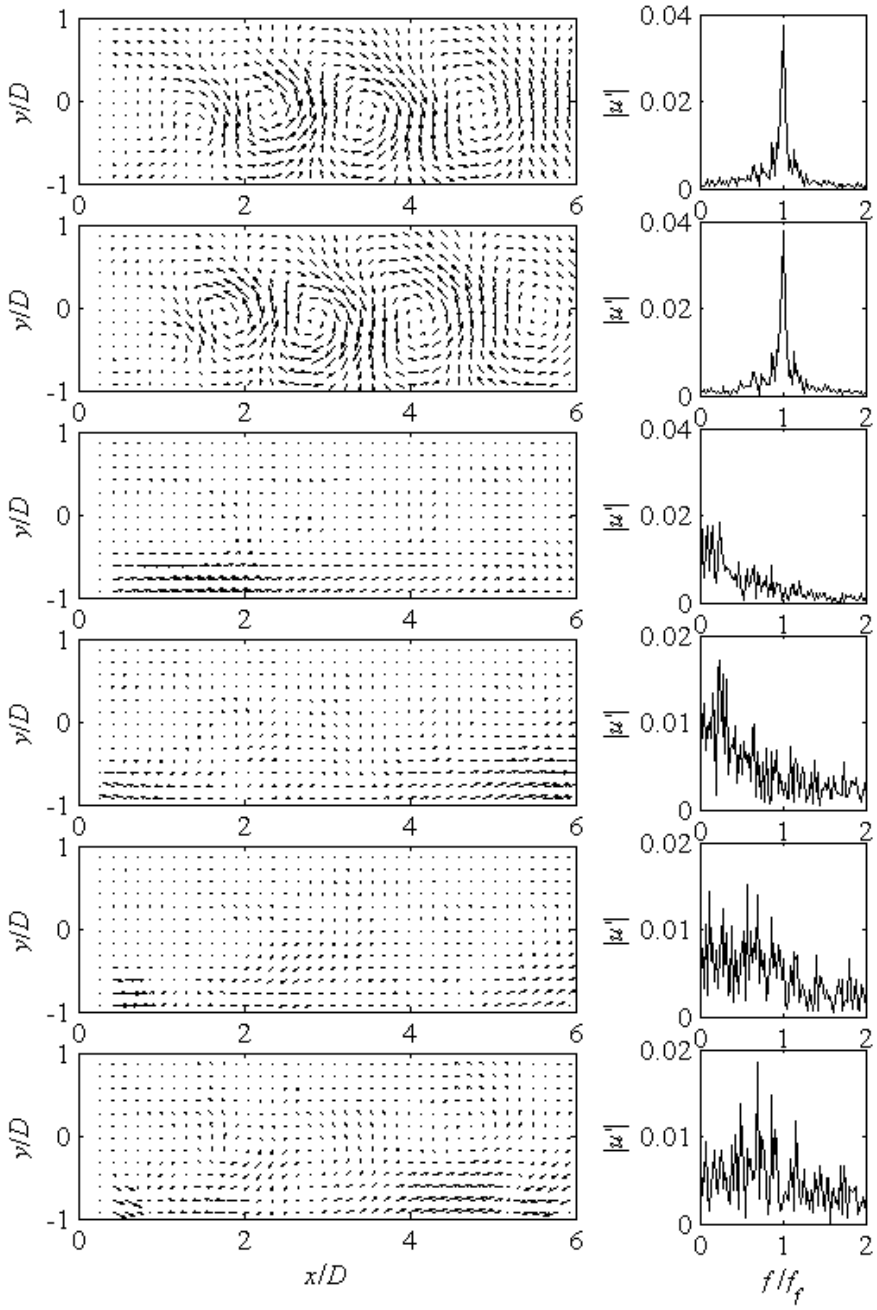

Figure 8-22. First six POD modes for $\rho_u/\rho_b = 1.7$, $A_f = 0.02$, $f_n/f_f = 1.0$

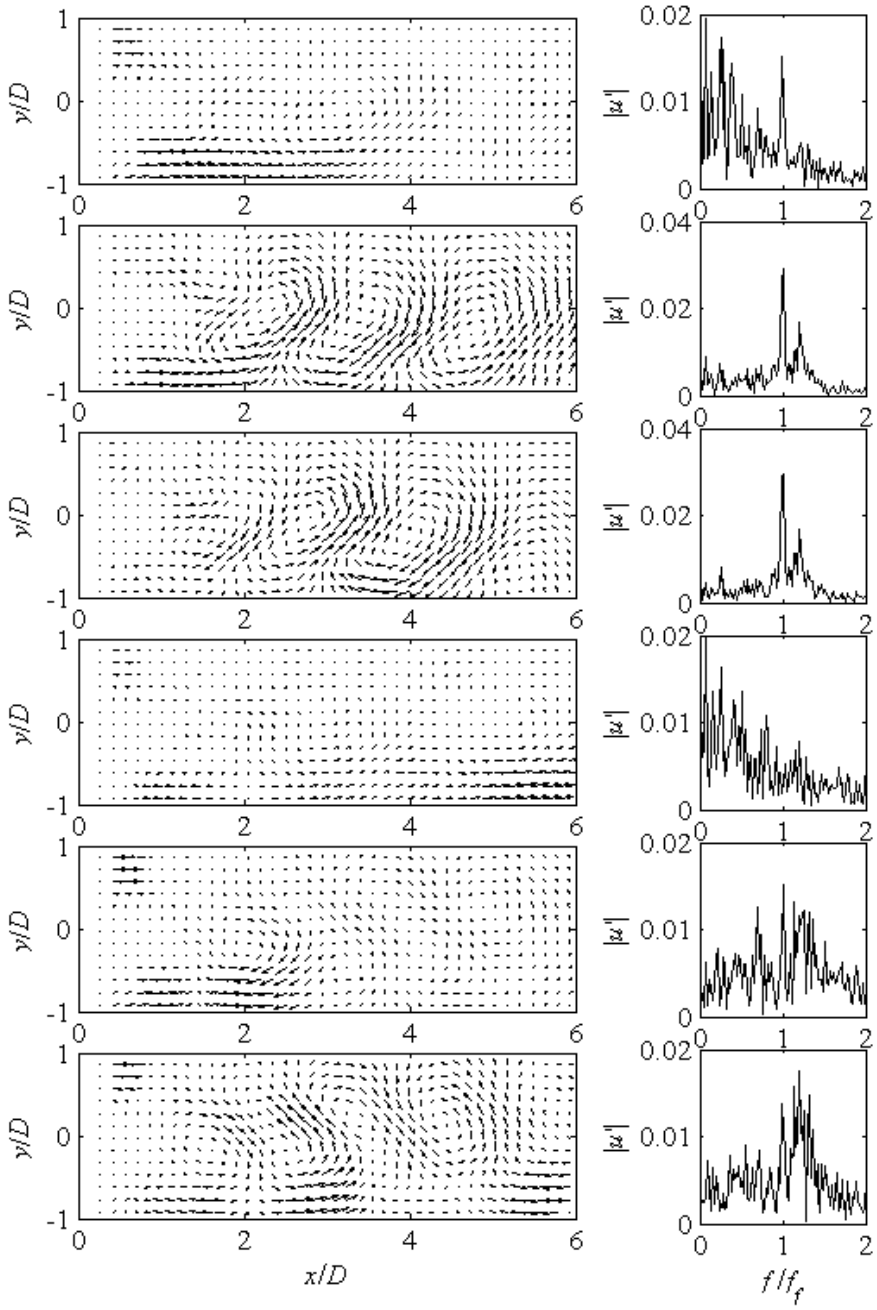

Figure 8-23. First six POD modes for $\rho_u/\rho_b = 1.7$, $A_f = 0.02$, $f_n/f_f = 1.1$

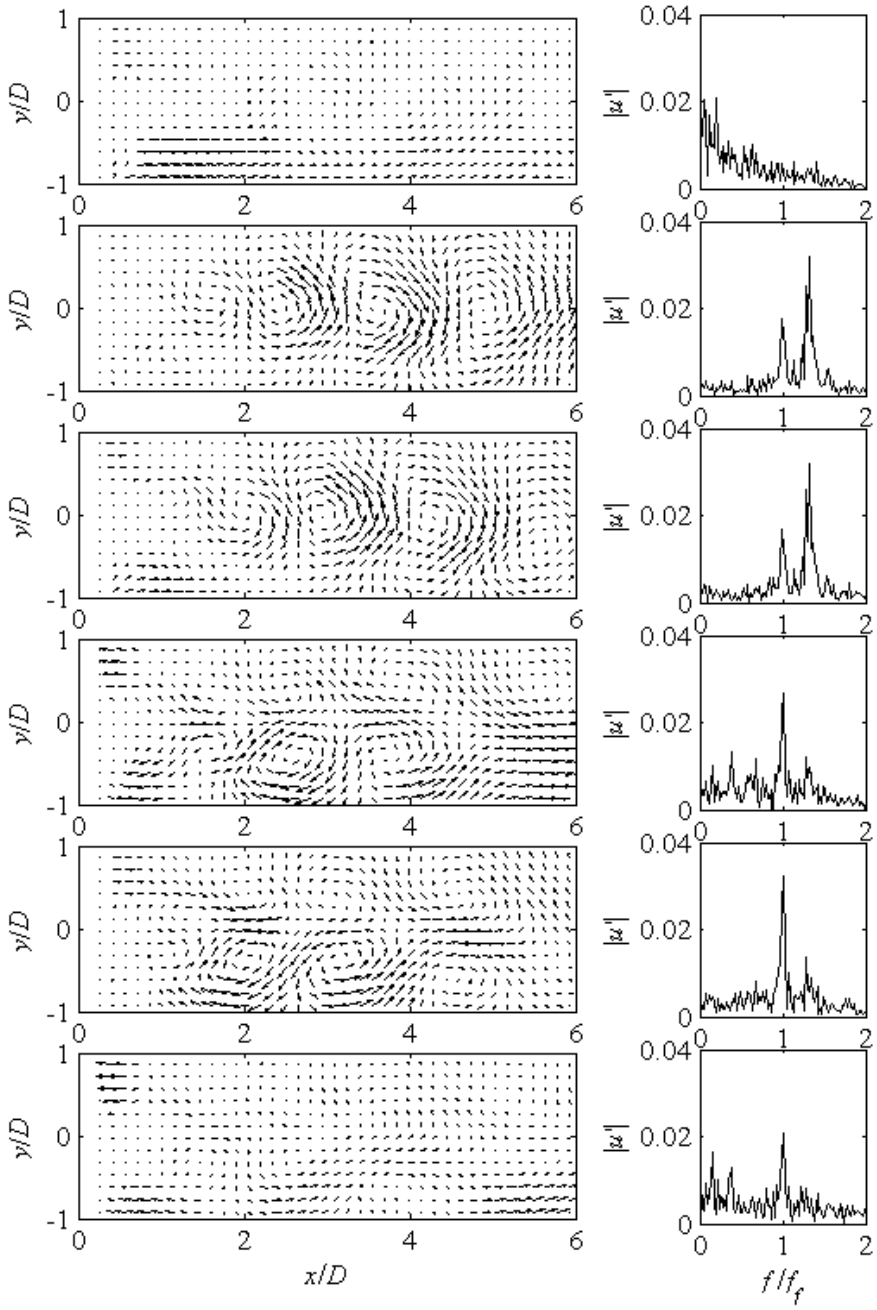

Figure 8-24. First six POD modes for $\rho_u/\rho_b = 1.7$, $A_f = 0.02$, $f_n/f_f = 1.2$

8.7 Forced Response Characteristics: Local Heat Release Response

This section considers the flame symmetry, the magnitude of the flame displacement and local heat release fluctuations, and their sensitivities to frequency and density ratio.

Here, the words "local heat release" will refer to the combined heat release of both flame branches at a single axial position. As would be expected, frequency locking is associated with large fluctuations in vorticity, flow velocity, and, therefore, flame edge displacement. For example, Figure 8-25 plots the dependence of the magnitude of flame wrinkling amplitude upon forcing frequency, showing that it peaks near $f_n = f_f$. Note that the peak is symmetric, however. In general, flame displacement response at values of f_n / f_f above the peak is greater than at values below the peak. This is likely due to the fact that f_n was varied by sweeping U_{lip}, which likely influences the global mode growth rate by altering the backflow ratio and degree of non-colocation of the flame and shear layer.

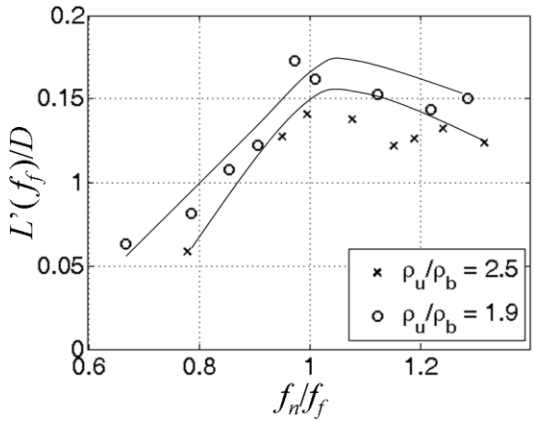

Figure 8-25. Flame edge displacement amplitude at $x/D = 3$ as a function of f_n / f_f, for $A_f = 0.02$.

The magnitude of flame flapping is roughly proportional to the local heat release rate fluctuations, as local heat release rate is proportional to flame area,

$dS \sim \sqrt{1+\left(dL/dx\right)^2}\,dx$. However, the heat release rate fluctuations at each axial location are controlled by the relative phasing of the upper and lower flame branches. As such, the degree of symmetry of the two branches has an important impact on the relationship between local flame flapping and the associated heat release fluctuations. In particular, varicose flow/flame oscillations cause the oscillations of the two flame branches to be in phase, while the converse occurs for sinuous oscillations. Thus, in terms of heat release oscillations, lock-in leads to two competing phenomena: large flame displacement and area fluctuations, but a sinuous flame structure. This is illustrated as follows. The local unsteady heat release rate is the sum of the heat release rate of the two flame branches as shown below:

$$q(x,f) = q_+(x,f) + q_-(x,f) \tag{8.7}$$

The heat release rate of one flame branch may be related to the heat release rate of the other by a phase offset, $\Delta\varphi$, such that $q_-(x,f) = q_+(x,f)\cos(\theta(x,f))$. Eq. (8.7) then reduces to the following expression:

$$q(x,f) = \underbrace{q_+(x,f)}_{\substack{Displacement\\ Effect}} \underbrace{\cos^2\left(\frac{\theta(x,f)}{2}\right)}_{\substack{Stagger\\ Effect}} \tag{8.8}$$

This expression illustrates the competing effects of flame edge displacement and staggering. Flame edge displacement drives the unsteady heat release rate of a given branch, and staggering affects the phase offset between the two branches. Note that a phase offset of $\theta = 180°$ drives this expression to zero, even if the local unsteady heat

release of the individual flame branches is large. Recall that the flame is sinuous when $\Delta\varphi = 0°$, since the upper and lower branches are moving "up" in sync. It is important to notice that this sinuous configuration, $\Delta\varphi = 0°$, occurs when the heat release of the two flame branches is out of phase, $\theta = 180°$.

The dependence of the local heat release fluctuations upon f_n / f_f is plotted in Figure 8-26. This figure shows that the local heat release oscillations decrease near lock-in, an effect that is more pronounced at lower density ratios.

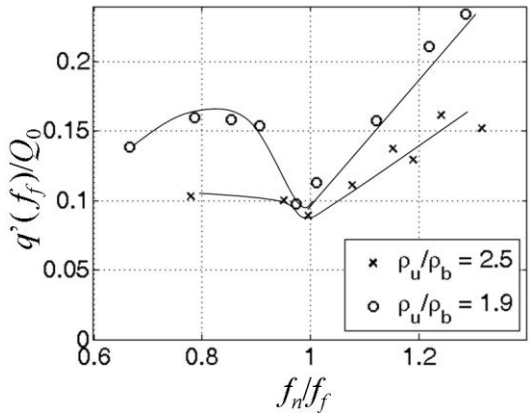

Figure 8-26. Local heat release amplitude at $x/D = 3$ vs f_n / f_f, for $A_f = 0.02$.

Here, the local unsteady heat release has been nondimensionalized by the mean spatially integrated heat release, Q_0. This local minimum in heat release reflects the fact that the staggering effect dominates the increased flame displacement effect, as shown in Figure 8-27a. This plot overlays the frequency dependence of the flame displacement amplitude, the degree of stagger between the two flame branches ($\Delta\varphi$), and the local heat release amplitude, for a low density ratio case. Notice that the flame displacement

amplitude is maximized when $f_n \sim f_f$. However, when $f_n \sim f_f$, the phase difference between the two flame branches indicates a sinuous configuration, and the local heat release amplitude is minimized. Figure 8-27b shows the same behavior for a higher density ratio, although the effects are less pronounced. Finally, Figure 8-27c shows the axial dependence of the relationship of local heat release amplitude to frequency ratio. As the figure suggests, the minimum in local heat release amplitude when $f_n \sim f_f$ persists at all axial positions downstream of the initial staggering. Thus, the local heat release response of low density ratio flames at lock-in is significantly less than that of flames away from lock-in. A comprehensive review of the flame response data is presented in *Appendix D*.

a)

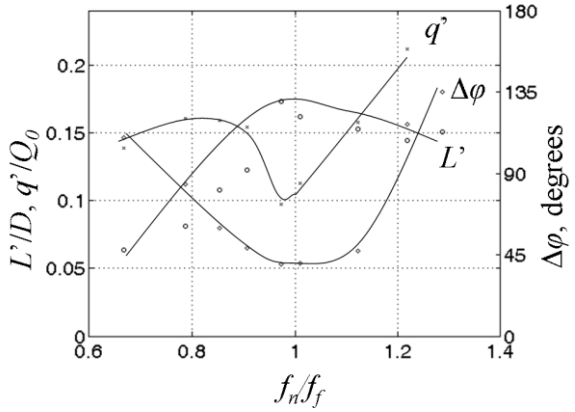

b)

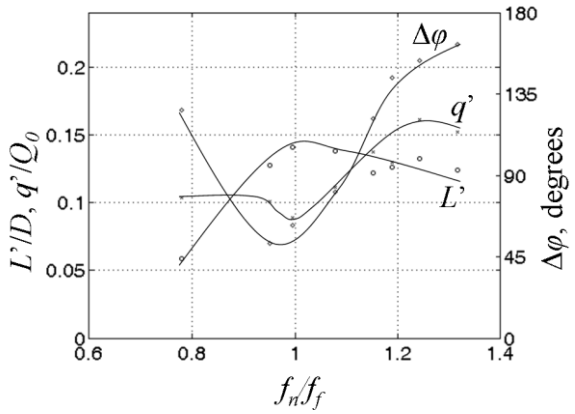

c)

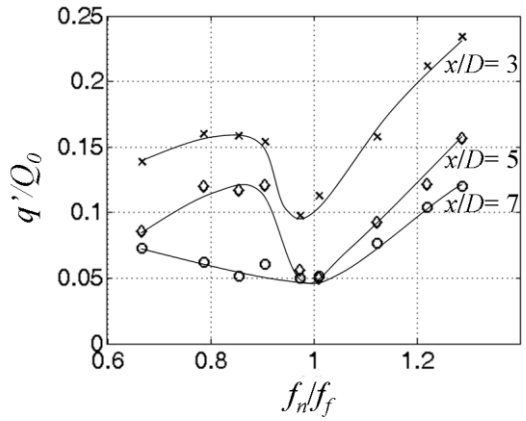

Figure 8-27. Frequency dependence of flame edge displacement amplitude, local heat release amplitude, and flame stagger at $x/D = 3$, $A_f = 0.02$, a) $\rho_u/\rho_b = 1.9$ and b) $\rho_u/\rho_b = 2.5$. c) Dependence of local heat release amplitude on axial position and f_n/f_f for $\rho_u/\rho_b = 1.9$, $A_f = 0.02$.

This has important and very non-intuitive implications. It shows that, for longitudinal acoustic modes, the hydrodynamic global mode of the wake inhibits the flame's forced heat release response, due to the flame's resulting sinuous structure. Thus, for low density ratio flames, overlap of the hydrodynamic global mode frequency and longitudinal acoustic modes is not as dangerous as previously thought.

8.8 Forced Response Characteristics: Global Heat Release Response

The response of the spatially integrated heat release, referred to here as the global heat release, is of particular interest from a combustion instability standpoint. The global heat release is defined as

$$Q\left(L_f,t\right)=\int_{x=0}^{x=L_f} q\left(x,t\right)dx \tag{8.9}$$

where L_f is the axial flame length. The global heat release is a strong function of L_f. This is due to the spatially oscillatory nature of the local heat release. The local heat release is spatially modulated at the flame surface wrinkle wavelength. The flame wrinkle wavelength is related to the flame wrinkle propagation speed and frequency, according to $\lambda_f = c_f / f_f$, which stems from the canonical relationship $k=\omega/c$. Here, λ_f is the flame wrinkle wavelength, and c_f is the flame wrinkle propagation speed. Rewriting Eq. (8.9) to consider only the component of the local heat release at the forcing frequency:

$$Q\left(L_f,t\right)=\int_{x=0}^{x=L_f} \left|q\left(x,f_f\right)\right|\exp\left\{-i\left(2\pi f_f t-\frac{2\pi}{\lambda_f}x\right)\right\}dx \tag{8.10}$$

For this study, λ_f is determined experimentally from the spatial evolution of the Fourier coefficients of the flame edge displacement according to

$$\lambda_f = 2\pi \frac{\Delta x}{\Delta \angle \hat{\zeta}} \tag{8.11}$$

The ratio in Eq. (8.11) is the inverse of the slope of the axially varying flame phase. For this work, Δx is 12 bluff body diameters and $\Delta \angle \hat{\zeta}$ is the flame displacement phase difference spanning the 12 bluff body diameters from $x/D = 2$ to 14. Therefore, the measured flame wrinkle wavelength is an axially averaged quantity from this domain.

Careful inspection of Eq. (8.10) reveals that the global heat release is an oscillatory function of the flame length. In fact, if the local heat release magnitude were a constant function of axial position, the global heat release would have a pattern of nodes and antinodes spaced at integer multiples of λ_f. Such a pattern is easily recognized in the data shown in Figure 8-28 and Figure 8-29, which show the global heat release magnitude at the forcing frequency as a function of flame length (integration length).

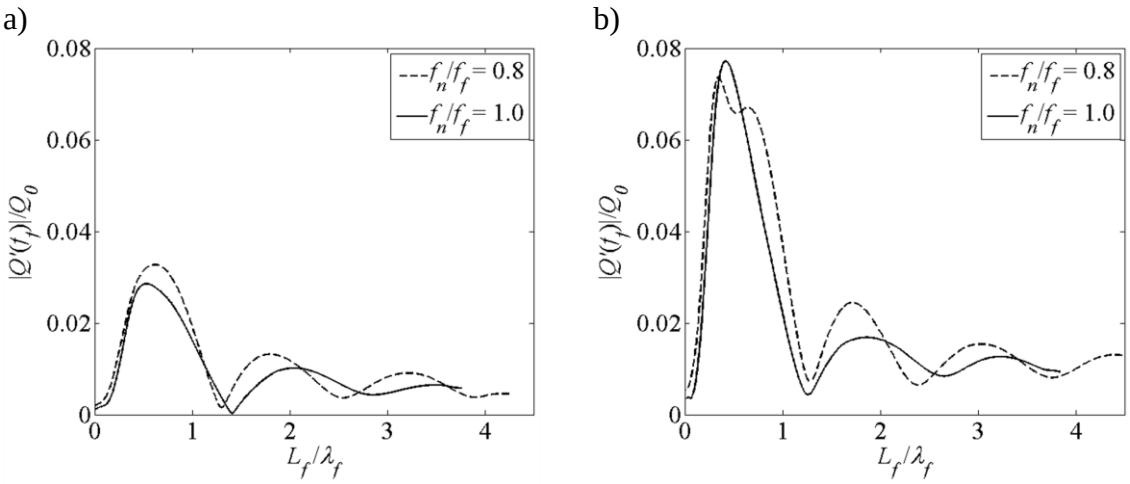

Figure 8-28. Spatially integrated heat release vs flame length for $A_f = 0.02$ and a) $\rho_u/\rho_b = 2.5$ and b) $\rho_u/\rho_b = 1.9$

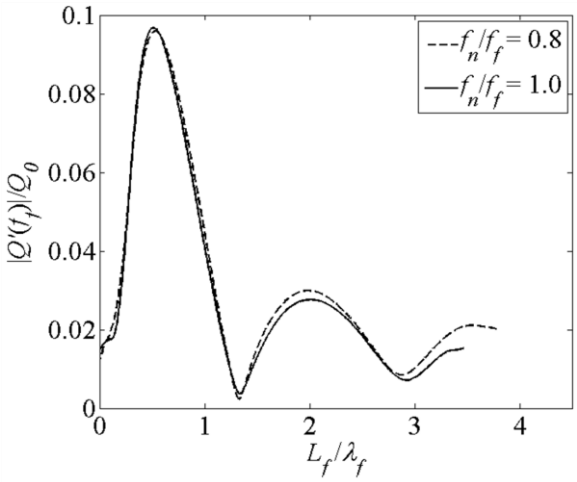

Figure 8-29. Spatially integrated heat release vs flame length for $A_f = 0.02$ and $\rho_u/\rho_b = 3.1$

The nodes and antinodes in this pattern simply arise due to destructive/constructive phase interference between the highs and lows on the instantaneous local heat release wave, $q'(x)$. Note that flame lengths corresponding to the peaks in this pattern stand to benefit the most from reduced heat release response. Figure 8-28 shows the globally

integrated heat release as a function of flame length for two density ratios and two values of f_n/f_f. The figure shows that during frequency locking, $f_n/f_f = 1.0$, there is a slight reduction in global heat release response for most flame lengths compared to $f_n/f_f = 0.8$. The effect is not as pronounced, however, as it is for the local heat release response (see Figure 8-27a). This does support the argument, however, that alignment of the hydrodynamic frequency with the acoustic frequency is not necessarily dangerous for a longitudinal mode. In fact, such frequency alignment may even be slightly beneficial.

Figure 8-29 shows global heat release response vs flame length for a higher density ratio, $\rho_u/\rho_b = 3.1$. At this density ratio the sinuous global mode is heavily damped, and no level of forcing amplitude or alignment of f_n and f_f resulted in vortex staggering. Not surprisingly, f_n/f_f has little effect on the global heat release in this case.

The effects of f_n/f_f and ρ_u/ρ_b may be summarized with the contour plots shown in Figure 8-30 and Figure 8-31. Figure 8-30 shows contours of global heat release magnitude as a function of flame length and f_n/f_f. Notice the slight valley that appears at $f_n/f_f = 1$, reinforcing the notion that the global heat release is slightly reduced during frequency locking (at flame lengths where the global heat release response is significant).

Figure 8-31a shows another such contour plot but at a higher density ratio, demonstrating that the global heat release is insensitive to f_n/f_f when the global mode is heavily damped. Figure 8-31b shows the global heat release as a function of flame length and density ratio. As density ratio is reduced, the global heat release first decreases and then increases. This is due to the competing effects of flame edge displacement and vortex staggering, as discussed in section 8.7, *Forced Response*

Characteristics: Local Heat Release Response. At high density ratios, the flow is convectively unstable and strongly amplifies the forcing with a varicose structure. When the density ratio becomes sufficiently low, vortex staggering occurs during frequency locking, with an associated reduction in the global heat release response. As the density ratio is reduced further, the global heat release begins increasing. Here, the flame edge displacement is increasing as the global mode amplification increases.

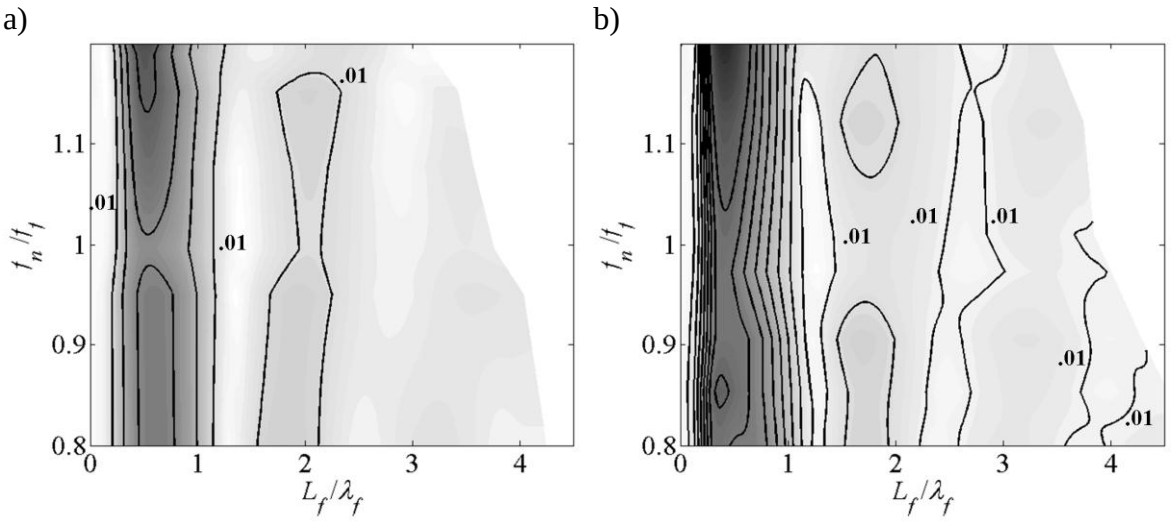

Figure 8-30. Contours of constant $\left|Q'\left(f_f\right)\right|/Q_0$ vs axial position and f_n/f_f for a) $\rho_u/\rho_b = 2.5$ and b) $\rho_u/\rho_b = 1.9$. Contours are labeled at $\left|Q'\left(f_f\right)\right|/Q_0 = 0.01$ for reference, and have increments of 0.01.

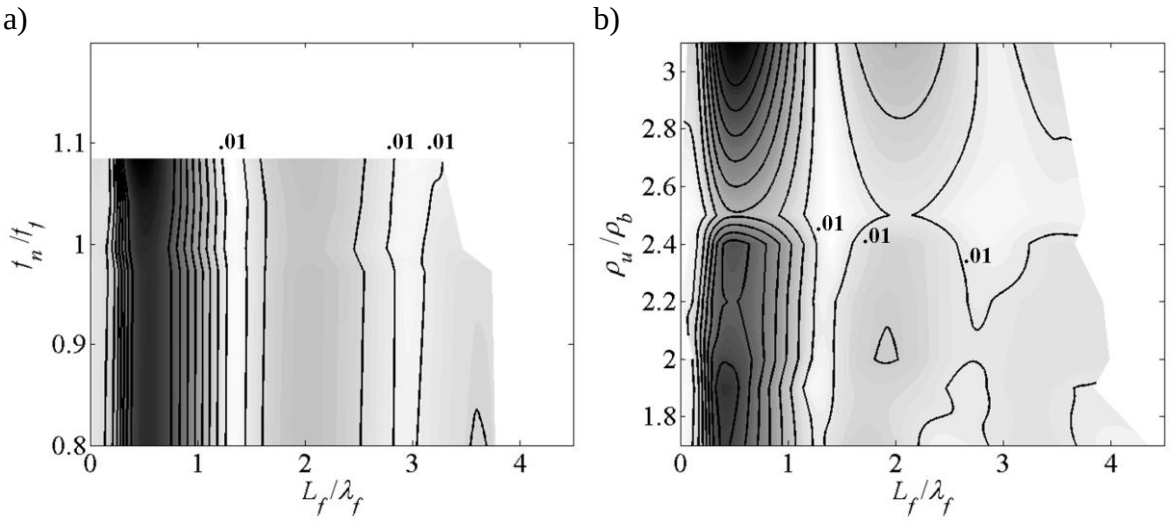

Figure 8-31. Contours of constant $\left|Q'\left(f_f\right)\right|/Q_0$ vs axial position and a) f_n/f_f for $\rho_u/\rho_b = 3.1$, b) ρ_u/ρ_b for $f_n = f_f$. Contours are labeled at $\left|Q'\left(f_f\right)\right|/Q_0 = 0.01$ for reference, and have increments of 0.01.

In summary, the global heat release is a strong function of the integration length (the flame length). At some flame lengths global heat release response amplitude is very small, while at others it is significant (as much as 10% of the total heat release rate). For flame lengths associated with significant global heat release, the global heat release is slightly minimized when the forcing frequency equals the natural asymmetric vortex shedding frequency, and when the density ratio is lowered only enough for the forced shedding to stagger to an asymmetric pattern. An important observation is that alignment of the forcing and hydrodynamic global mode frequencies does not cause a maximum in global heat release response, and therefore does not promote combustion instability. This conclusion is valid only for longitudinal acoustic modes, and is likely to be different for transverse forcing.

8.9 Closing Remarks

This chapter has addressed longitudinally acoustically forced, low density ratio flames. The experiments discussed show that when the forcing frequency is in the vicinity of the global mode frequency, frequency locking occurs; the wake and, hence, the flame then respond more strongly at the forcing frequency than the global mode frequency. When this happens, the vortices which were initially shed from the bluff body in a varicose configuration (due to the symmetric nature of the forcing) quickly stagger to a sinuous pattern. The flame also transitions from a varicose to a sinuous structure; this is associated with an increase in oscillatory flame edge displacement, but a decrease in local oscillatory heat release fluctuations at the forcing frequency. This effect is also present, although less pronounced, in the global heat release response. This is important and non-intuitive, as it suggests that forcing a flame on top of its hydrodynamic global mode actually leads to a slight reduction in the flame's heat release response. Finally, analysis showed that the global heat release response is a strong function of flame length, exhibiting a pattern of nodes and antinodes. For flame lengths associated with significant global heat release response, this response is minimized when the density ratio is just low enough (but no lower) for vortex staggering to occur, and when the acoustic and hydrodynamic frequencies are equal.

CHAPTER 9. CONCLUDING REMARKS

Combustion instabilities in bluff body combustors motivated this work. In particular, the effort was focused on combustors with low flame density ratios (due to highly preheated reactants), and longitudinal acoustic modes. This thesis has presented both experimental and theoretical work, designed to accomplish the goals laid out at the end of Chapter 2, *Background and Motivation*. This chapter summarizes the contributions of the work, draws conclusions about the important role that hydrodynamic instability plays in the combustion instability feedback loop, and provides recommendations to the combustion community.

9.1 Summary of Contributions

This thesis has explored the flame and flow dynamics of bluff body combustors at low flame density ratios. It has demonstrated that these flows tend to sit near a global hydrodynamic stability limit, and that the global mode is characterized by narrowband, asymmetric vortex shedding which wraps the flame into a sinuous structure. Experiments showed that such behavior becomes more prevalent as density ratio is reduced, and occurs in intermittent bursts due to parametric noise affecting the flow stability. This intermittency demonstrated that industrially relevant, high Reynolds number flows can have complex dynamics in the presence of sensitive hydrodynamics

The theoretical work has demonstrated the applicability of linear, local hydrodynamic stability analysis to these flows. Two different types of stability analysis were performed: one using the full measured base flow profiles, and one using simpler, model

base flow profiles. Both types of analysis turned out to have useful characteristics. Stability analysis of the full measured base flow profiles provided good quantitative prediction of the global mode frequency. This analysis lent itself to reconstruction of the direct global mode shape, which provided the adjoint global mode and the structural sensitivity. The stability analysis of the model base flow profiles identified key flow features to express as stability parameters. In this effort, a pre-existing model stability problem was further developed to include four important stability parameters: density ratio, backflow ratio, confinement, and density-shear layer offset. Owing to its simplicity, this analysis helped elucidate the underlying physics governing the hydrodynamic stability of the reacting wake.

The final study in this thesis experimentally explored the effects of the hydrodynamic stability characteristics on the velocity-coupled flame response. Experimental results showed that the global mode does interact significantly with the forced flame response. However, the results led to a counter-intuitive conclusion: when the hydrodynamic instability frequency equals a longitudinal acoustic mode frequency, the flame's heat release response amplitude does not become a local maximum in the studied parameter space, and can actually be minimized. Therefore, such frequency alignment is not especially dangerous for longitudinal combustion instability of bluff body combustors. This result demonstrates the important and non-intuitive role that hydrodynamic instabilities can play in the combustion instability feedback loop.

9.2 Conclusions

This thesis demonstrated the role of hydrodynamic instability in longitudinal bluff body combustion instabilities, thus emphasizing the important and complicated role that

hydrodynamic instability plays during combustion instabilities in general. The experiments showed that there can be an important, nonlinear interaction between a combustor's acoustics and fluid dynamics. In light of this interaction, hydrodynamic amplification of the acoustic velocity field can provide a non-intuitive fluid-dynamic response, and hence a velocity disturbance field that differs significantly from its acoustic origin. Therefore, the hydrodynamic stability characteristics of a given combustor's flowfield must be understood in order to understand the flame response. Specifically, it is of critical importance to identify any unstable or weakly damped hydrodynamic global modes, as well as their frequencies and mode shapes. Furthermore, it is of practical importance to determine the key flow features that govern these hydrodynamic characteristics. Stability analysis of the full base flow profiles is a helpful tool for quickly determining the global mode stability, frequency, and structure. Stability analysis of model base flow profiles is a perfect tool for parameterizing the base flow into key stability parameters, determining the effect of those parameters on the flow stability characteristics, and elucidating the physics governing the flow stability.

9.3 Recommendations to the Combustion Community

9.3.1 *Future Bluff Body Experimental Work*

The hydrodynamic stability analysis work discussed in this thesis motivates a study to experimentally verify the effect of density-shear layer offset. Such an offset was present in the current study, but remained relatively fixed over the range of conditions tested. This author recommends an experiment which varies the density-shear layer offset in the vicinity of the wave-maker region. The challenges associated with this study would be fixing the other stability parameters, especially the density ratio, while varying the

density-shear layer offset. Much like this study investigated the role of density ratio as a stability parameter, the recommended study should determine if the flow stability is as sensitive to the density-shear layer offset as stability analysis suggests. In the context of reacting wakes, this is unexplored experimental territory. To confirm this prediction would further support the use of linear, model stability analysis as a tool for parameterizing real reacting base flows into a manageable number of important parameters.

9.3.2 *Improved Model Stability Analyses*

This thesis showed that the stability analysis of model base flow profiles is reduced-order, such that the major flow features may be expressed as stability parameters. Therefore, it is a useful engineering tool that allows its user to determine how (and why) a given change to the base flow is expected to change the flow dynamics. For this flow, however, this level of simplification did not enable successful quantitative prediction.

The model used in this thesis assumed regions of uniform base flow velocity and density, separated by discontinuous jumps; this form of the base flow allows simplification of the Rayleigh equation, Eq. (6.17), to the much simpler form shown in Eq. (6.18). This simplification is still valid, however, for a linearly varying velocity profile as long as the base flow model is still limited to discontinuous regions of uniform density. Therefore, in an effort to improve the quantitative prediction of this model analysis, this author recommends development of a dispersion relation where the shear layer thickness is captured by a linear velocity profile model.

9.3.3 *Use of Nonlinear Stability Analysis*

The intermittency observed in the unforced flow inspired a discussion of bi-stable systems. Although the observed intermittency was not due to a bi-stable system, this serves as a reminder that not all bifurcations behave similarly. For example, the strong parametric noise present in the current study complicated the identification of the bifurcation as subcritical or supercritical. Although linear stability analyses are useful for locating these bifurcations, they cannot provide insight into important nonlinear behaviors such as hysteresis, intermittency and limit cycle amplitude. Therefore, nonlinear stability analysis via branch tracing and continuation software is recommended as a straightforward way to understand flow behavior in the vicinity of a stability bifurcation, and therefore to better understand the hydrodynamic stability of a given system. Nonlinear stability analysis would be extremely useful in the context of reacting wakes. The uniform density wake is well known to experience a supercritical Hopf bifurcation near $\mathrm{Re}_D = 40$. As density ratio increases, however, this bifurcation point moves to much higher Reynolds numbers, and its behavior is not well known. For example, in the Reynolds number – density ratio parameter space, the bifurcation diagram could hypothetically experience a cusped catastrophe such that the bifurcation transitions to subcritical. Although the present analysis suggests the bifurcation remains supercritical, nonlinear stability analysis would be useful to support this conclusion.

9.3.4 *The Role of Hydrodynamics in Combustion Instabilities*

The forced experiments in this thesis showed the important and non-intuitive role that hydrodynamic instabilities can play in combustion instabilities. For example, in some situations, it may not be helpful to avoid commensurate acoustic and hydrodynamic

global mode frequencies. Therefore, careful consideration of the hydrodynamics is strongly recommended for any effort to understand a velocity-coupled combustion instability problem. This consideration should aim to address the following sequence of questions:

1. Is there an unstable or weakly damped hydrodynamic global mode?
2. Under what flow/flame conditions does the global instability exist?
3. Does the global instability tend to exhibit frequency locking behavior when acoustically forced?
4. During frequency locking, does the flow structure shift from the convectively unstable response to a structure resembling the hydrodynamic global mode?
5. Which general flow/flame structure is likely to be more dangerous from a combustion instability standpoint: the structure associated with convectively unstable amplification of the acoustic forcing, or the global mode structure?
6. In consideration of the above questions, what are the conditions (flow/flame conditions as well as frequencies) where the velocity coupled heat release will be most severe?

This is the most valuable recommendation of the thesis, as it extends the established paradigm toward velocity coupled flame response in the combustion instability feedback loop to include a more careful consideration of the hydrodynamics.

APPENDIX A. SUPPLEMENTAL DATA FROM UNFORCED EXPERIMENTS

A.1 *Boundary Layer Measurements*

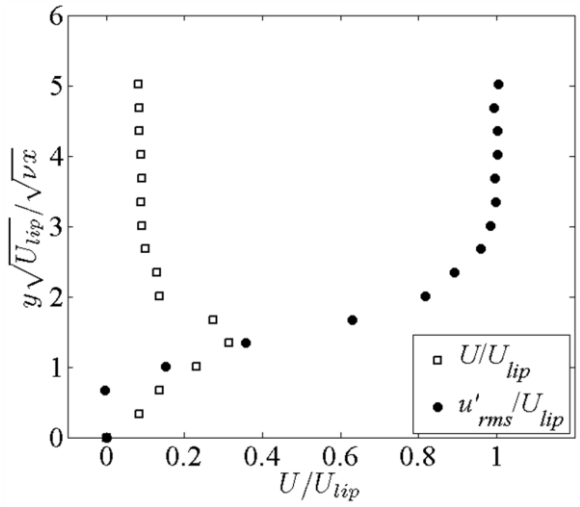

Figure A-1. Boundary layer measurement at the trailing edge of the v-gutter, unvitiated, nonreacting test section

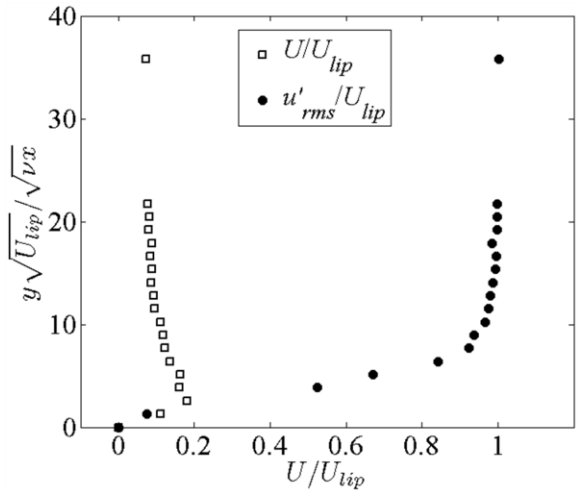

Figure A-2. Boundary layer measurement at the trailing edge of the v-gutter, vitiated, nonreacting test section

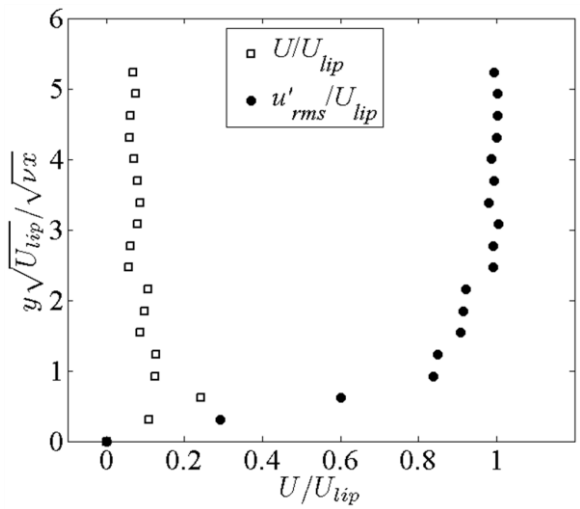

Figure A-3. Boundary layer measurement at the trailing edge of the v-gutter, $\rho_u/\rho_b = 1.7$

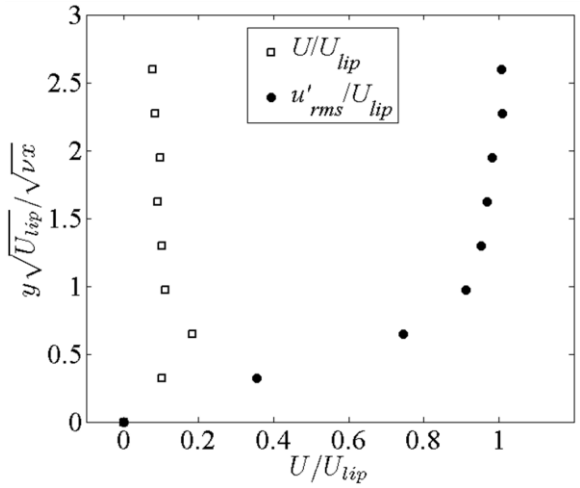

Figure A-4. Boundary layer measurement at the trailing edge of the v-gutter, $\rho_u/\rho_b = 2.0$

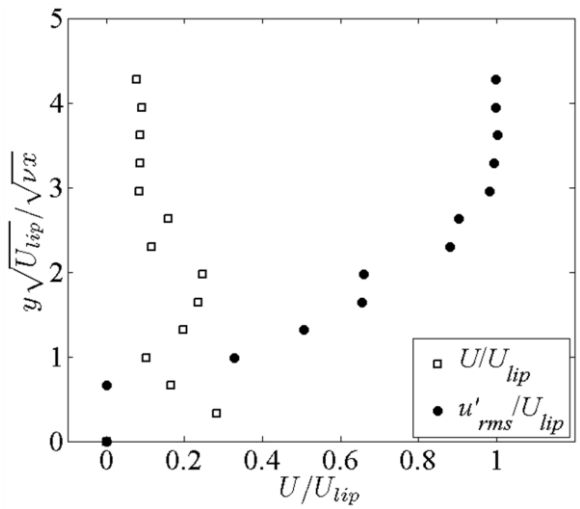

Figure A-5. Boundary layer measurement at the trailing edge of the v-gutter, $\rho_u/\rho_b = 2.4$

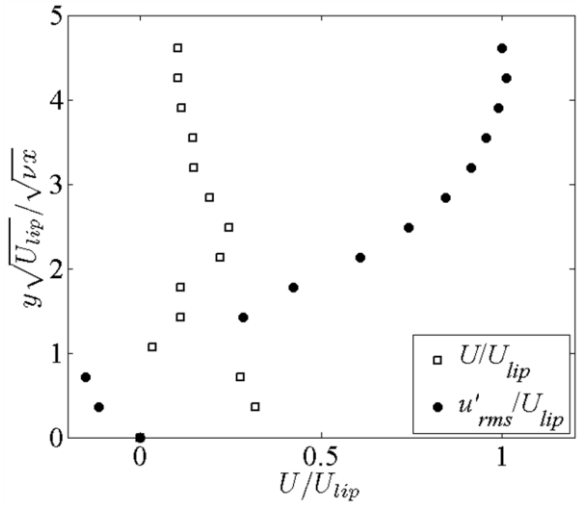

Figure A-6. Boundary layer measurement at the trailing edge of the v-gutter, $\rho_u/\rho_b = 2.7$

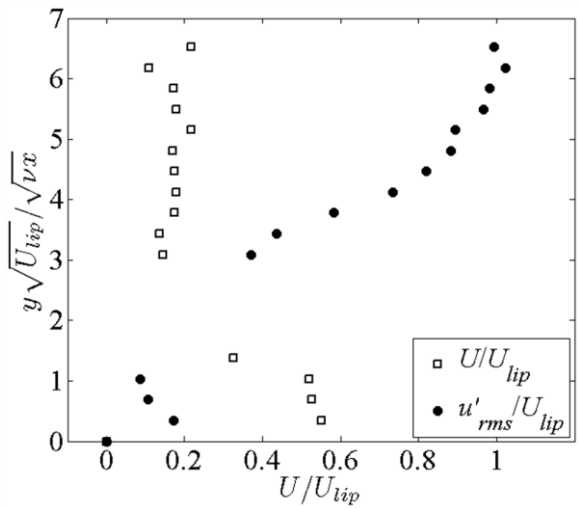

Figure A-7. Boundary layer measurement at the trailing edge of the v-gutter, $\rho_u/\rho_b = 3.2$

A.2 *Flame Images*

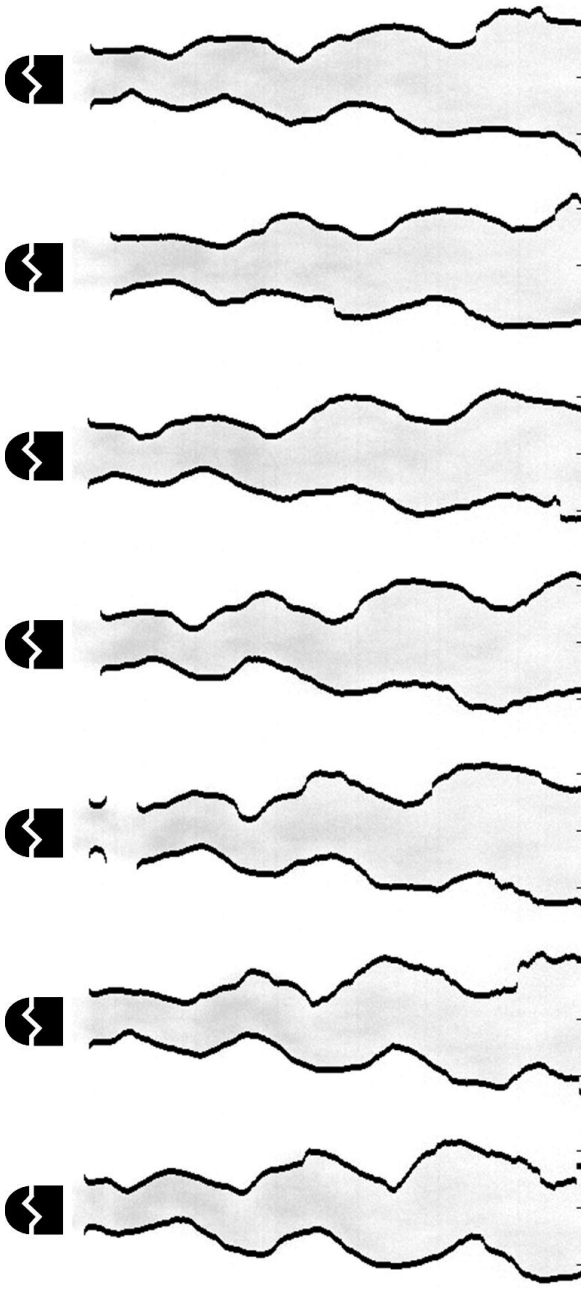

Figure A-8. Sequence of flame images for $\rho_u/\rho_b = 1.7$, spaced by 0.667 ms

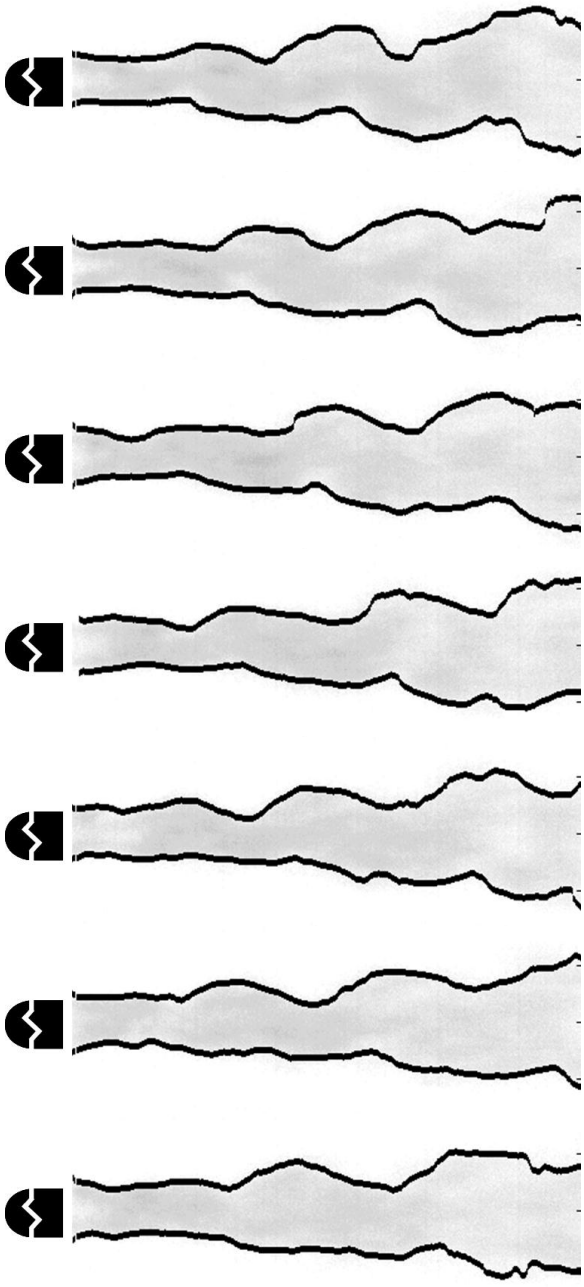

Figure A-9. Sequence of flame images for $\rho_u/\rho_b = 2.0$, spaced by 0.667 ms

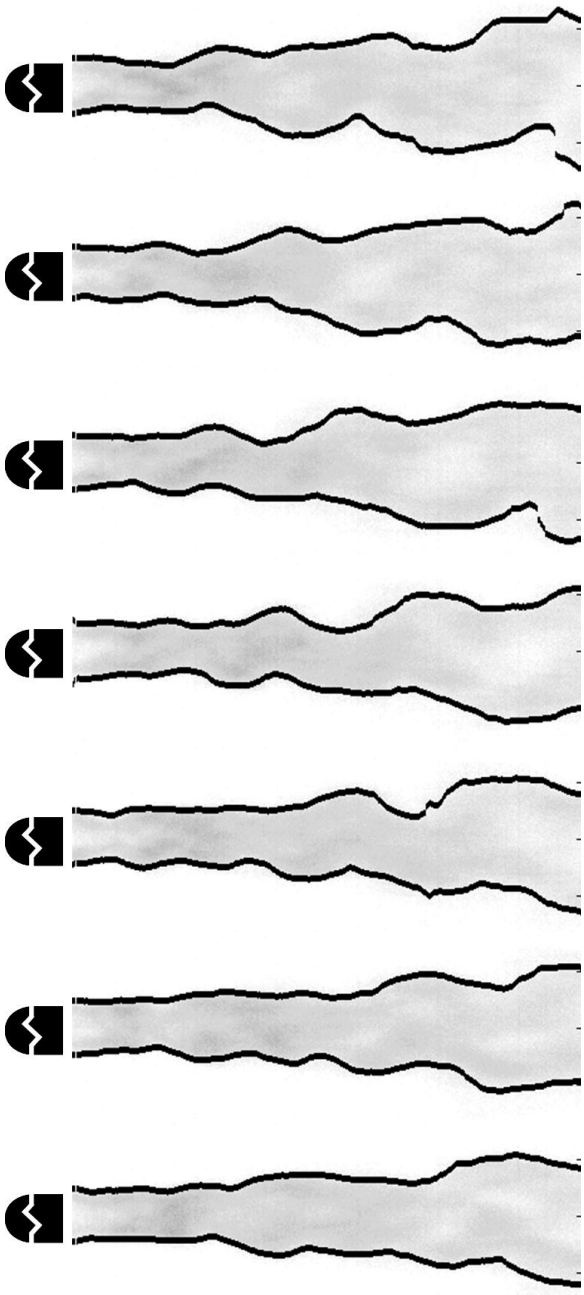

Figure A-10. Sequence of flame images for $\rho_u/\rho_b = 2.2$, spaced by 0.667 ms

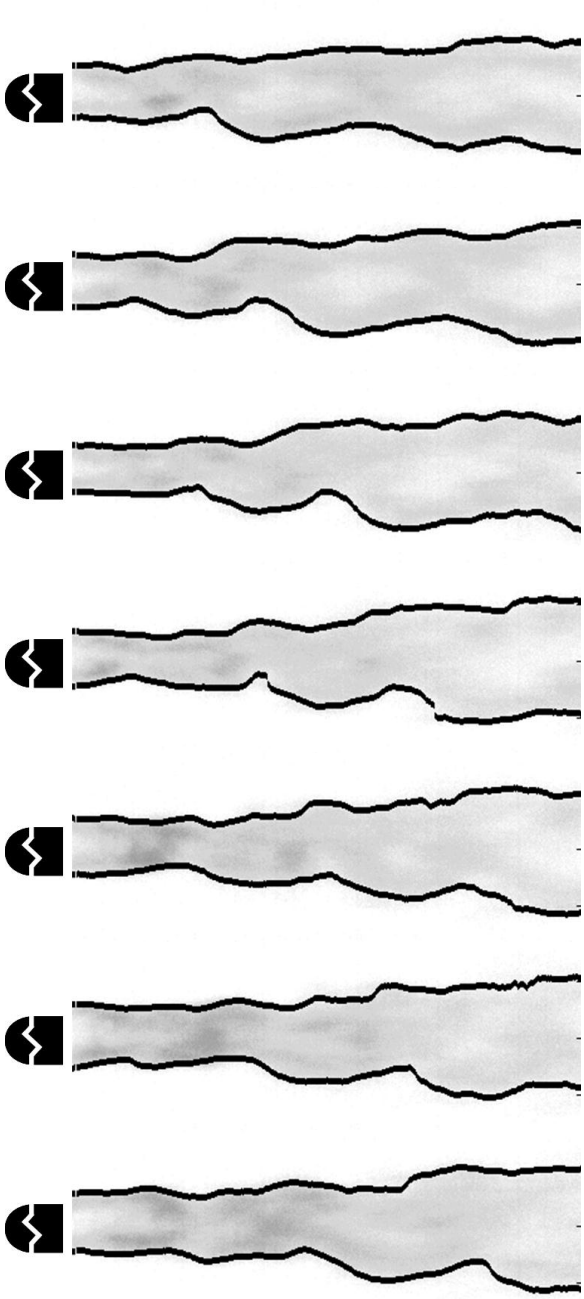

Figure A-11. Sequence of flame images for $\rho_u/\rho_b = 2.4$, spaced by 0.667 ms

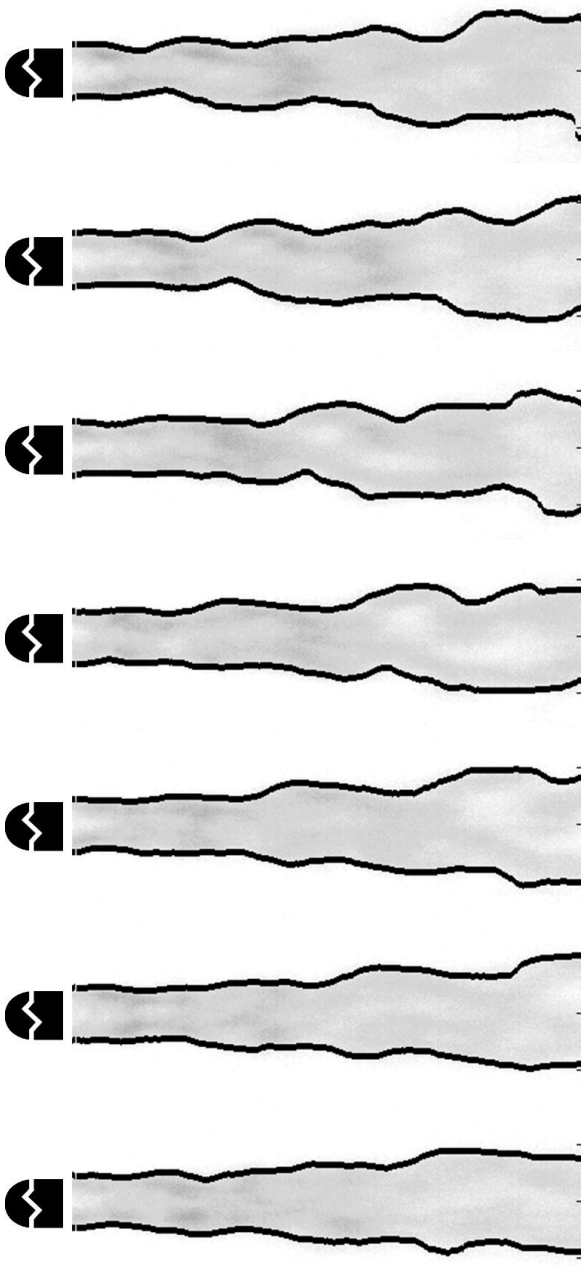

Figure A-12. Sequence of flame images for $\rho_u/\rho_b = 2.7$, spaced by 0.667 ms

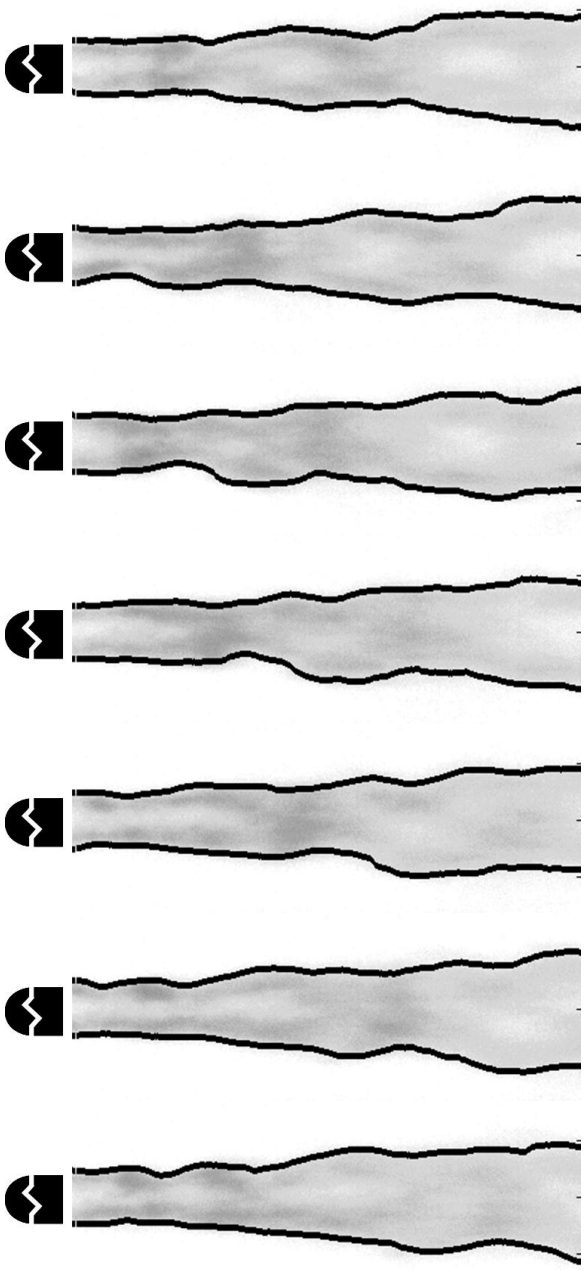

Figure A-13. Sequence of flame images for $\rho_u/\rho_b = 2.9$, spaced by 0.667 ms

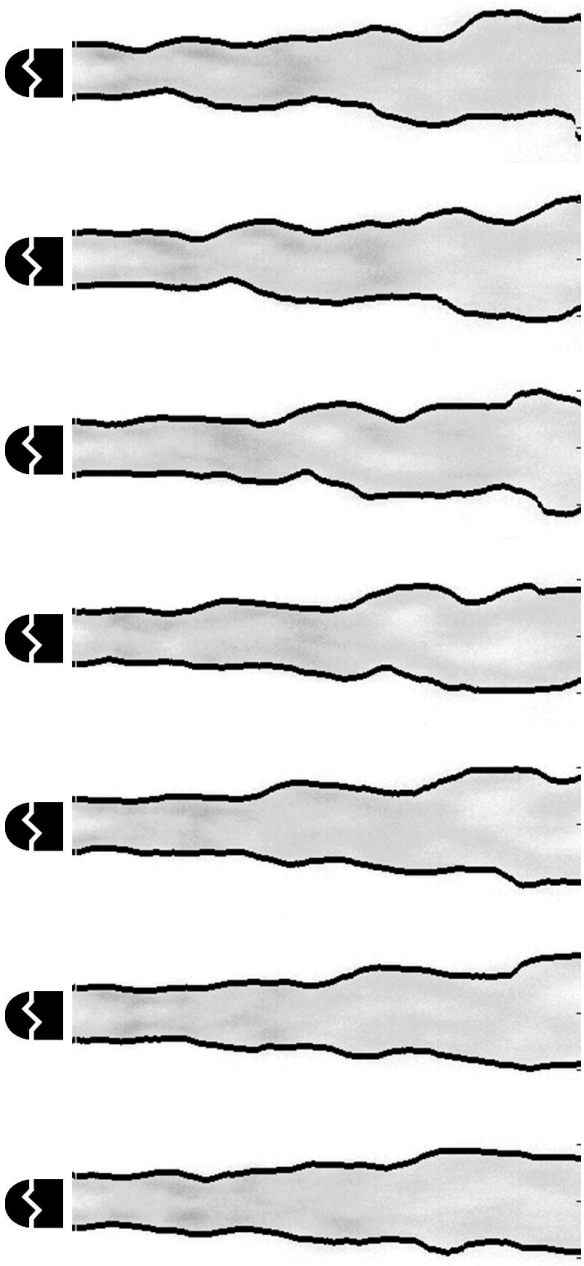

Figure A-14. Sequence of flame images for $\rho_u/\rho_b = 3.2$, spaced by 0.667 ms

A.3 *Flame Displacement Spectra: Waterfall Plots*

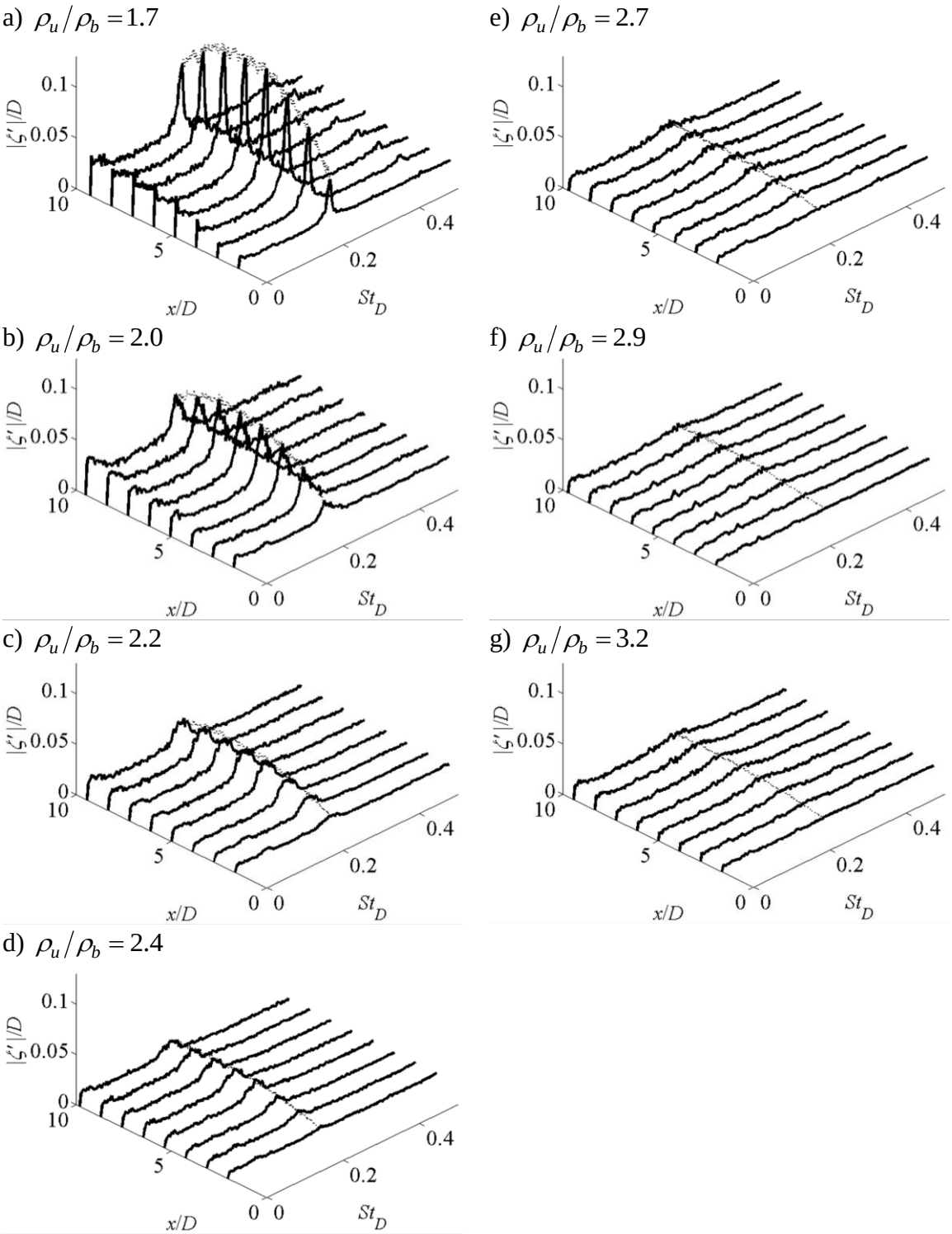

Figure A-15. Axial development of flame displacement spectra for the ballistic bluff body at $U_{lip} = 50$ m/s for several values of ρ_u/ρ_b (labeled above plots)

A.4 *Spatial Growth of Forced Flow Response*

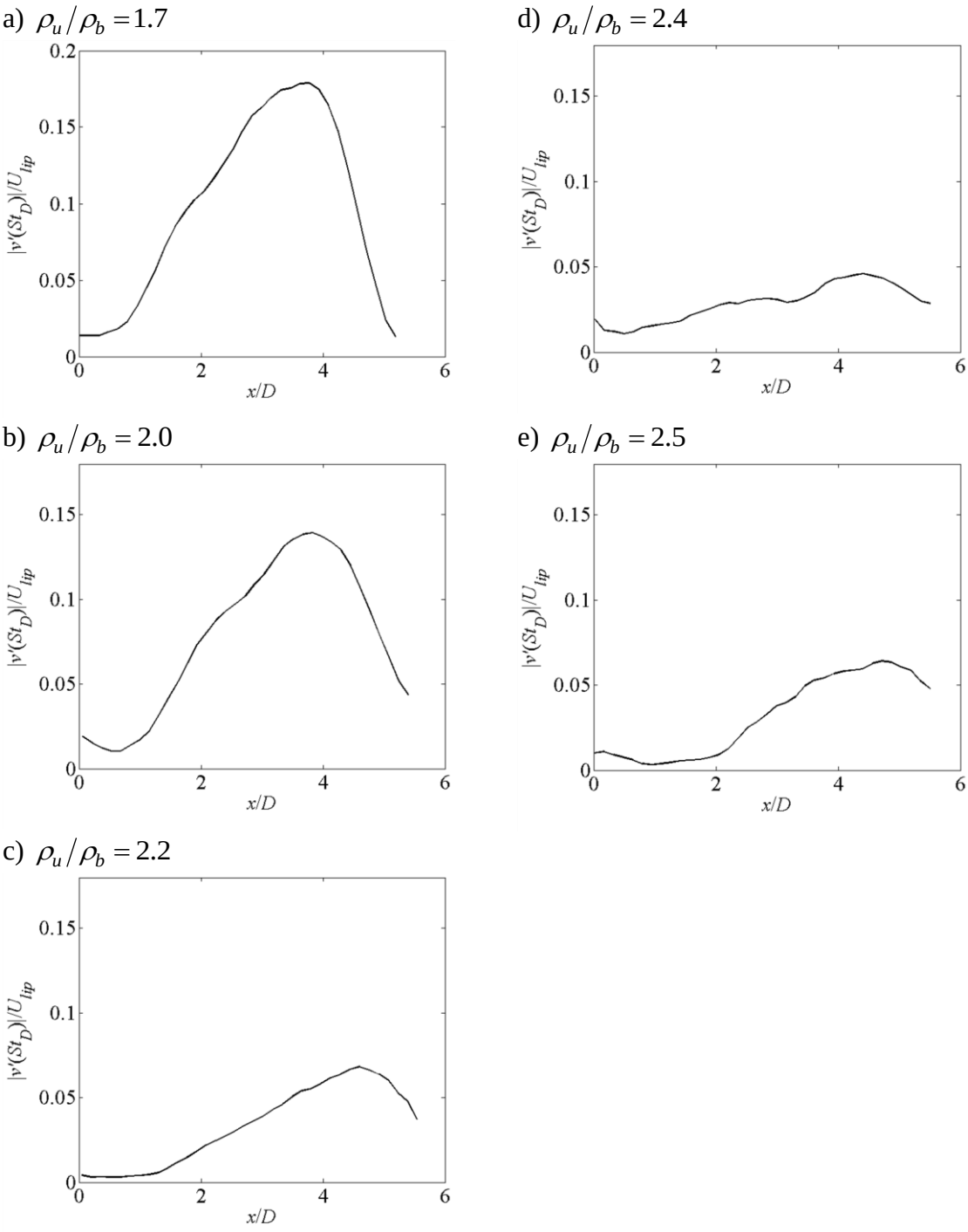

Figure A-16. Centerline transverse velocity fluctuation amplitude at $St_D = 0.24$ for the ballistic bluff body at $U_{lip} = 50$ m/s and several values of ρ_u/ρ_b (noted above figures)

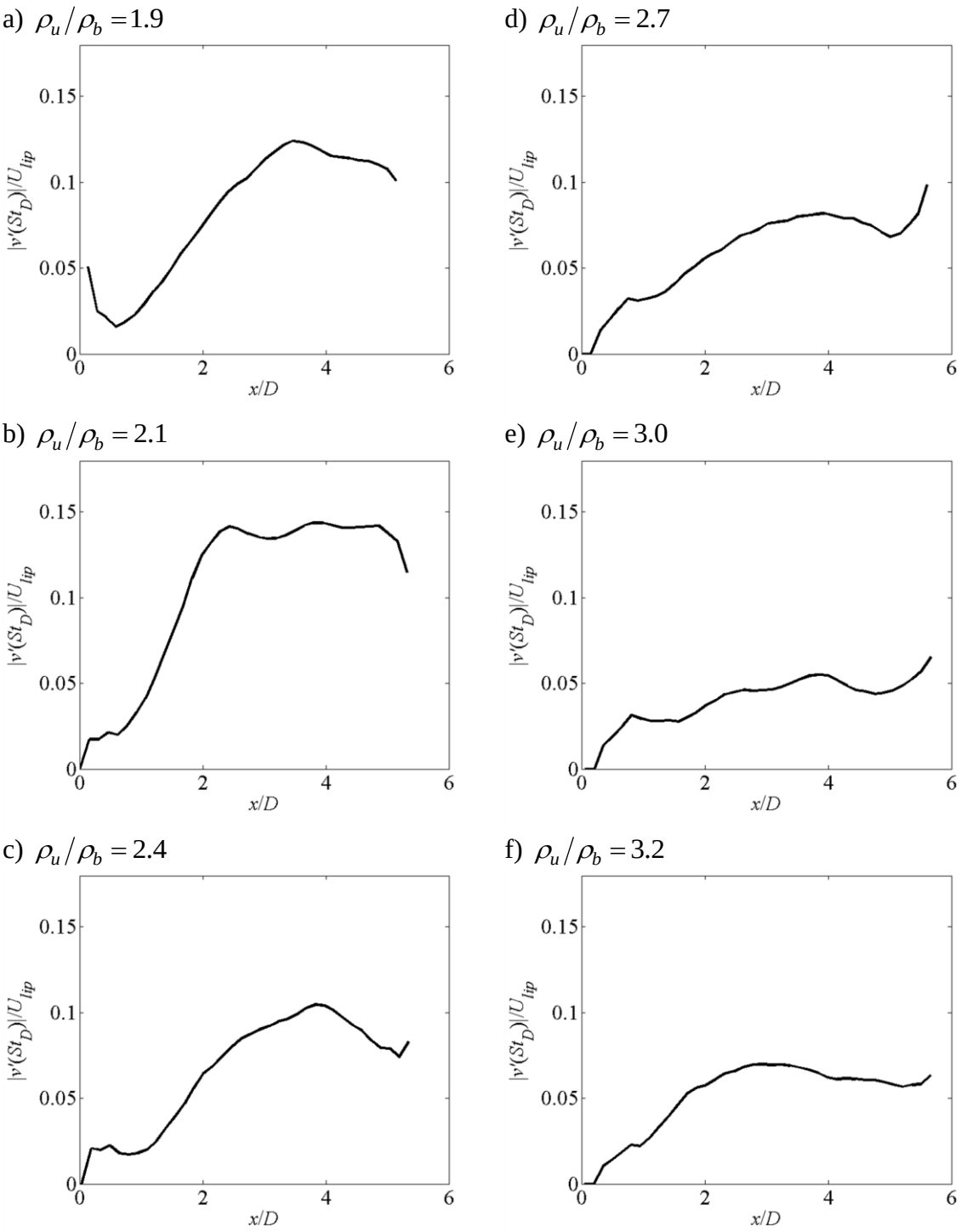

Figure A-17. Centerline transverse velocity fluctuation amplitude at $St_D = 0.24$ for the ballistic bluff body at $U_{lip} = 20$ m/s and several values of ρ_u/ρ_b (noted above figures)

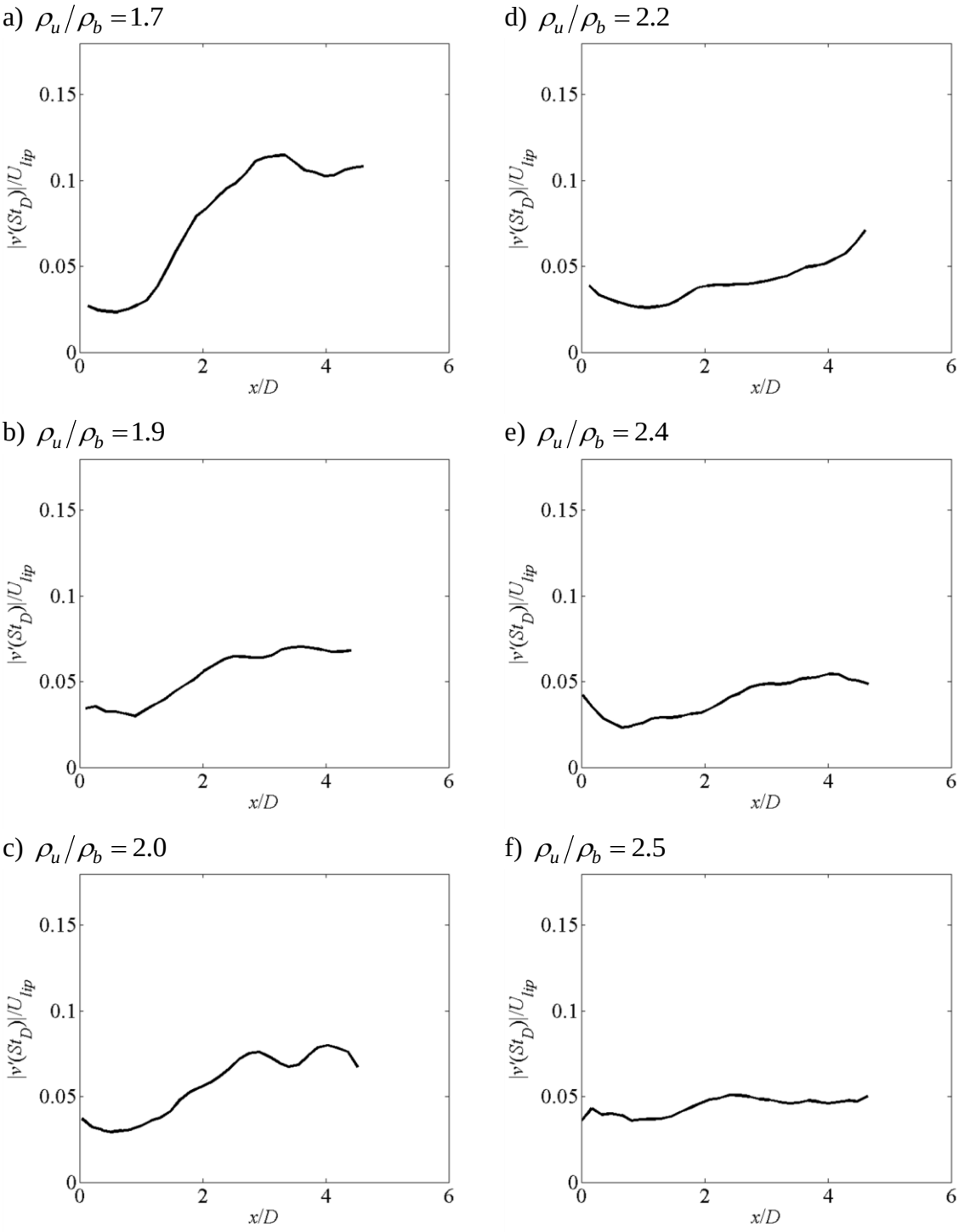

Figure A-18. Centerline transverse velocity fluctuation amplitude at $St_D = 0.24$ for the v-gutter at $U_{lip} = 50$ m/s and several values of ρ_u/ρ_b (noted above figures)

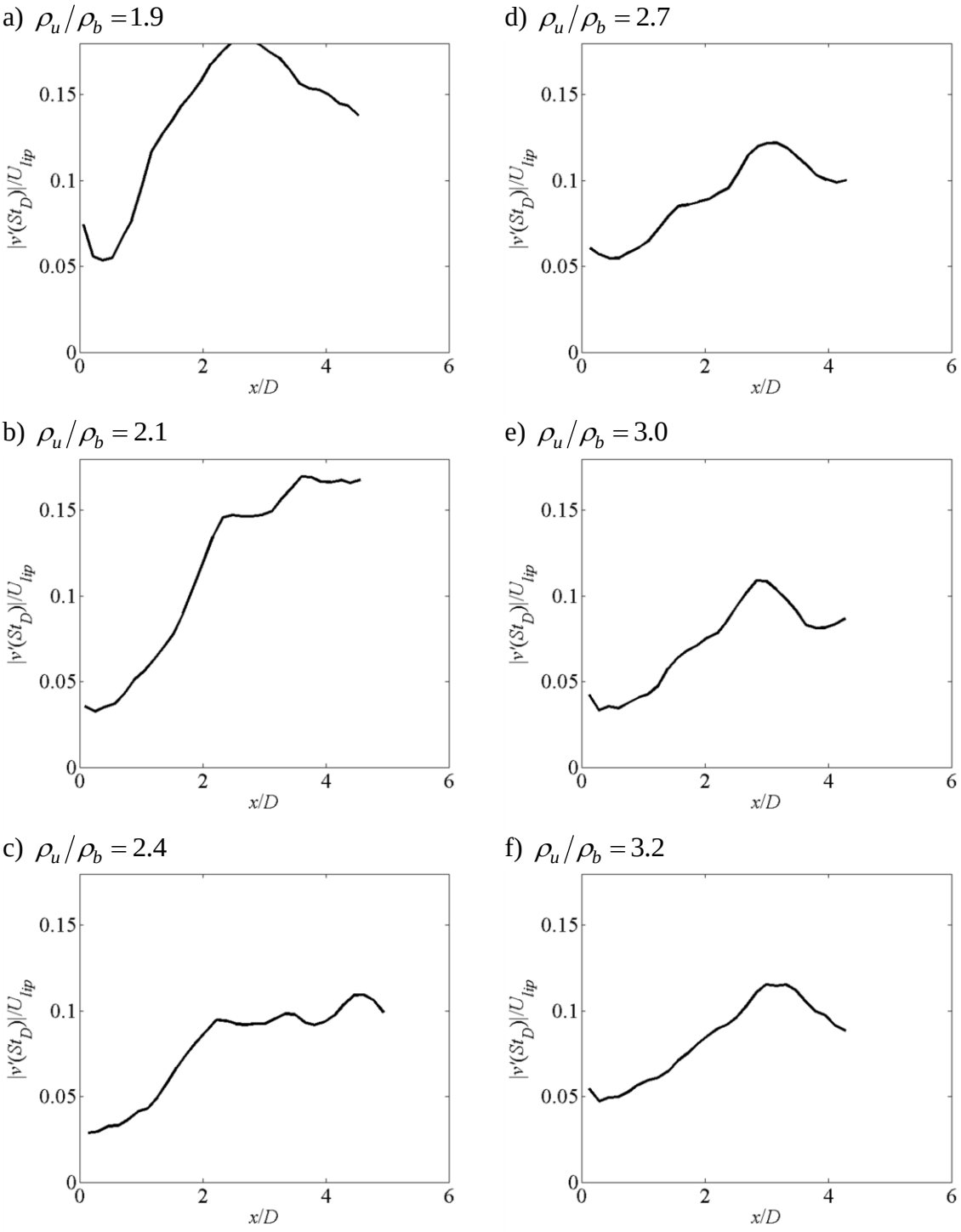

Figure A-19. Centerline transverse velocity fluctuation amplitude at $St_D = 0.24$ for the v-gutter at $U_{lip} = 20$ m/s and several values of ρ_u/ρ_b (noted above figures)

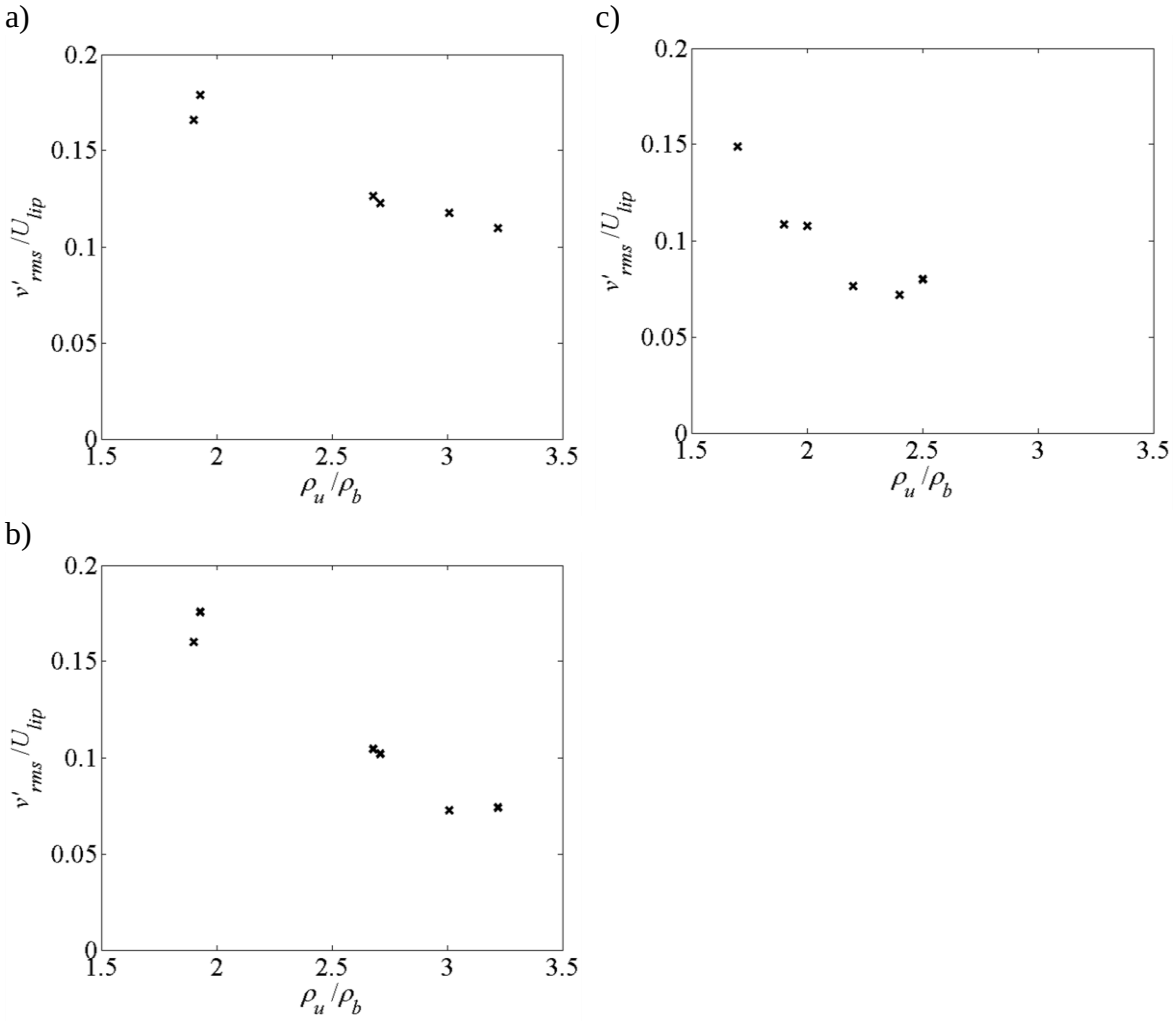

Figure A-20. Integrated spectral energy of centerline transverse velocity fluctuation about $St_D = 0.24$, expressed as an rms according to Parseval's theorem, for a) v-gutter at $U_{lip} = 20$ m/s, b) v-gutter at $U_{lip} = 50$, ballistic bluff body at $U_{lip} = 20$

APPENDIX B. SUPPLEMENTAL DATA FROM HYDRODYNAMIC STABILITY ANALYSIS

B.1 *Direct and Adjoint Global Modes*

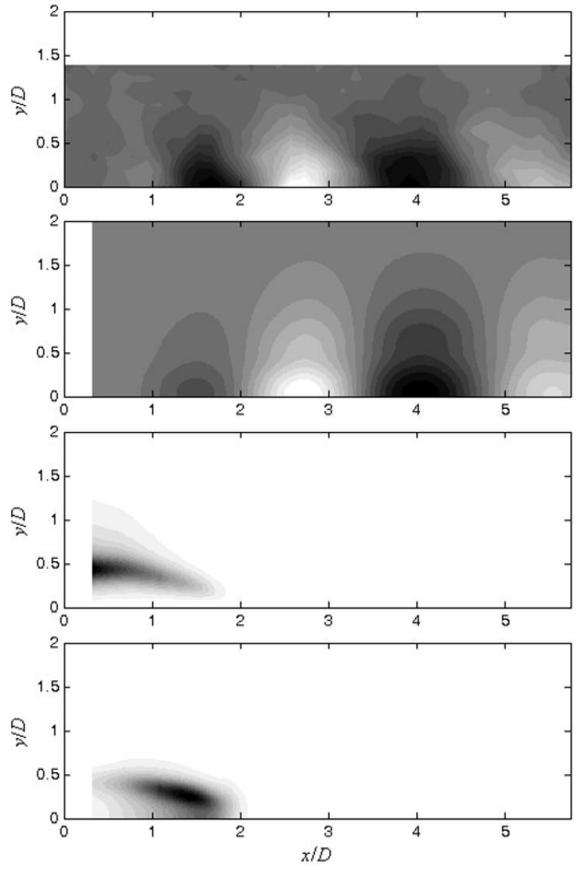

Figure B-1. Comparison of a) Measured global mode shape from conditionally averaged transverse velocity, b) direct global mode shape (transverse velocity) from detailed stability analysis, c) magnitude of adjoint global mode (axial velocity) from detailed stability analysis, d) magnitude of maximum energy of overlap of direct and adjoint global modes. Conditions are ρ_u/ρ_b = 1.7, U_{lip} = 28 m/s

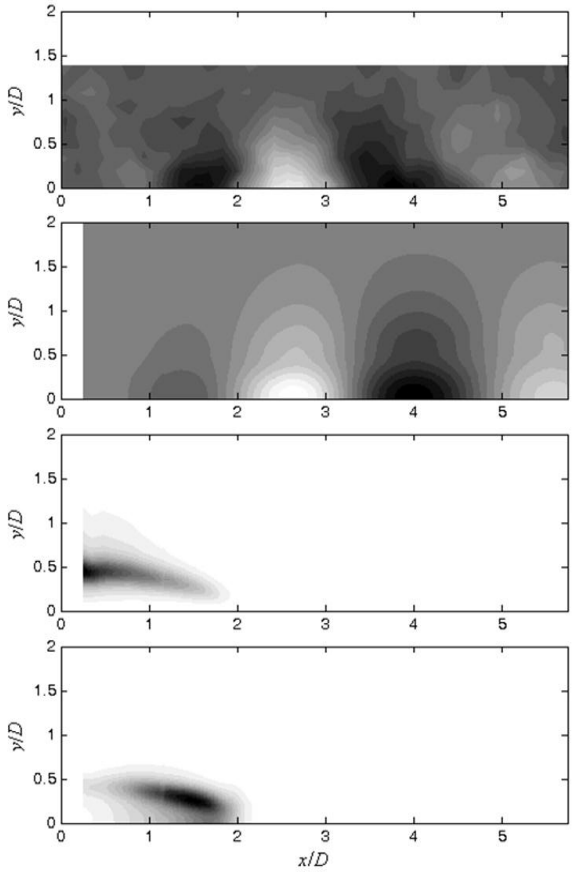

Figure B-2. Comparison of a) Measured global mode shape from conditionally averaged transverse velocity, b) direct global mode shape (transverse velocity) from detailed stability analysis, c) magnitude of adjoint global mode (axial velocity) from detailed stability analysis, d) magnitude of maximum energy of overlap of direct and adjoint global modes. Conditions are ρ_u/ρ_b = 1.7, U_{lip} = 37 m/s

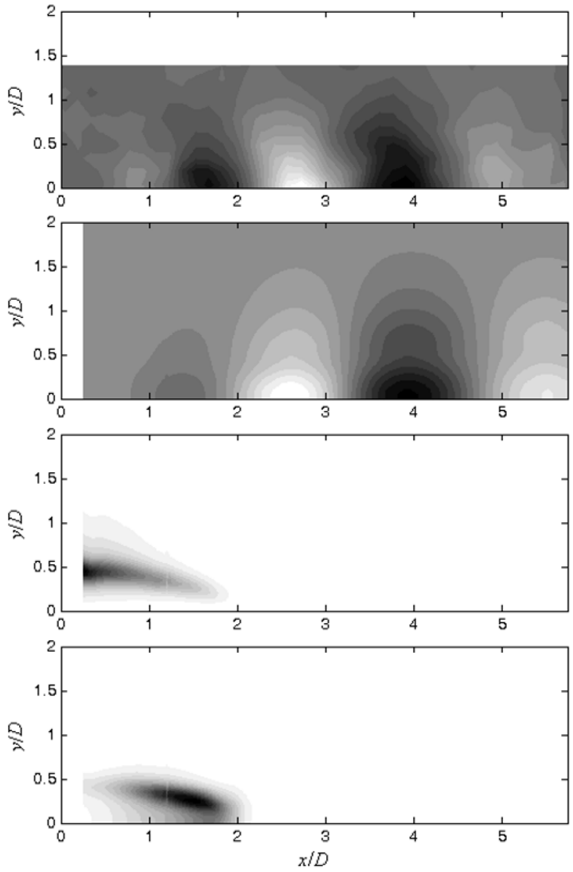

Figure B-3. Comparison of a) Measured global mode shape from conditionally averaged transverse velocity, b) direct global mode shape (transverse velocity) from detailed stability analysis, c) magnitude of adjoint global mode (axial velocity) from detailed stability analysis, d) magnitude of maximum energy of overlap of direct and adjoint global modes. Conditions are ρ_u/ρ_b = 1.7, U_{lip} = 40 m/s

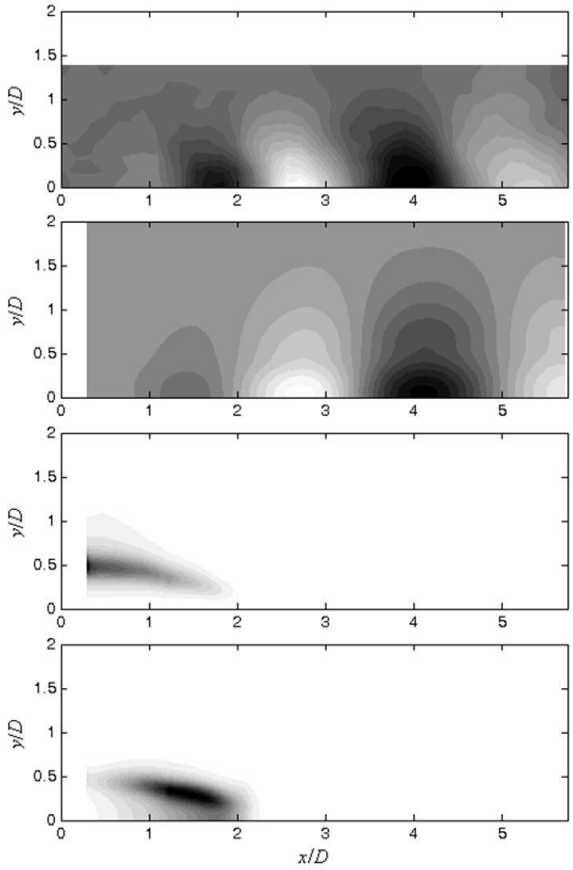

Figure B-4. Comparison of a) Measured global mode shape from conditionally averaged transverse velocity, b) direct global mode shape (transverse velocity) from detailed stability analysis, c) magnitude of adjoint global mode (axial velocity) from detailed stability analysis, d) magnitude of maximum energy of overlap of direct and adjoint global modes. Conditions are ρ_u/ρ_b = 1.7, U_{lip} = 44 m/s

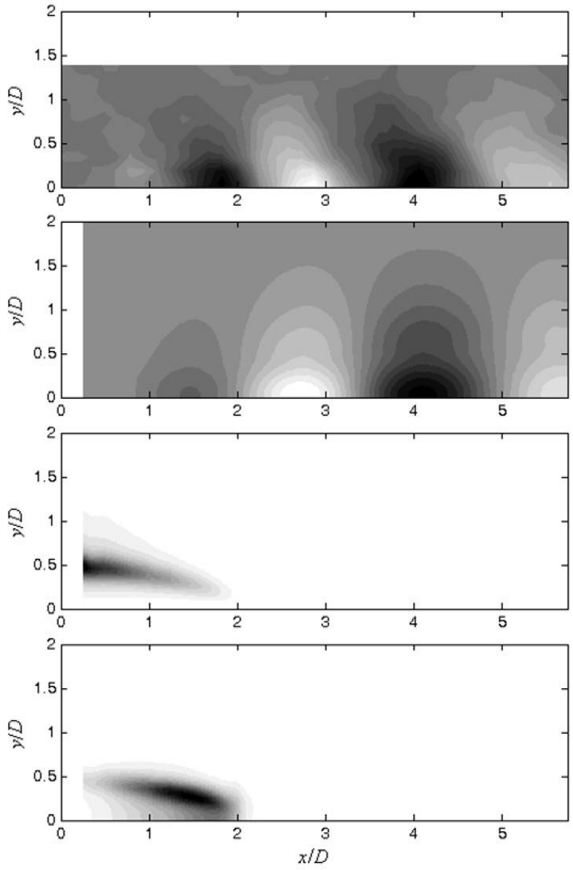

Figure B-5. Comparison of a) Measured global mode shape from conditionally averaged transverse velocity, b) direct global mode shape (transverse velocity) from detailed stability analysis, c) magnitude of adjoint global mode (axial velocity) from detailed stability analysis, d) magnitude of maximum energy of overlap of direct and adjoint global modes. Conditions are ρ_u/ρ_b = 1.7, U_{lip} = 44 m/s

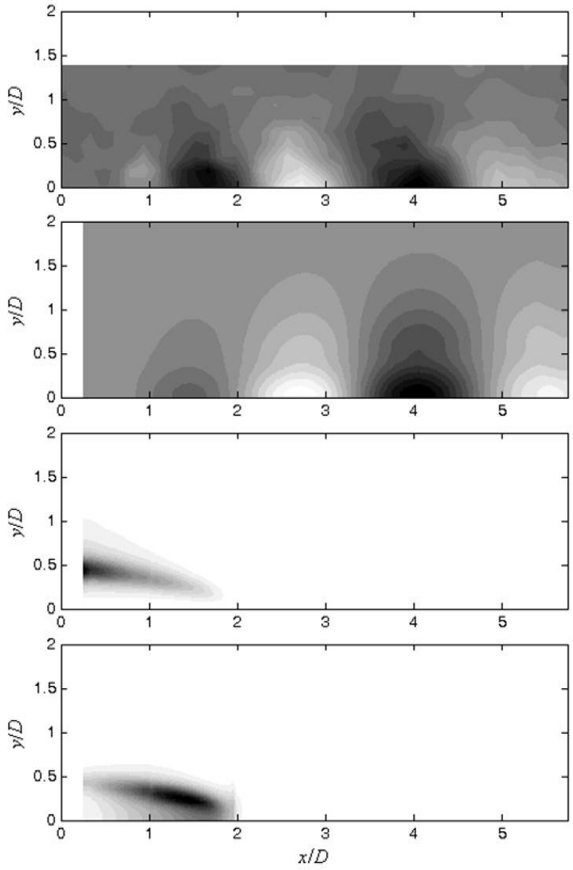

Figure B-6. Comparison of a) Measured global mode shape from conditionally averaged transverse velocity, b) direct global mode shape (transverse velocity) from detailed stability analysis, c) magnitude of adjoint global mode (axial velocity) from detailed stability analysis, d) magnitude of maximum energy of overlap of direct and adjoint global modes. Conditions are ρ_u/ρ_b = 1.7, U_{lip} = 48 m/s

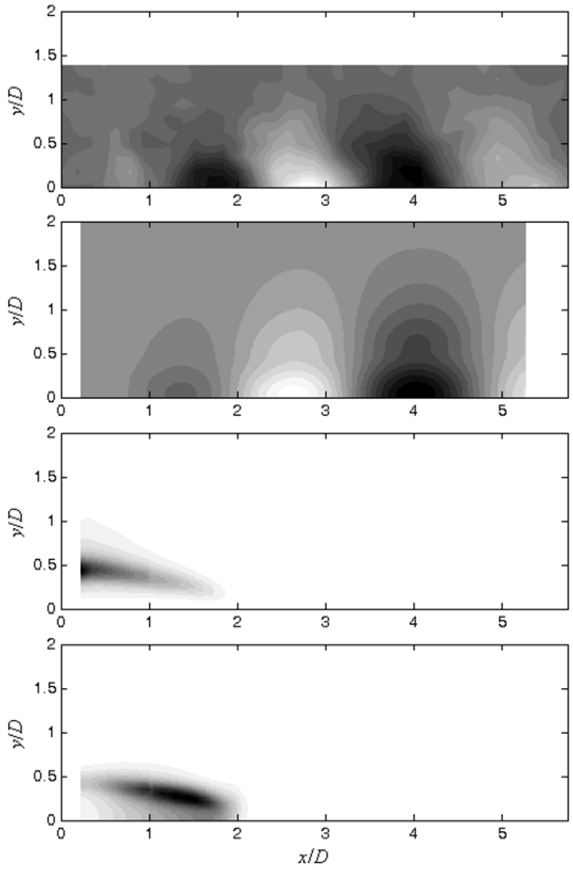

Figure B-7. Comparison of a) Measured global mode shape from conditionally averaged transverse velocity, b) direct global mode shape (transverse velocity) from detailed stability analysis, c) magnitude of adjoint global mode (axial velocity) from detailed stability analysis, d) magnitude of maximum energy of overlap of direct and adjoint global modes. Conditions are ρ_u/ρ_b = 1.7, U_{lip} = 51 m/s

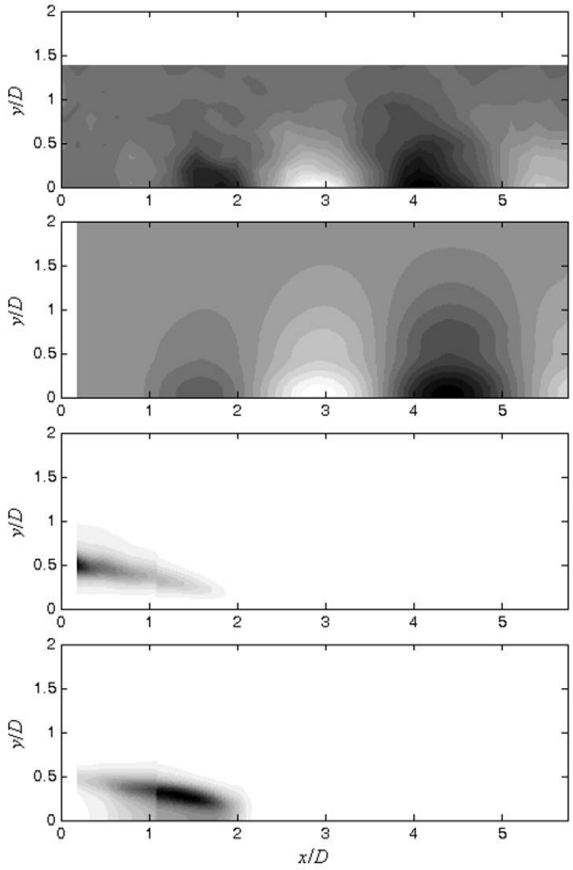

Figure B-8. Comparison of a) Measured global mode shape from conditionally averaged transverse velocity, b) direct global mode shape (transverse velocity) from detailed stability analysis, c) magnitude of adjoint global mode (axial velocity) from detailed stability analysis, d) magnitude of maximum energy of overlap of direct and adjoint global modes. Conditions are ρ_u/ρ_b = 1.7, U_{lip} = 56 m/s

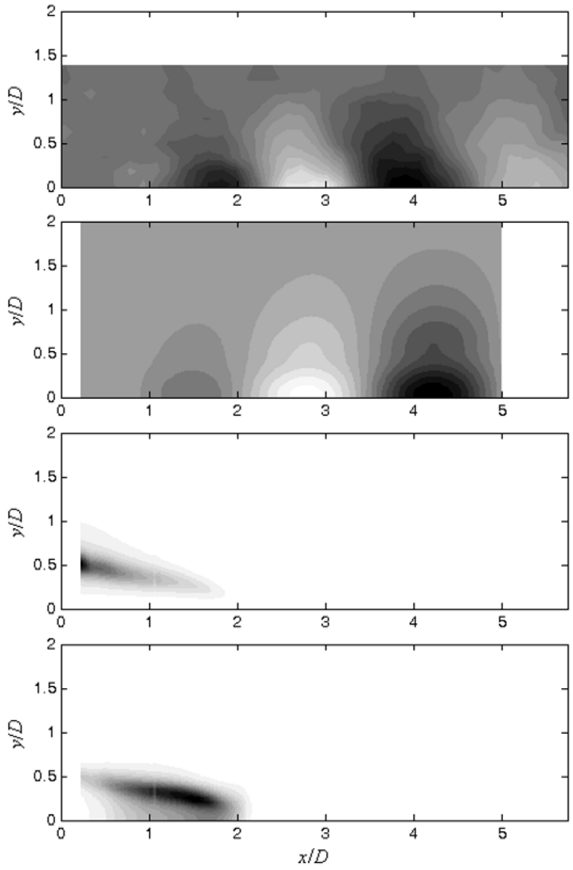

Figure B-9. Comparison of a) Measured global mode shape from conditionally averaged transverse velocity, b) direct global mode shape (transverse velocity) from detailed stability analysis, c) magnitude of adjoint global mode (axial velocity) from detailed stability analysis, d) magnitude of maximum energy of overlap of direct and adjoint global modes. Conditions are ρ_u/ρ_b = 1.7, U_{lip} = 60 m/s

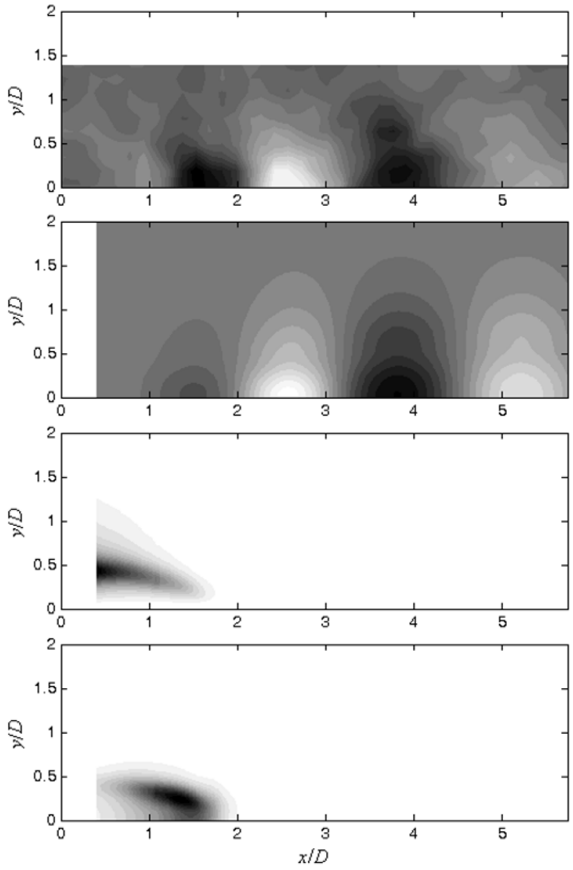

Figure B-10. Comparison of a) Measured global mode shape from conditionally averaged transverse velocity, b) direct global mode shape (transverse velocity) from detailed stability analysis, c) magnitude of adjoint global mode (axial velocity) from detailed stability analysis, d) magnitude of maximum energy of overlap of direct and adjoint global modes. Conditions are ρ_u/ρ_b = 1.9, U_{lip} = 29 m/s

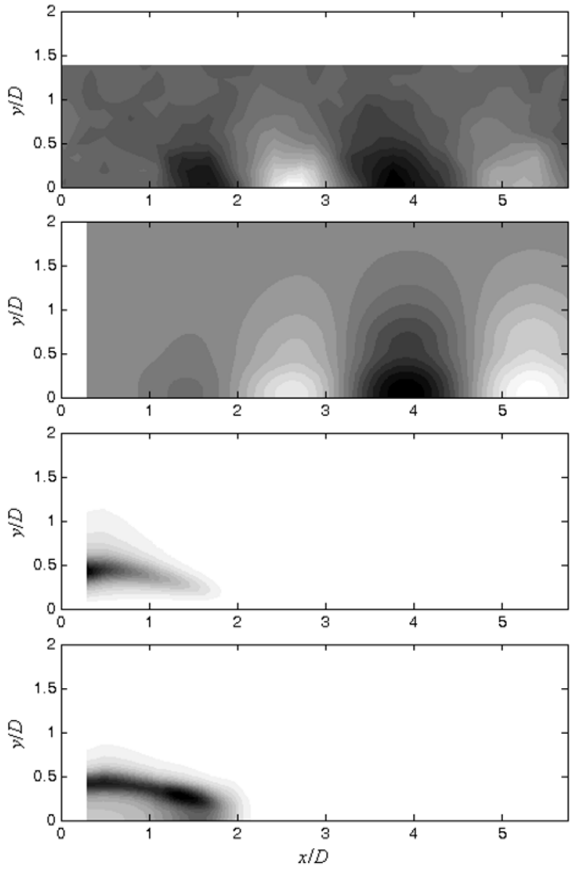

Figure B-11. Comparison of a) Measured global mode shape from conditionally averaged transverse velocity, b) direct global mode shape (transverse velocity) from detailed stability analysis, c) magnitude of adjoint global mode (axial velocity) from detailed stability analysis, d) magnitude of maximum energy of overlap of direct and adjoint global modes. Conditions are ρ_u/ρ_b = 1.9, U_{lip} = 33 m/s

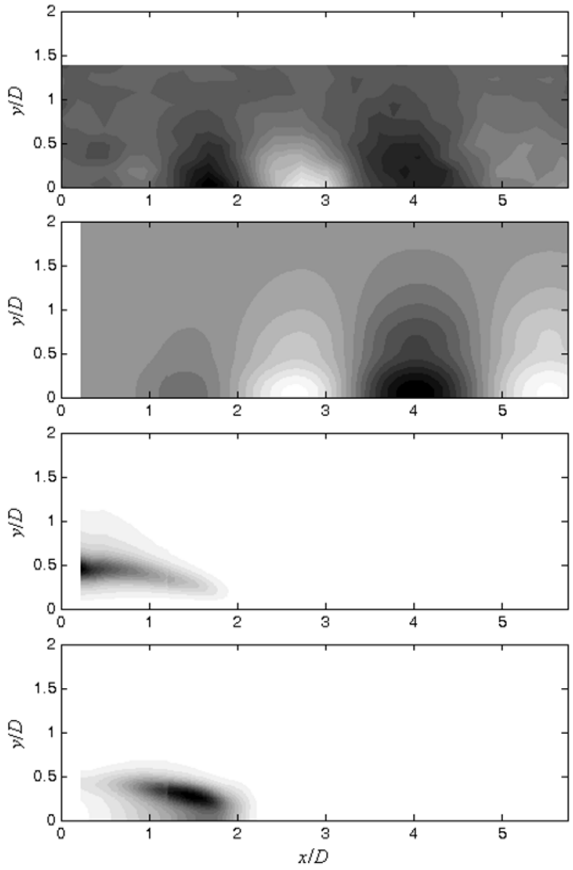

Figure B-12. Comparison of a) Measured global mode shape from conditionally averaged transverse velocity, b) direct global mode shape (transverse velocity) from detailed stability analysis, c) magnitude of adjoint global mode (axial velocity) from detailed stability analysis, d) magnitude of maximum energy of overlap of direct and adjoint global modes. Conditions are ρ_u/ρ_b = 1.9, U_{lip} = 37 m/s

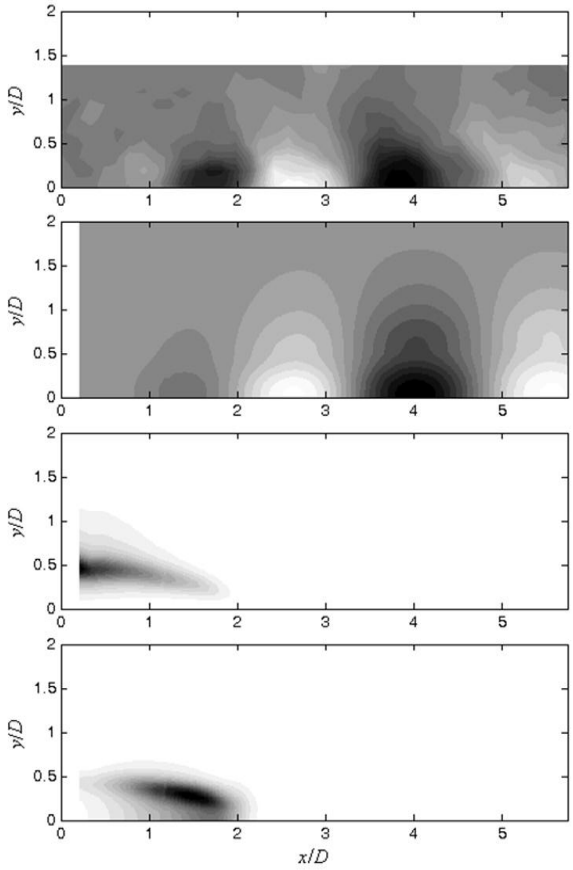

Figure B-13. Comparison of a) Measured global mode shape from conditionally averaged transverse velocity, b) direct global mode shape (transverse velocity) from detailed stability analysis, c) magnitude of adjoint global mode (axial velocity) from detailed stability analysis, d) magnitude of maximum energy of overlap of direct and adjoint global modes. Conditions are ρ_u/ρ_b = 1.9, U_{lip} = 39 m/s

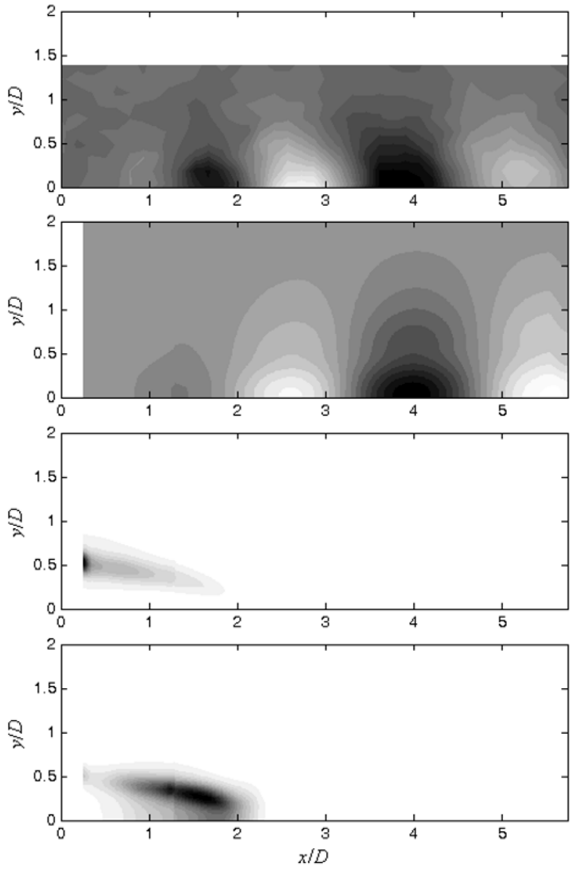

Figure B-14. Comparison of a) Measured global mode shape from conditionally averaged transverse velocity, b) direct global mode shape (transverse velocity) from detailed stability analysis, c) magnitude of adjoint global mode (axial velocity) from detailed stability analysis, d) magnitude of maximum energy of overlap of direct and adjoint global modes. Conditions are ρ_u/ρ_b = 1.9, U_{lip} = 43 m/s

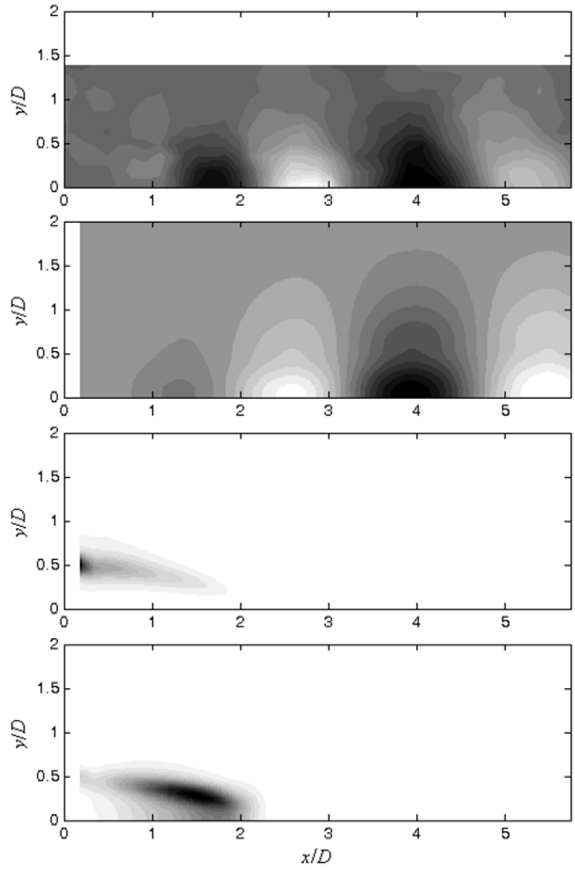

Figure B-15. Comparison of a) Measured global mode shape from conditionally averaged transverse velocity, b) direct global mode shape (transverse velocity) from detailed stability analysis, c) magnitude of adjoint global mode (axial velocity) from detailed stability analysis, d) magnitude of maximum energy of overlap of direct and adjoint global modes. Conditions are ρ_u/ρ_b = 1.9, U_{lip} = 44 m/s

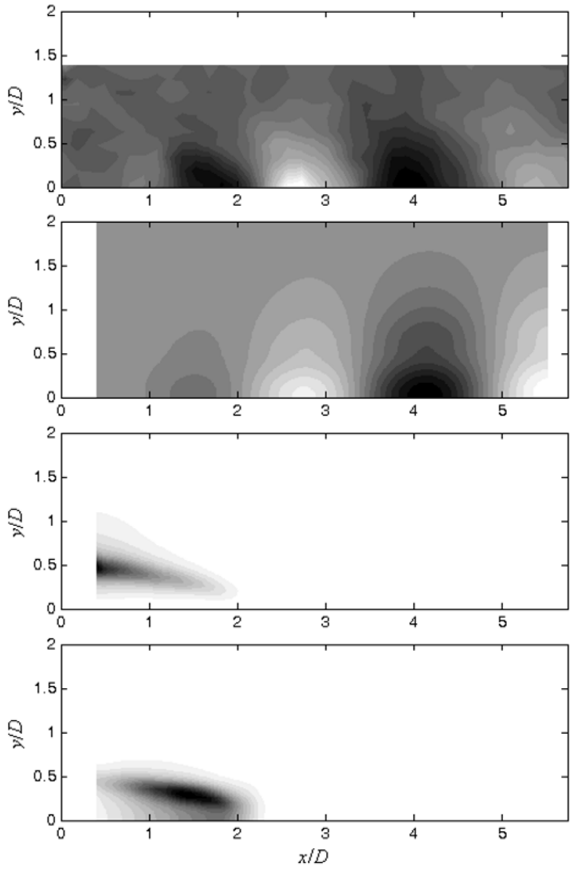

Figure B-16. Comparison of a) Measured global mode shape from conditionally averaged transverse velocity, b) direct global mode shape (transverse velocity) from detailed stability analysis, c) magnitude of adjoint global mode (axial velocity) from detailed stability analysis, d) magnitude of maximum energy of overlap of direct and adjoint global modes. Conditions are ρ_u/ρ_b = 1.9, U_{lip} = 47 m/s

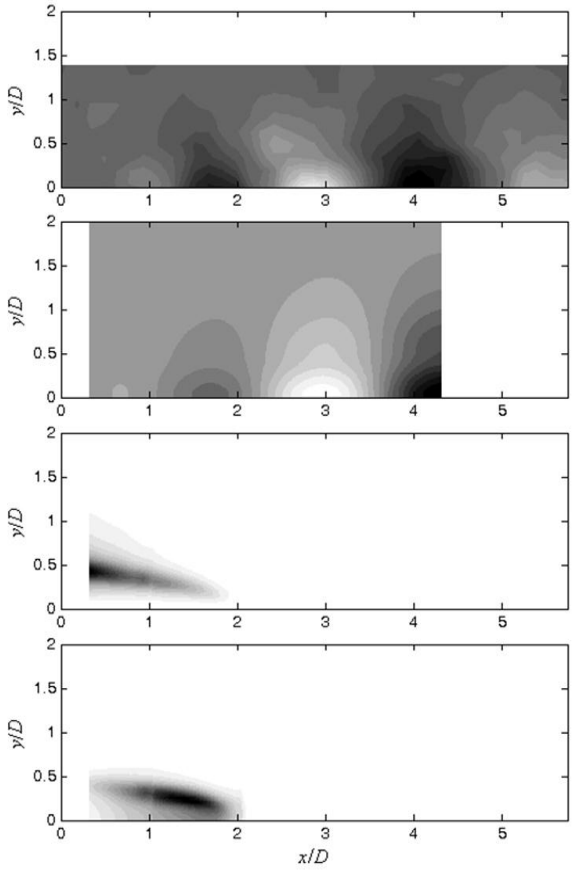

Figure B-17. Comparison of a) Measured global mode shape from conditionally averaged transverse velocity, b) direct global mode shape (transverse velocity) from detailed stability analysis, c) magnitude of adjoint global mode (axial velocity) from detailed stability analysis, d) magnitude of maximum energy of overlap of direct and adjoint global modes. Conditions are ρ_u/ρ_b = 1.9, U_{lip} = 57 m/s

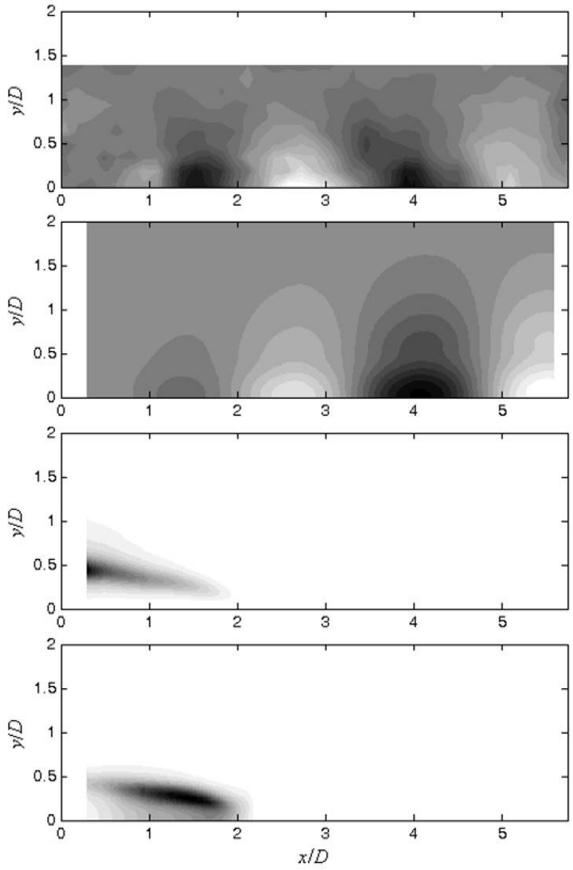

Figure B-18. Comparison of a) Measured global mode shape from conditionally averaged transverse velocity, b) direct global mode shape (transverse velocity) from detailed stability analysis, c) magnitude of adjoint global mode (axial velocity) from detailed stability analysis, d) magnitude of maximum energy of overlap of direct and adjoint global modes. Conditions are ρ_u/ρ_b = 1.9, U_{lip} = 58 m/s

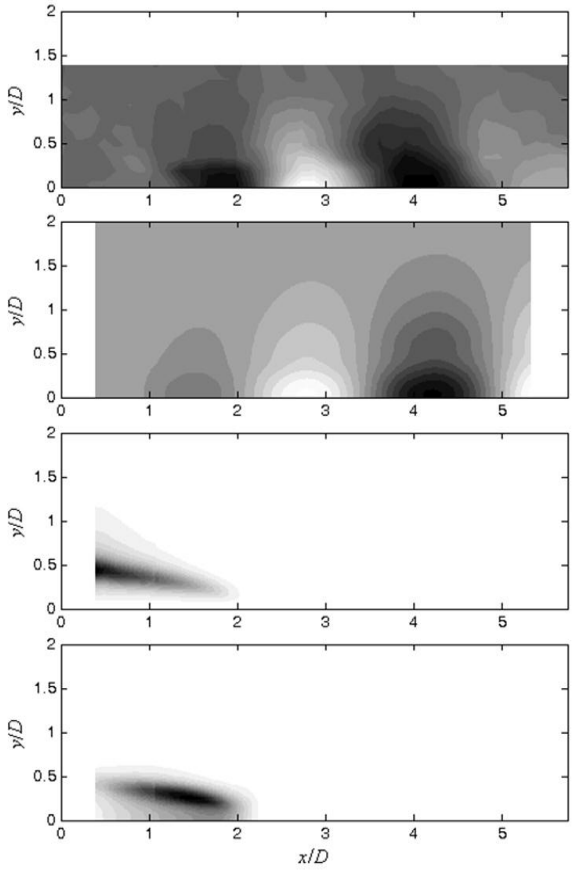

Figure B-19. Comparison of a) Measured global mode shape from conditionally averaged transverse velocity, b) direct global mode shape (transverse velocity) from detailed stability analysis, c) magnitude of adjoint global mode (axial velocity) from detailed stability analysis, d) magnitude of maximum energy of overlap of direct and adjoint global modes. Conditions are ρ_u/ρ_b = 1.9, U_{lip} = 64 m/s

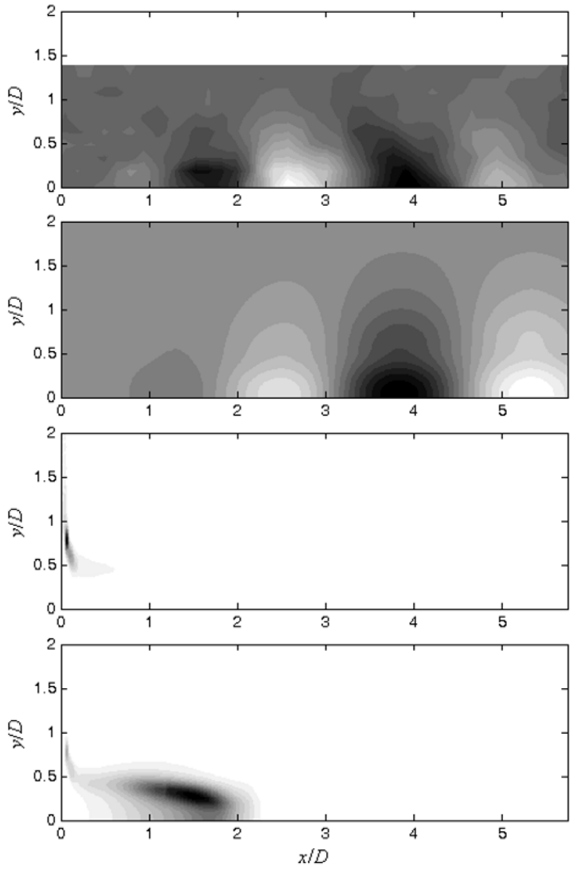

Figure B-20. Comparison of a) Measured global mode shape from conditionally averaged transverse velocity, b) direct global mode shape (transverse velocity) from detailed stability analysis, c) magnitude of adjoint global mode (axial velocity) from detailed stability analysis, d) magnitude of maximum energy of overlap of direct and adjoint global modes. Conditions are ρ_u/ρ_b = 2.0, U_{lip} = 37 m/s

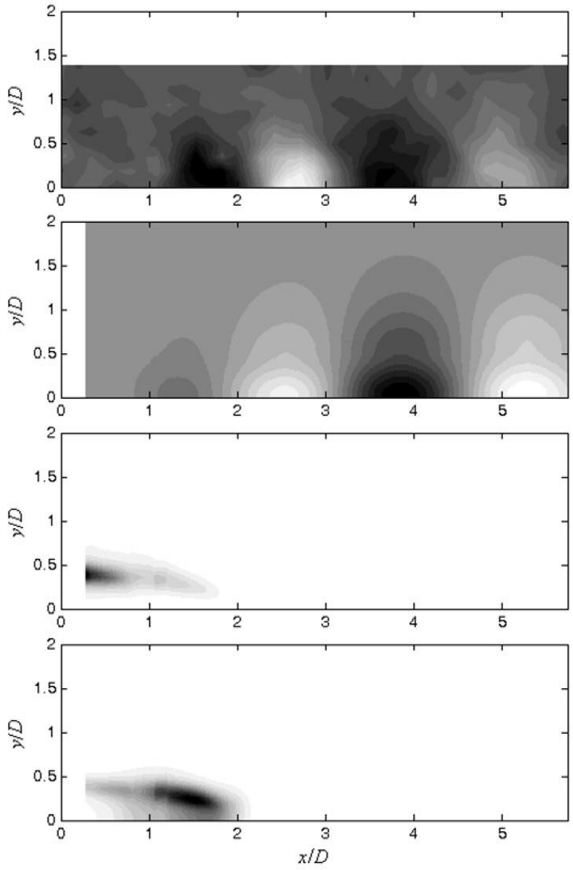

Figure B-21. Comparison of a) Measured global mode shape from conditionally averaged transverse velocity, b) direct global mode shape (transverse velocity) from detailed stability analysis, c) magnitude of adjoint global mode (axial velocity) from detailed stability analysis, d) magnitude of maximum energy of overlap of direct and adjoint global modes. Conditions are ρ_u/ρ_b = 2.0, U_{lip} = 38 m/s

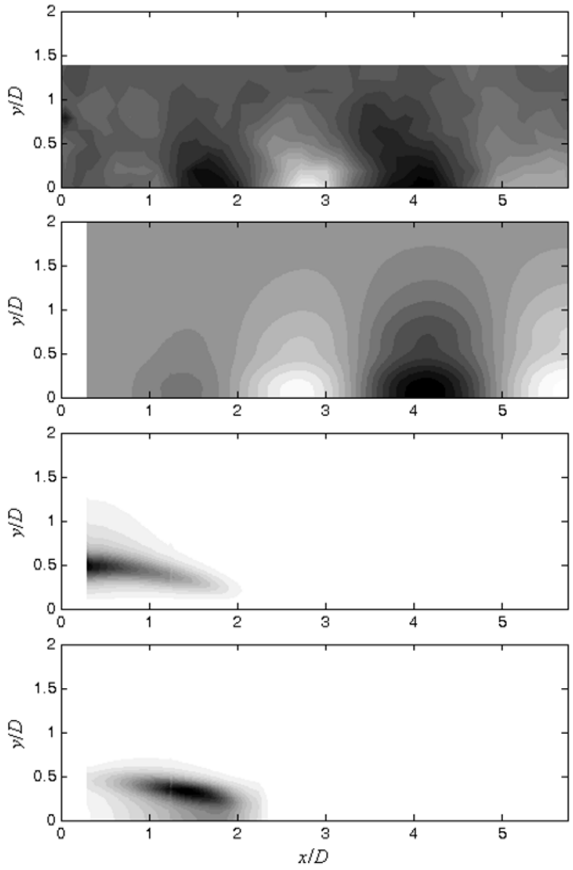

Figure B-22. Comparison of a) Measured global mode shape from conditionally averaged transverse velocity, b) direct global mode shape (transverse velocity) from detailed stability analysis, c) magnitude of adjoint global mode (axial velocity) from detailed stability analysis, d) magnitude of maximum energy of overlap of direct and adjoint global modes. Conditions are ρ_u/ρ_b = 2.0, U_{lip} = 41 m/s

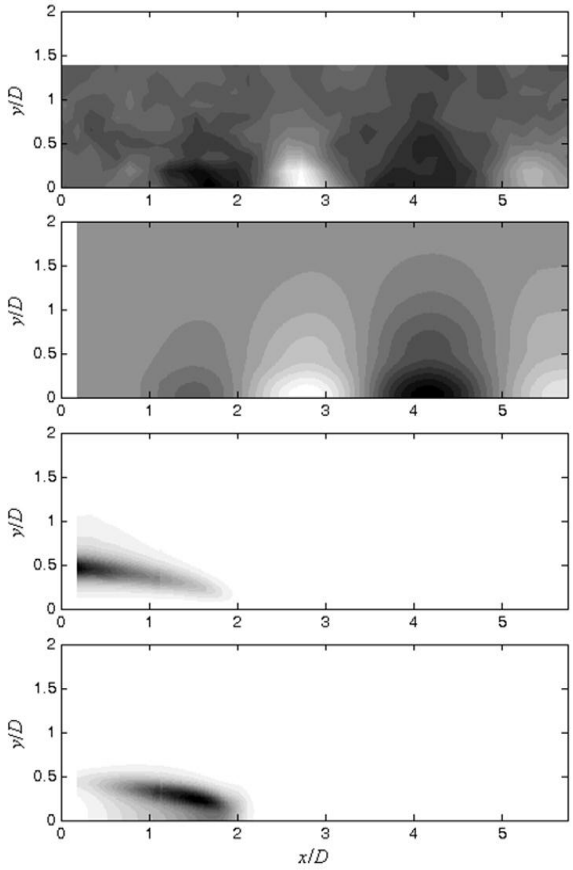

Figure B-23. Comparison of a) Measured global mode shape from conditionally averaged transverse velocity, b) direct global mode shape (transverse velocity) from detailed stability analysis, c) magnitude of adjoint global mode (axial velocity) from detailed stability analysis, d) magnitude of maximum energy of overlap of direct and adjoint global modes. Conditions are ρ_u/ρ_b = 2.0, U_{lip} = 43 m/s

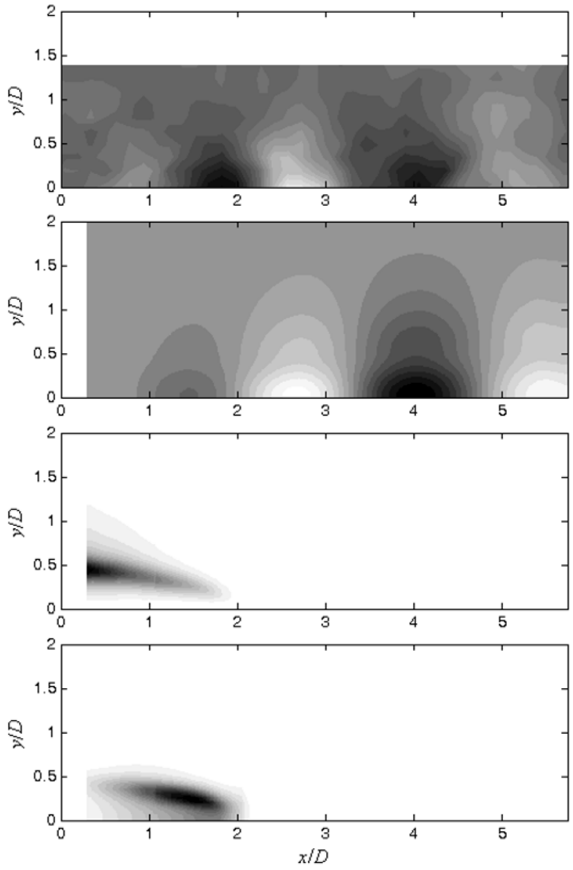

Figure B-24. Comparison of a) Measured global mode shape from conditionally averaged transverse velocity, b) direct global mode shape (transverse velocity) from detailed stability analysis, c) magnitude of adjoint global mode (axial velocity) from detailed stability analysis, d) magnitude of maximum energy of overlap of direct and adjoint global modes. Conditions are ρ_u/ρ_b = 2.0, U_{lip} = 44 m/s

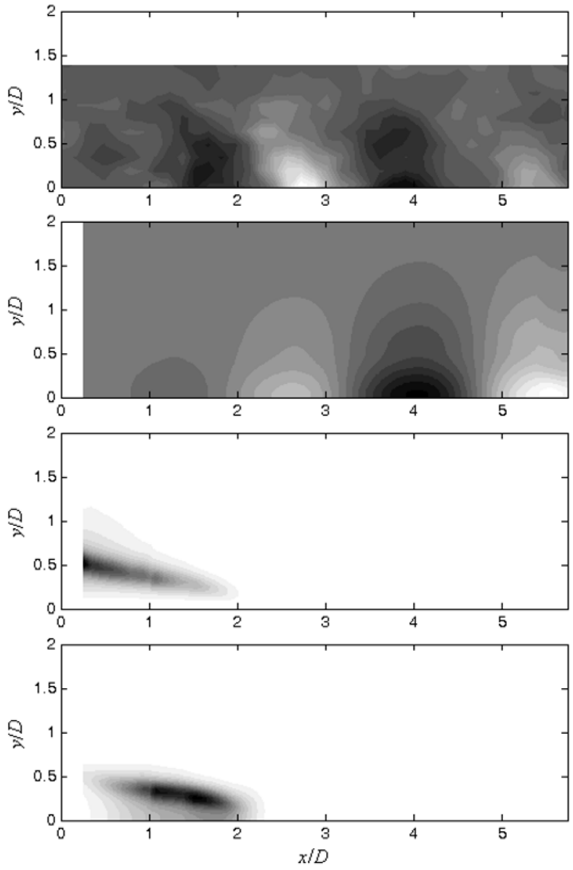

Figure B-25. Comparison of a) Measured global mode shape from conditionally averaged transverse velocity, b) direct global mode shape (transverse velocity) from detailed stability analysis, c) magnitude of adjoint global mode (axial velocity) from detailed stability analysis, d) magnitude of maximum energy of overlap of direct and adjoint global modes. Conditions are ρ_u/ρ_b = 2.0, U_{lip} = 49 m/s

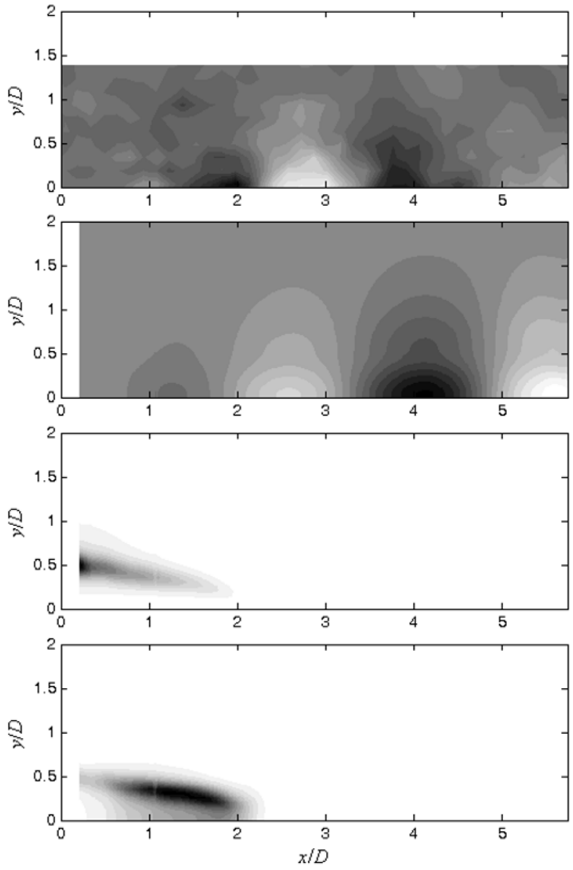

Figure B-26. Comparison of a) Measured global mode shape from conditionally averaged transverse velocity, b) direct global mode shape (transverse velocity) from detailed stability analysis, c) magnitude of adjoint global mode (axial velocity) from detailed stability analysis, d) magnitude of maximum energy of overlap of direct and adjoint global modes. Conditions are ρ_u/ρ_b = 2.0, U_{lip} = 55 m/s

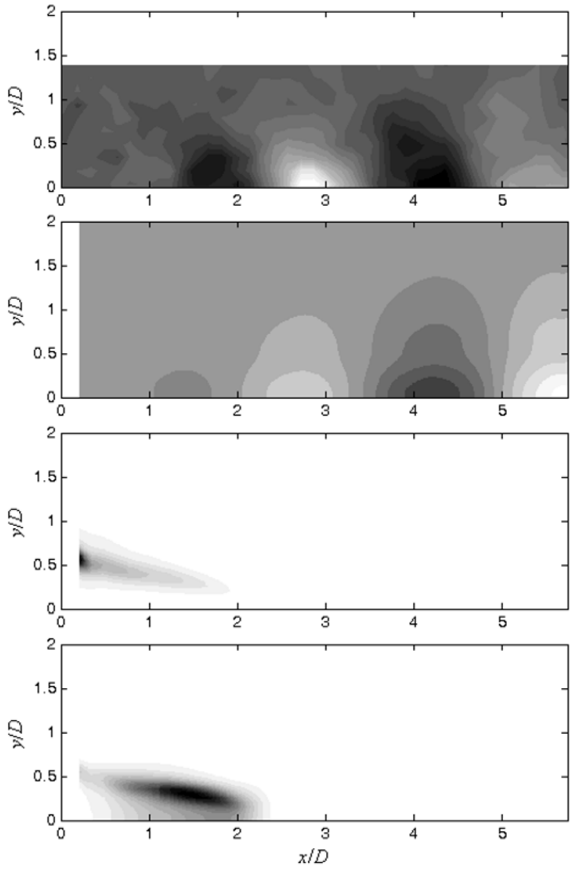

Figure B-27. Comparison of a) Measured global mode shape from conditionally averaged transverse velocity, b) direct global mode shape (transverse velocity) from detailed stability analysis, c) magnitude of adjoint global mode (axial velocity) from detailed stability analysis, d) magnitude of maximum energy of overlap of direct and adjoint global modes. Conditions are ρ_u/ρ_b = 2.0, U_{lip} = 62 m/s

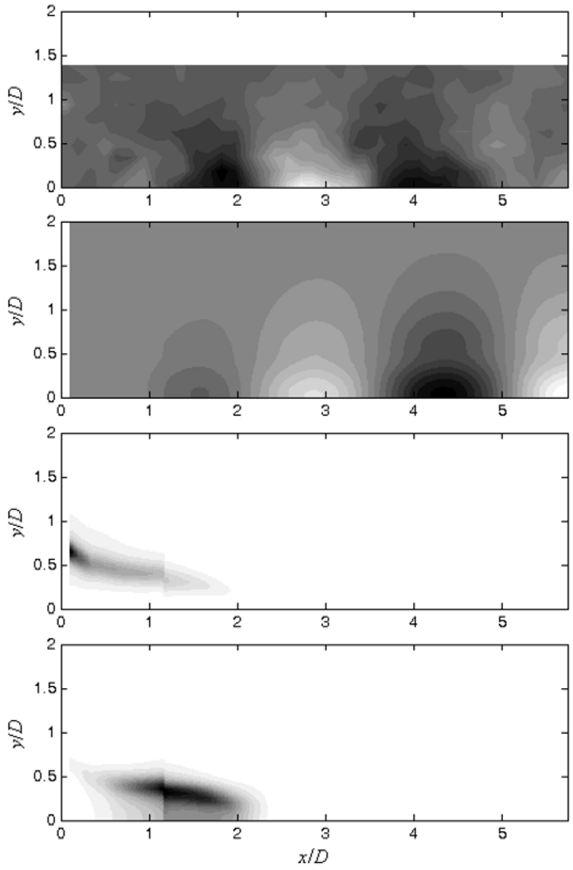

Figure B-28. Comparison of a) Measured global mode shape from conditionally averaged transverse velocity, b) direct global mode shape (transverse velocity) from detailed stability analysis, c) magnitude of adjoint global mode (axial velocity) from detailed stability analysis, d) magnitude of maximum energy of overlap of direct and adjoint global modes. Conditions are ρ_u/ρ_b = 2.0, U_{lip} = 66 m/s

APPENDIX C. SUPPLEMENTAL DATA FROM INTERMITTENCY OF LIMIT CYCLE EVENTS

C.1 *Intermittency Statistics*

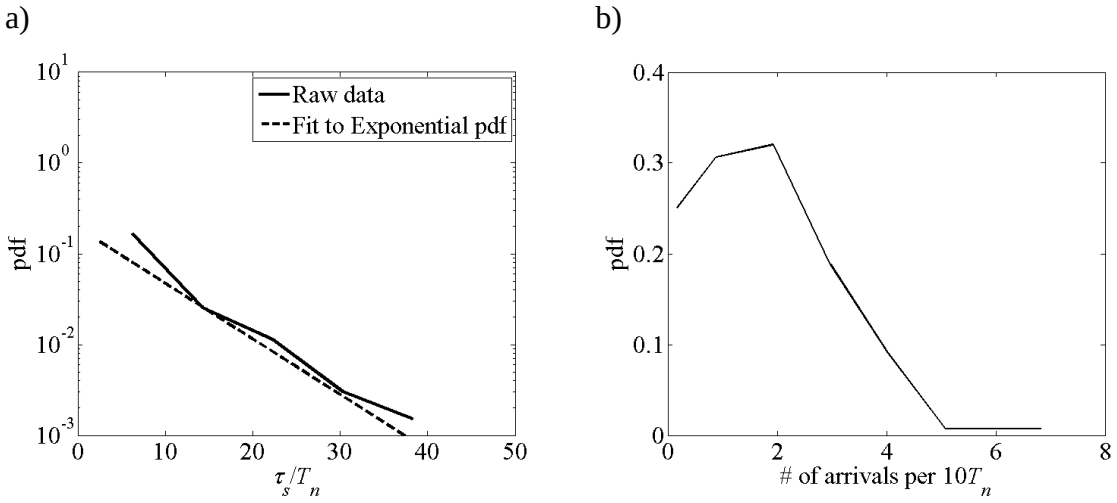

Figure C-1. Statistics of flame displacement limit cycle events for $\rho_u/\rho_b = 1.7$, $U_{lip} = 50$ m/s, showing a) pdf of event duration and b) pdf of event arrival rate

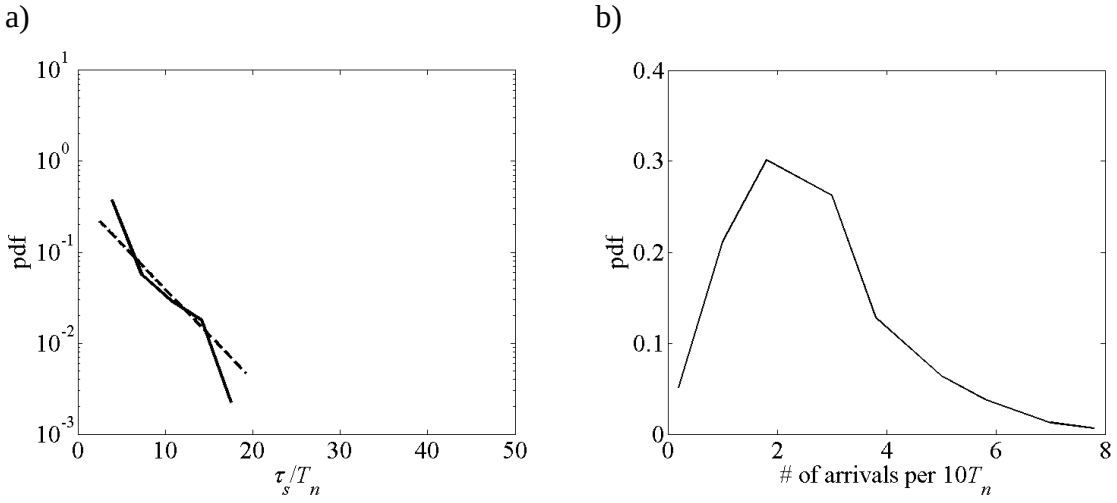

Figure C-2. Statistics of flame displacement limit cycle events for $\rho_u/\rho_b = 2.0$, $U_{lip} = 50$ m/s, showing a) pdf of event duration and b) pdf of event arrival rate

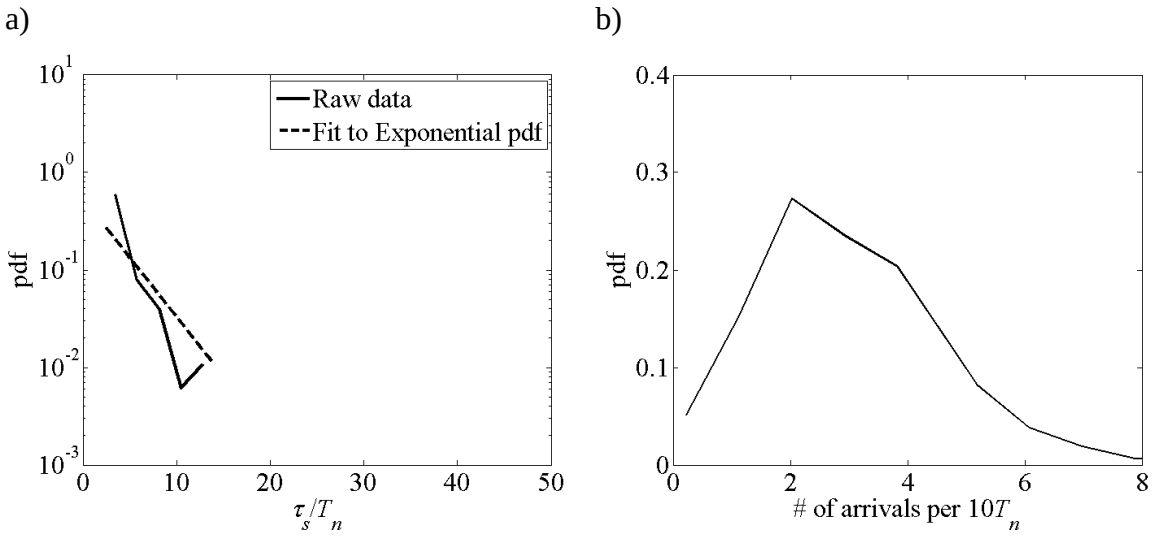

Figure C-3. Statistics of flame displacement limit cycle events for $\rho_u/\rho_b = 2.2$, $U_{lip} = 50$ m/s, showing a) pdf of event duration and b) pdf of event arrival rate

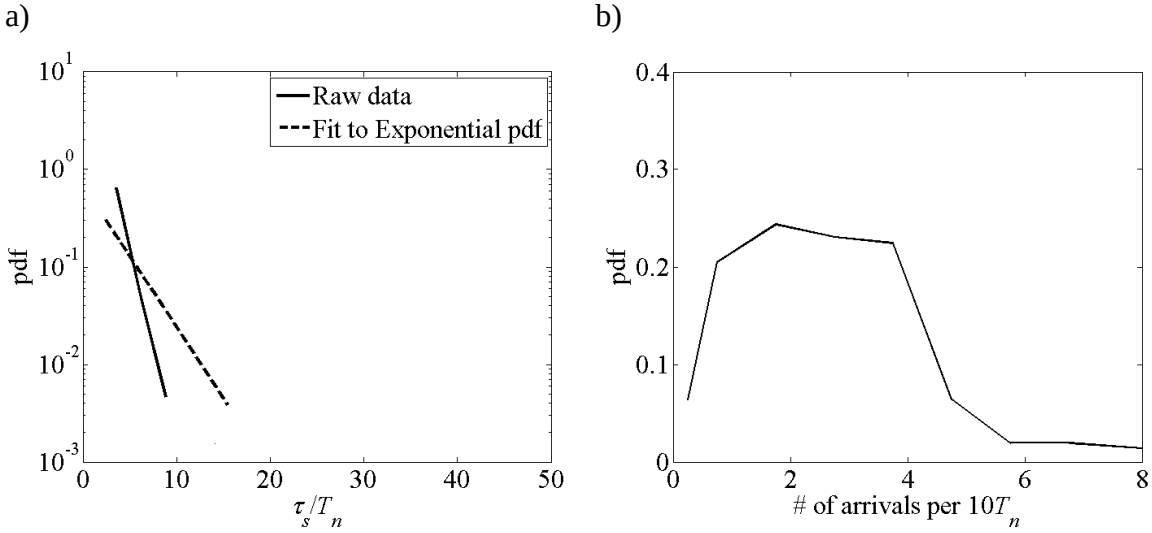

Figure C-4. Statistics of flame displacement limit cycle events for $\rho_u/\rho_b = 2.4$, $U_{lip} = 50$ m/s, showing a) pdf of event duration and b) pdf of event arrival rate

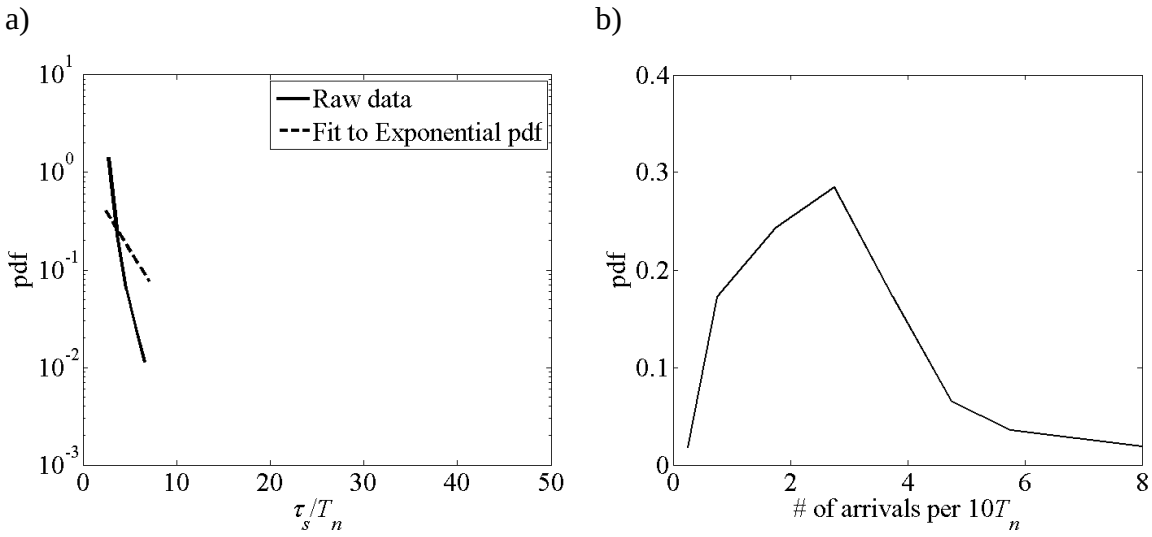

Figure C-5. Statistics of flame displacement limit cycle events for $\rho_u/\rho_b = 2.7$, $U_{lip} = 50$ m/s, showing a) pdf of event duration and b) pdf of event arrival rate

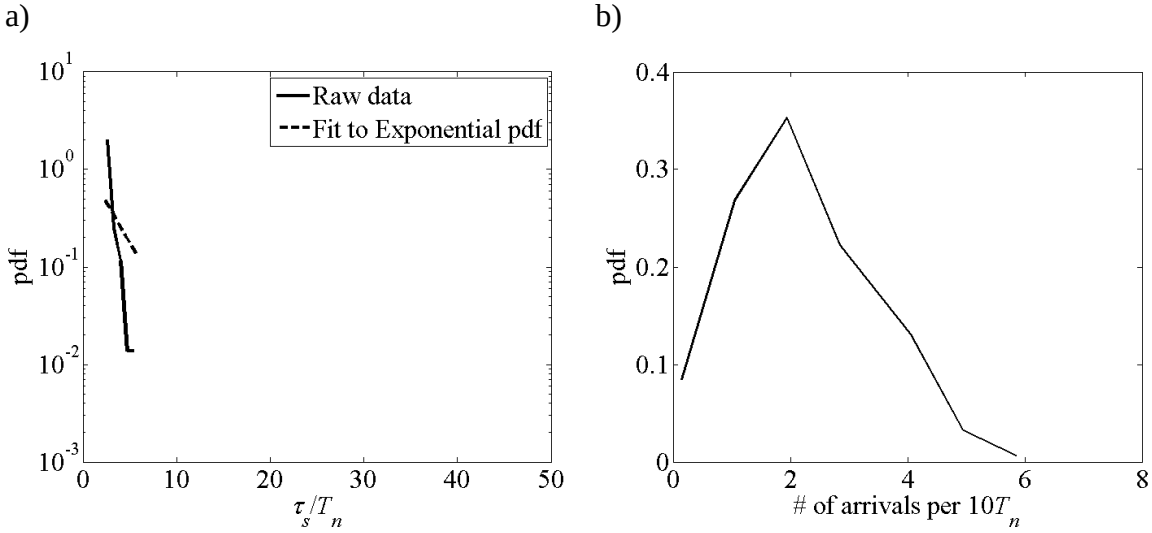

Figure C-6. Statistics of flame displacement limit cycle events for $\rho_u/\rho_b = 2.9$, $U_{lip} = 50$ m/s, showing a) pdf of event duration and b) pdf of event arrival rate

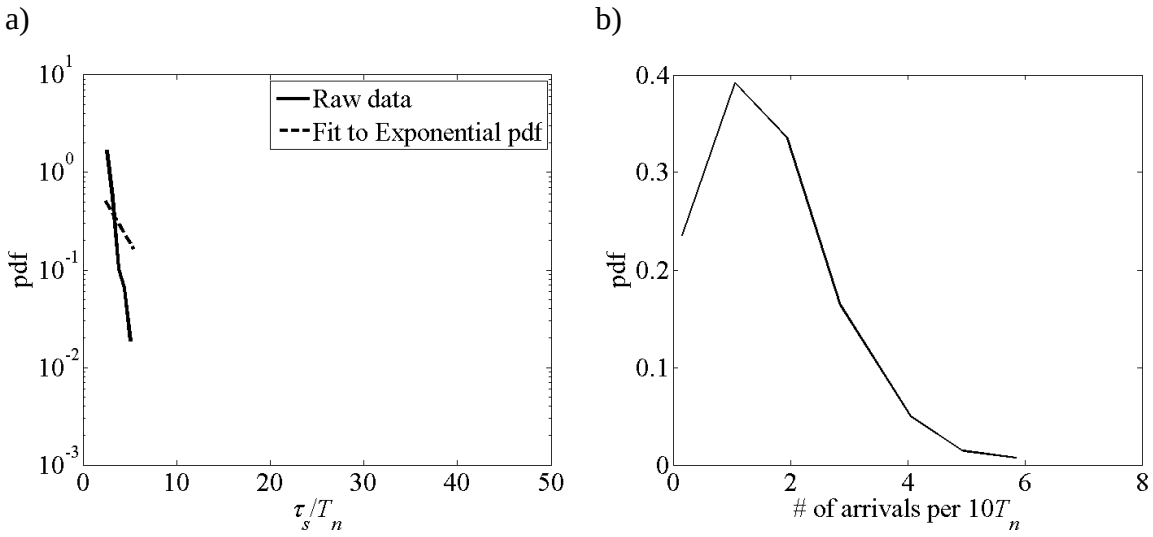

Figure C-7. Statistics of flame displacement limit cycle events for $\rho_u/\rho_b = 3.2$, $U_{lip} = 50$ m/s, showing a) pdf of event duration and b) pdf of event arrival rate

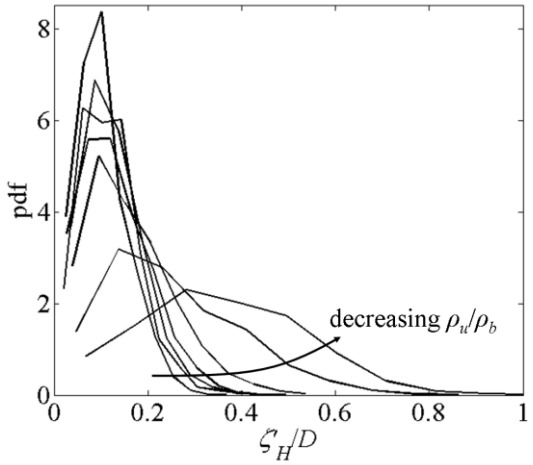

Figure C-8. pdfs of the Hilbert transform of the flame edge displacement for $\rho_u/\rho_b = 3.2$, $\rho_u/\rho_b = 2.9$, $\rho_u/\rho_b = 2.7$, $\rho_u/\rho_b = 2.4$, $\rho_u/\rho_b = 2.2$, $\rho_u/\rho_b = 2.0$, and $\rho_u/\rho_b = 1.7$

APPENDIX D. SUPPLEMENTAL DATA FROM FORCED EXPERIMENTS

D.1 *Forced Flame and Flow Spectra*

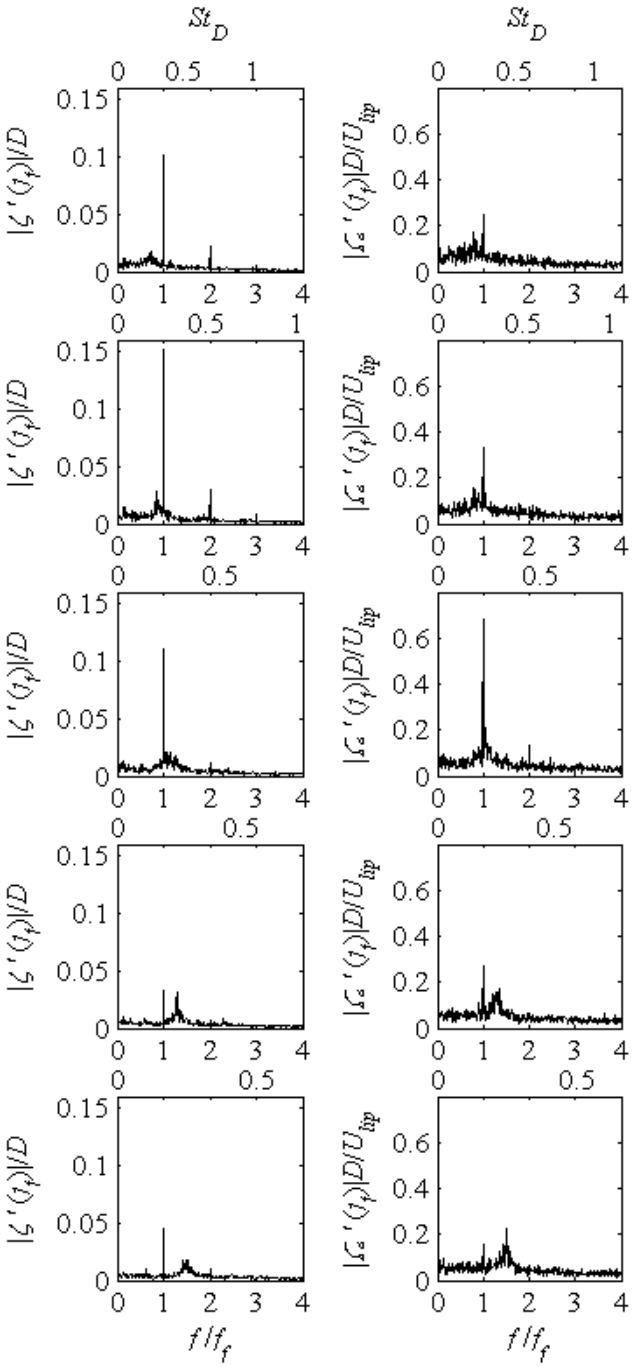

Figure D-1. Flame displacement (left column) and vorticity (right column) spectra as f_n/f_f is swept through values 0.8, 0.9, 1.1, 1.3, and 1.5 (top to bottom). Conditions are $\rho_u/\rho_b = 1.7$, $A_f = 0.020$

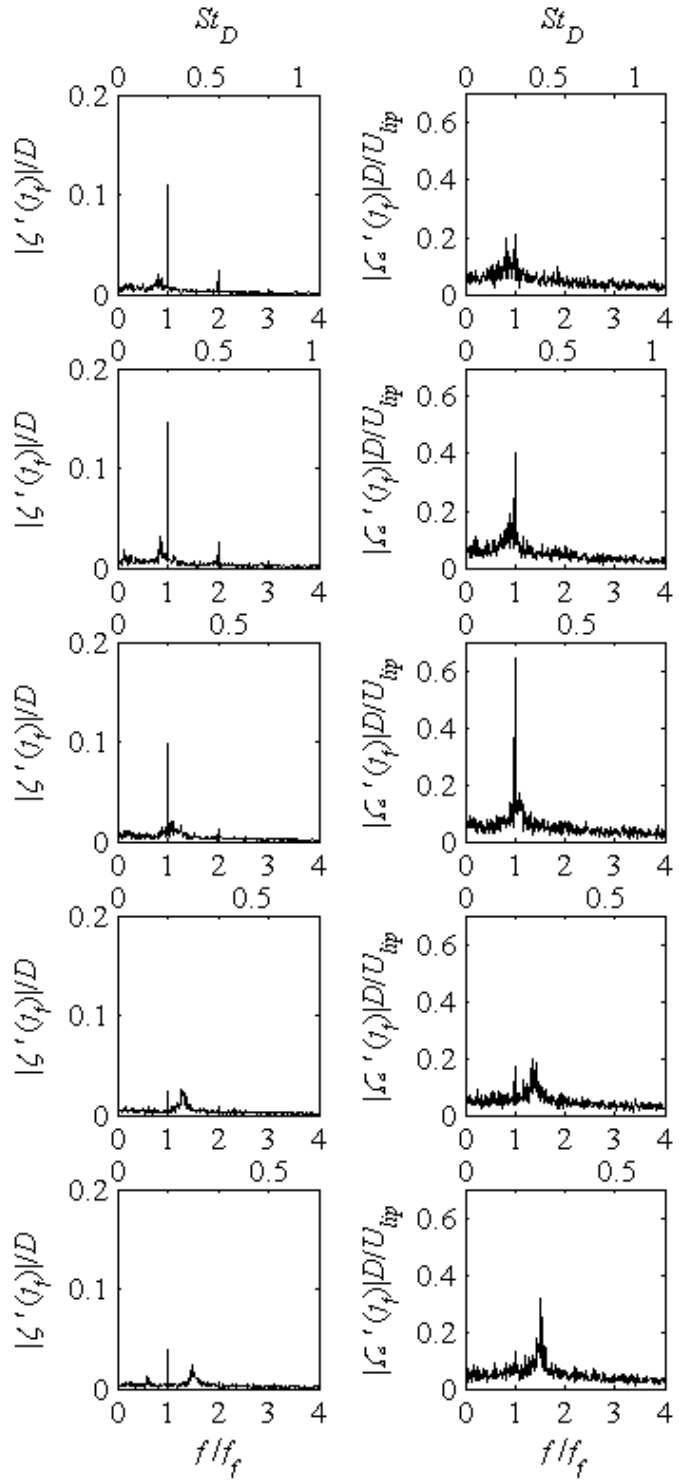

Figure D-2. Flame displacement (left column) and vorticity (right column) spectra as f_n/f_f is swept through values 0.8, 0.9, 1.1, 1.3, and 1.5 (top to bottom). Conditions are $\rho_u/\rho_b = 1.7$, $A_f = 0.015$

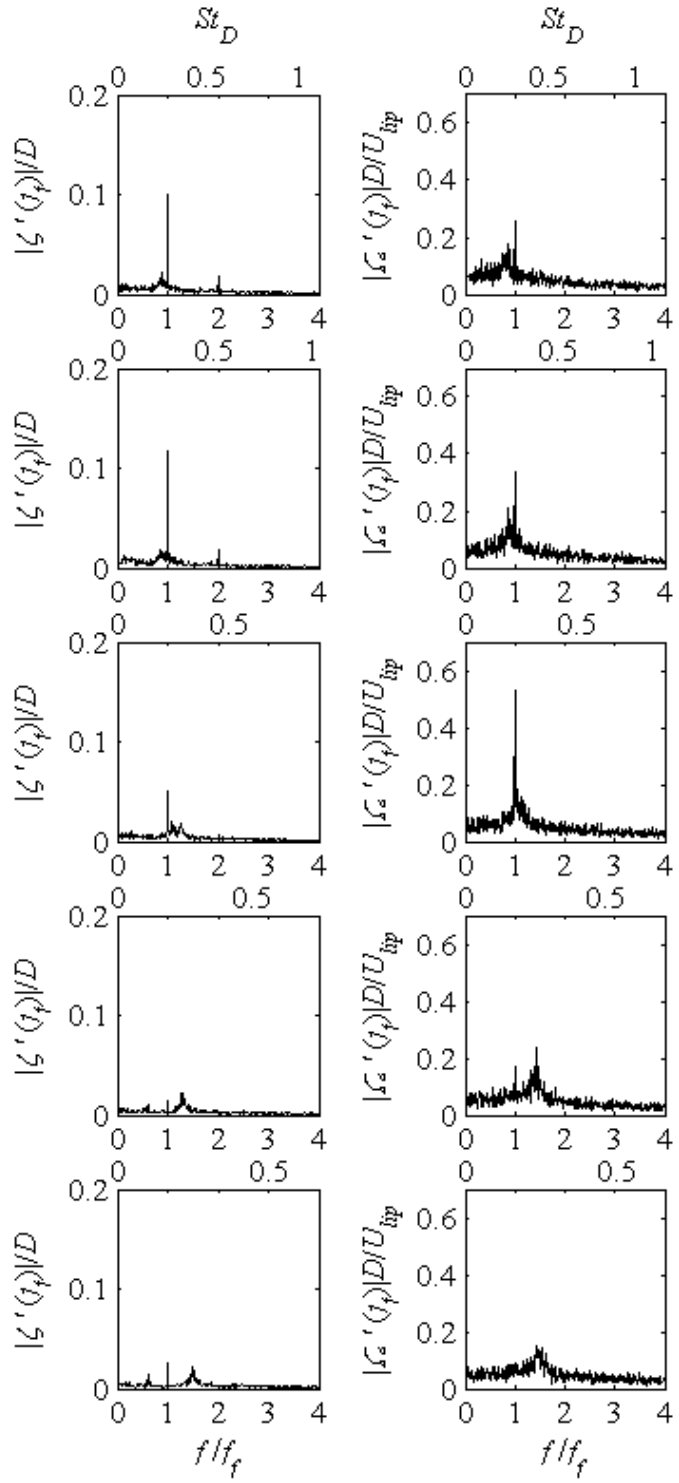

Figure D-3. Flame displacement (left column) and vorticity (right column) spectra as f_n/f_f is swept through values 0.8, 0.9, 1.1, 1.3, and 1.5 (top to bottom). Conditions are $\rho_u/\rho_b = 1.7$, $A_f = 0.010$

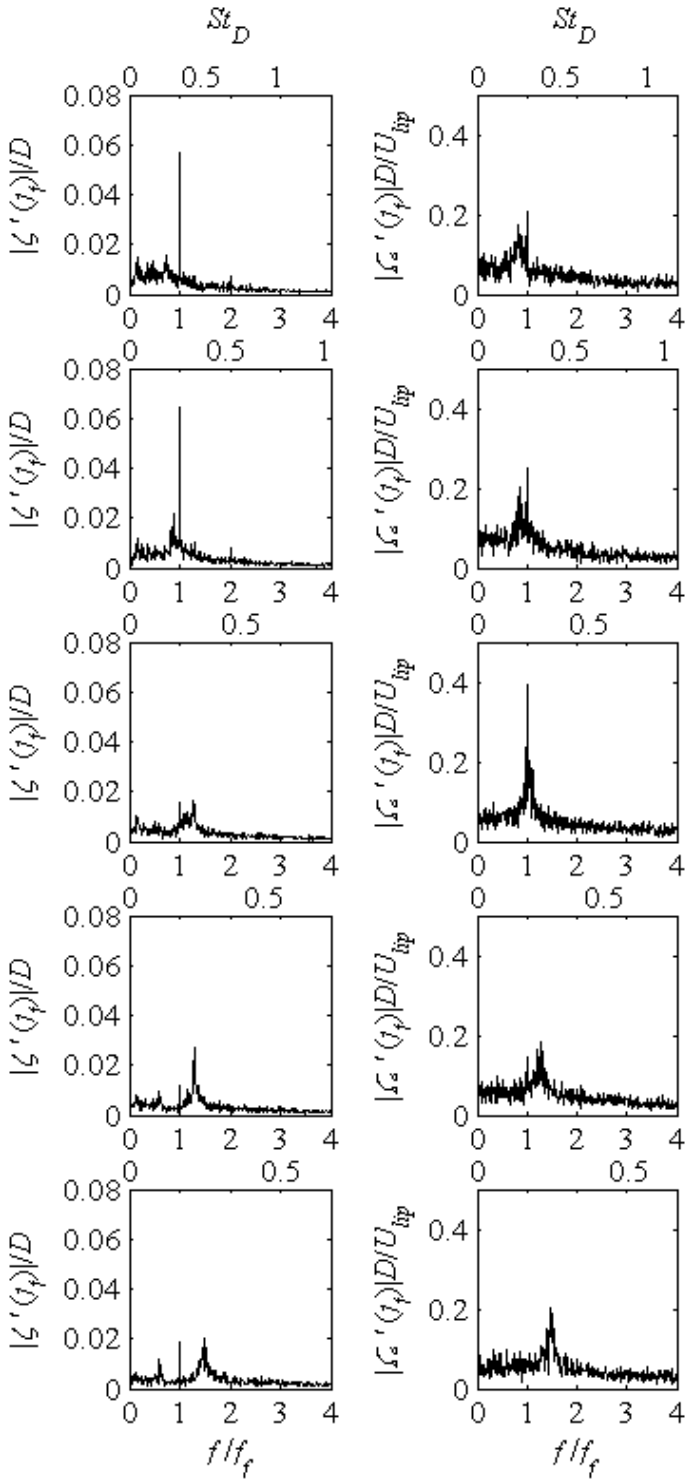

Figure D-4. Flame displacement (left column) and vorticity (right column) spectra as f_n/f_f is swept through values 0.8, 0.9, 1.1, 1.3, and 1.5 (top to bottom). Conditions are $\rho_u/\rho_b = 1.7$, $A_f = 0.005$

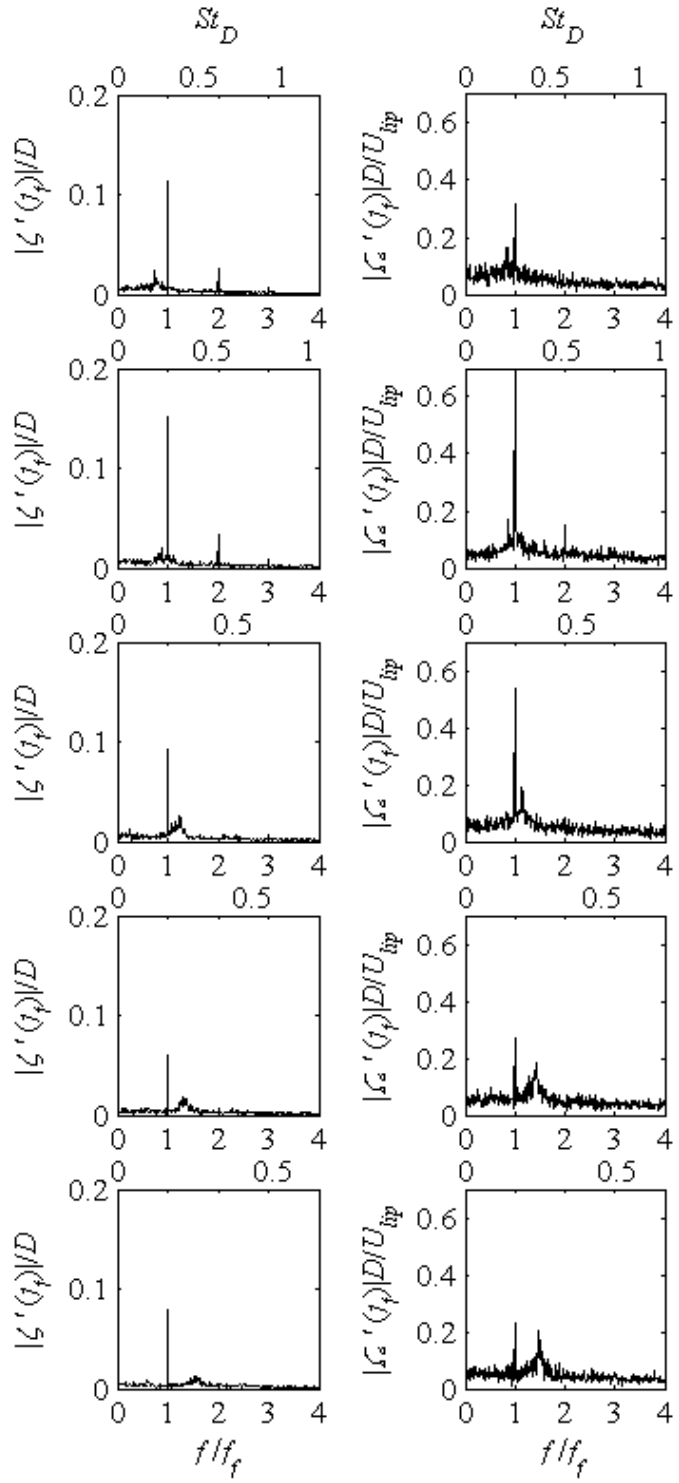

Figure D-5. Flame displacement (left column) and vorticity (right column) spectra as f_n/f_f is swept through values 0.8, 0.9, 1.1, 1.3, and 1.5 (top to bottom). Conditions are $\rho_u/\rho_b = 1.9$, $A_f = 0.020$

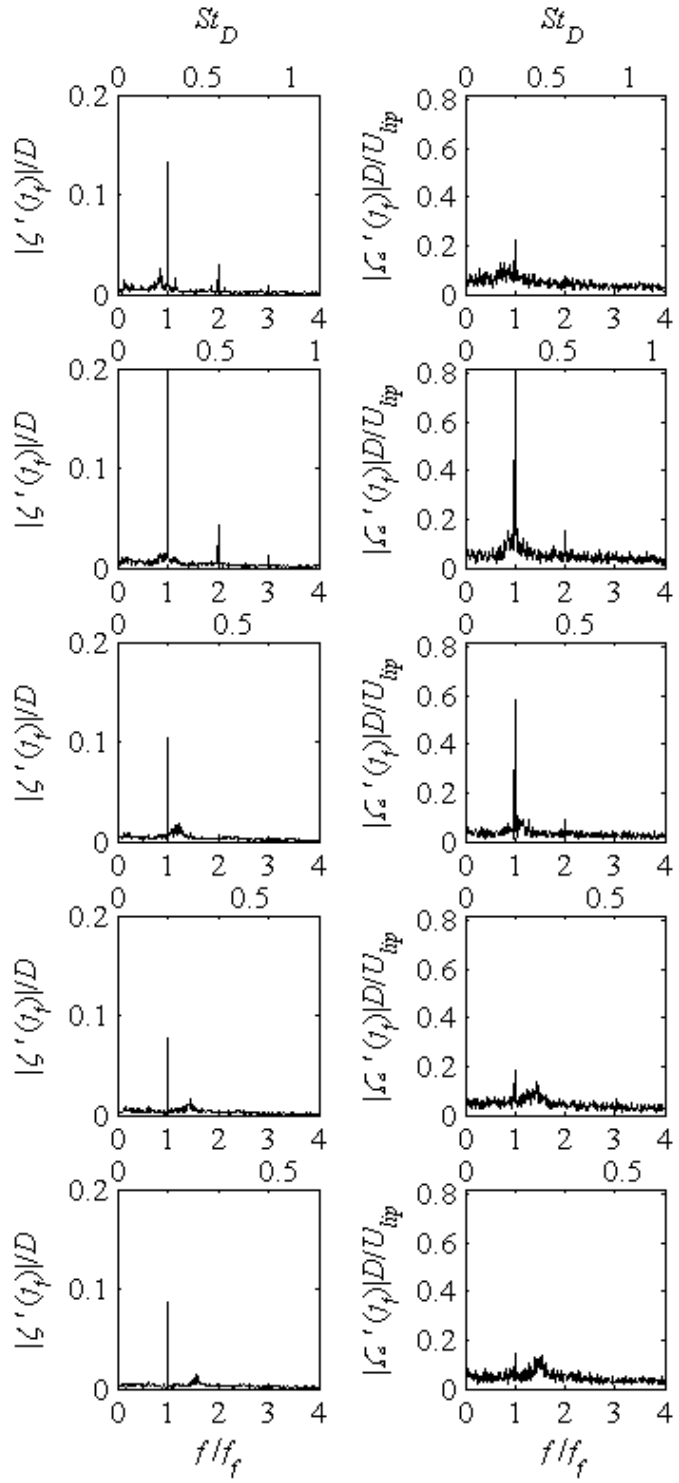

Figure D-6. Flame displacement (left column) and vorticity (right column) spectra as f_n/f_f is swept through values 0.8, 0.9, 1.1, 1.3, and 1.5 (top to bottom). Conditions are $\rho_u/\rho_b = 2.0$, $A_f = 0.020$

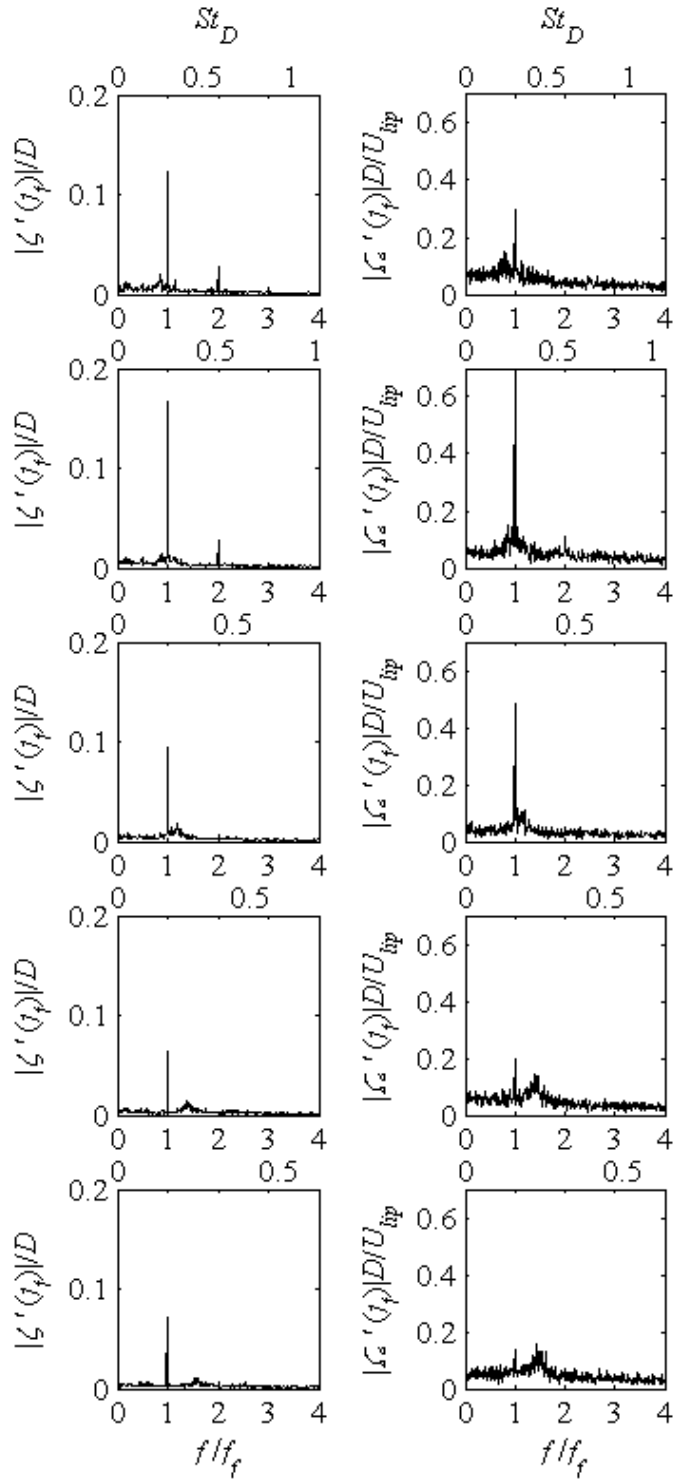

Figure D-7. Flame displacement (left column) and vorticity (right column) spectra as f_n/f_f is swept through values 0.8, 0.9, 1.1, 1.3, and 1.5 (top to bottom). Conditions are $\rho_u/\rho_b = 2.0$, $A_f = 0.015$

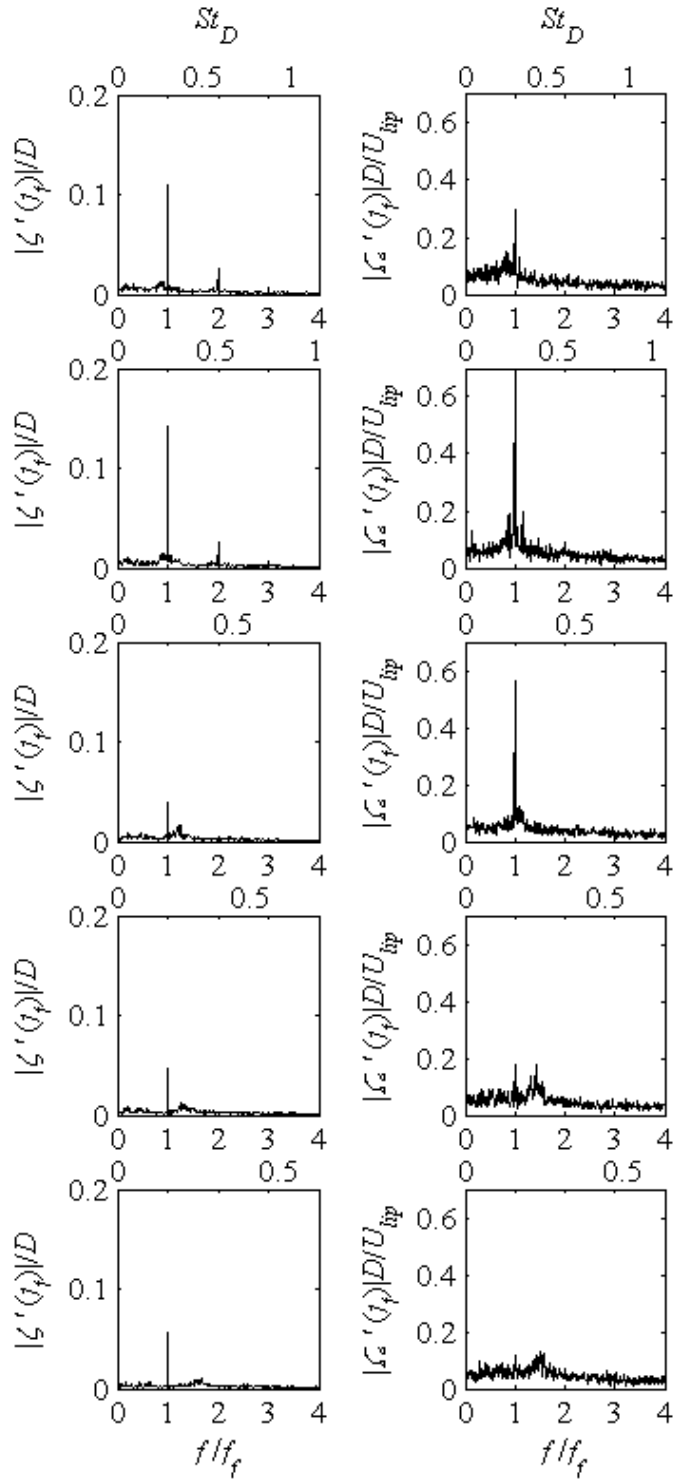

Figure D-8. Flame displacement (left column) and vorticity (right column) spectra as f_n/f_f is swept through values 0.8, 0.9, 1.1, 1.3, and 1.5 (top to bottom). Conditions are $\rho_u/\rho_b = 2.0$, $A_f = 0.010$

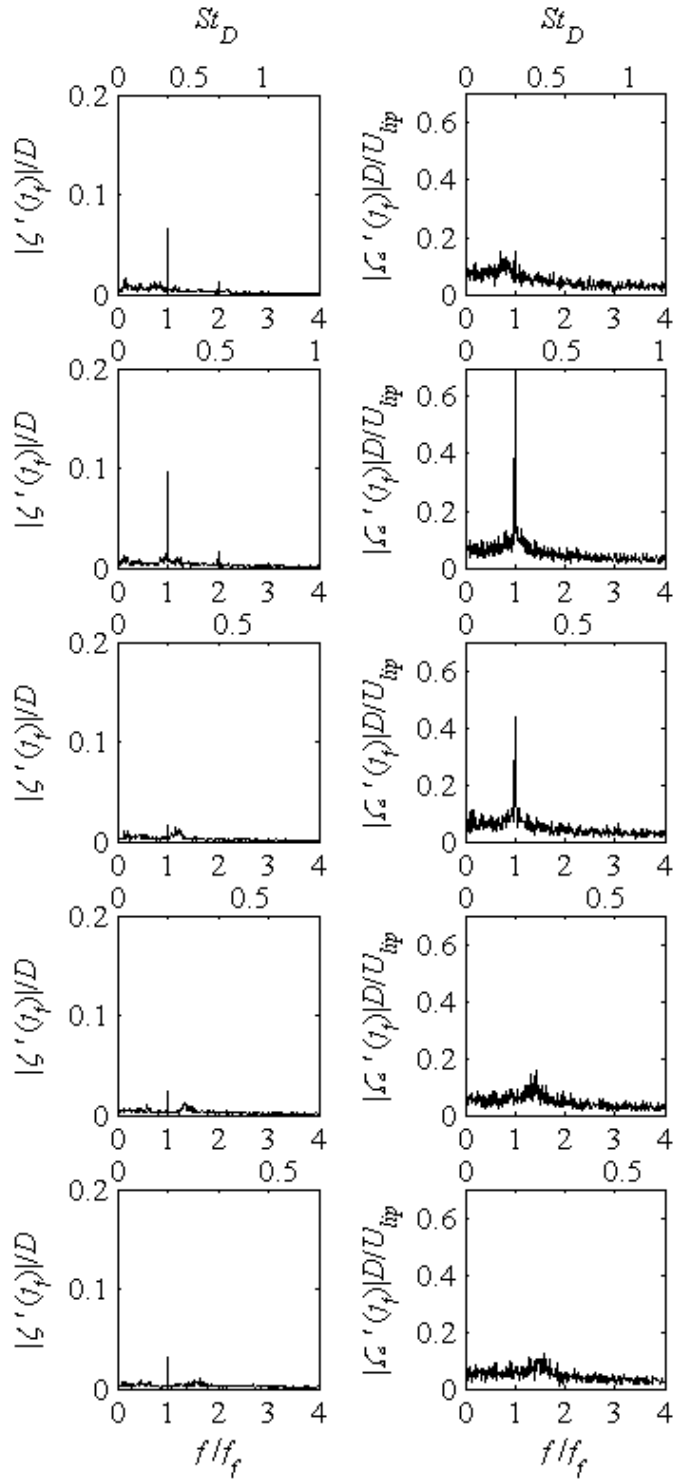

Figure D-9. Flame displacement (left column) and vorticity (right column) spectra as f_n/f_f is swept through values 0.8, 0.9, 1.1, 1.3, and 1.5 (top to bottom). Conditions are $\rho_u/\rho_b = 2.0$, $A_f = 0.005$

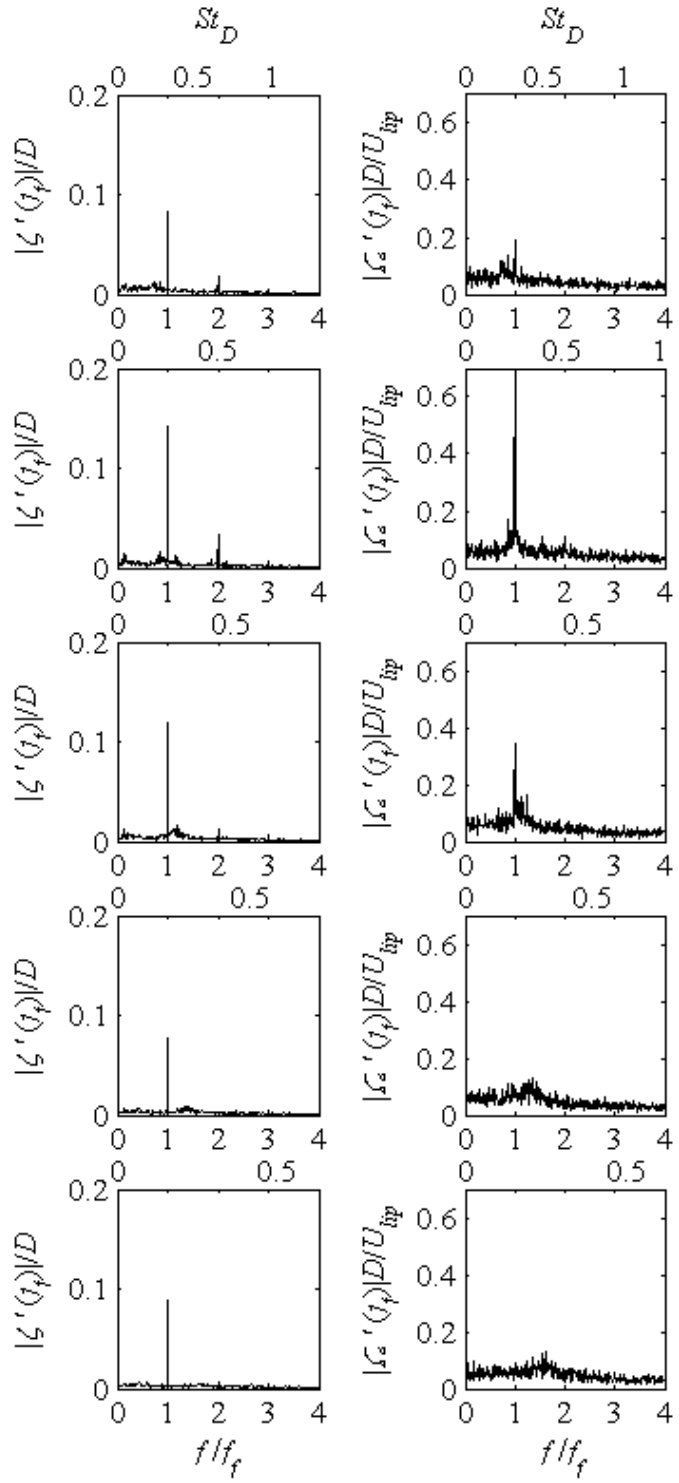

Figure D-10. Flame displacement (left column) and vorticity (right column) spectra as f_n/f_f is swept through values 0.8, 0.9, 1.1, 1.3, and 1.5 (top to bottom). Conditions are $\rho_u/\rho_b = 2.2$, $A_f = 0.020$

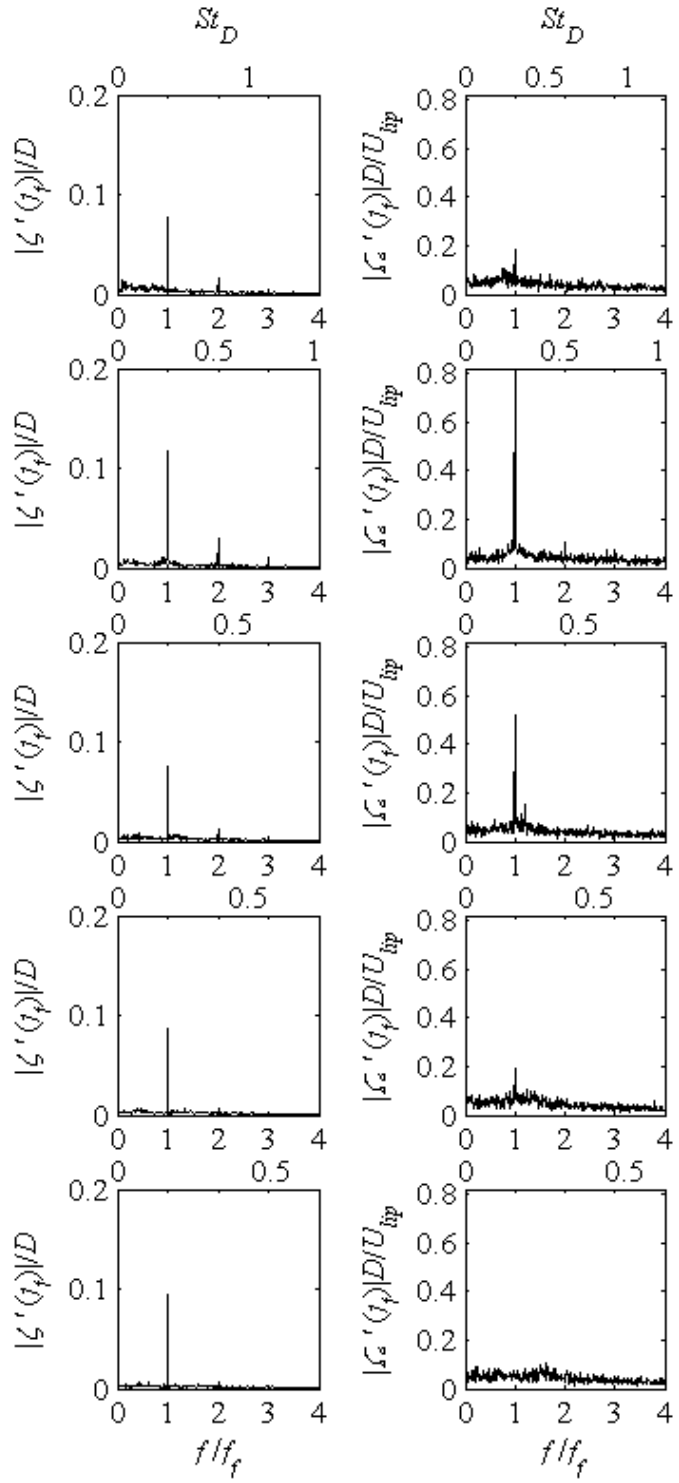

Figure D-11. Flame displacement (left column) and vorticity (right column) spectra as f_n/f_f is swept through values 0.8, 0.9, 1.1, 1.3, and 1.5 (top to bottom). Conditions are $\rho_u/\rho_b = 2.4$, $A_f = 0.020$

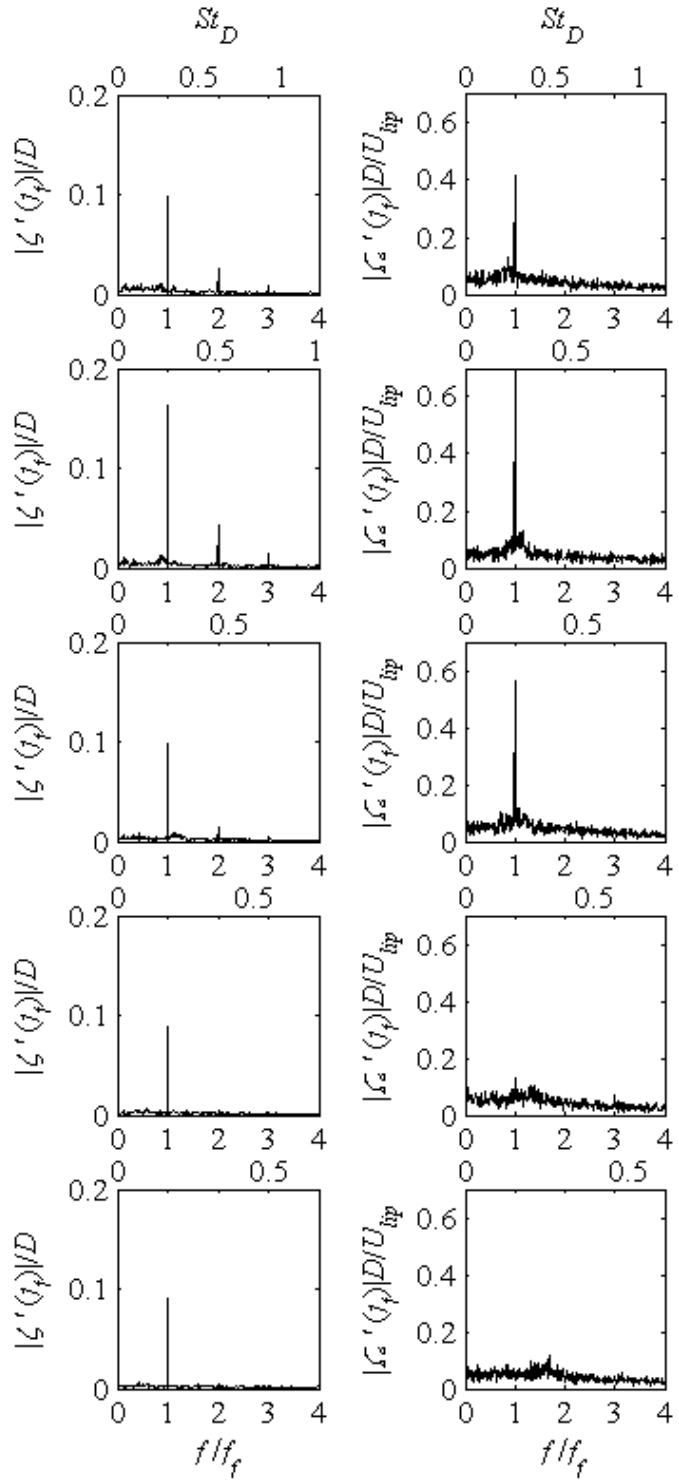

Figure D-12. Flame displacement (left column) and vorticity (right column) spectra as f_n/f_f is swept through values 0.8, 0.9, 1.1, 1.3, and 1.5 (top to bottom). Conditions are $\rho_u/\rho_b = 2.5$, $A_f = 0.020$

D.2 *Lock-in Maps for Cases with Amplitude Sweeps*

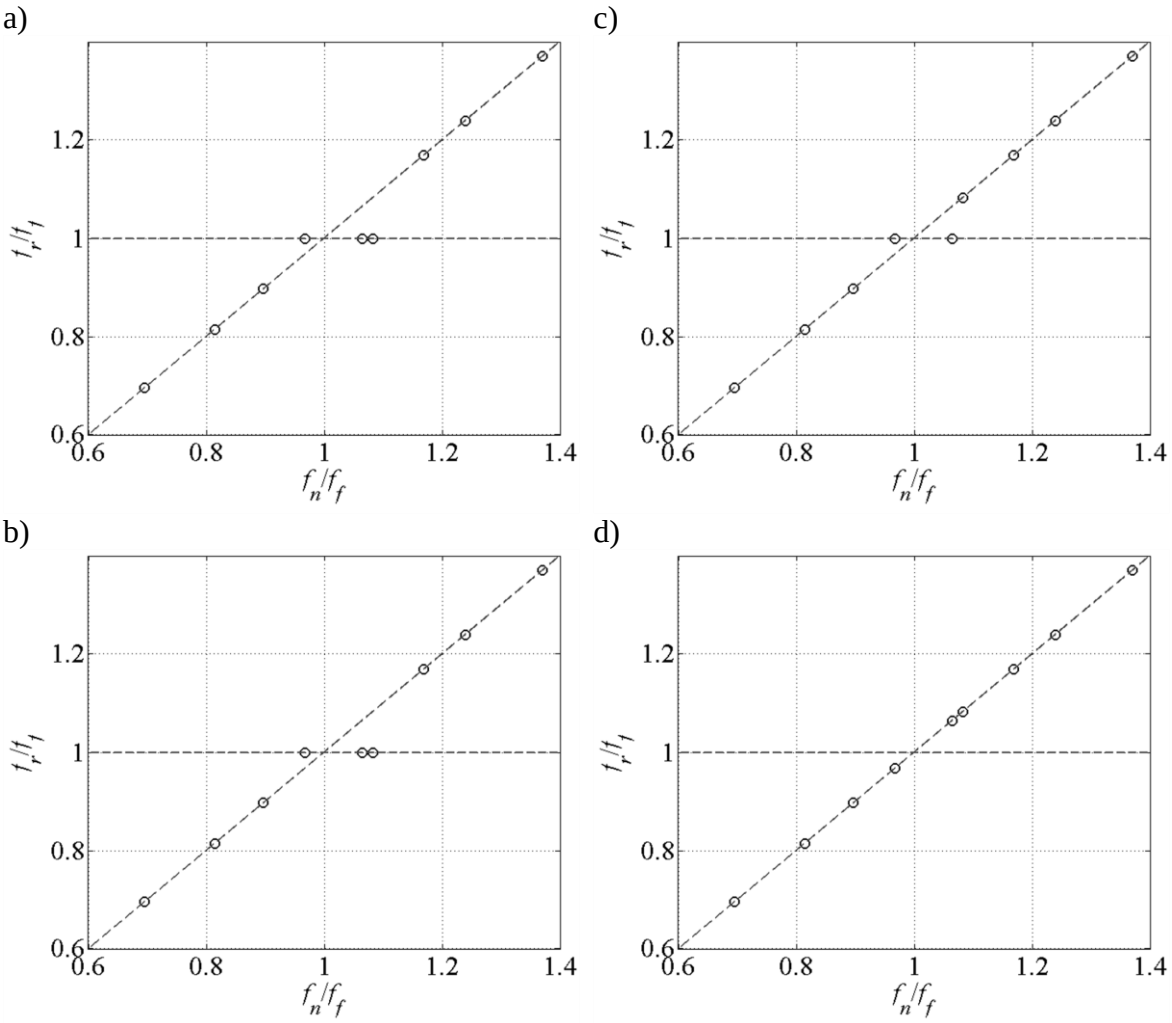

Figure D-13. Lock-in maps from centerline vorticity measured at $x/D = 3$ for $\rho_u/\rho_b = 1.7$ and a) $A_f = .020$, b) $A_f = .015$, c) $A_f = .010$, and d) $A_f = .005$

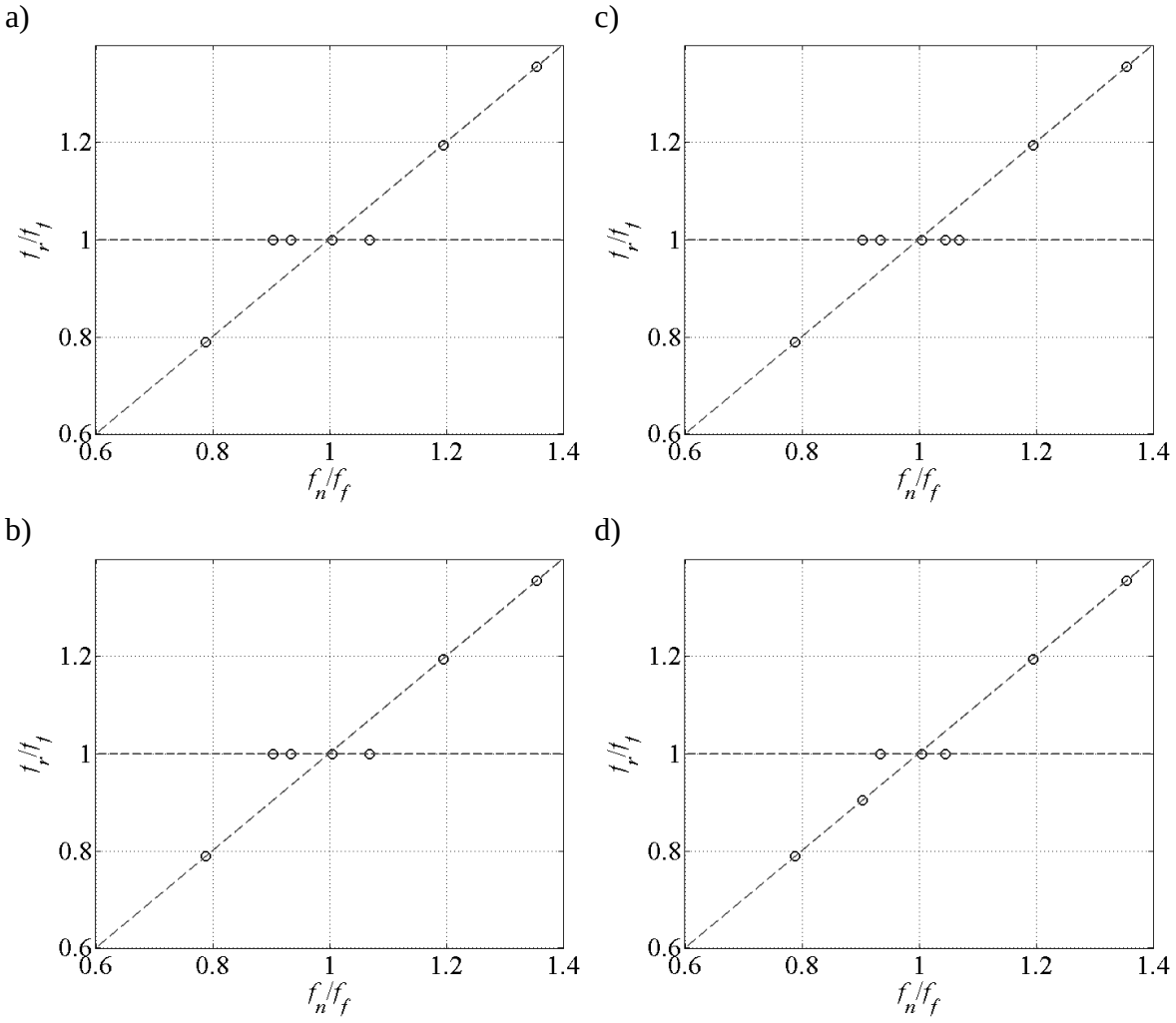

Figure D-14. Lock-in maps from centerline vorticity measured at $x/D = 3$ for $\rho_u/\rho_b = 2.0$ and a) $A_f = .020$, b) $A_f = .015$, c) $A_f = .010$, and d) $A_f = .005$

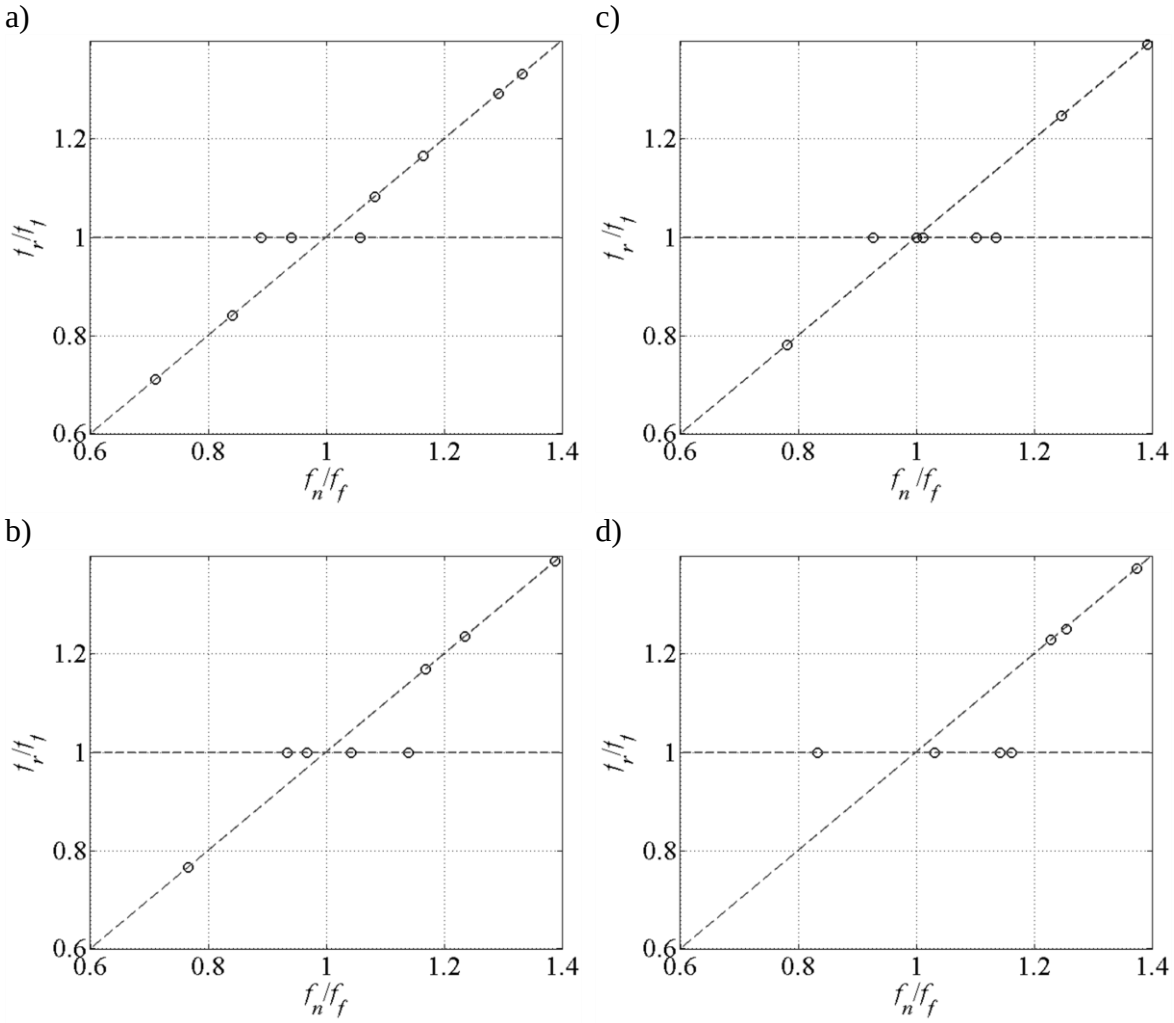

Figure D-15. Lock-in map from centerline vorticity measured at $x/D = 3$ for $A_f = .020$ and a) $\rho_u/\rho_b = 1.9$, b) $\rho_u/\rho_b = 2.2$, c) $\rho_u/\rho_b = 2.4$, and d) $\rho_u/\rho_b = 2.5$

D.3 *Flame Response at the Forcing Frequency*

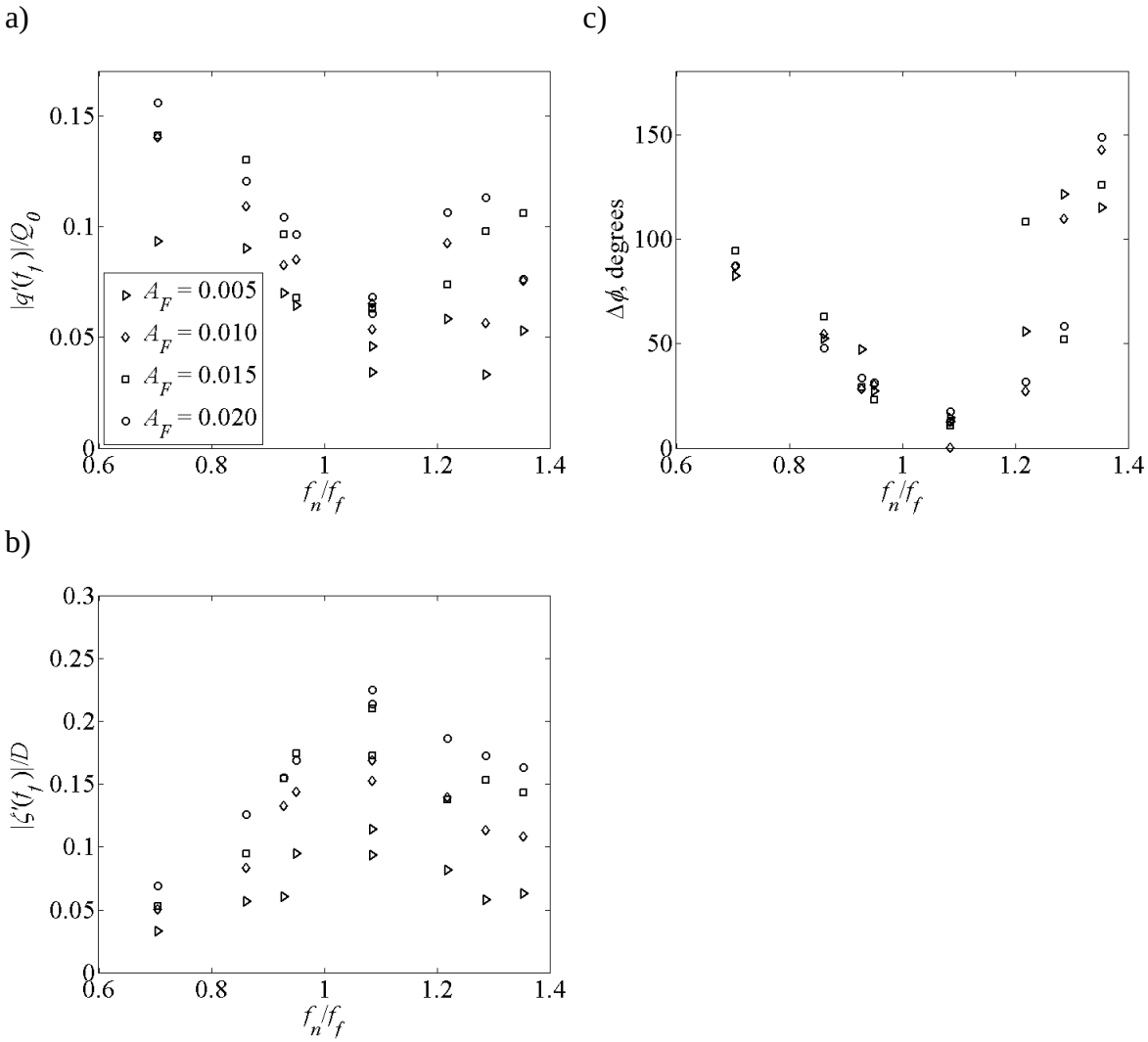

Figure D-16. Forced flame response for $\rho_u/\rho_b = 1.7$, showing a) local heat release, b) flame edge displacement, and c) flame edge phase difference (zero indicates sinuous)

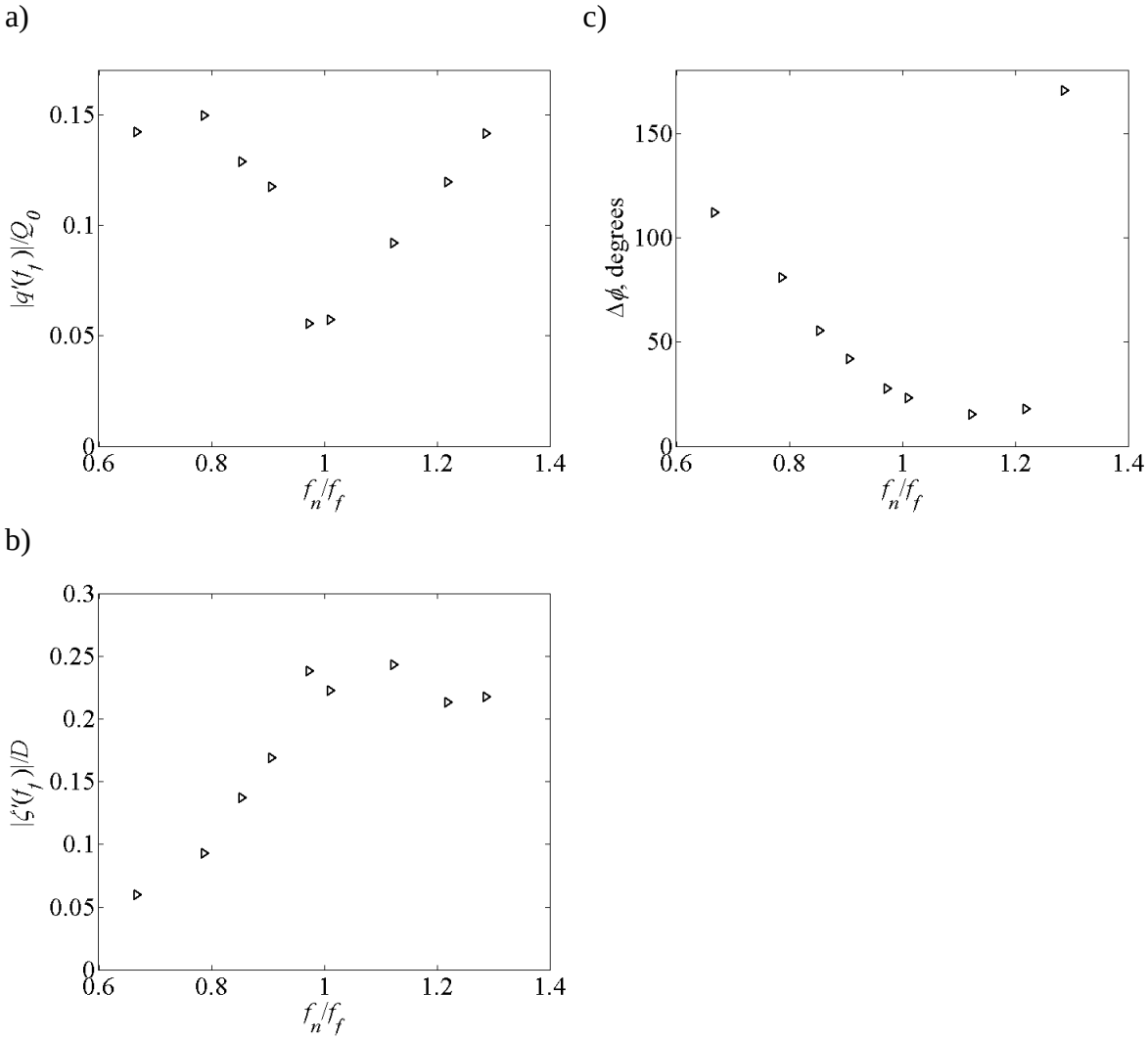

Figure D-17. Forced flame response for $\rho_u/\rho_b = 1.9$, showing a) local heat release, b) flame edge displacement, and c) flame edge phase difference (zero indicates sinuous)

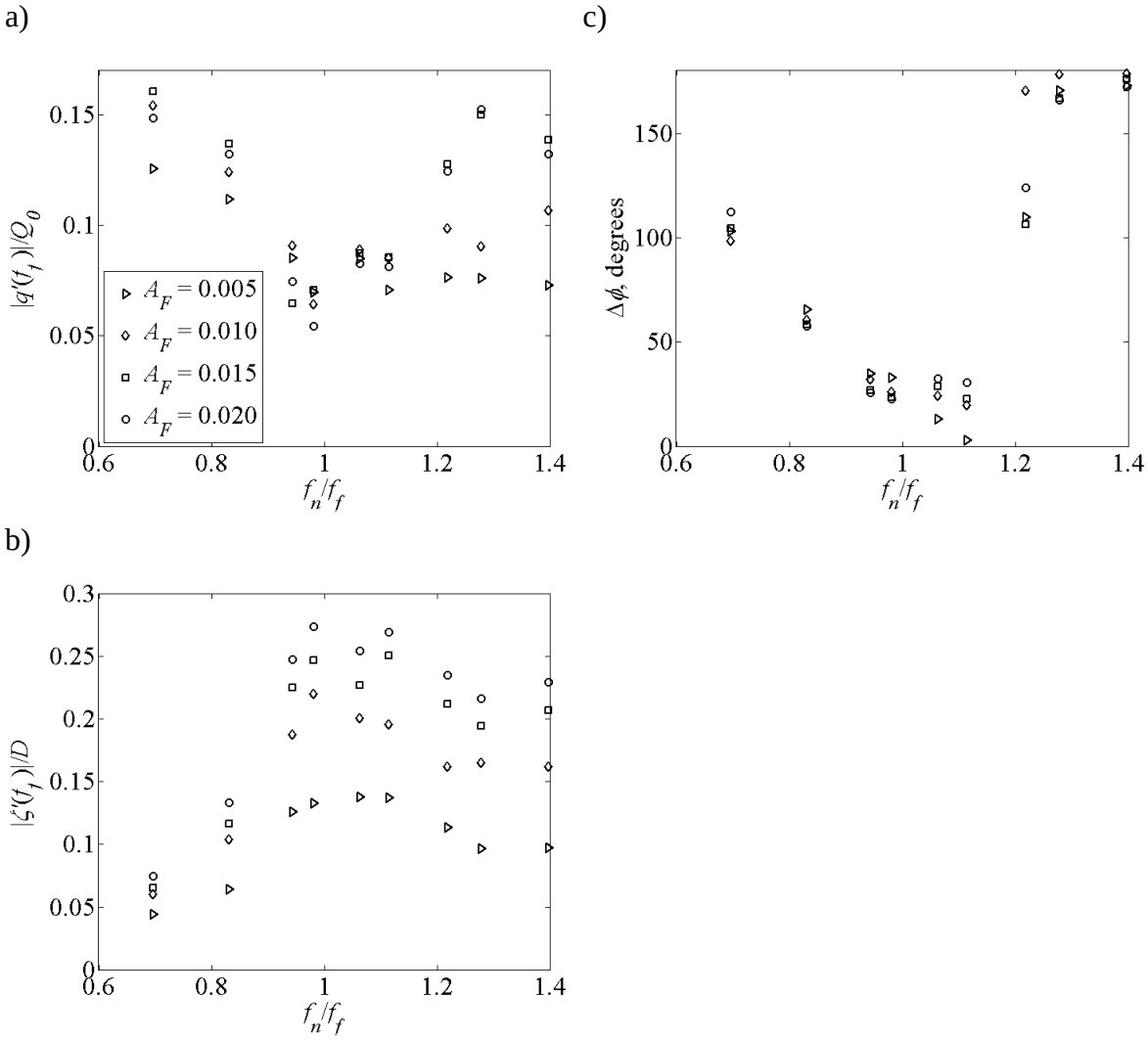

Figure D-18. Forced flame response for $\rho_u/\rho_b = 2.0$, showing a) local heat release, b) flame edge displacement, and c) flame edge phase difference (zero indicates sinuous)

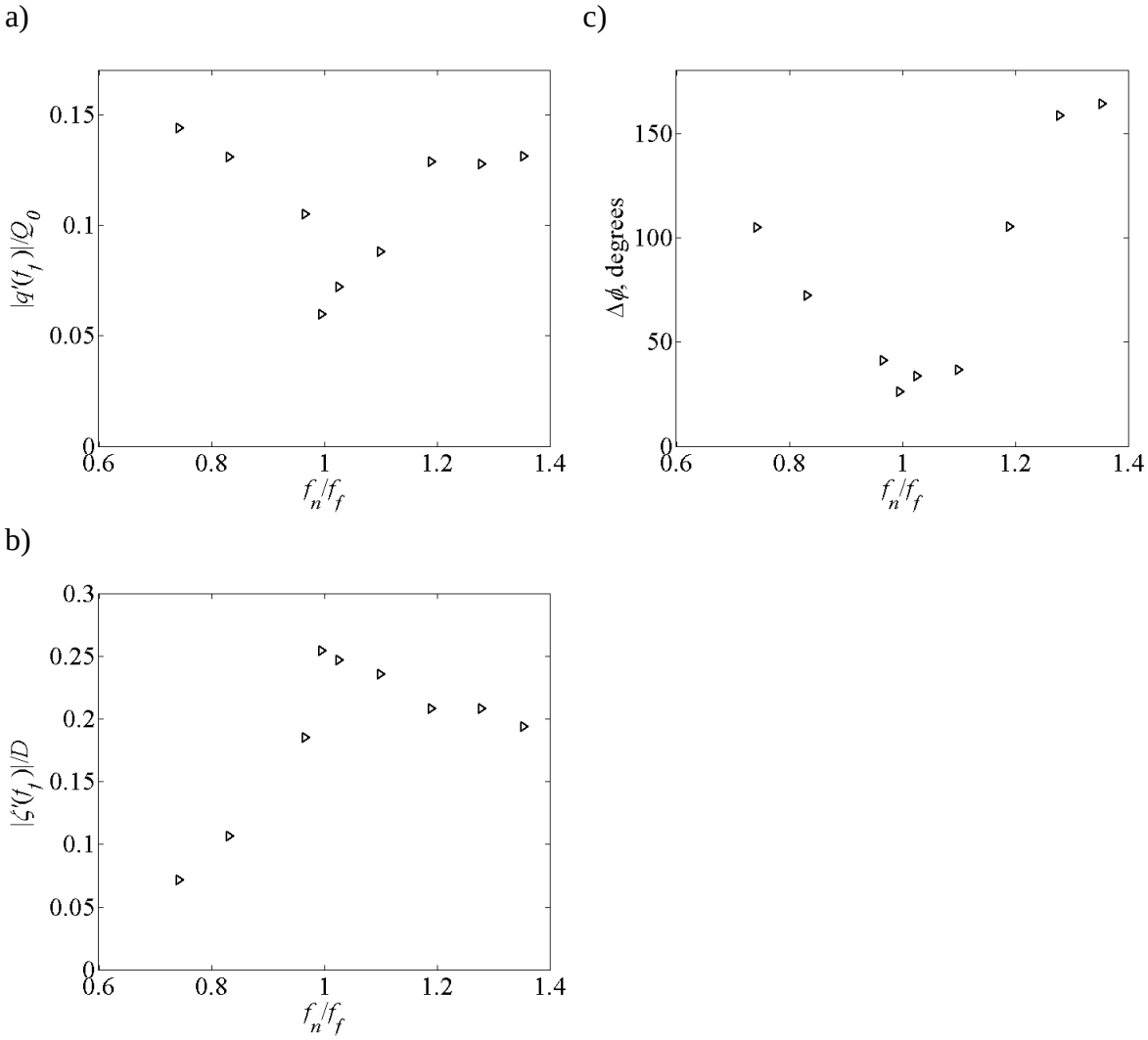

Figure D-19. Forced flame response for $\rho_u/\rho_b = 2.2$, showing a) local heat release, b) flame edge displacement, and c) flame edge phase difference (zero indicates sinuous)

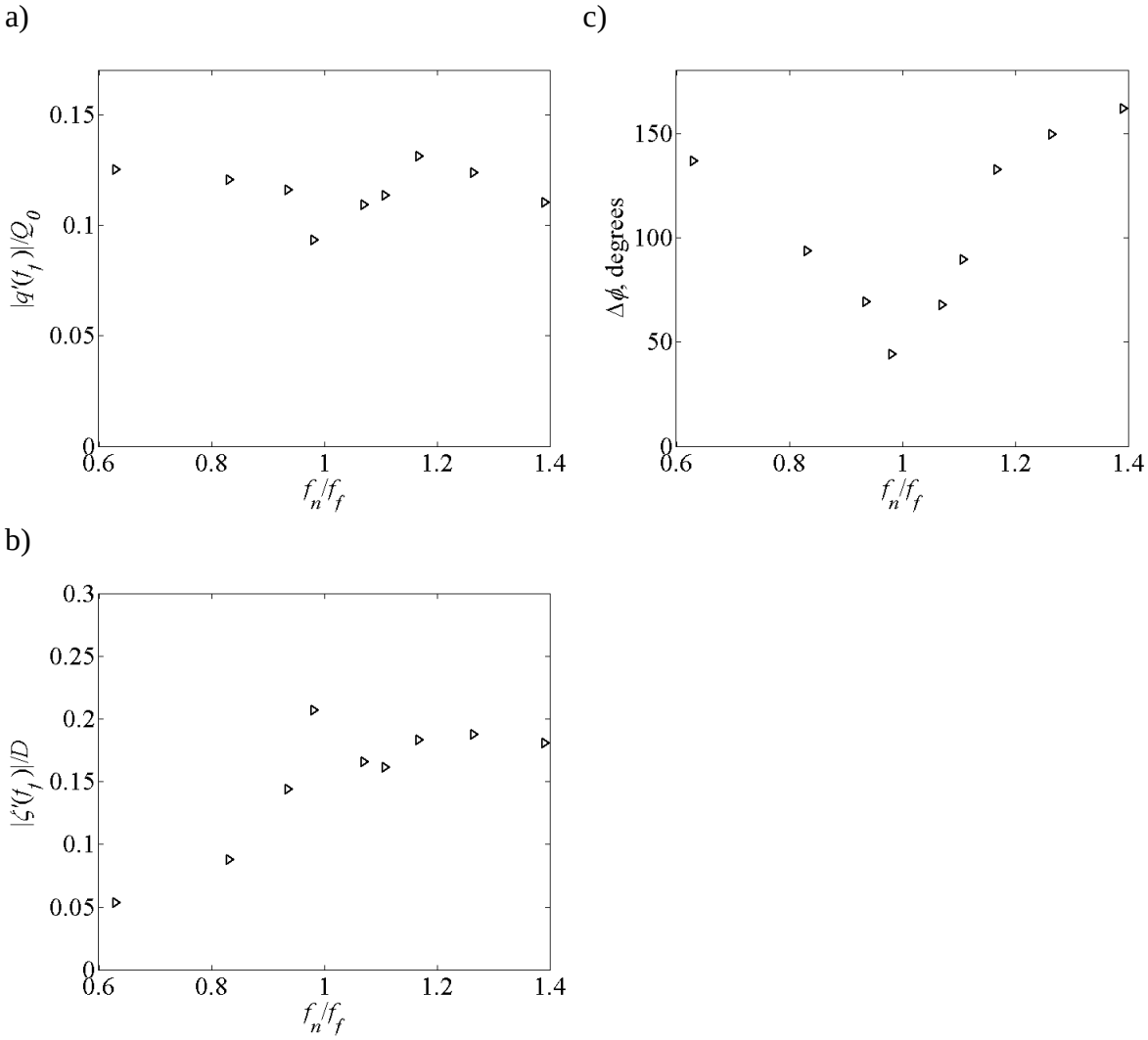

Figure D-20. Forced flame response for $\rho_u/\rho_b = 2.4$, showing a) local heat release, b) flame edge displacement, and c) flame edge phase difference (zero indicates sinuous)

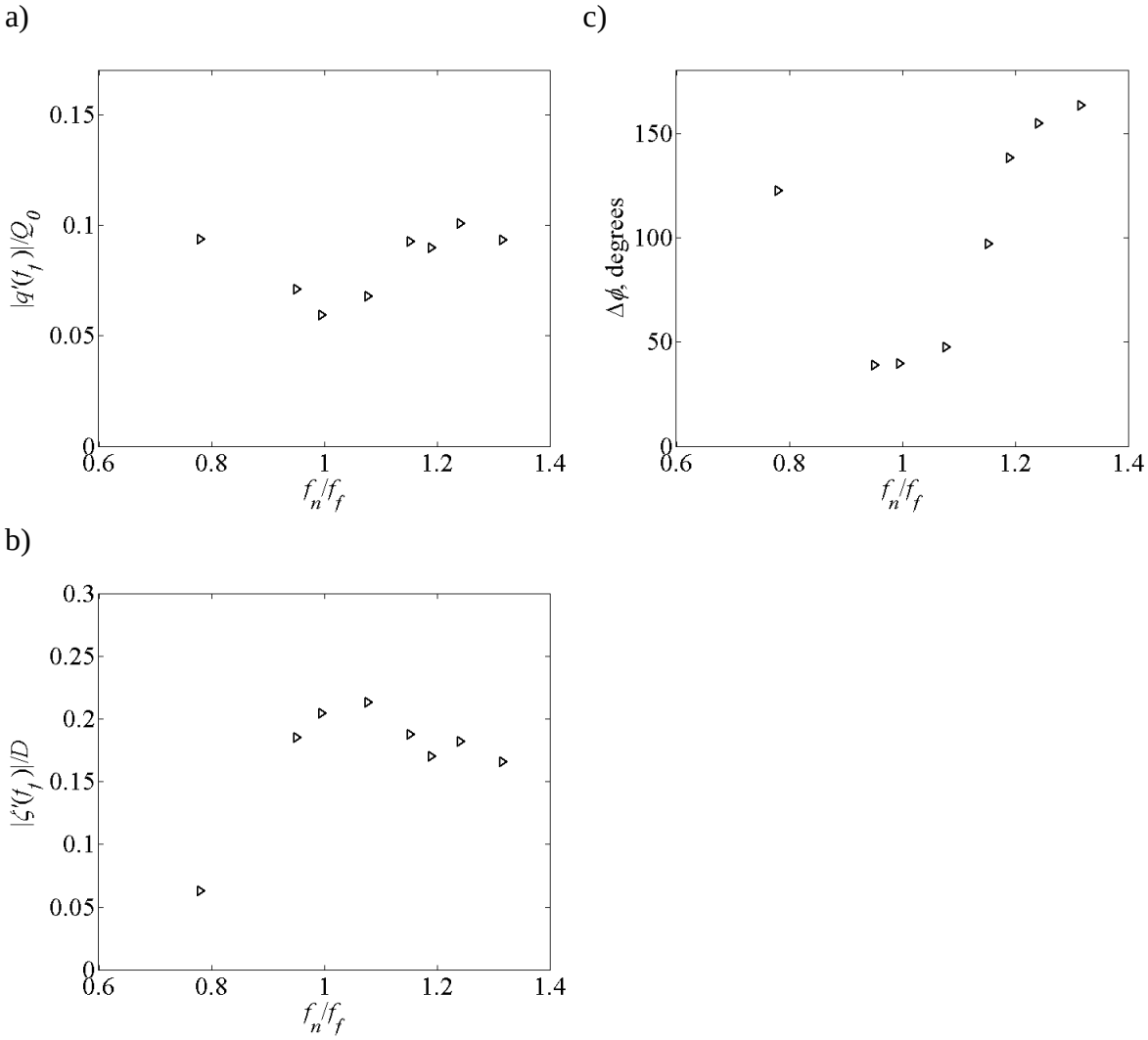

Figure D-21. Forced flame response for $\rho_u/\rho_b = 2.5$, showing a) local heat release, b) flame edge displacement, and c) flame edge phase difference (zero indicates sinuous)

REFERENCES

1. S. J. Shanbhogue; S. Husain; T. Lieuwen, Progress in Energy and Combustion Science 35 (1) (2009) 98-120
2. W. O. Criminale; T. L. Jackson; R. D. Joslin, Theory and Computation in Hydrodynamic Stability, The Press Syndicate of the University of Cambridge, Cambridge, 2003.
3. G. S. Cardell. Flow past a circular cylinder with a permeable splitter plate. California Insititute of Technology, Pasadena, 1993.
4. A. Prasad; C. H. K. Williamson, Journal of Fluid Mechanics 333 (1997) 375-402
5. S. Shanbhogue. Dynamics of Perturbed Exothermic Bluff-Body Flow-Fields. Georgia Institute of Technology, Atlanta, GA, 2008.
6. R. J. Briggs, Electron-stream interaction with plasmas, M.I.T. Press, Cambridge, Mass, 1964.
7. A. Bers, Handbook of Plasma Physics I: Basic Plasma Physics, North-Holland, Amsterdam, 1983.
8. P. Huerre; P. A. Monkewitz, Journal of Fluid Mechanics 159 (1985)
9. A. E. Perry; M. S. Chong; T. T. Lim, Journal of Fluid Mechanics 116 (1982) 77-90
10. B. Cantwell; D. Coles, Journal of Fluid Mechanics 136 (1983) 321-374
11. P. Bearman, J. Fluid Mech 37 (1969) 577
12. A. Roshko, Journal of Fluid Mechanics 10 (1961) 345-356
13. R. D. Blevins, Flow-Induced Vibration, Van Nostrand Reinhold Co., New York, 1977.
14. A. Roshko, Journal of the Aeronautical Sciences 22 (2) (1955) 124-132
15. R. F. Huang; K. T. Chang, Journal of Propulsion and Power 20 (5) (2004) 871-878
16. A. Roshko, in: National Advisory Committee on Aeronautics: 1954.
17. M. M. Zdravkovich, Flow Around Circular Cylinders: A Comprehensive Guide Through Flow Phenomena, Experiments, Applications, Mathematical Models, and Computer Simulations, Oxford University Press, 1997.
18. M.-H. Yu; P. A. Monkewitz, Phys. Fluids 2 (7) (1990)
19. M. P. Juniper; O. Tammisola; F. Lundell, Journal of Fluid Mechanics 686 (2011) 218-238
20. T. C. Lieuwen; V. Yang, Combustion Instabilities in Gas Turbine Engines: Operational Experience, Fundamental Mechanisms, and Modeling, 2005.
21. P. Huerre; P. A. Monkewitz, Annual Review of Fluid Mechanics 22 (1) (1990) 473-537
22. M. Masselin; C.-M. Ho, in: *AIAA Shear Flow Control Conference*, Boulder, CO, 1985.
23. R. R. Erickson; M. C. Soteriou; P. G. Mehta, in: *44th AIAA Aerospace Sciences Meeting & Exhibit*, Reno, Nevada, 2006.
24. R. R. Erickson; M. C. Soteriou, Combustion and Flame (2011)

25. P. A. Monkewitz, in: Department of Mechanical, Aerospace, and Nuclear Engineering: Los Angeles, CA, 1988.
26. J. Beer; N. Chigier, Combustion Aerodynamics, John Wiley and Sons, New York, 1972.
27. R. G. Bill, Jr.; K. Tarabanis, Combustion Science and Technology 47 (1986) 39-53
28. B. Kiel; K. Garwick; A. Lynch; J. R. Gord; T. Meyer, in: *42nd AIAA/ASME/SAE/ASEE Joint Propulsion Conference & Exhibit*, Sacramento, California, 2006.
29. C. Cross; A. Fricker; D. Shcherbik; E. Lubarsky; B. T. Zinn; J. A. Lovett, in: *ASME Turbo Expo*, Glasgow, UK, 2010.
30. J. R. Hertzberg; I. G. Shepherd; L. Talbot, Combustion and Flame 86 (1991) 1-11
31. S. Yamaguchi; N. Ohiwa; T. Hasegawa, Combustion and Flame 62 (1985) 31-41
32. J. T. Yang; C. W. Yen; G. L. Tsai, Combustion and Flame 99 (1994) 288-294
33. W. Kim; J. Lienau; P. van Slooten; M. Colket; R. Malecki; S. Syed, Journal of Engineering for Gas Turbines and Power 128 (2006) 40-48
34. B. Karlovitz; D. W. Denniston; D. H. Knapschaefer; F. E. Wells, Proceedings of the Combustion Institute 4 (1953) 613-620
35. K. R. Anderson; J. Hertzberg; S. Mahalingam, Combustion Science and Technology 112 (1) (1996) 257-269
36. J. A. Lovett; T. P. Brogan; D. S. Philippona; B. V. Keil; T. V. Thompson, in: *40th AIAA/ASME/SAE/ASEE Joint Propulsion Conference and Exhibit*, Fort Lauderdale, FL, 2004.
37. D. Aquaro; M. Pieve, Applied Thermal Engineering 27 (2-3) (2007) 389-400
38. A. Roshko, AIAA Journal 14 (1976) 1349-1357
39. R. E. D. Bishop; A. Y. Hassan, Proceedings of the Royal Society of London. Series A, Mathematical and Physical Sciences 277 (1368) (1964) 51-75
40. N. Ferguson; G. V. Parkinson, J. Engng Ind. 89 (4) (1967)
41. Y. Tanida; A. Okajima; Y. Watanabe, Journal of Fluid Mechanics 61 (4) (1973) 769-784
42. P. K. Stansby, Journal of Fluid Mechanics 74 (4) (1976) 641-665
43. O. M. Griffin; S. E. Ramberg, Journal of Fluid Mechanics 75 (2) (1976) 257-271
44. C. Barbi; D. P. Favier; C. A. Maresca; D. P. Telionis, Journal of Fluid Mechanics 170 (1986) 257-544
45. T. C. Lieuwen, Unsteady Combustor Physics, Cambridge University Press, New York, NY, 2012.
46. F. H. Abernathy; R. E. Kronauer, Journal of Fluid Mechanics 13 (1) (1962) 1-20
47. S. R. Chakravarthy; R. Sivakumar; O. J. Shreenivasan, Sadhana 32 (1-2) (2007) 145-154
48. T. Lieuwen, Unsteady Combustor Physics, Cambridge University Press, 2012.
49. V. Acharya; B. Emerson; U. Mondragon; D.-H. Shin; C. Brown; V. McDonell; T. Lieuwen, Combustion Science and Technology (Accepted January, 2012)
50. B. Emerson; U. Mondragon; V. Acharya; D.-H. Shin; C. Brown; V. McDonell; T. Lieuwen, Combustion Science and Technology (Accepted January, 2012)
51. T. Lieuwen; R. Rajaram; Y. Neumeier; S. Nair, Proceedings of the Combustion Institute 29 (2002) 1809-1815

52. S. Chaudhuri; S. Kostka; M. W. Renfro; B. M. Cetegen, Combustion and Flame 157 (2010) 790-802
53. S. Chaudhuri; S. Kostka; S. G. Tuttle; M. W. Renfro; B. M. Cetegen, in: *48th AIAA Aerospace Sciences Meeting and Exhibit*, Orlando, Florida, 2010.
54. A. Melling, Measurement Science and Technology 8 (1997) 1406-1416
55. R. Mei, Experiments in Fluids 22 (1996) 1-13
56. A. G. Gaydon; H. G. Wolfhard, Flames: their structure, radiation and temperature, Chapman and Hall, London, 1970.
57. C.-M. Ho; P. Huerre, in: University of Southern California: Los Angeles, 1984.
58. H. Schlichting; K. Gersten, Boundary-Layer Theory, Springer, Verlag Berlin Heidelberg, 2000.
59. J. C. Pan; M. D. Vangsness; D. R. Ballal, Journal of Engineering for Gas Turbines and Power 114 (October) (1992) 783-789
60. A. E. Potter, Jr. ; E. L. Wong, in: National Advisory Committee on Aeronautics: Cleveland, OH, 1958.
61. B. Kiel; K. Garwick; A. Lynch; A. Gord, in: *45th AIAA Aerospace Sciences Meeting & Exhibit*, Reno, Nevada, 2007.
62. S. J. Shanbhogue; D.-H. Shin; S. Hemchandra; D. Plaks; T. Lieuwen in: *Flame-sheet dynamics of bluff-body stabilized flames using longitudinal acoustic forcing.*, Proceedings of the Combustion Institute, 2009; 2009.
63. M. P. Juniper in: *Absolute and Convective Instability in Gas Turbine Fuel Injectors*, Proceedings of ASME Turbo Expo 2012: Power for Land, Sea and Air, Copenhagen, Denmark, 2012; Copenhagen, Denmark, 2012.
64. S. J. Rees. Hydrodynamic instability of confined jets & wakes and implications for gas turbine fuel injectors. University of Cambridge, 2009.
65. S. J. Rees; M. Juniper, Journal of Fluid Mechanics 656 (2010) 309-336
66. L. Raynal; J.-L. Harion; M. Favre-Marinet; G. Binder, Physics of Fluids 8 (1996)
67. J. W. Nichols; P. J. Schmid; J. J. Riley, Journal of Fluid Mechanics 582 (2007) 341-376
68. M. Furi; P. Papas; R. M. Rais; P. A. Monkewitz, Proceedings of the Combustion Institute 29 (2002) 1653-1661
69. R. R. Erickson; M. C. Soteriou, Combustion and Flame 158 (12) (2011)
70. E. Baudoin; R. Yu; Bai; K. J. Nogenmyr; X. S. Bai; C. Fureby, in: *47th AIAA Aerospace Sciences Meeting Including The New Horizons Forum and Aerospace Exposition*, Orlando, FL, 2009; Vol. AIAA-2009-1178
71. R. R. Erickson; M. C. Soteriou; P. G. Mehta, in: *44th AIAA Aerospace Sciences Meeting & Exhibit*, Reno, Nevada, 2006; Vol. AIAA Paper No. 2006-753.
72. R. D. Henderson; D. Barkley, Physics of Fluids 8 (1996) 1683-1685
73. C. Godreche; P. Manneville, Hydrodynamics and Nonlinear Instabilities, University Press, Cambridge, Cambridge, 1998.
74. S. B. Pope, Turbulent Flows, Cambridge University Press, 2000.
75. A. N. Kolmogorov, Journal of Fluid Mechanics 13 (1) (1962) 82-85
76. K. N. Rao; R. Narasimha; M. A. B. Narayanan, Journal of Fluid Mechanics 48 (2) (1971) 339-352
77. M. Kholmyansky; L. Moriconi; A. Tsinober, Physical Review E 76 (2007)
78. M. M. Rai, Journal of Fluid Mechanics 659 (2010) 375-404

79. R. C. Hilborn, Chaos and Nonlinear Dynamics, Oxford University Press, New York, 1994.
80. Y. Pomeau; P. Manneville, Communications in Mathematical Physics 74 (1980) 189-197
81. W. Horsthemke; R. Lefever, Noise Induced Transitions, Springer-Verlag, Berlin Heidelberg New York Tokyo, 1984.
82. I. C. Waugh; M. P. Juniper, International journal of spray and combustion dynamics 3 (3) (2011) 225-242
83. F. M. White, Viscous Fluid Flow, McGraw-Hill, New York, 2006.
84. T. Schuller; S. Ducruix; D. Durox; S. Candel, Proceedings of the Combustion Institute 29 (1) (2002) 107-113
85. A. A. S. Choudhury; S. L. Shah; N. F. Thornhill, Diagnosis of Process Nonlinearities and Valve Stiction, Springer, 2008.
86. C. L. Nikias; A. P. Petropulu, Higher-order Spectra Analysis- A Nonlinear Signal Processing Framework, PTR Prentice-Hall, Inc, Upper Saddle River, NJ, 1993.
87. M. J. Hinich, Journal of Time Series Analysis 3 (3) (1982) 169-176
88. A. Swami; J. M. Mendel; C. L. Nikias, in: United Signals & Systems, Inc: 1993.
89. B. Emerson; J. O'Connor; M. Juniper; T. Lieuwen, Journal of Fluid Mechanics 706 (2012)